UCLA
UCLA Electronic Theses and Dissertations

Title
Magnetic Topological Insulator and Quantum Anomalous Hall Effect

Permalink
https://escholarship.org/uc/item/2xr7g7nz

Author
Kou, Xufeng

Publication Date
2015

Peer reviewed|Thesis/dissertation

eScholarship.org Powered by the California Digital Library
University of California

UNIVERSITY OF CALIFORNIA

Los Angeles

Magnetic Topological Insulators and Quantum Anomalous Hall Effect

A dissertation submitted in partial satisfaction of the

requirements for the degree Doctor of Philosophy

in Electrical Engineering

by

Xufeng Kou

2015

© Copyright by

Xufeng Kou

2015

ABSTRACT OF THE DISSERTATION

Magnetic Topological Insulators and Quantum Anomalous Hall Effect

by

Xufeng Kou

Doctor of Philosophy in Electrical Engineering

University of California, Los Angeles, 2015

Professor Kang Lung Wang, Chair

The engineering of topological surface states is a key to realize applicable devices based on topological insulators (TIs). Among various proposals, introducing magnetic impurities into TIs has been proven to be an effective way to open a surface gap and integrate additional ferromagnetism with the original topological order. In this Dissertation, we study both the intrinsic electrical and magnetic properties of the magnetic TI thin films grown by molecular beam epitaxy. By doping transition element Cr into the host tetradymite-type V-VI semiconductors, we achieve robust ferromagnetic order with a strong perpendicular magnetic anisotropy. With additional top-gating capability, we realize the electric-field-controlled ferromagnetism in the magnetic TI systems, and demonstrate such magneto-electric effects can be effectively manipulated, depending on the interplays between the band topology, magnetic exchange coupling, and structural engineering.

Most significantly, we report the observation of quantum anomalous Hall effect (QAHE) in the Cr-doped $(BiSb)_2Te_3$ samples where dissipationless chiral edge conduction is realized in the macroscopic millimeter-size devices without the presence of any external magnetic field, and the stability of the quantized Hall conductance of e^2/h is well-maintained as the film thickness varies across the 2D hybridization limit. With additional quantum confinement, we discover the metal-to-insulator switching between two opposite QAHE states, and reveal the universal QAHE phase diagram in the thin magnetic TI samples.

In addition to the uniform magnetic TIs, we further investigate the TI/Cr-doped TI bilayer structures prepared by the modulation-doped growth method. By controlling the magnetic interaction profile, we observe the Dirac hole-mediated ferromagnetism and develop an effective way to manipulate its strength. Besides, the giant spin-orbit torque in such magnetic TI-based heterostructures enables us to demonstrate the current-induced magnetization switching with the critical current density much lower than other heavy metal/magnet systems. Our work on the magnetic TIs and their heterostructures thus unfolds new avenues for novel multifunctional nano-electronics and non-volatile spintronic applications.

The dissertation of Xufeng Kou is approved.

Benjamin Williams

Louis Bouchard

Oscar M. Stafsudd

Kang Lung Wang, Committee Chair

University of California, Los Angeles

2015

Long as the way is; I see no ending.

Yet I will search high and low with my will unbending.

– Yuan Qu

Table of Contents

Chapter 1_Introduction 1

1.1. The emergence of spintronics 3

1.2. Topological Insulators 6

1.2.1. Quantum spin Hall insulator and band inversion... 8

1.2.2. Discovery of QSHE in two-dimensional Topological Insulators 12

1.2.3. Extend Topological Insulators to three dimension 14

1.3. Magnetic Topological Insulators 16

1.3.1. Break the time-reversal-symmetry of Topological Insulators 17

1.3.2. Integrate magnetic order into Topological Insulators 18

1.3.3. RKKY interaction 20

1.3.4. Van Vleck mechanism and carrier-independent ferromagnetism................ 21

1.4. Organization 24

Chapter 2_Quantum Hall Trio 26

2.1. A brief history of Hall family 26

2.1.1. Scattering mechanisms of anomalous Hall effect 28

2.1.2. Spin Hall effect 30

2.2. Quantum Hall effect 32

2.2.1. The Discovery of integer Quantum Hall effect 32

2.2.2. The TKNN number in the integer quantum Hall effect 36

2.2.3. Quantum Hall effect in Dirac fermions systems 38

2.3. Quantum spin Hall effect 45

2.4. Quantum anomalous Hall effect 47

2.4.1. Construct QAHE from QSHE in a 2D System 48

2.4.2. Observation of QAHE in 5 QL $Cr_{0.15}(Bi_{0.1}Sb_{0.9})_{1.85}Te_3$ Film 50

2.4.3. Scale-invariant quantum anomalous Hall effect 52
2.5. Summary of Chapter 2 55

Chapter 3_Molecular Beam Epitaxy Growth of Magnetic Topological Insulators 57
3.1. Molecular beam epitaxy 58
3.2. Reflection High Energy Electron Diffraction 62
3.3. Magnetic topological insulators thin films growth 68
3.3.1. Crystal structure of 3D topological insulators 69
3.3.2. Cr-doped Bi_2Se_3 films grown on Si (111) 71
3.3.3. Cr-doped $(BiSb)_2Te_3$ films grown on GaAs (111)B 74
3.4. Superconducting Quantum Interference Device 81
3.4.1. SQUID results of $Bi_{2-x}Cr_xSe_3$ systems 81
3.4.2. SQUID results of $Cr_y(Bi_xSb_{1-x})_{2-y}Te_3$ systems 85
3.5. Magneto-transport measurement 86
3.6. Summary of Chapter 3 89

Chapter 4_Interplay between Different Magnetisms in Cr-Doped Topological Insulators 90
4.1. Electric-field-controlled anomalous Hall effect 90
4.2. Hole-mediated RKKY interaction in Cr-doped $(BiSb)_2Te_3$ system 95
4.3. Interplay between different FM orders – magnetic doping level 97
4.4. Interplay between different FM orders – band topology 102
4.5. Summary of Chapter 4 105

Chapter 5_Quantum Anomalous Hall Effect in Magnetic Topological Insulators 106
5.1. Observation of QAHE in the Cr-doped $(BiSb)_2Te_3$ thin films 107

5.2. Landauer-Büttiker Formalism 114

5.3. Physical Explanations about Chiral/Helical Edge Conductions 117

5.4. Dissipative side-surface edge conduction 120

5.5. Non-local transport measurements 123

5.6. Re-capturing the quantum Hall trio 128

5.7. Metal-to-insulator switching in quantum anomalous Hall states 131

5.8. Mapping the semicircle QAHE phase diagram 139

5.9. Summary of Chapter 5 145

Chapter 6_Surface-related Ferromagnetism and Giant Spin-Orbit Torques in Magnetic Topological Insulator Heterostructures 148

6.1. TI/Cr-doped TI heterostructures by MBE 149

6.2. Polar-mode MOKE measurements 152

6.3. Surface-related ferromagnetism in TI/Cr-doped TI heterostructures 156

6.4. Dirac-fermion-related ferromagnetism 163

6.5. TI/Cr-doped TI bilayer model 167

6.6. Current-induced magnetization switching in TI/Cr-doped TIs 169

6.7. Giant spin-orbit torque in TI/Cr-doped TI heterostructures 173

6.8. Summary of Chapter 6 176

Chapter 7_Conclusion and Perspective 178

References 184

List of Figures

Figure 1-1. Overview of Si-based MOSFETs. 3

Figure 1-2. Comparison between electronics and spintronics. 5

Figure 1-3. Topological Insulators and the spin-momentum locking mechanism. 8

Figure 1-4. HgTe-CdTe quantum wells. 10

Figure 1-5. Experimental observations of quantum spin Hall effect in the HgTe/CdTe QWs. 13

Figure 1-6. Experimental observation of quantum spin Hall effect in the InAs/GaSb QWs. . 14

Figure 1-7. TRS-breaking magnetic topological insulators. 17

Figure 1-8. Carrier-independent long-range ferromagnetic order in magnetic TI thin films. . 23

Figure 2-1. The Hall effects. 27

Figure 2-2. Illustration of the three main mechanisms that can give rise to an AHE. 30

Figure 2-3. Illustration of the connected family of the spin-dependent Hall effects. 31

Figure 2-4. Quantum oscillations and quantum Hall effect observed in Si-FETs. 33

Figure 2-5. Landau levels in 2DEG. 35

Figure 2-6. Quantum Hall effect in graphene systems. 40

Figure 2-7. Fan diagram for SdH oscillations in graphene. 42

Figure 2-8. Quantum Hall effect in 3D Topological Insulators. 44

Figure 2-9. Analogy between QHE and QSHE. 46

Figure 2-10. Transition between QSHE and QHE. 47

Figure 2-11. Construct quantum anomalous Hall in 2D regime. 50

Figure 2-12. The QAH effect in the 5QL $Cr_{0.15}(Bi_{0.1}Sb_{0.9})_{1.85}Te_3$ film. 52

Figure 2-13. Quantum anomalous Hall effect beyond 2D regime. 55

Figure 3-1. Solid-source MBE system designed for magnetic TIs growth. 60

Figure 3-2. Vacuum gauges used in the MBE system. 62

Figure 3-3. Schematic diagram of a RHEED system.. 63

Figure 3-4. Ewald sphere for the construction of RHEED pattern. 65

Figure 3-5. RHEED pattern for MBE-grown TI films... 66

Figure 3-6. Layer-by-layer and Step-flow growth modes. 68

Figure 3-7. Crystal structure of 3D TIs and energy gap-lattice constant chart. 70

Figure 3-8. Cr-doped Bi_2Se_3 thin film grown on H^+-terminated Si (111) substrate. 72

Figure 3-9. Tunable $(Bi_xSb_{1-x})_2Te_3$ compound TI system. 75

Figure 3-10. Cr-doped $(Bi_xSb_{1-x})_2Te_3$ grown on GaAs (111)B substrate. 77

Figure 3-11. Crystalline structure and doping profile of the $Cr_{0.2}(Bi_{0.5}Sb_{0.5})_{1.8}Te_3$ thin film. 79

Figure 3-12. Cross-sectional TEM and EDX near the TI/GaAs interface. 80

Figure 3-13. SQUID results of the 50 QL $Bi_{1.9}Cr_{0.1}Se_3$ sample grown on the Si (111) substrate. 83

Figure 3-14. Arrott-Noakes plots of the 50 QL $Bi_{1.9}Cr_{0.1}Se_3$ sample grown on the Si (111) substrate. 84

Figure 3-15. SQUID results of the 50 QL $Cr_{0.3}(Bi_{0.5}Sb_{0.5})_{1.7}Te_3$ sample grown on the GaAs (111)B substrate. 86

Figure 3-16. Magneto-transport measurement of 6 QL $Cr_{0.2}(Bi_{0.5}Sb_{0.5})_{1.8}Te_3$ thin film. 88

Figure 4-1. Top-gated Hall bar device structure used for exploring the gate-dependent anomalous Hall effect... 91

Figure 4-2. Gate-dependent anomalous Hall results for the 6 QL $Cr_{0.04}(Bi_{0.5}Sb_{0.5})_{1.96}Te_3$ sample.. 92

Figure 4-3. Electric-field-controlled ferromagnetism in the 6 QL $Cr_{0.04}(Bi_{0.5}Sb_{0.5})_{1.96}Te_3$ sample.. 94

Figure 4-4. Energy band diagram and DOS distribution of Cr-doped 3D TIs. 96

Figure 4-5. Gate-dependent AHE results for 6 QL $Cr_y(Bi_{1-x}Sb_x)_2Te_3$ thin films with different Cr doping concentrations.. 100

Figure 4-6. Gate-dependent Magneto-resistance for $Cr_y(Bi_{1-x}Sb_x)_2Te_3$ thin films with different Cr doping concentrations.. 102

Figure 4-7. Magnetic doping effect on the band topology of the Cr-doped Bi_2Se_3 systems. 104

Figure 5-1. Cr-doped $(Bi_xSb_{1-x})_2Te_3$ film structure and properties. 108

Figure 5-2. Anomalous Hall measurement of the 10 QL $Cr_{0.24}(Bi_{0.3}Sb_{0.7})_{1.76}Te_3$ film. 110

Figure 5-3. QAHE in the $Cr_{0.24}(Bi_{0.3}Sb_{0.7})_{1.76}Te_3$ thin films. 111

Figure 5-4. Importance of the Fermi level position on the QAHE state. 112

Figure 5-5. Quantum Anomalous Hall effect on the 10 QL $Cr_{0.4}(Bi_{0.3}Sb_{0.7})_{1.6}Te_3$ film 113

Figure 5-6. Chiral edge current conduction in the QHE/QAHE states and helical edge current conduction in the QSHE state with different device configurations. 116

Figure 5-7. Contact effect and equivalent circuit of six-terminal Hall bar in the QSHE state. 120

Figure 5-8. Non-zero longitudinal resistance in the 10 QL $Cr_{0.24}(Bi_{0.3}Sb_{0.7})_{1.76}Te_3$ film...... 121

Figure 5-9. Possible side-surface conduction in 3D magnetic TIs. 123

Figure 5-10. Field-dependent results for two non-local resistances $R_{12,16}$ and $R_{12,32}$. 124

Figure 5-11. Temperature-dependent non-local results for both the six-terminal Hall bar and the quasi H-bar devices. 127

Figure 5-12. Illustration of the quantum Hall trio. 128

Figure 5-13. Quantum anomalous Hall effect in the 6 QL $Cr_{0.24}(Bi_{0.3}Sb_{0.7})_{1.76}Te_3$ film....... 134

Figure 5-14. Quantum phase transition of quantum anomalous Hall effect. 136

Figure 5-16. Angle-dependent transport measurements in the quantum anomalous Hall regime. 141

Figure 5-17. Angle-dependent magneto-conductance (left-σ_{xy} and right-σ_{xx}) results of the 6 QL $Cr_{0.24}(Bi_{0.3}Sb_{0.7})_{1.76}Te_3$ film in the QAHE regime. 141

Figure 5-18. Universal phase diagram of quantum anomalous Hall effect in the 2D regime. 144

Figure 6-1. Modulation-doped $(Bi_xSb_{1-x})_2Te_3$ / $Cr_z(Bi_ySb_{1-y})_{2-z}Te_3$ bilayer structure........... 150

Figure 6-2. Optimization of the TI/Cr-doped TI bilayer structures. 152

Figure 6-3. Schematic optical bench setup of the polar MOKE measurement. 153

Figure 6-4. Temperature-dependent magnetization MOKE measurement. 156

Figure 6-5. Ambipolar effects and gate-modulations in TI/Cr-doped TI samples. 157

Figure 6-6. Surface-mediated magneto-electric effects in TI/Cr-doped TI bilayers. 159

Figure 6-7. Manipulation of surface-related ferromagnetism in TI/Cr-doped TI heterostructures. 162

Figure 6-8. Optimization of surface-related ferromagnetism. 163

Figure 6-9. The range functions of surface-related RKKY interaction with fixed exchange parameter. 166

Figure 6-10. Coupling between surface carriers and magnetic dopants. 169

Figure 6-11. Bilayer structures used for the SOTs study. 170

Figure 6-12. Magnetization switching due to the SOT induced by an in-plane DC current. 171

Figure 6-13. Giant spin-orbit torque realized in the TI/Cr-doped TI structures. 175

Acknowledgements

I am extremely grateful to the community of people that facilitated this work. First of all, my completion of these research projects on magnetic topological insulators could not have been accomplished without the instructions and support from my PhD advisor, Prof. Kang L. Wang. I am entirely grateful for his kindness, endless patience and enthusiasm. Prof. Wang's rich experience and unmatched wisdom have provided me the best opportunities to work in the frontiers of semiconductor device and physics fields. Although he is running such a large research lab, he is always right there to give me the most instructive suggestions and directions whenever I am in trouble with my research. Besides, his passion and persistence towards research and life have all influenced me a lot when I am building my own career.

I would also like to express my great gratitude to my committee members: Prof. Louis Bouchard, Prof. Oscar M. Stafsudd, and Prof. Benjamin Williams, for their great kindness and help during my PhD study. I greatly appreciate their time and deep consideration of the work presented here, and I will always cherish the insightful guidance and collaborations they offered at UCLA. Besides, I especially appreciate all the outside collaborations (Prof. Yong Wang at Zhejiang University for his beautiful TEM work, Dr. Alexei V. Fedorov at Lawrence Berkeley National Laboratory for his excellent ARPES study, Prof. Shou-Cheng Zhang and Dr. Jing Wang at Stanford University for their insightful theoretical support, Prof. Wei-Li Lee at Institute of Physics in Taiwan and Dr. Eun-Sang Choi at National High Magnetic Field Lab in Tallahassee for their great help with the low-temperature

magneto-transport measurements). Without the great help and efforts from them, we cannot achieve all the research highlights which I am truly proud of. In addition, I also would like to thank Dr. Yang Du at Qualcomm Inc. for his extraordinary guidance during my Qualcomm Innovation fellowship project between 2012 and 2013.

My PhD life could not been so wonderful without members of the Device Research Laboratory. In particular, I would first give my special thanks to Prof. Faxian Xiu and Prof. Liang He: it was Prof. Xiu (and Prof. Wang) who brought me into the MBE world, and it was Prof. He who led me carry out most the work on TI. I also greatly appreciate Dr. Wanjun Jiang who had done a great deal to assist me when I was dealing with the magnetic TI study. Their passion and attitude toward work and research set up the highest example and standard for my future career. I am additionally thankful for my dear colleagues. Dr. Murong Lang, Yabin Fan, and I are the same year graduate students; in the past five years, we have been working so efficiently as a team to explore the TI world. All the TI devices I investigated were all fabricated by Murong, and Yabin provided me with the best ideas and suggestions ever since we started to explore the magnetic TI area. In the meanwhile, I would like to thank Lei Pan, Dr. Koichi Murata, Dr. Tianxiao Nie who helped me a lot on the MBE growth, Dr. Jianshi Tang and Li-Te Chang on the device measurement part, and Pramey Upadhyaya and Qiming Shao for their great help on the theory part.

Finally, there are no other words in the world to express my deepest gratitude to my unbelievably supportive family and friends. I want to thank my parents and my wife, for their

unconditional love and support, for encouraging and helping me to break through anything even seemingly impossible.

In this Dissertation, Chapters 3 and 4 are based on two of our manuscripts titled with "Magnetically doped semiconducting topological insulators" and "Interplay between different magnetisms in Cr-doped topological insulators". Chapter 5 describes work from two of our manuscripts titled with "Scale-invariant quantum anomalous Hall effect in magnetic topological insulators beyond two-dimensional limit" and "Mapping the global phase diagram of quantum anomalous Hall effect". Chapter 6 relates to two of our manuscripts titled with "Manipulating surface-related ferromagnetism in modulation-doped topological insulators" and "Magnetization switching through giant spin-orbit torque in a magnetically doped topological insulator heterostructure".

I also gratefully acknowledge sources of financial support for this work. Studies presented in Chapters 3-6 of this Dissertation are supported by the DARPA Meso program under contract No.N66001-12-1-4034 and N66001-11-1-4105, and the ARO program under contract No.W991NF-14-1-0607. I also acknowledge the support from the Western Institute of Nanoelectronics (WIN) and the support from the FAME Center sponsored by MARCO and DARPA. A portion of this work is performed at the National High Magnetic Field Laboratory, which is supported by National Science Foundation Cooperative Agreement No.DMR-1157490 and the State of Florida. Xufeng Kou is also partially supported by the Qualcomm Innovation Fellowship (2012-2013).

VITA

Education:

2009 B.S. in Optical Engineering
Zhejiang University
Hangzhou, China

2012 M.S. in Electrical Engineering
University of California, Los Angeles
Los Angeles, California

Employment:

2009-2015 Graduate Student Researcher
Department of Electrical Engineering
University of California, Los Angeles
Los Angeles, California

Publications (*co-first author):

X.F Kou, Y.B Fan, M.R Lang, P. Upadhyaya, and K.L Wang, Magnetic topological insulators and quantum anomalous Hall effect. *Solid State Commun.* (2014 in press)

X.F Kou*, S.T Guo*, Y.B Fan*, L. Pan, M.R Lang, *et al.,* Scale-invariant quantum anomalous Hall effect in magnetic topological insulators beyond two-dimensional limit. *Phys. Rev. Lett.* 113, 137201 (2014)

Y.B Fan*, P. Upadhyaya*, **X.F Kou***, M.R Lang, S. Takei, *et al.,* Magnetization switching through giant spin-orbit torque in a magnetically doped topological insulator heterostructures. *Nature Materials* 13, 699-704 (2014)

X.F Kou*, L. He*, M.R Lang*, Y.B Fan, K. Wong, *et al.,* Manipulating surface-related ferromagnetism in modulation-doped topological insulators. *Nano Lett.* 13, 4587-4593 (2013)

X.F Kou, M.R Lang, Y.B Fan, Y. Jiang, *et al.,* Interplay between different magnetisms in Cr-doped topological insulators. *ACS Nano* 7, 9205-9212 (2013)

L. He*, **X.F Kou***, M.R Lang*, E.S Choi, Y. Jiang, *et al.* Evidence of the two surface states of $(Bi_{0.53}Sb_{0.47})_2Te_3$ films grown by van der Waals epitaxy. *Scientific Reports*, 3:3406 (2013)

M.R Lang*, L. He*, **X.F Kou***, P. Upadhyaya, Y.B Fan, *et al.,* Competing weak localization and weak antilocalization in ultrathin topological insulators. *Nano Lett*. 13, 48-53 (2013)

X.F Kou, W.J Jiang, M.R Lang, F.X Xiu, *et al.,* Magnetically doped semiconducting topological insulators. *J. Appl. Phys.*112, 063912 (2012)

X.F Kou, L. He, F.X Xiu, M.R Lang, *et al.,* Epitaxial growth of high mobility of Bi_2Se_3 thin film on CdS. *Appl. Phys .Lett.* 98*,* 242102 (2011)

X.F Kou, G. Vienne, and G.H. Wang, Modeling light Propagation through taper-microfiber structures integrated on substrates. *Chinese Optics Lett.*, 8, 560-563 (2010)

A.J Bestwick, E.J Fox, **X.F Kou**, L. Pan, K.L Wang, and D. Goldhaber-Gordon, Precise quantization of the anomalous Hall effect near zero magnetic field, *Phys. Rev. Lett.* 114, 187201 (2015)

T.X Nie, **X.F Kou**, J.S Tang, Y.B Fan, *et al.,* Supperlattice of Fe_xGe_{1-x} nanodots and nanolayers of spintronics application, *Nanotechnology* 25, 505702 (2014)

J.S Tang, L.T Chang, **X.F Kou**, K. Murata, E.S Choi, *et al.,* Electrical detection of spin-polarized surface states conduction in $(Bi_{0.53}Sb_{0.47})_2Te_3$ topological insulator. *Nano Lett.*14, 5423-5429 (2014)

M.R Lang, M. Montazeri, M.C Onbasli, **X.F Kou**, Y.B Fan, P. Upadhyaya, *et al.*, Proximity induced high-temperature magnetic order in topological insulator-ferrimagnetic insulator heterostructure. *Nano Lett.* 14, 3459-3465 (2014)

L. He, **X.F Kou**, and K.L Wang, Review of 3D topological insulator thin-film growth by molecular beam epitaxy and potential applications. *Phys. Status Solidi RRL* 7, 50-63(2013)

Y. Jiang, Y. Wang, J. Sagendorf, D. West, **X.F Kou**, X. Wei, L. He, K.L Wang, S.B Zhang, and Z. Zhang, Direct atom-by-atom chemical identification of nanostructures and defects of topological insulators. *Nano Lett.* 13, 2851-2856 (2013)

K.W Post, B.C Chapler, L. He, **X.F Kou**, K.L Wang, and D.N Basov, Thickness-dependent bulk electronic properties in Bi_2Se_3 thin films revealed by infrared spectroscopy. *Phys. Rev. B* 88, 075121 (2013)

J.M Zhang, W.M Ming, Z.G Huang, G.B Liu, **X.F Kou**, Y.B Fan, K.L Wang, and Y.G Yao, Stability electronic, and magnetic properties of the magnetically doped topological insulators: Bi_2Se_3, Bi_2Te_3, and Sb_2Te_3. *Phys. Rev. B* 88, 235131 (2013)

X.X Yu, L. He, M.R Lang, W.J Jiang, F.X Xiu, Z.M Liao, Y. Wang, **X.F Kou**, P. Zhang, J.S Tang, G. Huang, J. Zou and K.L Wang, Separation of top and bottom surface conduction in Bi_2Te_3 thin films. *Nanotechnology* 24, 015705(2013)

C.P Chu, S. Arafin, T.X Nie, K.Y Yao, **X.F Kou**, L. He, C.Y Wang, *et al.,* Nanoscale growth of GaAs on patterned Si(111) substrate by Molecular Beam Epitaxy. *Cryst. Growth Des.*, 14(2), 593-598 (2013)

W.J Jiang, Y.B Fan, P. Upadhyaya, M.R Lang, M.S Wang, L.T Chang, K. Wong, J.S Tang, M. Lewis, J. Zhao, L. He, **X.F Kou**, C.F Zeng, X.Z Zhou, R.N. Schwartz, and K.L Wang, Mapping the Domain Wall Pinning Profile by Stochastic Imaging Reconstruction. *Phys. Rev. B* 87, 014427(2013)

F.X Xiu, N. Meyer, **X.F Kou**, L. He, M.R Lang, *et al*., Quantum Capacitance in Topological Insulators. *Scientific Reports*, 2:669/1-7 (2012)

L.H Bao, L. He, N. Meyer, **X.F Kou**, P. Zhang, Z.G Chen, *et al.,* Weak anti-localization and quantum oscillations of surface states in Topological Insulator Bi_2Se_2Te. *Scientific Reports*, 2:726/1-7 (2012)

L. He, F.X Xiu, X.X Yu, M. Teague, W.J Jiang, Y.B Fan, **X.F Kou**, M.R Lang, Y. Wang, G. Huang, N.C Yeh, and K.L Wang, Surface-dominated conduction in a 6 nm thick Bi_2Se_3 thin film. *Nano. Lett.*12 (2012)

Y. Wang, F.X Xiu, L. Cheng, L. He, M.R Lang, J.S Tang, **X.F Kou**, X.X Yu, X.W Jiang, Z.G Chen, J. Zou, and K.L Wang, Gate-controlled surface conduction in Na-doped Bi_2Te_3 topological insulator nanoplates. *Nano. Lett.* 12 (2012)

M.R Lang, L. He, F.X Xiu, X.X Yu, J.S Tang, Y. Wang, **X.F Kou**, W.J Jiang, A.V. Fedorov, and K.L Wang, Revelation of topological surface in Bi_2Se_3 thin films by in situ Al passivation. *ACS Nano*, 6, 295-302 (2012)

F.X. Xiu, L. He, Y. Wang, L. Cheng, L.T. Chang, M.R. Lang, G. Huang, **X.F. Kou**, Y. Zhou, X.W. Jiang, Z.G. Chen, J. Zou, A. Shailos, and K.L. Wang, Manipulating surface states in topological insulator nanoribbons. *Nature Nanotechnology*, 6, 216-221 (2011)

L. He, F.X Xiu, Y. Wang, A.V Fedorov, G. Huang, **X.F Kou**, M.R Lang, W.P Beyermann, J. Zou, and K.L Wang, Epitaxial Growth of Bi_2Se_3 Topological Insulator Thin Film on Si (111). *J. Appl. Phys.*109, 103702 (2011)

F.X. Xiu, Y. Wang, **X.F. Kou**, P.Upadhyaya, Y.Zhou, J.Zou, and K.L Wang, Synthesis of

high Curie temperature $Fe_{0.02}Ge_{0.98}$ quantum dots. *J. Am. Chem. Soc.*, 132, 11425-11427 (2011)

Y. Wang, Z.M Liao, H.Y Xu, F.X Xiu, **X.F Kou**, Y. Wang, K.L Wang, J. Drennan, and J. Zou, Structural evolution of GeMn/Ge supperlattice grown by molecular beam epitaxy under different growth conditions. *Nano. Res. Lett.* 6, 624 (2011)

F.X. Xiu, Y. Wang, J.Y. Kim, P. Upadhyaya, Y. Zhou, **X.F. Kou**, W. Han, R.K. Kawakami, J. Zou, and K.L. Wang, Room-temperature electric-field controlled ferromagnetism in $Mn_{0.05}Ge_{0.95}$ quantum dots. *ACS Nano*, 4(8), 4948-4954 (2010)

F.X. Xiu, Y. Wang, K. Wong, Y. Zhou, **X.F. Kou**, J. Zou, and K.L. Wang, MnGe magnetic nanocolumns and nanowells. *Nanotechnology*, 21, 255602, (2010)

F.X. Xiu, I.V. Oychinnikov, P. Upadhyaya, K. Wong, **X.F. Kou**, Y. Zhou, and K.L. Wang, Voltage-controlled ferromagnetic order in MnGe quantum dots. *Nanotechnology*, 21, 357606, (2010)

Y. Wang, F.X. Xiu, Y. Wang, H.Y. Xu, D. Li, **X.F. Kou**, K.L. Wang, A.P. Jacob, and J. Zou, Effect of Mn concentration and growth temperature on nanostructures and magnetic properties of $Ge_{1-x}Mn_x$ grown on Si. *J. Crystal Growth* 20, 3034-3039 (2010)

Y. Wang, F.X. Xiu, Y. Wang, **X.F. Kou**, A.P. Jacob, K.L. Wang, and J. Zou, Mn-rich clusters in GeMn magnetic semiconductors: Structural evolution and magnetic property. *J. Alloys and Compounds* 2, 273-377 (2010)

F. Papoff and **X.F. Kou**, Spatial distribution of the total field of a spherical scatterer. *Opto-Electronic Eng.* 35, 137-144 (2008)

Presentations:

X.F Kou, Y.B Fan, L. Pan *et al.*, Investigation of quantum anomalous Hall effect in Magnetic topological insulators. *APS March Meeting*, San Antonio TX, 2015.

X.F Kou, L. He, M.R Lang, *et al.*, Manipulating surface-induced ferromagnetism in modulation-doped topological insulators. *APS March Meeting*, Baltimore MD, 2013.

X.F Kou, L. He, F.X Xiu, *et al.,* Epitaxial growth of high quality Bi_2Se_3 thin films on CdS. *APS March Meeting*, Boston MA, 2012.

L. He, **X.F Kou**, M.R Lang, *et al.,* Evidence of the two surface states of $(Bi_{0.53}Sb_{0.47})_2Te_3$ films grown by van der Waals epitaxy. *APS March Meeting*, Denver CO, 2014.

T.X Nie, **X.F Kou**, Y.B Fan, *et al.,* MBE growth of Si/MnGe quantum dot superlattice with Curie temperature beyond 400 K. *APS March Meeting*, Denver CO, 2014.

Y.B Fan, P. Upadhyaya, **X.F Kou**, M.R Lang, *et al.,* Magnetization switching via giant spin-orbit torque in a magnetically doped topological insulator heterostructures. *APS March Meeting*, Denver CO, 2014.

M. Montazeri, M.R Lang, M.C Onbasli, **X.F Kou**, L. He, C.A Ross, and K.L Wang, Proximity effect induced magnetoresistance hysteresis loops in a topological insulator/YIG heterostructures. *APS March Meeting*, Denver CO, 2014.

L. He, X.X Yu, **X.F Kou**, M.R Lang, K.L Wang, F.X Xiu, M. Teague, and N.C Yeh, Surface-dominated conduction in a 6nm-thick Bi_2Se_3 thin film. *APS March Meeting*, Boston MA, 2012.

M.R Lang, L. He, X.X Yu, J.S Tang, **X.F Kou**, K.L Wang, and A. Federov, Clear revelation of topological surface states in Bi_2Se_3 thin films by in situ Al passivation. *APS March Meeting*, Boston MA, 2012.

G. Vienne, A. Goillet, **X.F Kou**, P. Greiu, and L. Tong, Performance of microfiber ring resonators. *11th International Conference on Materials for Advanced Technologies*, Singapore, 2009

Honors & Awards:

2012-2013	Qualcomm Innovation Fellowship
2013	Chinese Outstanding Student Abroad Scholarship

Chapter 1
Introduction

If a genius arises in art, he outlives his times; if such a critical moment occurs in the world, it transcends its own time for decades and centuries. When J. Bardeen and W.H Brattain found the current modulation effect via a third contact in their rather primitive germanium point-contact diode on December 16th 1947, they probably did not realize the forthcoming prairie fire ignited by their tiny sparkle. When we retrospect the human achievements marked in the 2nd-half of the 20th century, it is always astonishing to appreciate the fact that the third industry revolution, which is featured by electronics and information technology, has completely transformed every aspect of our civilization within the narrowest span of time in human history.

Gordon E. Moore, the co-founder of Intel Corporation, once commented that "I think information technology will create its own revolution in society over a much shorter time scale, primarily because of the semiconductor technology you are driving" [1]. As the mainstay of such information revolution, the blossom of today's semiconductor industry is built on the Si-based electronics. For more than 50 years, the Moore's Law has been successfully applied to guide the scaling strategies of CMOS technology: the number of transistors in a dense integrated circuit doubles approximately every two years [2-4]. Most importantly, by making transistors smaller, it turned out that everything got better

simultaneously – the speed of our microprocessor kept becoming faster and the system reliability improved by leaps and bounds; while the cost of doing thing electronically has dropped significantly. Unfortunately, such "scaling without tradeoffs" benefit did not last forever. In fact, even before we talked about the single-electron transistor, the energy dissipation for nanometer-scale transistors has become the most critical challenge for today's silicon industry. From the band diagram of MOSFET, we know that the turn-on voltage V_{ON} could not scale-down well due to the theoretical 60 mV/dec subthreshold swing (SS) limit, as shown in Fig. 1-1(b) [5, 6]. Under such circumstances, the dynamic power consumption is proportional to the frequency under the fixed V_{on}, given that [7, 8]

$$P_{dynamic} = ACV_{ON}^2 f \tag{1-1}$$

where A is the device size, C is the capacitance, and f is the clock frequency. As a result, in order to balance the power consumption issue, the clock frequency of the microprocessors has stopped increasing above 3 GHz since 2005, as highlighted by the red dashed line in Fig. 1-1(c) [9]. Even advanced multi-core structures and parallel computing algorithms have been adopted to compensate the frequency issue in today's CPUs, there is still another fundamental challenge limited by the physical structure of MOSFET. In particular, as the device size further scales down, the tunneling current between source and drain, and the leakage currents from the gate-oxide layer and the sub-threshold regime would contribute to larger static power consumption, as summarized in Fig. 1-1(d). In the extreme "quantum limit" case where the device dimension is 8 nm and below, we cannot even turn off the switch [10-13].

Consequently, the whole semiconductor community is now looking desperately for any alternative solution in the upcoming post-Si era.

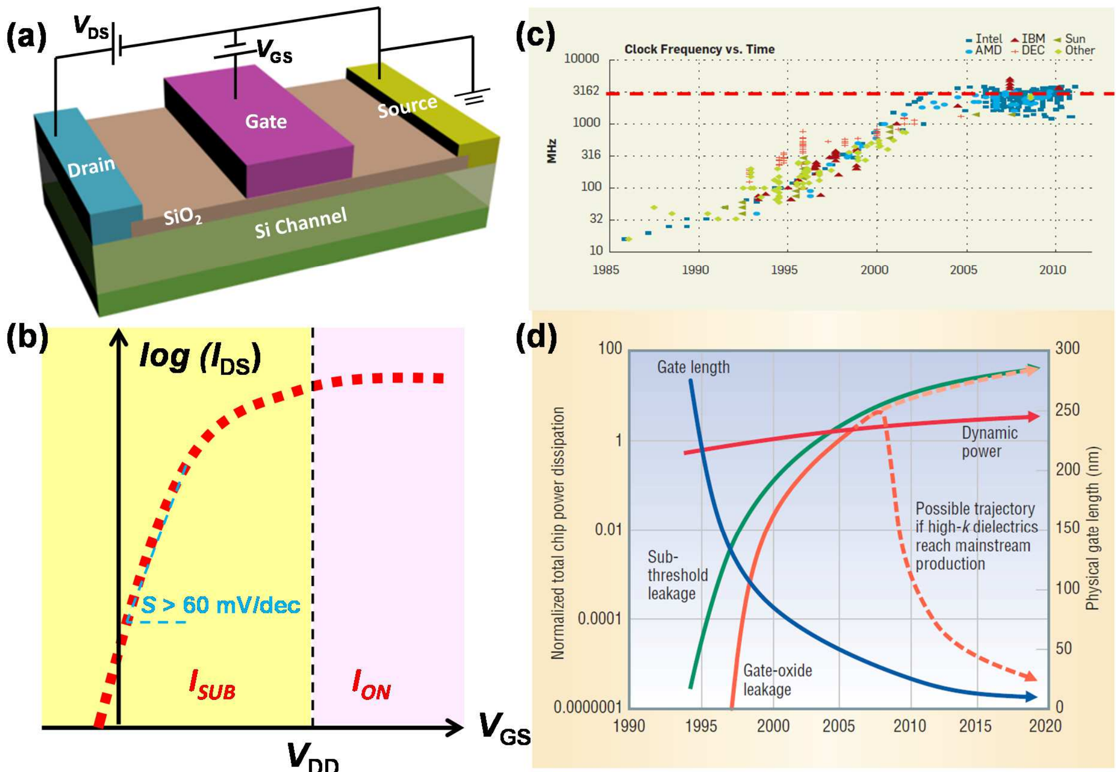

Figure 1-1. Overview of Si-based MOSFETs. (a) Schematic of the MOSFET structure. The applied gate voltage is used to modulate the source-to-drain current, therefore realizing the switching behavior. (b) Typical I_{DS} - V_{GS} curve for the MOSFET. In the subthreshold regime, the current follows an exponential relation with respect to the gate voltage and SS is always larger than 60 mV/dec. (c) Processor frequency scaling with time. As illustrated, f has largely leveled off since 2005. Adopted from Ref. [9]. (d) Total chip dynamic and static power dissipation trends. Adopted from Ref. [7].

1.1. The emergence of spintronics

Seventy years has passed since the birth of the first transistor (germanium point-contact diode). At the end of the silicon golden age, we have to launch another Renaissance for the

new semiconductor era. At current stage, semiconductor tycoons like Intel and TSMC still follow the mature Si-based state-of-art, which is to continuously improve the instrument resolution as well as refine the transistor structure. By spending astronomical budget on the fab upgrades and process technology development, we hope to maintain both the spirits and benefits endowed by the Moore's Law as long as possible. However, spending trends for the semiconductor industry have changed since 2009; it was observed that "now more money is spent on upgrading existing facilities, while new capacity additions are occurring at a slower pace" [14]. In the meanwhile, worldwide universities and research institutes are extensively investigating III-V heterostructures and novel 2D materials (*i.e.,* graphene, MoS_2, and black phosphorus) as alternative channel candidates with higher carrier mobility so that the scaling issue can be alleviated. Nevertheless, all these approaches are more or less modifications since the operational principles of transistor and the underlying physical limits still remain unchanged; in other words, as long as there are thermal activation and random electron scatterings in the conduction channel, the energy loss cannot be eliminated.

In contrast to the above "reforms", a more revolutionized plan to deal with the power dissipation dilemma is to regulate the electron motion. Just like how architects designed the freeway networks to solve the traffic problems in urban cities, we can also construct the electron highway system so that electrons travelling along opposite directions are separated, and all electron collisions are forbidden. In fact, for conventional electronics, we only utilize the charge feature of electron. Alternatively, if we further take the advantage of electron's

unique spin property, we are able to better manipulate the information process, thus leading to the next-generation low-power, high-speed electronics applications. Such emerging research field regarding to this revolution is called spintronics.

	Electronics	Spintronics
Basis	CHARGEs	CHARGEs + SPINs
Bit (1 or 0)	number of the charges	spin up or down (quantum logic operation)
Materials	Semiconductors	Semiconductors Ferromagnetic Materials
Advantages	Mass Production	Scaling, nonvolatile with low power consumption
Challenges	Close to the Quantum Limit Large power consumption	Spin Selection Long-Distant Transport

Figure 1-2. Comparison between electronics and spintronics.

The spin angular momentum ***S*** is an intrinsic property of electron that is associated with its angular momentum ***J*** and orbital angular moment ***L*** (*i.e.,* $\boldsymbol{J} = \boldsymbol{L} + \boldsymbol{S}$). Governed by the quantum mechanics and particle physics theory, an electron, which belongs to the spin-½ fermions, can only have either "spin-up" or" spin-down" state relative to a reference (an applied magnetic field or magnetization orientation of a magnetic film). Therefore, spin itself, as a natural binary system, can also carry information. As it is shown in Fig. 1-2, by

combining the spin degree of freedom, spintronics will add substantially more functionalities and performance to conventional semiconductor charge-based electronic products. In the meanwhile, the use of additional ferromagnetic (FM) material offers opportunities for a new generation of devices integrating the spin-dependent effects that arise from the interaction between the spin and the magnetic properties of the material. Consequently, the advantages of these novel spintronics devices would be non-volatility, increased data processing speed, decreased electric power consumption, and increased integration densities [15-20].

Although it sounds promising, the development of spintronics still remains in the incubation stage, and current challenges mainly come from the material aspect. On one hand, it turns out to be difficult to inject spin and maintain robust spin signal in most conventional semiconductors (*i.e.,* Si, Ge, and III-V materials) [21-26]; on the other hand, normal ferromagnetic metals (*i.e.,* Fe, Co, Ni, and their alloys) have high spin selectivity, yet it is almost impossible to manipulate the spin state by electric field, thus making them impractical for spintronics logic operations. Accordingly, to explore novel material candidates which combine the advantages of semiconductor band gap engineering with controllable magnetic properties in a single system is the primary motivation of this Dissertation.

1.2. Topological Insulators

The name of topological insulator (TI) originates from the fact that such material has a bulk insulating gap while exhibiting topologically protected metallic states at its boundary

when it is placed next to a vacuum or an ordinary insulator [27-32]. Figure 1-3(a) shows the band structure of one TI material (Bi_2Se_3) [33]. It can be clearly seen that in addition to the ordinary parabolic bulk band, a unique gapless surface state with a single Dirac cone is also resolved. Given its linear $E - k$ relation, the surface electrons can be reviewed as massless Dirac fermions with ultra-high mobility. The most striking feature which distinguishes TI from other ordinary band insulators is the surface spin-momentum locking mechanism: due to the giant spin-orbit coupling (SOC) in TI, the spin polarization of surface electron is tightly locked to its momentum direction; in other words, once the current is applied, itinerant electrons with opposite spins are well-separated along the TI edges, as illustrated in Fig. 1-3(b). Moreover, due to the π-Berry phase nature of the spin-½ Dirac fermions and the protection of time-reversal-symmetry (TRS), back-scatterings by non-magnetic impurities are forbidden during electron transport, thus leading to the quantum spin Hall effect (QSHE) where a dissipationless helical spin-polarized conduction is realized without the presence of any external field [30]. Consequently, the QSH insulator, TI, is regarded as the most suitable candidate to implement the "electron/spin highway" concept. In fact, ever since its discovery, TI has raised broad interest not only in spintronics, but also among condensed-matter physics, material science, and energy harvesting applications. In this section, we would like to briefly overview the TI-related research milestones during the past ten years.

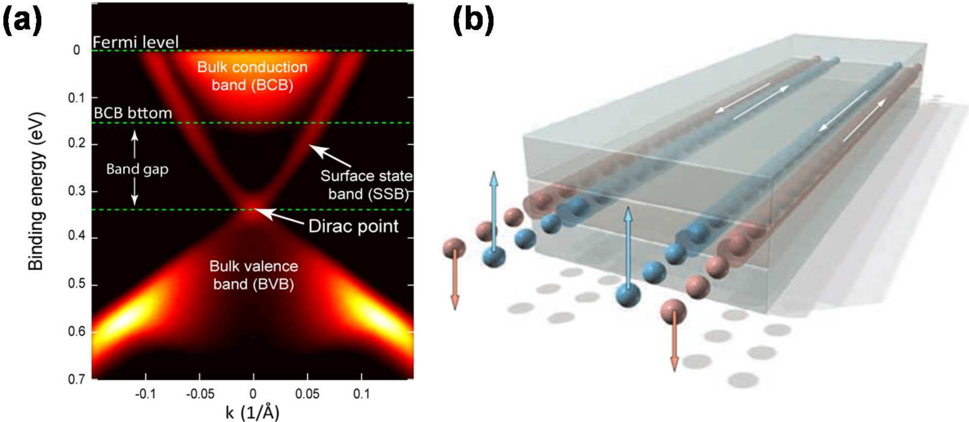

Figure 1-3. Topological Insulators and the spin-momentum locking mechanism. (a) Energy band structure of Bi_2Se_3. Adopted from Ref. [33]. (b) Illustration of the spin-polarized helical edge channels in a TI material. Adopted from Ref. [34].

1.2.1. Quantum spin Hall insulator and band inversion

The centerpiece of QSHE is the intrinsic spin-orbit coupling. By coupling the electron's spin and orbital angular momentum degrees of freedom, the electron band structure of the lattice is modified, and this subsequently causes electrons that are moving through the crystal to feel a spin-dependent force [28]. In 2005, C.L. Kane and E.J. Mele investigated the effects of SOC on the low energy electronic band structure of the graphene strip [35]. By considering a second neighbor tight binding model with a spin-dependent amplitude determined by the sublattice orientation, they found that the symmetry allowed spin-orbit potential to convert graphene from an ideal 2D semi-metallic state to a QSH insulator which had a gapped bulk band but supported the transport of spin and charge in the gapless edge state at the sample boundaries [35]. Although SOC exists in all materials, it is obvious that

not all of them belong to the QSH insulator. So in the following work, C.L. Kane and E.J. Mele further showed that the QSH phase was a time reversal invariant electronic state associated with a novel Z_2 topological invariant, and the resultant 2D state was the first topological insulator to be understood [36]. More importantly, such Z_2 classification could be generally computed for any 2D material system and would allow the prediction of whether the material had a stable spin-filtered edge state [36].

In reality, since the SOC in graphene is quite small, it is thus impractical to pursue QSHE in this system. Alternatively, B.A. Bernevig, T.L. Hughes, and S.C. Zhang proposed another guideline in the search for the QSHE insulator – band inversion caused by SOC [37]. It is well-known that in most common semiconductors, the conduction band which is formed from electrons in *s* orbitals is always above the valence band that is formed from electrons in *p* orbitals (*i.e.,* the band gap E_g is positive). In contrast, for certain heavy elements, the SOC is so strong that the *p*-orbital band is pushed above the *s*-orbital band—that is, the bands are *inverted* (*i.e.,* the band gap E_g is negative). Accordingly, if we combine one $+E_g$ material with another $-E_g$ material, due to the boundary condition that the waveform has to be continuous, it is therefore expected that an extraordinary edge/surface state will be formed at the interface.

Following this argument, in 2006, B.A Bernevig *et al.* proposed the CdTe/HgTe/CdTe quantum well (QW) structure as a suitable platform to investigate QSHE [37]. From the theoretical calculations, they found that the barrier material (CdTe) has a normal band structure, with the *s*-type Γ_6 band lying above the *p*-type Γ_8 band, while the SOC of the well

material (HgTe) is so large that Γ_8 band is pushed above the Γ_6 band. Figure 1-4 shows the thickness-dependent quantum phase transition of the HgTe/CdTe QW. Specifically, for a thin HgTe layer thickness *d*, the QW is in the "normal" regime, where the CdTe has the dominant effect and the band energy at the Γ point satisfies $E(\Gamma_6) > E(\Gamma_8)$. On the contrary, for the thick *d* case, the well is in the inverted regime, where HgTe dominates and $E(\Gamma_6) < E(\Gamma_8)$. As the thickness of the well varies, the E_1 and H_1 bands will cross at $d_c \sim 6.5$ nm where the energy gap at $d = d_c$ vanishes.

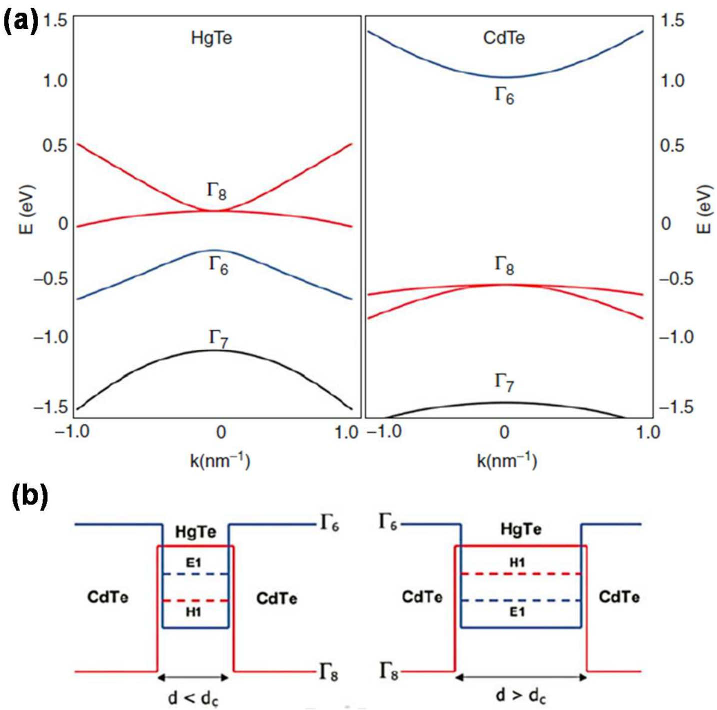

Figure 1-4. HgTe-CdTe quantum wells. (a) Bulk energy bands of HgTe and CdTe near the Γ point. **(b)** The CdTe/HgTe/CdTe quantum well in the normal regime $E_1 > H_1$ with $d < d_c$ and in the inverted regime $H_1 > E_1$ with $d > d_c$. Adopted from Ref. [37].

In fact, the 2D TI CdTe/HgTe QW can be described by an effective Hamiltonian that is essentially a Taylor expansion in the wave vector k of the interactions between the lowest conduction band and the highest valence band [37]

$$H_{eff}(k_x,k_y)=E(k)+\begin{bmatrix} m(k) & A(k_x+ik_y) & 0 & 0 \\ A(k_x+ik_y) & -m(k) & 0 & 0 \\ 0 & 0 & m(k) & -A(k_x-ik_y) \\ 0 & 0 & -A(k_x+ik_y) & -m(k) \end{bmatrix}=\begin{bmatrix} h(k) & 0 \\ 0 & h^*(-k) \end{bmatrix} \quad (1\text{-}2)$$

where $E(k)=C+D(k_x^2+k_y^2)$ is the trivial band bending, $m(k)=m_0+B(k_x^2+k_y^2)$ is the gap parameter, the energy gap between the bands is $2m(k)$, A incorporates the interband coupling to the lowest order, B (typically negative) describes the band curvature of the band, and $h(k)=E(k)+m(k)\sigma_z+A(k_x\sigma_y-k_y\sigma_x)$. For $m/B < 0$ (*i.e., $d < d_c$*), the eigenstates of the model describe a trivial insulator. As the thickness of the HgTe quantum well increases, m becomes negative due to band inversion, and the $m/B > 0$ condition gives rise to the edge states of the QSH insulator. Accordingly, the wavefunction for the edge states at the Γ point is given by

$$\psi_0(x)=\begin{cases} a(e^{\lambda_1 x}-e^{\lambda_2 x})\phi_+, & A/B<0 \\ c(e^{-\lambda_1 x}-e^{-\lambda_2 x})\phi_-, & A/B>0 \end{cases} \quad (1\text{-}3)$$

where $\lambda_{1,2}=\frac{1}{2B}(A\pm\sqrt{A^2-4mB})$, and $\phi_\pm$ are the two-component spinor. The sign of the A/B determines the spin polarization of the edge states, which is the key to determine the helicity of the Dirac Hamiltonian for the topological edge states. This effective edge model

(*i.e.,* the Dirac Hamiltonian for the edge states) can be obtained by projecting the bulk Hamiltonian onto the edge states defined above, and the result is given by $H_{edge} = Ak_y\sigma^z$. From this linear Dirac Hamiltonian we can see that the edge states with opposite spins have opposite momentum directions. Therefore, the spin-momentum locking mechanism is generated on the edge.

1.2.2. Discovery of QSHE in two-dimensional Topological Insulators

Less than one year after the prediction, König *et al.* provided the experimental observation of QSHE in the 2D HgTe/(Hg,Cd)Te QWs grown by molecular beam epitaxy (MBE) [34]. In their experiments, several samples were prepared with different HgTe layer thickness. For thin QWs with d < 6.3 nm (Sample I), the longitudinal resistance became giant (*i.e.,* $R_{14,23} > 10^7$ Ω) when the Fermi level was tuned within the bulk gap, reflecting the normal insulating state as highlighted by the black curve in Fig. 1-5. As the well thickness increased (d > 6.3 nm), the edge state due to the QW band inversion started to develop. Significantly, both Samples III and IV (*i.e.,* with the same length L = 1 μm but different widths W = 0.5 and 1 μm, respectively) exhibited a quantized conductance of $2e^2/h$ at zero magnetic field when T = 30 mK. Accordingly, the size-independent quantized longitudinal conductance results convincingly demonstrated the existence of the helical edge states of the QSH insulator.

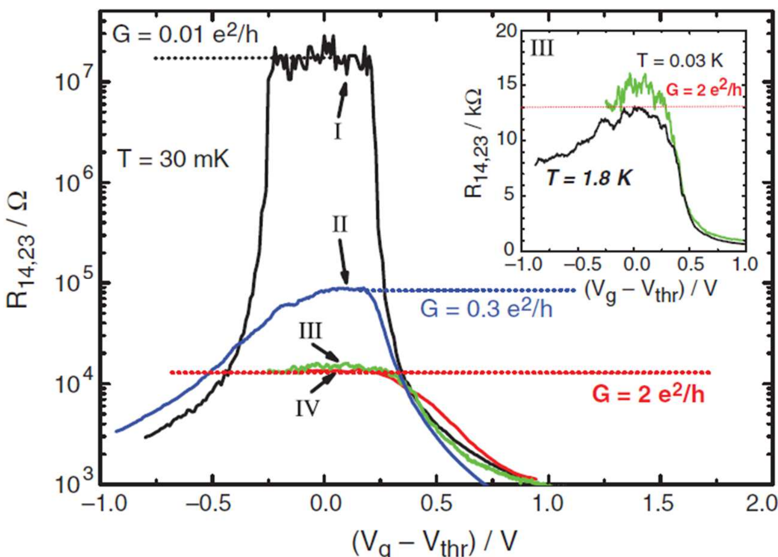

Figure 1-5. Experimental observations of quantum spin Hall effect in the HgTe/CdTe QWs. The longitudinal four terminal resistance, $R_{14,23}$, of various normal (d = 5.5 nm) (I) and inverted (d = 7.3 nm) (II, III, and IV) QW structures as a function of the gate voltage measured for B = 0 T at T = 30 mK. The device sizes are (20.0×13.3) μm^2 for devices I and II, (1.0×1.0) μm^2 for device III, and (1.0×0.5) μm^2 for device IV. The inset shows $R_{14,23}$ as a function of V_g of two samples from the same wafer, having the same device size (III) at 30 mK (green) and 1.8 K (black) on a linear scale. Adopted from Ref. [34].

Beside the CdTe/HgTe QWs, R.R Du's group also experimentally demonstrated the QSHE on the InAs/GaSb QWs [38, 39]. In this system, the band inversion is achieved at the type-II InAs/GaSb heterostructures that are confined by the neighboring AlSb barriers, as shown in Fig. 1-6(a). Most importantly, Fig. 1-6(b) revealed that a wide longitudinal conductance plateau of 2e^2/h value was observed by appropriately tuning front gate voltage, and such quantized helical edge conduction was probed up to 4 K, which was much higher than the CdTe/HgTe system.

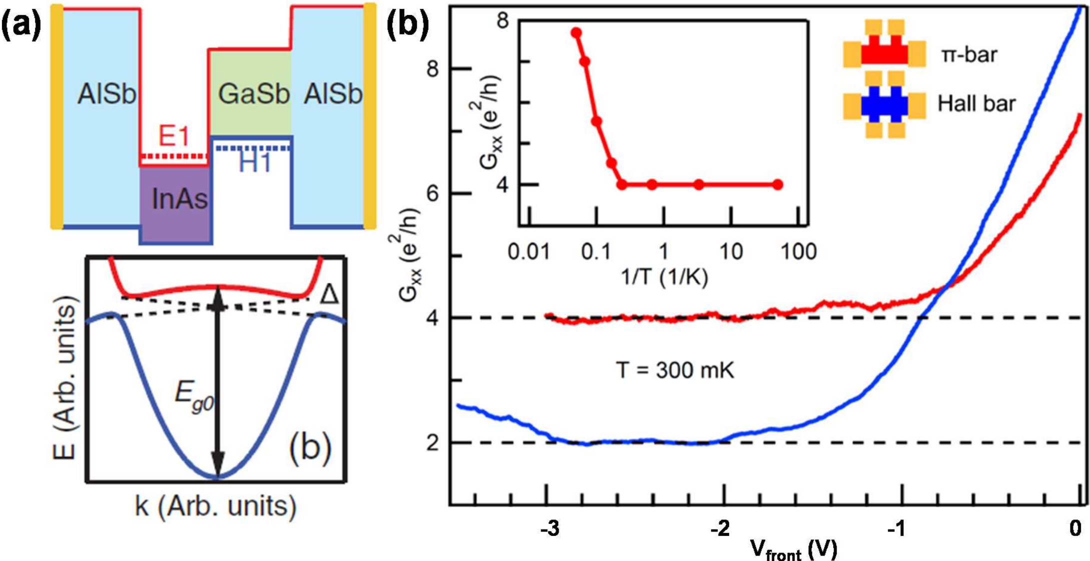

Figure 1-6. Experimental observation of quantum spin Hall effect in the InAs/GaSb QWs. (a) The energy spectrum of inverted InAs/GaSb QW. Adopted from Ref. [38]. (b) Wide conductance plateau quantized to $2e^2/h$ and $4e^2/h$, respectively for two device configurations (four-terminal π-bar and six-terminal Hall bar) as shown in the inset. Adopted from Ref. [39].

1.2.3. Extend Topological Insulators to three dimension

From the above review, we can conclude that non-trivial band inversion due to SOC in 2D material gives rise to the QSH insulators, and the Z_2 topological invariant is the key to distinguish TI from an ordinary insulator. In this section, we will show that the same criteria can be generalized to build a 3D-version of topological insulator, for which the topologically non-trivial boundaries extend from the 1D edge to 2D surface state, and the Dirac cone is located at a TR-invariant point [30].

Actually, the first predictions of 3D TIs were proposed by three independent research groups. In July 2006, J.E. Moore and L. Balents applied the homotopy theory to demonstrate that the TR-invariant energy band in 3D could be explicitly characterized by four Z_2 invariants instead of only one in the 2D case (and it was them to name the materials with non-zero Z_2 number as “topological insulators”) [40]. Only one week later, R. Roy uploaded his own work to arXiv.org. In that paper, he provided a set of “topology number" to mathematically classify all the phases of band insulators in 3D and later showed that some of the topological phases could only be revealed in 3D [41]. Such progress in math-topology also propelled the discovery of 3D TI in physics realm. After another week, F. Liang and C.L. Kane used the four Z_2 numbers to describe all the 16 phases with two general classes: weak (WTI) and strong (STI) topological insulators in the 3D regime [42]. They found that the WTI behaved like layered 2D QSH states, but were vulnerable to disorder; in contrast, the STI with odd number of Dirac cones on the surface had robust QSH states. Based on this interpolation, they predicted that the $Bi_{1-x}Sb_x$ alloy with a critical Bi/Sb ratio would be a 3D TI candidate [43].

Experimentally, it was D. Hsieh *et al.* who applied the surface-sensitive angle-resolved photoemission spectroscopy (ARPES) to first observe the topological surface states in $Bi_{0.9}Sb_{0.1}$, manifesting the birth of 3D TI [44]. However, due to the random substitutional disorders in such alloy, its surface states and the underlying mechanism turned out to be extremely complex. Instead, tetradymite-type materials Bi_2Se_3, Bi_2Te_3, and Sb_2Te_3 were later

proposed [45] and demonstrated [46-48] to be the better 3D TIs candidates with single Dirac cone and large bulk band gap up to 0.3eV. Ever since then, enormous efforts have been extensively performed on these systems.

1.3. Magnetic Topological Insulators

In Section 1.2, we showed that the spin-orbit coupling is an effective way to control the electron spin state, and in the extreme case where SOC is large enough to invert the energy band, quantum spin Hall effect is expected in 2D TIs. In addition to SOC, it is also known that the electron spin can be manipulated by magnetic moment, as the case in magnetic materials. Accordingly, it was suggested that the spin controllability can be further enhanced if additional magnetic order was integrated into TIs. In this section, we will discuss several important concepts regarding to the magnetic TI system, and show how the functionalities of associated TRS-breaking physics and applications can be multiplied through the interplay among the band topology (SOC strength), the magnetic orders (magnetic exchange coupling strength), and structural engineering (Fig. 1-7).

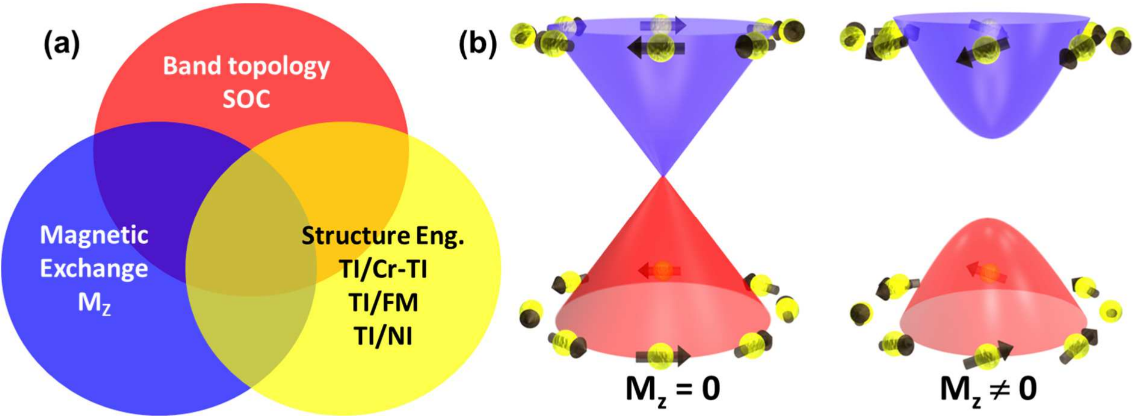

Figure 1-7. TRS-breaking magnetic topological insulators. (a) The interplay among band topology, magnetic exchange, and structure engineering in the TRS-breaking phenomena. (b) Topological surface band diagram in undoped TI (massless) and magnetically doped TI (massive), respectively.

1.3.1. Break the time-reversal-symmetry of Topological Insulators

From Eq. (1-2), it is clearly seen that for original undoped TIs, TRS is protected given that $h(k) = h^*(-k)$. However, once additional magnetic exchange M_z is introduced, the mass term changes to

$$m(k, M_z) = m_0 + B(k_x^2 + k_y^2) + gM_z \tag{1-4}$$

Consequently, $h(k, M_z) \neq h^*(-k, M_z)$ and $H_{eff}(k_x, k_y)$ no longer has the TRS-protected property, and the massless surface Dirac fermions degrade to the massive case where the surface opens a gap Δ, as shown in Fig. 1-7(b) [49].

Experimentally, the topological surface band gap was first observed by ARPES. Y.L. Chen *et al.* performed the measurements on the transition-metal doped Bi_2Se_3 materials, and observed a small surface band gap (~ 7 meV) opening in the $(Bi_{0.99}Mn_{0.01})_2Se_3$ sample [33]. In the meanwhile, L.A. Wray *et al.* also observed the surface gap opening when they deposited the Fe ions on top of the Bi_2Se_3 film [50]. Recently, S.Y. Xu *et al.* used the more advanced spin-resolved ARPES to visualize the spin textures in the Mn-doped Bi_2Se_3 thin films [51]. The resolved unique hedgehog-like spin reorientations around the surface electronic groundstate provided additional information about the mechanics of TRS breaking on the TI surface.

1.3.2. Integrate magnetic order into Topological Insulators

In general, there are two methods to introduce the magnetic exchange term M_z in order to break the TRS of the topological surface states. First of all, by combing the TI material with a topologically trivial magnetic material, the magnetic proximity effect at the interface is able to locally align the spin moments of the TI band/itinerant electrons out of plane, therefore breaking the TRS at the TI interface [52, 53]. To date, such magnetic proximity effects have been observed in both TI/YIG [54] and TI/EuS [55, 56] heterostructures. However, since the interface qualities are usually poor in these systems, the

magnetizations introduced by the short-range magnetic exchange coupling are therefore quite weak.

Alternatively, incorporating magnetic ions into the host TI materials has been proven to be the most effective way to generate robust magnetism and open a gap of the surface states [33, 51, 57]. Theoretically, Zhang *et al.* reported a detailed theoretical study of the formation energies, charge states, band structures, and magnetic properties of transition metal (V, Cr, Mn, and Fe) doped 3D TIs [58, 59]. By using first-principles calculations based on the density functional theory, they found that most transition metals favored the substitutional doping into the host TI cation-site, indicative of robust magnetic moments formed in such magnetically doped TI systems. More importantly, A.S Nunez *et al.* found that the exchange-induced single ion magnetic anisotropy in such systems was along the perpendicular orientation [60]. As a result, the magnetic anisotropy easy-axis is expected to be out-of-plane in the magnetically doped 3D TIs regardless of the film thickness.

At current stage, the transition-metal doped TI materials have been successfully grown by chemical vapor deposition (CVD) [61], bulk Bridgeman growth [62-65], and MBE [66, 67]. Among them, the MBE technique has advantages in terms of non-equilibrium physical deposition, accurate layer thickness/doping profile control, wafer-scale growth capability, and potential integration of heterostructures and/or super-lattices for multi-functional device applications. In this Dissertation, all experiments were done on the MBE-grown (magnetic) TI thin films in our lab, as we will elaborate in Chapter 3.

1.3.3. RKKY interaction

The first study on the transition metal doped Bi_2Se_3 / Bi_2Te_3 / Sb_2Te_3 materials was carried out even before the discovery of topological insulators [68-75]. At that time, such systems were treated as conventional dilute magnetic semiconductors (DMS). Compared with III-V based DMS counterparts [76-78], it was found that the solubility in the tetradymite-type thin film could be as high as 0.35 and the corresponding Curie temperature T_C as high as 190 K was obtained [70].

In magnetically doped semiconductors, it is known that neighboring magnetic dopants can be aligned through the Ruderman-Kittel-Kasuya-Yoshida (RKKY) interaction [79-81] In the RKKY model, the itinerant carriers are polarized in the form of long-range oscillatory waves, and the general interaction is described by [82, 83]

$$H^{RKKY} = \frac{i}{\pi}\int_{-\infty}^{E_F} dE \sum_{i\neq j} \mathrm{Tr}\{[-J(E)\vec{\sigma}\cdot\vec{S}_i]\, G(\vec{R}_{ij})[-J(E)\vec{\sigma}\cdot\vec{S}_j]\, G(-\vec{R}_{ij})\} \tag{1-5}$$

where $J(E)$ is the exchange coupling coefficient, S_i is the spin of local magnetic ion, σ is the Pauli matrix of itinerant electrons, R_{ij} is the distance between the two localized ions, and the Green's function has the form that[82, 83]

$$G(\vec{R}_{ij}) = \frac{1}{4\pi^2}\int \frac{1}{E-H_0}\exp(-i\vec{k}\cdot\vec{R}_{ij})\, d^2k \tag{1-6}$$

The presence of the RKKY interaction can be probed from the Curie temperature. In general, the Curie temperature under the mean-field Zener theory is given by [84, 85]

$$T_C = \frac{S(S+1)}{3k_B}\frac{x_M}{\Omega_0}J^2\frac{m^*k_F}{4\pi^2} = \frac{S(S+1)}{3^{2/3}4\pi^{4/3}k_B}\frac{x_M}{\Omega_0}J^2m^*p^{1/3} \quad (1\text{-}7)$$

where m^* is the effective mass, p is the free carrier (hole) density, x_M is the magnetic doping level, and the Fermi wave vector $k_F = (3\pi^2 p)^{1/3}$. Accordingly, for a given magnetic system with RKKY interaction, T_C is expected to scale with $x_M p^{1/3}$. Recently, both Z.H. Zhou *et al.* [70] and B. Li *et al.* [65] reported the experimental observations of such linear $T_C - x_M p^{1/3}$ relationship in both the $Sb_{2-x}Cr_xTe_3$ and the $(Cr_xBi_ySb_{1-y-x})_2Te_3$ bulk samples, which implied that the hole-mediated RKKY interaction was responsible for the ferromagnetism in Cr-doped magnetic TI materials. In this Dissertation (Chapter 4), we will provide straightforward evidence, namely the gate-dependent magneto-transport measurements, to demonstrate the carrier-dependent RKKY interaction in our MBE-grown magnetic TI thin films.

1.3.4. Van Vleck mechanism and carrier-independent ferromagnetism

In a dilute magnetically doped semiconductor system, it was found possible that the magnetic exchange among local moments could also be mediated by the band electrons other than the RKKY coupling through itinerant carrier [86]. In 2010, R. Yu *et al.* predicted that tetradymite TI materials (Bi_2Se_3/Bi_2Te_3/Sb_2Te_3) could form such magnetically ordered

insulator when doped with Cr or Fe [49]. They used the first-principles calculations to investigate the total free energy of the system that

$$F_{total} = \frac{1}{2}\chi_L^{-1}M_L^2 + \frac{1}{2}\chi_e^{-1}M_e^2 - J_{eff}M_L M_e - (M_L + M_e)H \tag{1-8}$$

where χ_L (χ_e) is the spin susceptibility of the local moments (band electrons), M_L (M_e) denotes the magnetization for the local moment (electron) subsystem, and J_{eff} is the magnetic exchange coupling between them. Accordingly, the onset of the FM phase can be determined when the minimization procedure of the free energy gives a non-zero magnetization without the presence of external magnetic field, which leads to $J_{eff}^2 - \chi_L^{-1}\chi_e^{-1} > 0$, or equivalently $\chi_L > (J_{eff}^2 \cdot \chi_e)^{-1}$; in other words, a larger χ_e gives rise to more prominent local coupling [49]. In fact, a considerable χ_e value can be obtained through the Van Vleck mechanism that [49]

$$\chi_e = \sum 4\mu_0\mu_B^2 \frac{< nk\,|\,\hat{S}_z\,|\,mk >< mk\,|\,\hat{S}_z\,|\,nk >}{E_{mk} - E_{nk}} \tag{1-9}$$

where μ_0 is the vacuum permeability, μ_B is the Bohr magneton, S_z is the spin operator, $|mk>$ and $|nk>$ are the Bloch functions in the conduction and valence bands, respectively. In normal IV and III-V DMS systems where the conduction and valence bands are well-separated by the band gap E_g, there is no overlap between $|mk>$ and $|nk>$, and χ_e is thus negligible. In contrast, the giant SOC in Bi_2Se_3-type materials causes the band inversion [45], and the mixing Bi p_{1z}-state ($|nk>$) and Se p_{2z}-state ($|mk>$) therefore leads to a sizable $<nk|S_z|mk>$ [49]. Under such circumstances, large magnetization can be generated through direct coupling between

the Cr *d*-orbit moment and the host TI valence electron without the assistance of any itinerant carriers.

In 2013, C.Z Chang *et al.* carried out the systematic study to investigate the Van Vleck mechanism in magnetic TIs [66]. In their experiments, they prepared a set of Cr-doped $(Bi_xSb_{1-x})_2Te_3$ thin films with a fixed Cr doping level of 12 % and same film thickness of 5 quintuple-layer (QL) in order to ensure that both χ_L and M_L remain constant. They found that although the carrier type was tuned from *n*-type ($x > 0.3$) to *p*-type ($x < 0.2$) by varying the Bi/Sb ratio, the ferromagnetism of the $Cr_{0.22}(Bi_xSb_{1-x})_{1.78}Te_3$ films remained regardless of the carrier density. Most importantly, the Curie temperature T_C showed little dependence on the carrier density and type (Figs. 1-8 (a)-(b)). Together with gate-independent AHE data shown in Fig. 1-8(c), their observations thus provided a direct evidence of the long-range FM order through the Van Vleck mechanism in the magnetic TI materials.

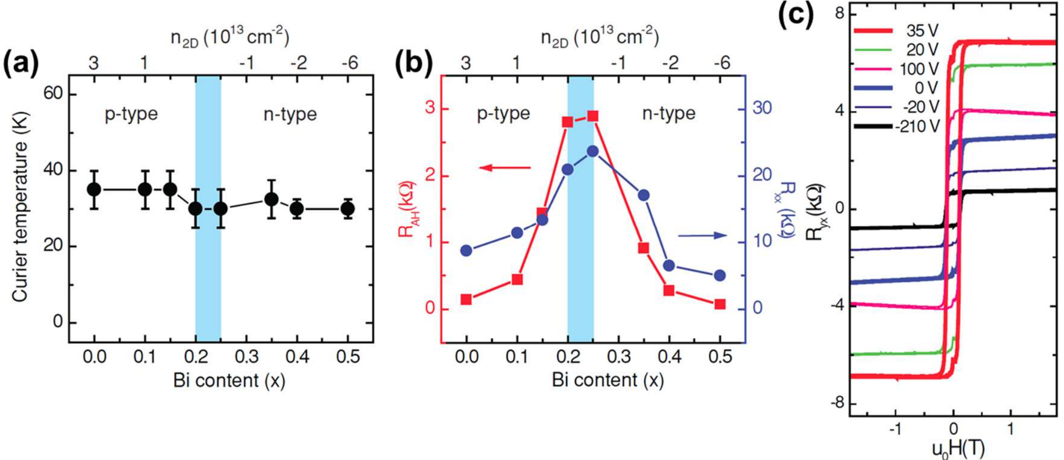

Figure 1-8. Carrier-independent long-range ferromagnetic order in magnetic TI thin films. (a) Dependence of Curie temperature (T_C) on Bi content (x) (bottom axis) and carrier

density (top axis) in the MBE grown $Cr_{0.22}(Bi_xSb_{1-x})_{1.78}Te_3$ films. (b) Dependence of AHE resistance (R_{AH}) (red solid squares) and longitudinal resistance (R_{xx}) (blue solid circles) at 1.5 K on Bi content x (bottom axis) and carrier density (top axis). (c) Magnetic field dependent Hall resistance R_{xy} of a 5QL $Cr_{0.22}(Bi_{0.2}Sb_{0.8})_{1.78}Te_3$ film grown on $SrTiO_3$ (111) at different back-gate voltages measured at 250 mK. Adopted from Ref. [66].

Since both the hole-mediated RKKY coupling and the carrier-independent Van Vleck magnetism are possible in the magnetic TIs, it is thus important to understand the fundamental physics of these different FM orders, and the interplay/controllability of each contribution. Most importantly, the large Van Vleck susceptibility resulting from the bulk band inversion and the long-range exchange coupling through the band electrons distinguish the magnetic TIs from conventional DMS systems. As will be discussed in Chapter 5, this unique magnetism is essential to form the Chern insulator and realize the quantum anomalous Hall effect [87].

1.4. Organization

In this Dissertation, we summarize our work on the (magnetic) TI thin films and relevant phenomena. The contents are arranged as follows. In Chapter 2, we discuss the physics background about the quantum Hall trio (quantum Hall effect, quantum spin Hall effect, and quantum anomalous Hall effect) and the correlations between them. In Chapter 3, we describe the experimental instruments used to grow the (magnetic) TI thin films and

characterize their properties. In Chapter 4, we show the presence of both the RKKY interaction and van Vleck mechanisms in the Cr-doped $(BiSb)_2Te_3$ thin films through the electric-field-controlled magneto-transport measurements. By optimizing the doping strategy, we present in Chapter 5 the experimental evidence of quantum anomalous Hall effect where the scale-invariant disspationless chiral edge conduction is observed in the macroscopic millimeter-size magnetic TI device up to 0.3 K. In addition, by applying the modulation-doped MBE growth method, we successively prepare the TI/Cr-doped TI bilayer systems with controllable structural engineering. In Chapter 6, we provide both the extraordinary surface-related ferromagnetism and the giant spin-orbit torque in such TI-based heterostructures. Finally, the conclusion of this Dissertation is given in Chapter 7.

Chapter 2

Quantum Hall Trio

2.1. A brief history of Hall family

The stories about Hall effect family all started with Edwin H. Hall. In his paper titled as "On a new action of the magnet on electric currents" [88], he recorded the momentous discovery obtained on the 28th of October, 1887. In his experiment, he placed a gold leaf strip (on a plate of glass) between the poles of an electro-magnet, and detected a voltage change between two vertical probes (*i.e.,* transverse to the current direction) before and after he turned on the elecro-magnet. This famous Hall effect was later explained in terms of the classical Lorentz force acting on a moving electron by the magnetic field in the classical diffusion regime. It is found that the slope of the linear field dependence of the Hall resistance, defined as the transvers voltage divided by the current, has a close relation to the type and density of carriers:

$$R_{xy} = \frac{V_{xy} d}{I \cdot B} = -\frac{1}{n_{2D} \cdot e} \tag{2-1}$$

where d is the sample thickness. Therefore, the ordinary Hall effect has been widely used to study the electrical properties of materials due to its convenience.

Soon after the discovery of the OHE, Hall tried similar experiments on ferromagnetic materials. He observed that the magnetic-field-dependent Hall resistance showed an unusually large slope at a low field [89]. It was recognized that this unusually large Hall effect originates from the magnetization of FM materials, which was later known as the anomalous Hall effect (AHE) [87]. Since a FM material keeps its spontaneous magnetization even when the external magnetic field is removed, the AHE can be measured in the zero magnetic field. Unlike ordinary Hall effect, the AHE has been an enigmatic problem ever since its discovery. Although it is generally believed that SOC plays a fundamental role in the AHE, its exact mechanism still remains to be debatable. Today, the most commonly used empirical relation to describe AHE is given by [87]

$$R_{xy} = R_0 \cdot H + R_A \cdot M(H) \tag{2-2}$$

while the ordinary Hall coefficient R_o is inversely proportional to the Hall density, the anomalous Hall coefficient R_A is experimentally found to depend subtly on a variety of material specific parameters and, in particular, on the longitudinal resistivity ρ_{xx}.

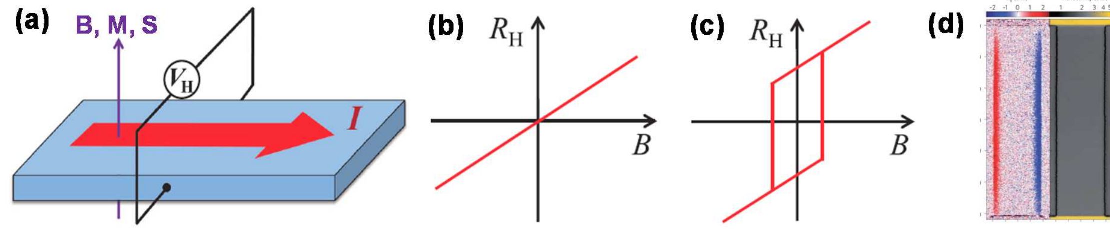

Figure 2-1. The Hall effects. (a) Three ways to deflect the electron motion in a conductor. (b) Magnetic field dependence of ordinary Hall effect. (c) Magnetic field dependence of

anomalous Hall effect. (d) Observation of spin Hall effect by magneto-optical Kerr microscope. Adopted from Ref. [90].

2.1.1. Scattering mechanisms of anomalous Hall effect

Generally speaking, the full modern semiclassical treatment of the AHE can be reviewed based on the anomalous contribution to wave-packet group velocity due to momentum-space Berry curvatures and the consideration of the intrinsic/extrinsic scattering-related mechanisms. As shown in Fig. 2-2, both skew scattering and side-jump mechanisms are focused on the influence of disorder scattering in imperfect crystals. In particular, skew scattering is due to chiral features which appear in the disorder scattering of spin-orbit coupled ferromagnets. In the presence of SOC, a transition which is right handed with respect to the magnetization, M_S, is different to the corresponding left-handed transition, therefore leading to the asymmetric transition probability [91, 92]

$$W^{A}_{k->k'} = -\tau_A^{-1} k \times k' \cdot M_S \tag{2-3}$$

As a result, scattering of a carrier from an impurity introduces a momentum perpendicular to both the incident momentum k and the magnetization M_S. Consequently, the Hall conductivity σ_{xy} and the longitudinal conductivity σ_{xx} are both proportional to the transport time τ. Equivalently, $\rho_{xy} \sim \sigma_{xy} \cdot (\rho_{xx})^2$ is proportional to ρ_{xx} (Note that here we make the assumption that $\rho_{xy} << \rho_{xx}$; otherwise, the $\rho_{xy} \propto \rho_{xx}$ relation is not valid any more).

On the other hand, the basic semiclassical argument for a side-jump contribution can be stated straightforwardly: when considering the scattering of a Gaussian wave packet from a spherical impurity with SOC, a wave packet with incident wave vector k will suffer a displacement transverse to k with a microscopic displacement that is independent of the details of the impurity potential or of the scattering process [93-95]. Equivalently, the side-jump contribution to motion during a scattering event is analogous to the anomalous velocity contribution to wave-packet evolution between collisions, with the role of the disorder potential in the former case taken over in the latter case by the external electric field. Therefore, the side-jump contribution to the conductivity ends up being independent of τ, and therefore $\rho_{xy} \propto (\rho_{xx})^2$.

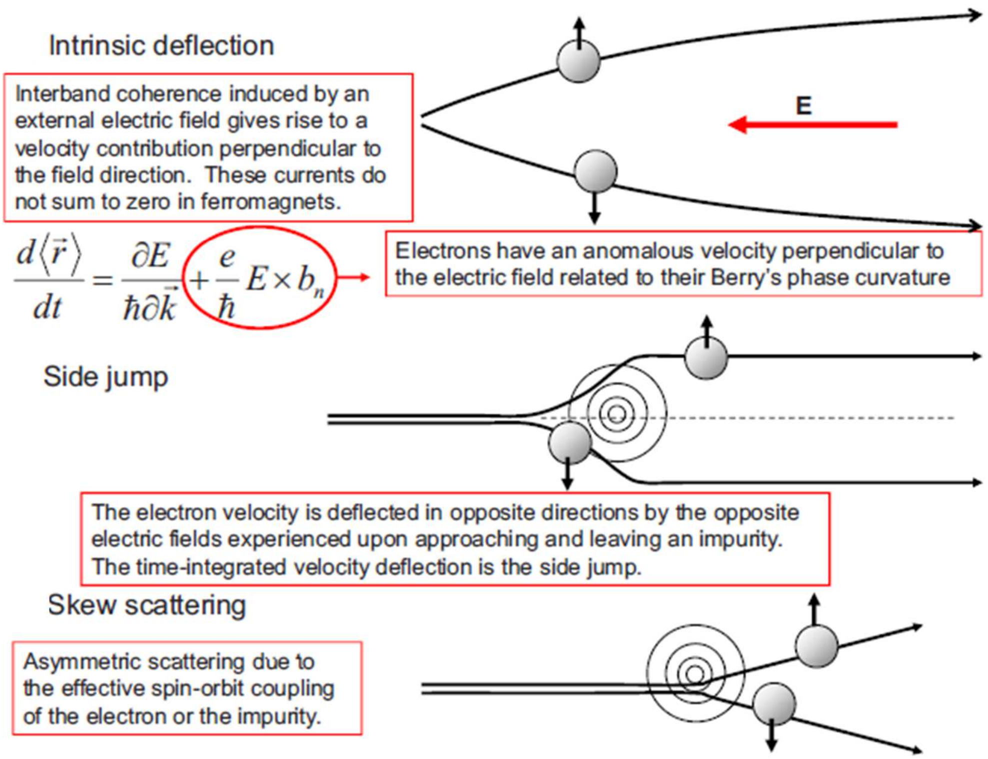

Figure 2-2. Illustration of the three main mechanisms that can give rise to an AHE. In any real material all of these mechanisms act to influence electron motion. Adopted from Ref. [87].

Beside the extrinsic scattering mechanisms, people argue that there also exists the intrinsic contribution which is directly linked to the topological properties of the Bloch states, and thus is dependent only on the band structure of the perfect crystal. Specifically, it is proportional to the integration over the Fermi sea of the Berry curvature of each occupied band or equivalently, to the integral of the Berry phases over cuts of the Fermi-surface (FS) segments [96, 97]. Accordingly, the intrinsic anomalous Hall can be described by:

$$\sigma_{ij}^{AH-\mathrm{int}} = -\varepsilon_{ijl}\frac{e^2}{\hbar}\int\frac{dk}{(2\pi)^d}f(\varepsilon_n(k))\nabla_k\times a_n^l(k) \qquad (2\text{-}4)$$

where ε_{ijl} is the antisymmetric tensor, $a_n(k)$ is the Berry phase connection, and $\nabla_k\times a_n^l(k)$ is the Berry phase curvature. It is noted that since the intrinsic AHE is independent on impurity, $\sigma_{xy}^{AH-\mathrm{int}}$ is thus constant with respect to σ_{xx}, the same behavior of side-jump mechanism. Therefore, we normally cannot distinguish the intrinsic AHE and side-jump contributions from the anomalous Hall magneto-transport measurements.

2.1.2. Spin Hall effect

From the above discussions about AHE, we know that the relativistic SOC generates an asymmetric deflection of the charge carriers depending on their spin direction. Following the same scenario, it is reasonable to expect that the SOC can also induce the spin-dependent

deflection in non-FM materials (NMs) through exact the same skew-scattering/side-jump mechanisms, and the corresponding transport phenomenon is called spin Hall effect (SHE). Figure 2-3 illustrates the relation between AHE and SHE. It can be clearly seen that in NMs where $M_Z = 0$, the numbers of spin-up and spin-down electrons are in equilibrium, therefore no transverse charge imbalance will occur. Instead, the SHE generates an edge spin-accumulation that has opposite polarization at opposite edges; in other words, SHE in NMs enables pure spin current along the transvers direction (whereas for the AHE case, the non-zero M_Z breaks the spin equilibrium in FMs, thus leading to a polarized transverse charge current).

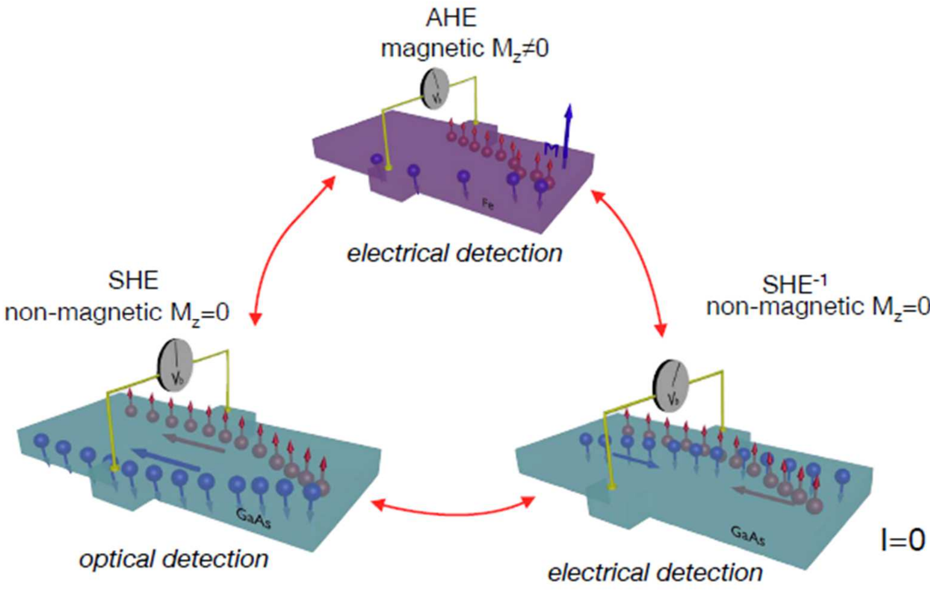

Figure 2-3. Illustration of the connected family of the spin-dependent Hall effects. In the AHE system, a charge current generates a polarized transverse charge current. In the SHE regime, an unpolarized charge current generates a transverse pure spin-current. Adopted from Ref. [98].

Although the idea of SHE was proposed as early as 1971 [99] (and re-captured by Hirsch in 1999 [100]), the initial challenge for SHE detection was primarily the lack of direct electrical signals. Therefore, the first experimental detections of the SHE signal in NMs were reported in 2004 from optical measurements [90, 101]. Since then, the rapid developments and progress of SHE and its related spintronics physics (*i.e.,* inverse spin Hall effect, spin-transfer torque, and spin galvanic effect) have become one of the hottest research frontiers in condensed-matter physics.

2.2. Quantum Hall effect

2.2.1. The Discovery of integer Quantum Hall effect

The discovery of the quantum Hall effect (QHE) was the result of systematic measurements on the two-dimensional electron gas (2DEG) systems, where the motion of electron along *z*-direction is fixed. It is known that when a strong magnetic field is applied perpendicular to such 2DEG system, the Hamiltonian is described by:

$$\{-\frac{\hbar^2}{2m}\nabla_z{}^2+\frac{m\omega_c^2}{8}(x^2+y^2)-i\hbar\omega_c[x\frac{\partial}{\partial y}+y\frac{\partial}{\partial x}]\}\psi=E\psi \tag{2-5}$$

where $\omega_C = eB/m$ is the cyclotron frequency. Under such circumstances, the electron in the conduction band will behave like simple harmonic oscillator, and the eigenstates of energy, so-called Landau Levels (LLs), are quantized in the x-y plane as

$$E_n = (\frac{\hbar^2 k_z^2}{2m}) + (n + \frac{1}{2})\hbar\omega_c \tag{2-6}$$

In such quantized LLs condition, it was first proposed by L.W Schubnikov and W.J de Haas that the longitudinal conductivity σ_{xx} would oscillate periodically with the change of applied magnetic field. On the basis of the well-known Onsager equation that [102]

$$S_F = \pi k_F^2 = (n + \gamma)\frac{2\pi e}{\hbar} B_n \tag{2-7}$$

where S_F is the cross sectional area of Fermi surface in k-space, n is the LL index, and γ is directly related to the Berry phase, the corresponding Shubnikov-de Haas (SdH) oscillation period only depends on the carrier density n_{2D} in the 2DEG system:

$$\frac{1}{f} = \Delta(\frac{1}{B}) = \frac{1}{B_{N+1}} - \frac{1}{B_N} = \frac{2e}{\hbar k_F^2} = \frac{2e}{n_{2D} h} \tag{2-8}$$

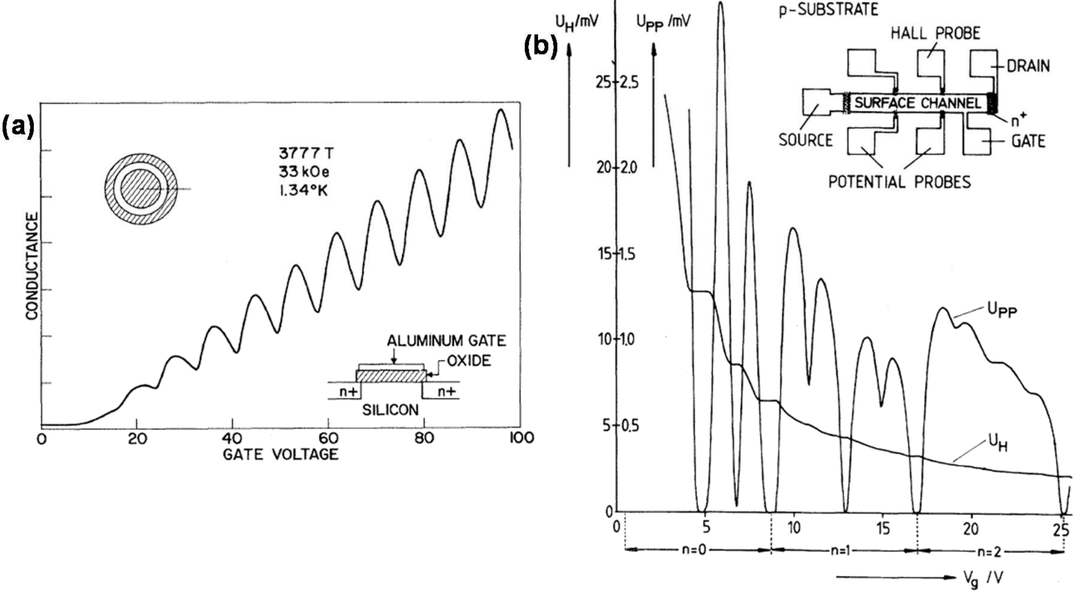

Figure 2-4. Quantum oscillations and quantum Hall effect observed in Si-FETs. (a) Observation of SdH oscillation on Si-based FETs by A.B Fowler *et al.,* in 1966. Adopted

from Ref. [103]. (b) First observation of QHE on Si-based FETs by K.V Klitzing in 1980. Adopted from Ref. [104].

In fact, the SdH quantum oscillation was observed in 1966 on silicon-based field effect transistors (FETs) [103], however, it was only in 1980 that German physicist Klaus von Klitzing, working at the high magnetic field laboratory with high mobility 2D silicon-based FET developed by Pepper and Dorda, made the unexpected discovery that the Hall conductivity was precisely quantized (no need of any corrections) [104].

In summary, QHE can be qualitatively understood from the semiclassical picture as shown in Fig. 2-5. In the 2DEG with large magnetic field, the LLs in the inner part of the sample are discrete, as described by Eq. (2-6). On the other hand, due to the finite-size of the 2DEG sample, the carrier density close to the sample edge will become finally zero. This in turns corresponds to an increase in the LL energies at the edge so that these levels become unoccupied outside the sample. Therefore, all occupied LLs inside the sample have to cross the Fermi level close to the boundary of the device, as shown in Fig. 2-5(c). Consequently, metallic properties are expected to resume at such crossing points along the edge states. Under such circumstances, when the Fermi level is located between two neighboring LLs, the cyclotron orbit localizes the conduction and bulk will thus be insulating; while the edge is conducting in the ballistic regime (as a result, there is no chemical potential drop along one edge in the longitudinal direction), and the longitudinal resistance will be zero. As we increase the magnetic field monotonically, we will see the longitudinal resistance oscillates

between the peaks and minimals; in the meanwhile, the Hall resistance will take the form of plateaus when the Fermi energy is located between two LLs since the chiral edge state has an integer number of e^2/h, and changes its value by one e^2/h as the Fermi level moves across each LL (note here we do not consider any spin or band degeneracy).

With the development of QHE over the past 30 years (especially the discovery of topological insulators since 2005), the whole condensed-matter physics community started to realize the intrinsic relation between the IQHE and the band structure topology such that the dissipationless chiral edge states formed in the IQHE state is a natural result of the change in the topological invariant, namely the TKNN number (or the first Chern number C_1) [105]. From this point of view, the IQHE state can be regarded as a new quantum state of matter that is distinct topologically from the traditional states of matter, and such quantum Hall insulator, in principle, belongs to a TI with broken TRS, as we will elaborate in the following section.

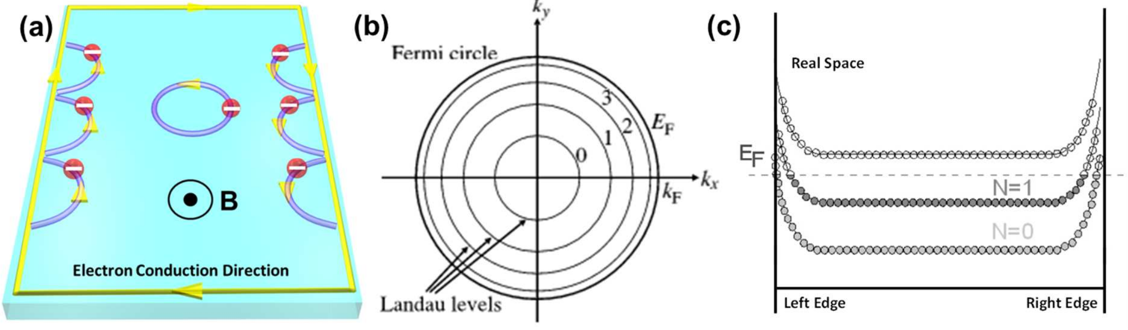

Figure 2-5. Landau levels in 2DEG. (a) Visualization of the cyclotron orbits and the chiral edge states on a 2DEG system subject to a strong perpendicular magnetic field. The yellow

arrows represent the conduction direction of electrons in the conduction band. (b) Landau level quantization in the momentum *k*-space. (c) Landau levels spectrum in real space for a finite-size device with boundaries.

2.2.2. The TKNN number in the integer quantum Hall effect

In a general 2DEG system with a periodic potential $U(x,y)$ (*i.e.,* it has periods a and b along the x and y directions, respectively), the band structure of such 2DEG under a perpendicular magnetic field B depends on the number of magnetic flux quanta per unit cell $\varphi = abeB/h = p/q$, where p and q are integer numbers. From the Bloch theorem, it is known that the eigenfunctions $\psi(x,y)$ satisfy the periodic condition that

$$\psi_{k_1k_2}(x+qa,y)e^{(-2\pi ipy/b-ik_1qa)} = \psi_{k_1k_2}(x,y+b)e^{(-ik_2b)} = \psi_{k_1k_2}(x,y) \tag{2-9}$$

where $u_{k_1k_2} = \psi_{k_1k_2}e^{(-ik_1x-ik_2y)}$, k_1 (modulo $2\pi/aq$) and k_2 (modulo$2\pi/b$) are good quantum numbers. Given the $\hbar\nu = \partial\hat{H}/\partial k$ relation, the conductor of the 2DEG system is given by

$$\sigma_{xy} = \frac{ie^2}{A_0\hbar}\sum_{\varepsilon_\alpha<E_F}\sum_{\varepsilon_\beta<E_F}\frac{(\partial\hat{H}/\partial k_1)_{\alpha\beta}(\partial\hat{H}/\partial k_2)_{\beta\alpha} - (\partial\hat{H}/\partial k_2)_{\alpha\beta}(\partial\hat{H}/\partial k_1)_{\beta\alpha}}{(\varepsilon_\alpha - \varepsilon_\beta)^2} \tag{2-10}$$

where A_0 is the area of the system and ε_α, ε_β are eigenvalues of the Hamiltonian. Eq. (2-10) can be further written as

$$\sigma_{xy} = \frac{ie^2}{4\pi h}\sum_{j\in(x.y)}\oint dk_j\int d^2r(u^*\frac{\partial u}{\partial k_j} - \frac{\partial u^*}{\partial k_j}u) \tag{2-11}$$

where the sum is over the occupied electron sub-bands and the integrations are over the unit cells in both the real and momentum spaces (Note that the integral over the *k*-space unit cell has been converted to an integral around the unit cell by Stokes's theorem). For the non-degenerate subband, ψ is a single-valued analytic function, and can be only changed by an *r*-independent phase factor θ at the Brillouin boundaries. Under such circumstances, the overall Hall conductance in the IQHE regime is given by

$$\sigma_{xy} = n\frac{e^2}{h}, \quad n = \frac{1}{4\pi i}\sum_{j\in(x.y)}\oint dk_j \int d^2r(u^*\frac{\partial u}{\partial k_j} - \frac{\partial u^*}{\partial k_j}u) \qquad (2\text{-}12)$$

where the TKNN number (or first Chern number C_1) n is an integer number and is the number of Landau levels under the Fermi energy. Consequently, C_1 gives the quantized Hall conductance, and this Hall conductance will give the chiral edge states in the 2DEG system. The bulk expression of the Hall conductance is given by the integral over the Brillouin zone and the edge expression of the Hall conductance is given by the winding number of the zero of the edge state energy on the Riemann surface (a complex-energy surface). In order to construct this Riemann surface, the fibre bundles on the isolated magnetic Brillouin zones have to be connected, and this gives rise to the topologically non-trivial chiral edge states.

2.2.3. Quantum Hall effect in Dirac fermions systems

As addressed in Section 2.2.1, for conventional 2DEG systems with the ordinary parabolic $E - k$ band structure, IQHE is the result of the quantization of the LLs under a perpendicular magnetic field. From Eq. (2-6), we know that the LLs are equally separated by $\Delta E = \hbar\omega_c$ along the energy axis, and the step of neighboring quantum Hall plateaus is given by $\Delta\sigma_{xy} = e^2 / h$ without considering any spin or sub-lattice degeneracy. However, with the developments on novel 2D Dirac-fermion systems (*i.e.,* graphene, topological insulators), different types of QHE have been observed.

2.2.3.1. Quantum Hall effect in graphene

Graphene is a monolayer of carbon atoms packed into a dense honeycomb crystal structure that can be viewed as an individual atomic plane extracted from graphite. It can be viewed as bipartite lattice composed of two interpenetrating triangular sublattices, with the "A" sublattice at vectors $\vec{R} = n_1\vec{a} + n_2\vec{b}$ (n_1 and n_2 are integers), and the "B" sublattice at vectors $\vec{R} = \vec{R} - (\vec{a} + \vec{b})/3$, as shown in Fig. 2-6(a). Using the phenomenological nearest-neighbor tight-binding model, the energy of the graphene electrons is given by [106]

$$E = \pm\sqrt{t_0^2[1 + 4\cos^2(\frac{k_y a_0}{2}) + 4\cos(\frac{k_y a_0}{2}) \cdot \cos(\frac{k_x\sqrt{3}a_0}{2})]} \qquad (2\text{-}13)$$

where t_0 is the nearest-neighbor hopping energy, and a_0 = 2.46 Å is the lattice constant. Most importantly, the conduction and valence bands correspond to the different signs; they touch each other at six points, the "K-values" of the two-dimensional hexagonal Brillouin zone. Two of these six points are independent (termed as K and K' in Fig. 2-6(a)), while the rest are equivalent by symmetry. In the vicinity of the K-points the energy depends linearly on the wave vector that

$$E = \pm \hbar v_F \sqrt{k_x^2 + k_y^2} \tag{2-14}$$

In this unique Dirac-cone-like system, electrons and holes are degenerate at the Dirac point, and the LL formation under a perpendicular magnetic field, is given by [107, 108]

$$E_n = \pm \sqrt{2e\hbar v_F^2 B \cdot |(n + \frac{1}{2}) \pm \frac{1}{2}|} \tag{2-15}$$

In 2005, A.K Geim group [108] and P. Kim group [107] reported the experimental observations of QHE in graphene. The observed quantized Hall conductance in graphene showed dramatic differences compared with the conventional 2DEGs. From Figs. 2-6(c) and (d), it can be seen that the σ_{xy} quantization is in accordance with

$$\sigma_{xy} = \pm 4(n + \frac{1}{2})e^2 / h \tag{2-16}$$

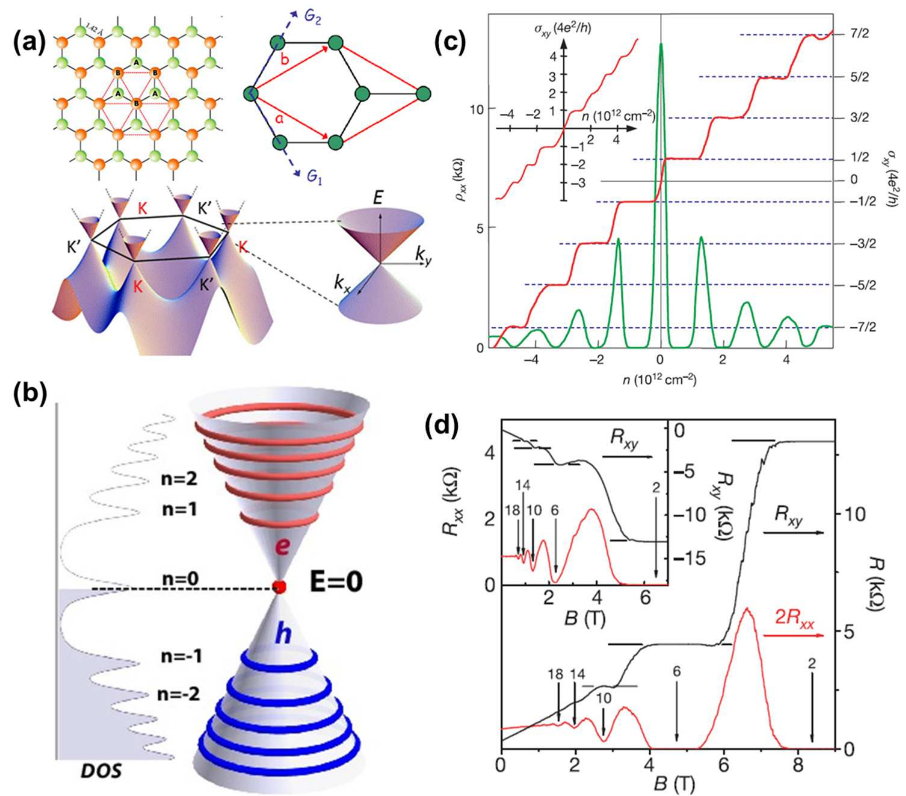

Figure 2-6. Quantum Hall effect in graphene systems. (a) Honeycomb lattice and the band structure of graphene. (b) LL distribution in graphene. (c) QHE observed in graphene by A.K Geim *et. al.* Adopted from Ref. [108]. (d) QHE observed in graphene by P. Kim *et. al.* Adopted from Ref. [107]

To understand the physics of such extraordinary QHE in graphene, it is noted that when only low-lying LLs ($|n| < 10$ for $B = 10$ T) are occupied, the separation of E_n is much larger than the Zeeman splitting energy, so each LL has a degeneracy $g_s = 4$, accounting for both the spin degeneracy and sublattice degeneracy. Consequently, the step between neighboring Hall plateaus is $\Delta\sigma_{xy} = 4e^2/h$ in the graphene system. In the meanwhile, it is also noted that the quantization condition is shifted by a half-integer, and the sequence of such half-integer multiples of quantum Hall plateau is on the basis of "relativistic" LLs with the particle-hole

symmetry of graphene. Specifically, time-reversal invariance guarantees particle–hole symmetry; σ_{xy} is therefore an odd function in energy across the Dirac point. However, in graphene, the zero LL is robust—that is, $E_0 = 0$ regardless of the magnetic field—provided that the sublattice symmetry is preserved [106]. In other words, all higher LLs ($n \geq 1$) are occupied by fermions with both (±) pseudospins, while for the $n = 0$ case, the degeneracy is half, and the zero LL is shared equally by electrons and holes. Consequently, the first Hall plateau of σ_{xy} for electron and hole is situated exactly at $\pm(g_s \cdot e^2/h)/2$.

More fundamentally, the consequence of the half integer quantum Hall effect in graphene can be viewed in terms of Berry's phase arising from the band degeneracy point. Specifically, let us consider a circular path in k-space at the vicinity of point K or K' where the energy is a linear function of $\delta\vec{k} = \vec{k} - \vec{K}$. Now, if we expand the wavefunction to first order in $\delta\vec{k}$ around the K point based on Eq. (2-13), we can obtain that

$$E(\vec{k}) \approx t_0[-\frac{1}{2}i\delta\vec{k}\cdot(\vec{a}+\vec{b}) + \frac{\sqrt{3}}{2}i\delta\vec{k}\cdot(\vec{a}-\vec{b})] = \frac{\sqrt{3}}{2}|\delta\vec{k}|\,at_0 e^{-i\pi/2}e^{-i\theta} \quad (2\text{-}17)$$

where θ is the angle from the x-axis in the k_x-k_y plane. Therefore, $E(\vec{k})$ has a phase of $\phi = \theta - \pi/2$. Since the wavefunctions have phases of $\pm\phi/2$, they change phase by π when θ increases by 2π, that is, when the k-vector goes once around a loop surrounding a K point. Equivalently, if we move adiabatically in k-space around the K point, the wavefunction acquires a "Berry phase" $e^{i\pi} = -1$ when completing a circuit. Therefore, the massless Dirac

state gives rise to a π–Berry phase in graphene, and causes the half-integer-shift in the QHE results in the graphene system.

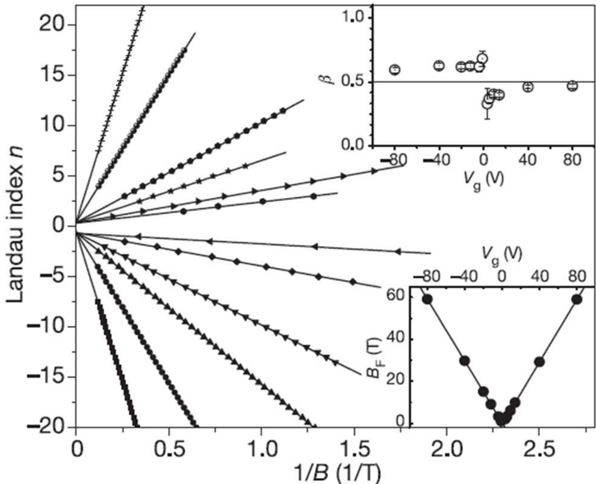

Figure 2-7. Fan diagram for SdH oscillations in graphene. Adopted from Ref. [107].

In fact, the π–Berry phase in graphene can be further probed from the SdH oscillation, given the Onsager relation described in Eq. (2-7). Specifically, in the magnetic field regime, the semiclassical magneto-oscillation description holds:

$$\Delta R_{xx} = R(B,T)\cos[2\pi(B_F / B + 1/2 + \gamma)] \tag{2-18}$$

where $R(B,T)$ is the SdH oscillation amplitude, B_F is the frequency of the SdH oscillation in $1/B$. In graphene, the Berry phase-associated term γ = 1/2, and experimentally, this phase shift is obtained from the SdH fan diagram, in which the sequence of values of $1/B_n$ for the

nth minimum in R_{xx} are plotted against their LL index n, and the intercept of linear fit to the data is found to be 0.5, as shown in Fig. 2-7.

2.2.3.2. Quantum Hall effect in 3D Topological Insulators

From Section 1.2, we know that for a perfect 3D TI system with the bulk states truly insulating, the gapless topological surface states on both the top and bottom surfaces can be regarded as two independent $g_s = 1$ Dirac system since there is neither spin nor sub-lattice degeneracy. Accordingly, when large perpendicular magnetic field is applied, both surfaces are driven into two half-integer QHE states with

$$\sigma_{xy}(top) = (n + \frac{1}{2})e^2/h, \quad \sigma_{xy}(bottom) = (m + \frac{1}{2})e^2/h \qquad (2\text{-}19)$$

And the total conduction $\sigma_{xy}(total) = (n + +m + 1)e^2/h$ is expected to persist in the 3D system (whereas for conventional IQHE, 2D is strictly required in order to form the discrete LLs, as discussed in Section 2.2.1). Unfortunately, struggled by the poor TI sample quality with remnant bulk conduction, it is extremely difficult for us to verify the 3D QHE phenomena over the past a few years.

Finally in 2014, Y. Chen's group successfully prepared the intrinsic bulk $BiSbTeSe_2$ (BSTS) material where the bulk is highly insulating with negligible conductance [109]. After transferring a 160-nm-thick exfoliated BSTS flake onto the SiO_2/Si substrate, they demonstrated the gated-tuned QHE in the 3D regime. As shown in Fig. 2-8(a), quantized (and developing) plateaus in σ_{xy} at $\nu e^2/h$ with integer ν = 1, 2 (and 3) are clearly observed,

concomitant with vanishing σ_{xx} (minimum in σ_{xx}), and the observation is consistent with the $\sigma_{xy}(top) = \frac{1}{2}e^2/h$ - $\sigma_{xy}(bottom) = (m+\frac{1}{2})e^2/h$ situation.

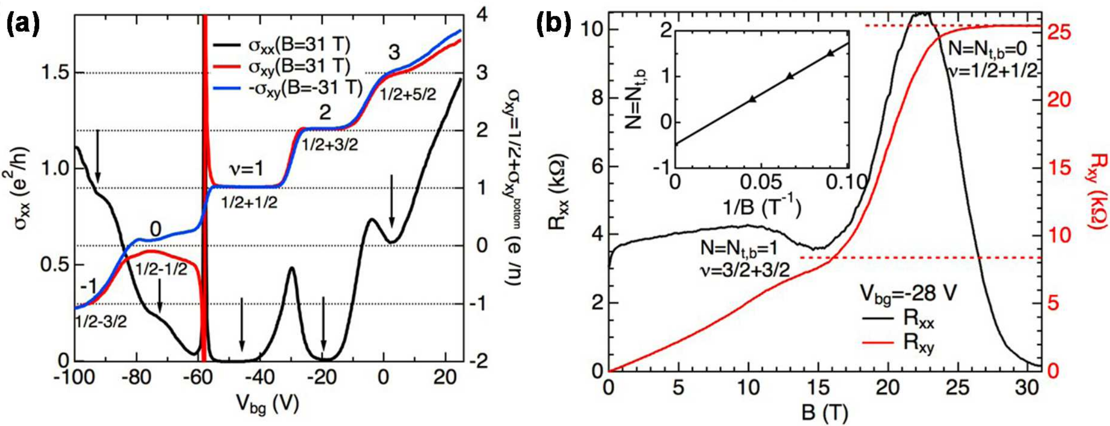

Figure 2-8. Quantum Hall effect in 3D Topological Insulators. (a) Gate-tuned QHE in the 160 nm BSTS sample. 2D longitudinal and Hall conductivities are extracted in units of e^2/h. (b) Magnetic-field-dependent QHE in the 160 nm BSTS sample. The back-gate voltage is firstly applied to tune both the top and bottom surfaces into the first LL states at low magnetic field $B \sim 10$ T. Adopted from Ref. [109].

To further manifest the Dirac-fermions-related QHE states on both the top and bottom surfaces, they carried out the following experiments: they first applied the back-gate voltage to move the Fermi level position of the bottom surface states such that both surfaces were tuned into the first LL regime at low $B \sim 10$ T. Then by sweeping the magnetic field, they observed that the step of neighboring quantum Hall plateau was $2e^2/h$, indicating the equal contribution from both surfaces. Subsequently, the results shown in Fig. 2-8(b) provides the direct evidence of double half-integer QHE states in the 3D TI regime.

2.3. Quantum spin Hall effect

In Section 1.2, we summarized the discovery of QSHE in 2D HgTe/CdTe and InAs/GaSb systems and the related TR-invariant physics. In contrast to QHE, the realization of disspationless helical edge conduction in the QSHE insulators does not need the presence of external magnetic fields. Nevertheless, under particular condition, it is possible to convert QSHE into the QHE state.

One way to understand the QSHE insulators is to regard them as two copies of the QHE system, as illustrated in Fig. 2-9 [30]. In principle, for a given spinless 1D system, both forward and backward electron movements are allowed. In a QHE bar, due to the TRS-breaking by the magnetic field, these two basic degrees of freedom are spatially separated, as expressed by the symbolic equation "2 = 1 + 1". In Fig. 2-9(a), the upper edge supports only a forward mover and the chiral edge conduction is robust (*i.e.,* immune to any scattering process). On the other hand, the QSHE system has four basic degrees of freedom, which are spatially separated as "4 = 2 + 2" [30].

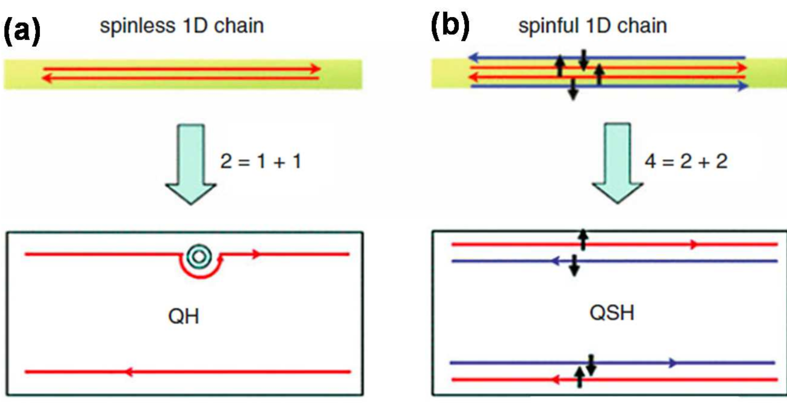

Figure 2-9. Analogy between QHE and QSHE. The spatial separations can be expressed by the symbolic equation (a) “2 = 1+1” for QHE, and (b) “4 = 2+2” for QSHE. Adopted from Ref. [30].

From Fig. 2-9, it is reasonable to argue that if we apply external magnetic field in the QSHE system, then the “4 = 2+2” situation is expected to reduce to the QHE “2 = 1+1” condition, as the result of TRS-breaking. In other words, by applying perpendicular magnetic field, a QSHE state will be reduced to the QHE state. In fact, in their first experimental QSHE work, M. König *et al.* indeed observed the QSHE-QHE transition in the CdTe/HgTe QWs [34]. Figure 2-10(a) shows the magnetic-field-dependent Hall resistance results. It can be clearly seen that with non-zero magnetic field, R_{xy} quickly deviates from the original R_{xy} = 0 Ω point, and gradually exhibits the quantized step with respect to the applied magnetic field. In the meanwhile, the longitudinal resistance also vanishes to almost zero as long as the applied magnetic field is larger than 0.05 T, as shown in Fig. 2-10(b).

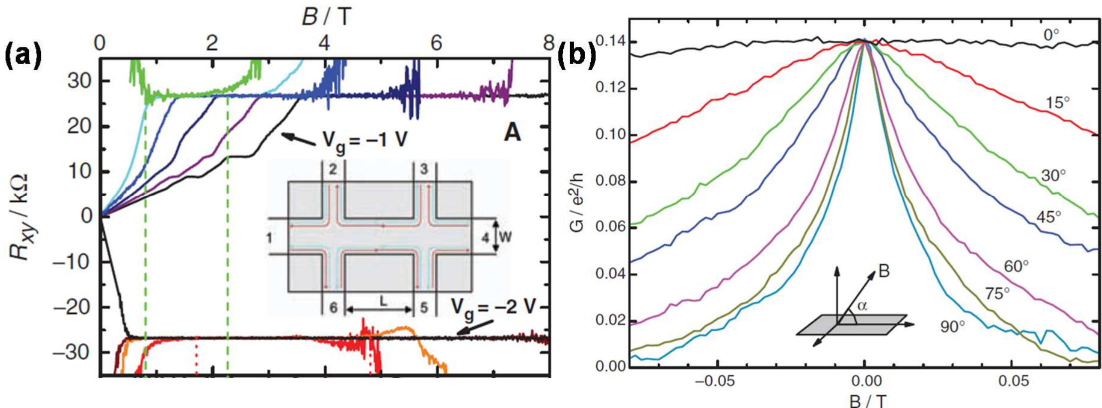

Figure 2-10. Transition between QSHE and QHE. (a) After applying external perpendicular magnetic field, QHE is observed in the CdTe/HgTe QWs. (b) Angle-dependent magneto-resistance measurements in the QSHE regime. Adopted from Ref. [34].

2.4. Quantum anomalous Hall effect

It is known that both the ordinary Hall effect and anomalous Hall effect in the solid-state transport are the result of the breaking of TRS. Specifically, in the former case, a perpendicular magnetic field is needed to deflect the conduction charge particles in order to generate the transverse voltage V_{xy}; in the latter case, spontaneous magnetization replace the external magnetic field, and V_{xy} arises from the spin-orbit interaction between charge current and magnetic moments. Since the discovery of the quantum Hall effect (QHE) 1980 [104], quantized dissipationless chiral edge conduction have been observed in various high-mobility 2DEG systems under high magnetic field. On the contrary, for decades, little progress was made on the realization of quantum anomalous Hall (QAHE) effect after the first theoretical model proposed by Haldane in 1988 [106]. It was not until the discovery of TI materials that the search for the suitable non-zero Chern insulators and QAHE became practical. In this section, we will briefly introduce both the theoretical predictions and experimental observations of QAHE in the magnetic TI materials, and we will also compare the physics among these different transport quantum phases.

2.4.1. Construct QAHE from QSHE in a 2D System

Since 2007, the realization of QSHE in the HgTe/CdTe 2D TI system brought a new impetus to construct QAHE [34, 37]. Given the close topological relation between these two quantum phenomena, it is argued that the helical edge state in the QSHE regime can be viewed as two copies of the QAHE channels with opposite chirality [29, 31]. Therefore, if one spin block can be suppressed due to TRS-breaking, the single QAHE conduction is thus realized. In 2008, based on the 2D TI four-band model described by Eq. (1-2), C.X. Liu *et al.* investigated the topological surface band change by introducing additional Mn ions into the HgTe/CdTe QWs [110]. In this case, the spin splitting term induced by magnetization can be expanded into a phenomenological form as

$$H_s = \begin{bmatrix} G_E & 0 & 0 & 0 \\ 0 & G_H & 0 & 0 \\ 0 & 0 & -G_E & 0 \\ 0 & 0 & 0 & -G_H \end{bmatrix} \qquad (2\text{-}20)$$

where the spin splitting energy difference is $2G_E$ for the two electron sub-bands $|E_1, \pm\rangle$, and $2G_H$ for the two hole sub-bands $|H_1, \pm\rangle$. Under such condition, if $G_E \cdot G_H < 0$ (*i.e.,* assume $G_E < 0$ and $G_H > 0$), the spin splitting for $|E_1, \pm\rangle$ and $|H_1, \pm\rangle$ would have opposite signs; with large enough splitting energy, the band inversion of the $|E_1, +\rangle$ and $|H_1, +\rangle$ states still holds, while the $|E_1, -\rangle$ and $|H_1, -\rangle$ sets finally enter the normal regime, leaving only spin-up edge states in the quantum transport (QAHE) regime, as illustrated in Fig. 2-11(a). Following the same spin splitting (*i.e.,* $G_E \cdot G_H < 0$) scenario, R. Yu *et al.* later pointed out that even the

four-band system was originally in the topological trivial (non-inverted) phase, proper exchange field would also induce a band inversion in the spin-up sub-bands (|E_1, +> and |H_1, +>) while pushing the spin-down sub-bands (|E_1, -> and |H_1, ->) even further away from each other (Fig. 2-11(b)) [49]. Under such circumstances, the single QAHE conduction could also be constructed.

In fact, although C.X. Liu *et al.*'s model sounds feasible, in reality, the Mn moments in the $Hg_{1-x}Mn_xTe$ system do not order spontaneously, therefore they fail to generate required spin splitting energy. Alternatively, since pronounced magnetization can be generated from the bulk Van Vleck susceptibility in the Cr-doped TI films even if the bulk reaches the insulating state, R. Yu *et al.* proposed an improved model to realize QAHE in the Cr-doped tetradymite-type TI systems [49]. They found that when these Cr-doped 3D TI films reduced their thickness into a 2D hybridization regime, quantum tunneling between the top and bottom surfaces became pronounced [29, 111-113], giving rise to a finite mass term, $m_k = m_0 + B(k_x^2 + k_y^2)$, and the surface Hamiltonian could be further modified as [49]

$$H = \begin{bmatrix} h_k + \mathrm{gM}\sigma_z & 0 \\ 0 & h_k^* - \mathrm{gM}\sigma_z \end{bmatrix} \quad (2\text{-}21)$$

where $h_k = m_k\sigma_z + v_F(k_y\sigma_x - k_x\sigma_y)$. Under the spatial inversion symmetry assumption (*i.e.*, neglecting the band bending of the top/bottom surface states in the thin film), v_F, g, and M were of same values for the top and bottom surfaces, and therefore, the requirement of $G_E \cdot G_H < 0$ was

automatically achieved. In the subsequent section, we will discuss the realization of QAHE in Cr-doped TI in the 2D hybridization regime based on R. Yu *et al.*'s model.

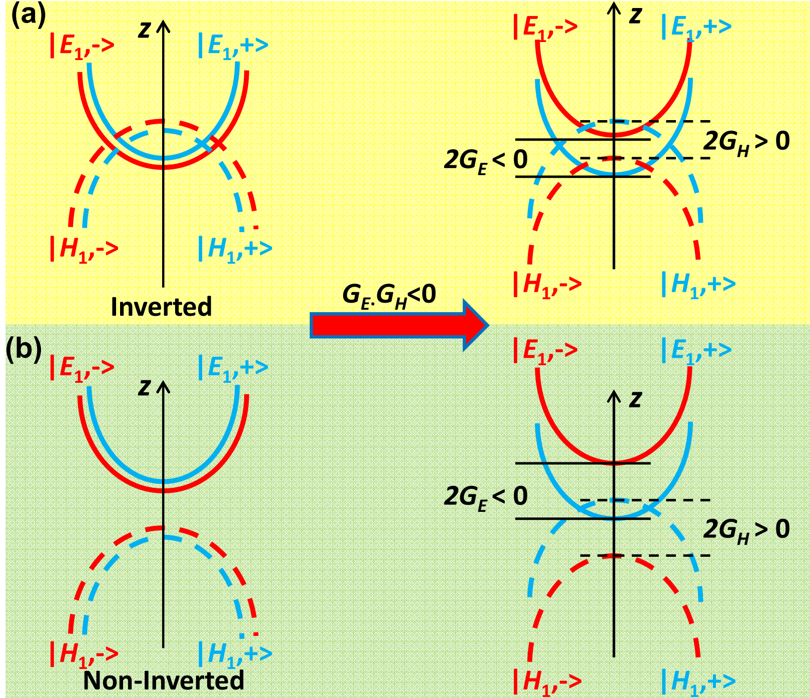

Figure 2-11. Construct quantum anomalous Hall in 2D regime. Evolution of band structure and edge states upon increasing the spin splitting for (a) Inverted band and (b) Non-inverted band. In both cases, $G_E < 0$ and $G_H > 0$; the spin-up sub-bands ($|E_1$, +> and $|H_1$, +>) remain inverted, while the spin-down sub-bands ($|E_1$, -> and $|H_1$, ->) enter the normal insulating states.

2.4.2. Observation of QAHE in 5 QL $Cr_{0.15}(Bi_{0.1}Sb_{0.9})_{1.85}Te_3$ Film

In 2013, C.Z Chang *et al.* from Tsinghua University firstly reported the observation of QAHE on the 5 QL $Cr_{0.15}(Bi_{0.1}Sb_{0.9})_{1.85}Te_3$ film grown on the $SrTiO_3$ (111) substrate [114]. In their work, QAHE was achieved at 30 mK, as shown in Figs. 2-12(a) and (c). Specifically, when

the Fermi level was electrically tuned into the surface gap (V_g ~ -1.5 V), R_{xy} was quantized at h/e^2 (25.8 kΩ), and such quantized value was nearly invariant with the external magnetic field, suggesting perfect edge conduction and charge neutrality of the film. In the meanwhile, the giant MR (2251%) was observed in Fig. 2-12(c), and it related to the quantum phase transition between the two opposite QAHE states via a highly dissipative bulk channel.

In addition, the gate-dependent R_{xy} and R_{xx} at zero field were provided in Fig. 2-12(b), and authors showed that R_{xy} exhibited a distinct plateau with the quantized value h/e^2; correspondingly, the longitudinal R_{xy} experienced a sharp dip down to 0.098 h/e^2. Recently, H.Z. Lu *et al.* fitted these transport data with an effective conduction model, and the agreement between the theory and the experiment confirmed that the transport in the QAHE regime indeed originated from the topological non-trivial conduction band, which had a concentrated Berry curvature and a local maximum in the group velocity [115]. Besides, in C.Z Chang *et al.*'s experiments on the 5 QL film, a non-zero longitudinal resistance R_{xx} was observed in the QAHE regime at zero field. By further applying a large perpendicular magnetic field (*i.e., B* > 10 T), the 5 QL film was finally driven into a perfect QHE regime, and R_{xx} diminished almost to zero [114]. The origins of such phenomenon have been further analyzed, and both the variable range hopping (VRH) [114] and the gapless quasi-helical edge states in the 5 QL Cr-doped TI film [116] have been proposed to explain such field-dependent R_{xx} results.

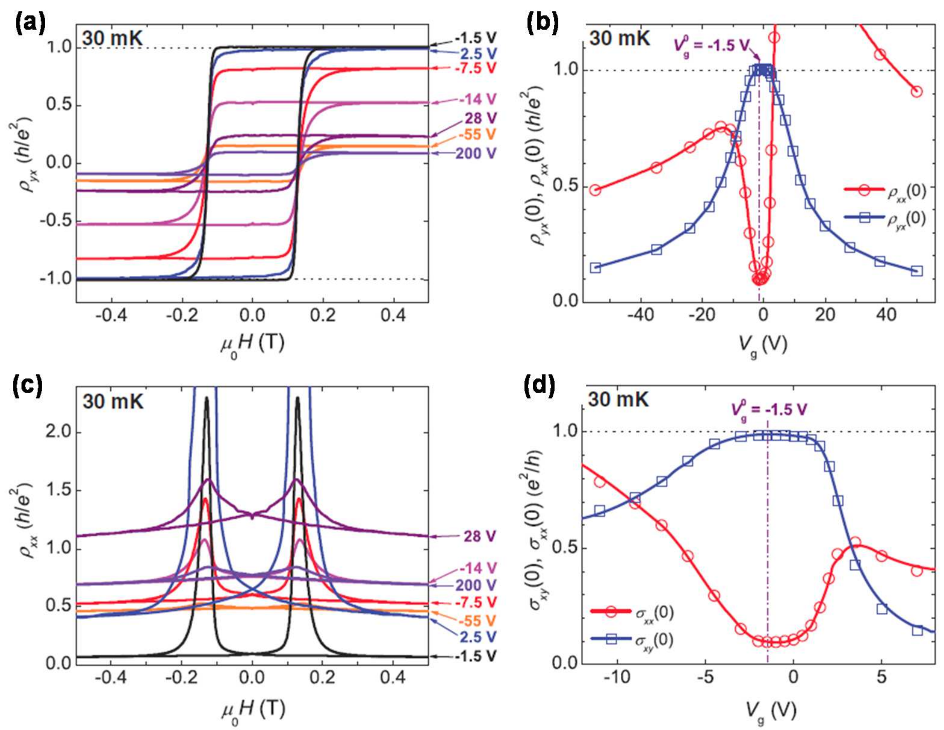

Figure 2-12. The QAH effect in the 5QL $Cr_{0.15}(Bi_{0.1}Sb_{0.9})_{1.85}Te_3$ film. (a) Magnetic field dependence of R_{xy} at different V_g. (b) Dependence of $R_{xy}(0)$ (empty blue squares) and $R_{xx}(0)$ (empty red circles) on V_g. (c) Magnetic field dependence of R_{xx} at different V_g. (d) Dependence of $\sigma_{xy}(0)$ (empty blue squares) and $\sigma_{xx}(0)$ (empty red circles) on V_g. The vertical purple dashed-dotted lines in (b) and (d) indicate the V_g for the charge neutral point. Adopted from Ref. [114]

2.4.3. Scale-invariant quantum anomalous Hall effect

Section 2.4.1 discussed the roadmap to construct the QAHE from QSHE in the 2D hybridized magnetic TI system. In general, given the intrinsic relation between the Berry phase and the anomalous Hall conductance [105, 117, 118], it has been suggested that the quantized Hall conductance without the presence of external magnetic field can be realized in

a ferromagnetic insulator which has a non-zero first Chern number (C_1) due to the non-zero integral of the energy band Berry curvature [29, 87]. To this regard, it was proposed by several groups that QAHE could also be derived from the gapped top and bottom surfaces in a 3D magnetic TI systems [29, 119-121]. In fact, for an ideal 3D magnetic TI material with insulating bulk state, the out-of-plane magnetization opens gaps on the top and bottom surfaces, and changes each surface into a non-zero C_1 phase with a half-quantized Hall conductance ($e^2/2h$), as illustrated in Fig. 2-13(a) [29, 119]. Due to the opposite local basis defined with respect to the normal direction $\hat{n}$ (Fig. 2-13(b)), the effective Hamiltonians of the top and bottom surfaces can be written as

$$H_{eff} = \pm v_F \hbar (k_x \sigma_y - k_y \sigma_x) + \Delta_z \sigma_z \tag{2-22}$$

where +/- represents the top/bottom surfaces, and $\Delta_z = gM_z$. Therefore, the massive Dirac fermions at the top and bottom surfaces have opposite masses ($\pm\Delta_z/v_F^2$) [119]. In the meanwhile, since the side surfaces in the thick 3D magnetic TI system is parallel to the magnetic moments, their topological surface bands remain massless. Under such circumstances, we can regard the 3D magnetic TI system as two massive Dirac fermions with opposite masses separated by a massless Dirac fermion in between, or equivalently, the gapless side surface acts as the domain wall between the two topologically different phases, as shown in Fig. 2-13(b). Just like the case in a usual QHE system, the half-quantized chiral edge channels will be trapped at this interface between the side surface and the top/bottom surface. More importantly, since the TRS is protected for the gapless side surface states, the

side-surface conduction is non-chiral, and it does not contribute to the Hall conductance; in other words, the stability of the quantized chiral edge state is well-maintained. As a result, QAHE can always be realized in the thick 3D magnetic TI samples as long as the bulk remains insulating and the quantized chiral channels are well-confined at the domain interface.

More recently, both H. Jiang *et al.* [122] and J. Wang *et al.* [120] proposed a more generic way to construct QAHE with tunable Chern number in thick magnetic TIs. Following the same spin splitting process as elaborated in Fig. 2-11, they found that the on-site band inversion depended on the critical film thickness d_n as [120]

$$d_n > n\pi\sqrt{B_z/(\pm\Delta_z - m_0)} \tag{2-23}$$

where n represents the nth-order sub-bands, m_0 is the energy difference between the lowest-order inverted conduction and valence sub-bands, and B_z is the z-axis coefficient of the gap parameter $m(k)$ defined in Eq. (1-2). Consequently, with a given exchange field strength, QAHE with higher plateaus is possible in the thick magnetic TI films with insulating bulk states, and the QAHE is, in principle, a universal quantum phase regardless of thickness (whereas in the QHE regime, the formation of the precise Landau level quantization requires the electrons to be strictly confined in the 2D region [123]).

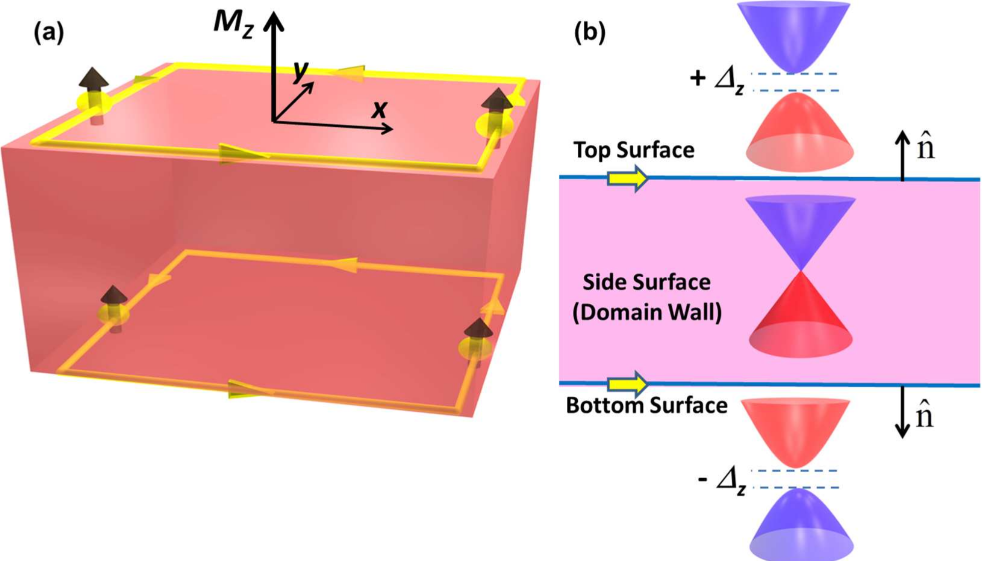

Figure 2-13. Quantum anomalous Hall effect beyond 2D regime. (a) Schematic of a 3D magnetic TI with an out-of-plane magnetization M_z, and the formation of chiral current on the top and bottom surface boundaries. (b) A chiral edge state will form around the domain wall between the 2D Dirac fermions with positive and negative masses. The arrows indicate the flow of the edge current.

2.5. Summary of Chapter 2

The completion of quantum Hall trio has greatly broadened our understandings about the electron movement in solids. Likewise, the discovered scale-invariant dissipationless conduction in these three quantum transport states has inspired us to the development of practical low-power-consumption electronics/spintronics applications. In this chapter, we outline the fundamental physics and relations between different Hall effects. In general, QSHE is a result of band inversion due to large SOC; since TRS is well-protected in such QSH insulators, helical edge states with both spin-up and spin-down electrons are allowed

and the conduction is immune to non-magnetic impurities. On the other hand, when TRS is broken by either perpendicular magnetic field or magnetic order, helical edge states are reduced to the single chiral channel, which in turn gives rise to QHE and QAHE, and backscattering from any impurity is strictly forbidden owing to the nature of chirality. In the meanwhile, it can be seen that the quantum Hall trio can convert to each other in certain conditions, depending on whether magnetic field or magnetic dopant is applied to the system. More importantly, due to the exotic bulk-insulating, surface-conducting feature of (magnetic) TIs, the QAHE state is expected to persist beyond the 2D limit, leading to the scale-invariant dissipationless conduction in all dimensions. In Chapter 5, we will show our detailed experimental work on the MBE-grown Cr-doped $(BiSb)_2Te_3$ thin films to demonstrate QAHE and its universal quantum phase diagram across the 2D hybridization limit.

Chapter 3
Molecular Beam Epitaxy Growth of Magnetic Topological Insulators

In this Dissertation, all the magnetic TI thin films were grown in an ultra-high vacuum Perkin-Elmer MBE system at the Device Research Laboratory (DRL) of UCLA. The growth process was monitored by *in-situ* reflection high-energy electron diffraction (RHEED). After magnetic TI thin film growth, atomic force microscopy (AFM) was applied to visualize the surface morphology, and magnetic properties were examined by superconducting quantum interference device (SQUID); both AFM and SQUID were provided by Materials Lab at The Molecular Instrumentation Center (MIC) of UCLA. In addition, detailed characterizations of the crystal structures and chemical composition were performed on the FEI TITAN Cs-corrected high-resolution transmission electron microscopy (HRTEM) operating at 200 KV at Center for Electron Microscopy of Zhejiang University, China.

For quantitative electrical, magnetic, and optical characterizations, the magnetic TI thin films were first patterned into the Hall bar geometry using conventional optical photolithography method. For top-gated devices, high-κ Al_2O_3 deposited by atomic layer deposition (ALD) was used as the dielectric layer, and the gate contact were prepared via standard e-beam evaporation. All the fabrication process was done at Nanoelectronics Research Facilities (NRF) of UCLA. Magneto-transport measurements were conducted in the

Quantum Design Physical Property Measurement System (PPMS) at UCLA, Institute of Physics (IOP) at Academia Sinica Taiwan, and National High Magnetic Field Laboratory (NHMFL) at Tallahassee. Besides, magneto-optic Kerr effect (MOKE) system was also used to study the magnetic properties of our samples. Accordingly, in this Chapter, brief introductions regarding the basic operational principles of some techniques and relevant experimental results will be addressed.

3.1. Molecular beam epitaxy

Molecular Beam Epitaxy (MBE) has become a very popular growth method ever since its invention in 1970s [124]. It possesses huge advantages over other growth methods, in terms of perfect crystalline quality growth, excellent thickness and doping level control, possible surface engineering, and potential integration of heterostructures and superlattices for more complex device structures. Therefore, even though MBE systems are not suitable for the production line due to its low throughput and difficult maintenance, they are still a very useful tool for research laboratories to realize all kinds of thin films.

MBE operates in an ultra-high vacuum (UHV) environment with the base pressure below 10^{-10} torr. By thermally evaporating highly purified elemental sources (*i.e.,* atomic beams), atomic layers can be deposited on the substrate one-at-a-time, and the term "epitaxy" refers to the growth mechanism that the adhesion layer is forced to mimic the lattice

configuration of the substrate. Therefore, by choosing a particular substrate and a set of growth parameters, we can achieve non-equilibrium growth and produce single-crystalline thin films. In general, the standard MBE process usually involves a sequence of meticulously executed steps, typically starting from substrate preparation, stabilizing evaporation sources, the preparation of a buffer layer, the growth of thin film, the subsequent post-growth annealing, and finally the passivation/cap layer deposition.

At DRL, our MBE system is modified from the original Perkin-Elmer solid source one, and has been fully implemented with various capabilities to synthesize and characterize tetradymite-type magnetic TI thin films (Figure 3-1). Since most elements (Bi, Te, Sb, Se, Al, Cr) used in this Dissertation have relatively low melting points (*i.e.,* below 1500 °C), regular high-temperature effusion cells (Knudsen cells) are used. The operational principle of the MBE growth is to use radiation heating of pyrolytic boron nitride (pBN) crucibles by tungsten heating filaments. During the thin film growth, the flux rate can be very stable by accurately controlling the Knudsen cell temperature (± 0.1 °C) since the atom vapor pressure is directly proportion to the source temperature. In addition, for special atoms like Se and Sb, their product distributions strongly depend on the cell temperature, and the principal thermal dissociation reactions at reduced pressures are governed by

$$\begin{aligned} Sb^4 &\Leftrightarrow 2Sb^2 \qquad T > T_1 \\ Sb^2 &\Leftrightarrow 2Sb \qquad T > T_2 \end{aligned} \tag{3-1}$$

Therefore, in order to fully utilize the monomeric element, valved crackers are added to the basic Se and Sb effusion cells to offer higher temperature for cracking.

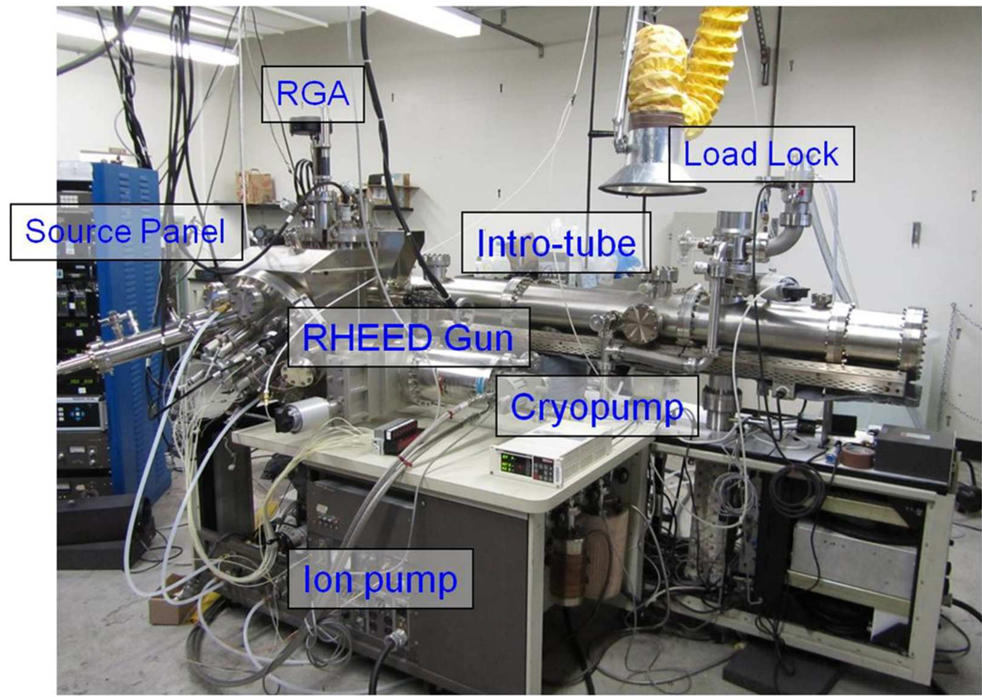

Figure 3-1. Solid-source MBE system designed for magnetic TIs growth. Currently, we have installed five Knudsen cells and two valved cracker cells in the source panel on our MBE system.

In our MBE system, UHV condition is achieved by successive pumping through three cascade chambers. Specifically, combined with the roughing pump, the turbo pump in the load-lock chamber is first used to pump down the pressure from atmosphere to 10^{-6} torr. This value is then lowered down to 10^{-8} torr in the intro-tube stage by the ion pump. Finally in the growth chamber, the base pressure is well-maintained under 10^{-10} torr with the co-pumping of both the ion pump and the cryo-pump. Meanwhile, the use of a liquid N_2 shroud around the

inner chamber of the growth system can provide effective radiation shield around the hot sources and sample heater, and it thus helps to maintain the vacuum as low as 10^{-10} torr during deposition.

To monitor the vacuum condition, two kinds of vacuum gauges are used in our TI MBE system based on their operation ranges, namely the thermocouple gauge and ion gauge. The thermocouple gauge is used to read out the pressure by measuring the temperature of filament inside since the heat conduction between the filament and its enclosure is proportional to the pressure in molecular flow. However, when the base pressure is below 10^{-3} torr, thermocouple gauge fails to work since wire thermal conductance becomes dominant in the lower pressure regime. Instead, ion gauge is used in the pressure region as low as 10^{-11} torr by measuring the electrical ions when the localized gas is bombarded with thermionic emission generated electrons. In addition, the components of gas species inside the chamber are monitored in real-time residual gas analyzer (RGA). The principle mechanism of the RGA is shown in Fig. 3-2(c): the neutral gas molecules in the growth chamber are firstly ionized and gain enough kinetic energy through the ionizer region, then it will diffract when both the vertical voltage and the magnetic field are applied, and only those ions with m/e equals to $2KB^2/eE^2$ will be collected by the detector. Consequently, by sweeping the voltage, we can obtain the components of the gas species and their pressure magnitudes from the RGA spectrum.

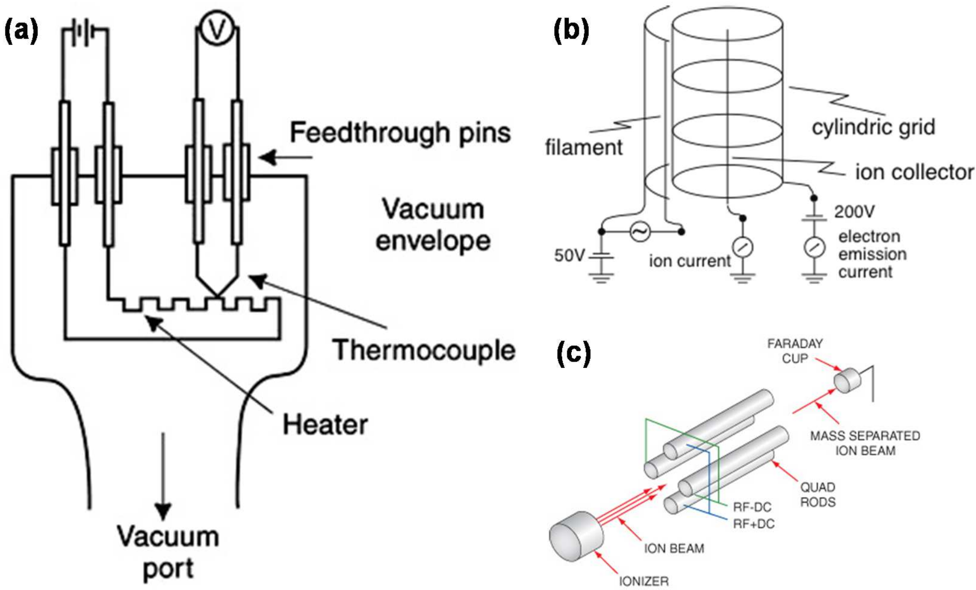

Figure 3-2. Vacuum gauges used in the MBE system. (a) thermocouple gauge, (b) ion gauge, and (c) RGA.

3.2. Reflection High Energy Electron Diffraction

RHEED is the most useful tool for real-time quantitative characterization of epitaxial growth, owing to its surface sensitivity, large working distance, and the reflection geometry compatible with deposition [125]. The RHEED system used in our MBE system consists of an 8 keV coherent electron gun (e-gun) and a phosphor screen/CCD imaging system developed by KSA Associates to record the diffraction patterns for the as-grown surface configuration. As illustrated in Fig. (3-3), coherent electrons are firstly accelerated by the e-gun, and then pass through two pairs of deflection control coils to form the incident beam with the specific angle onto the sample. The reflected beam will then reach the phosphor

screen and generate fluorescent light. The appeared RHEED pattern will finally be captured by the CCD camera.

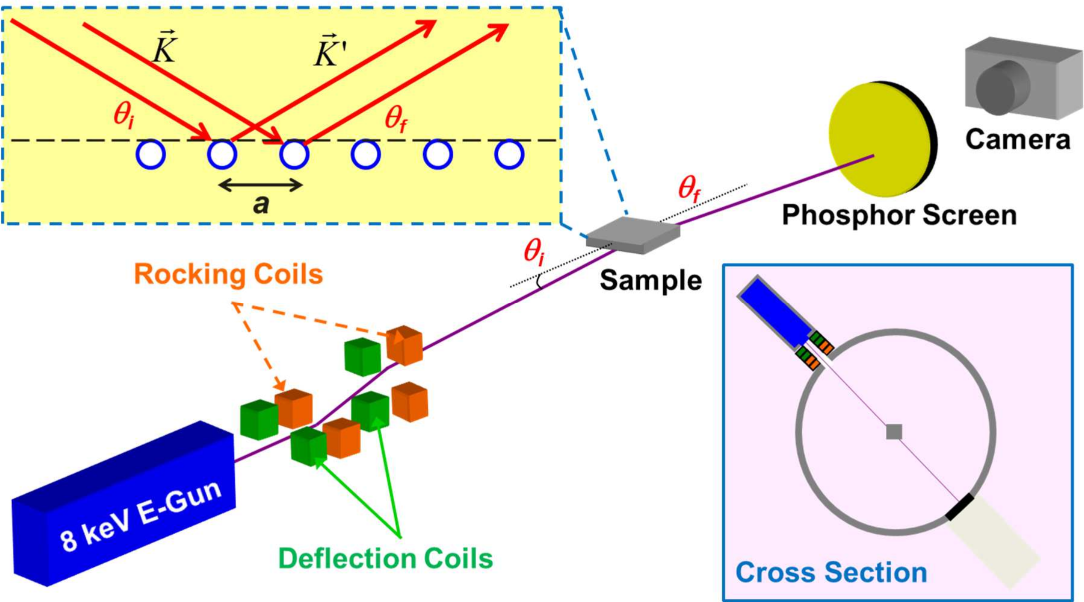

Figure 3-3. Schematic diagram of a RHEED system. Inset: Diffraction of the incident electron beam by the surface lattice.

In our RHEED system, the 8 keV e-gun beam provides a coherent electron beam wavelength of $\lambda = 0.26$ Å, given by the relativistic expression:

$$\lambda = \frac{h}{\sqrt{2m_e eV + \left(\frac{eV}{c}\right)^2}} \cong \frac{12.3}{\sqrt{V\left(1 + 1.95 \times 10^{-6} V\right)}} \tag{3-2}$$

where m_e is the electron rest mass, e is the electron charge, V is the acceleration potential in volts, c is the speed of light, and h is the Planck's constant. Such wavelength is quite small compared to atomic spacing in crystal lattice (3~5 Å), thus making RHEED sensitive to the

interatomic structures. In the meanwhile, the small grazing incident angle of the RHEED beam with respect to the surface (typically 1 - 5°) corresponds to a very small penetration depth, which in turn makes the diffraction pattern extremely sensitive to the surface layer of the as-grown films. Therefore, by monitoring the RHEED patterns during the sample, *in-situ* growth condition, along with the evolution of surface structures, can be examined systematically.

In practice, the reflection electron beam always carries both elastic and inelastic scattered components. However, because of the small grazing incidence angle θ_i, most electrons are elastically forward scattered. Consequently, by neglecting inelastic part, RHEED patterns can be modeled by using the Laue diffraction condition [125]

$$|\mathrm{K}| = |\mathrm{K}_{//} + \mathrm{K}_{\perp}| = \frac{2\pi}{\lambda}, \quad \mathrm{G} = \mathrm{K}'_{//} - \mathrm{K}_{//} = h\mathrm{A} + k\mathrm{B} \tag{3-3}$$

where $\boldsymbol{K}'_{//}$ and $\boldsymbol{K}_{//}$ are the electron wavevectors parallel to the surface for the diffracted and the incident beams, respectively. $\boldsymbol{G}$ is the reciprocal-lattice vector, and $\boldsymbol{A}$ and $\boldsymbol{B}$ are the reciprocal basis vectors corresponding to the unit vector ($a\hat{x} + b\hat{y}$) of the surface structure in real space. Energy conservation law would require:

$$\mathrm{K}^2 = \mathrm{K}'^2 = \mathrm{K}_{//}^2 + \mathrm{K}_{\perp}^2 = \mathrm{K}'^2_{//} + \mathrm{K}'^2_{\perp} \tag{3-4}$$

where $\boldsymbol{K}'_{\perp}$ and $\boldsymbol{K}_{\perp}$ are the electron wavevectors perpendicular to the surface for the diffracted and the incident beams, respectively. It is thus concluded that all possible solutions of the diffracted beam $\boldsymbol{K}'$ for Eqs. (3-3) and (3-4) will form the so-called Ewald sphere, and the

Laue condition is re-formulated as the intersections between the reciprocal lattice points and the Ewald sphere, as highlighted in Fig 3-4 (a).

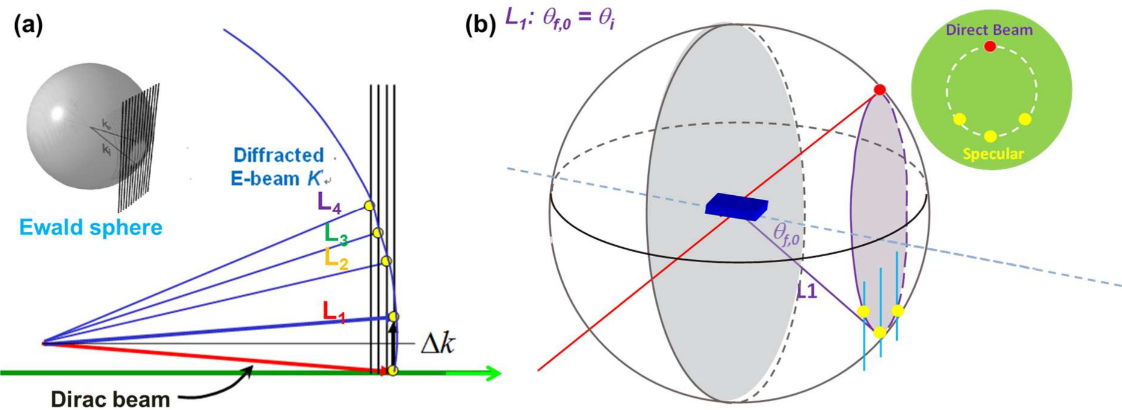

Figure 3-4. Ewald sphere for the construction of RHEED pattern. (a) The allowed diffracted beam must satisfy the diffraction condition that $\vec{k}_i \cdot \vec{r}_i - \vec{k}_f \cdot \vec{r}_f = n \cdot 2\pi / a + m \cdot 2\pi / b$ (b) RHEED pattern corresponds to a perfectly flat 2D surface in the *k*-space.

Mathematically, since the reciprocal *k*-space is the Fourier transform of the real space, we can therefore quantitatively construct the surface morphology from the observed RHEED pattern. For the ideal infinite perfect 2-D surface, the in-plane rectangular lattice with lattice constants *a* and *b* corresponds a reciprocal lattice with a set of 2D line matrix with infinite length and zero width, and neighboring lines are spaced at $\frac{2\pi}{a}$ and $\frac{2\pi}{b}$ in the two respective orthogonal directions. Under such circumstances, when the reciprocal line matrix is cut by Ewald sphere, RHEED patterns with concentric rings of dots are produced, as shown in Fig. 3-4(b).

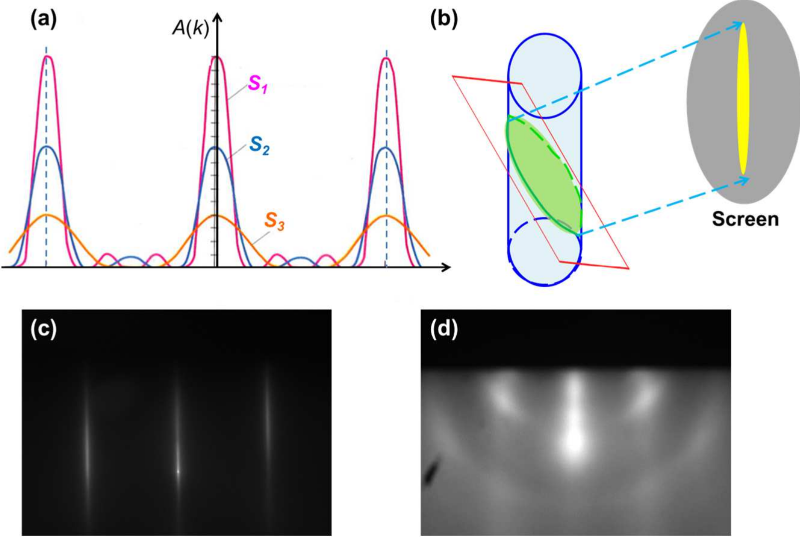

Figure 3-5. RHEED pattern for MBE-grown TI films. (a) Diffraction pattern for a finite 2D sheet. The amplitude is proportional to the size ($S_1 > S_2 > S_3$). (b) The projection of the truncation rod onto the RHEED screen. (c) RHEED patterns for the 2D Cr-doped $(BiSb)_2Te_3$ thin film surface. (d) RHEED patterns for the poly-crystalline Bi_2Se_3 thin film surface.

In reality, the surface of the as-grown film always has a finite size, and the diffraction pattern of such finite 2D sheet is shown in Fig. 3-5(a) with the amplitude distribution $A(k)$ given by

$$A(k) = \frac{1-\exp(i\Delta k_x Na)}{1-\exp(i\Delta k_x a)} \frac{1-\exp(i\Delta k_y Mb)}{1-\exp(i\Delta k_y b)} \tag{3-5}$$

where N ad M are integer numbers, and $\Delta K = K' - K = \Delta k_x \cdot \hat{x} + \Delta k_y \cdot \hat{y}$. In other words, the diffraction patterns are an array of infinitely long rods with the diameter inversely proportional to the coherence length of the atomically flat area in the real space. Moreover, given the small angle between such rod array and the RHEED screen, which is the same as

the diffraction angle θ_f, the resulting RHEED pattern will appear to be the elongated steaks instead of dots, as shown in Fig. 3-5(b). Alternatively, if the surface contains terraces with random orientations which means arbitrary combination of (a, b) can be allowed along the surface, and the RHEED pattern will evolve from distinctive diffraction spots to poly-ring-like shape, as shown in Fig. 3-5(d).

Another important feature for RHEED monitor is the observation of intensity oscillation versus growth time during the epitaxial growth. If the diffusion length (L_{diff}) of the adatoms is smaller than the size of the single terrace (L_{2D}), layer-by-layer growth mode (also called Frank-van der Merwe growth) is expected where one layer is completed before molecular atoms are added to the following layer, as shown in Fig. 3-6(a). As a result, the surface (and thus the RHEED intensity) periodically changes its morphology because of the nucleation and coalescence of islands in the growing layer. Accordingly, we can infer the growth rate by counting the periodicity of the RHEED oscillation spectrum. The damping of the oscillations and the recovery after growth both happen on a timescale considerably longer than the oscillation period. We can interpret this as an increase of long-range roughness that approaches a steady state in the limit of totally damped oscillations. On the other hand, if $L_{diff} > L_{2D}$ (this condition is normally achieved when the substrate temperature is increased), the 2D epitaxial growth is dominated by the step-flow growth mode. In this case, the monatomic step edge (due to slightly mis-cut during the wafer preparation) will act as the major sink for the

diffusing adatoms and there be no 2D nucleation on the terrace, thus resulting in no L_{2D} and RHEED intensity change during the step-flow growth [126].

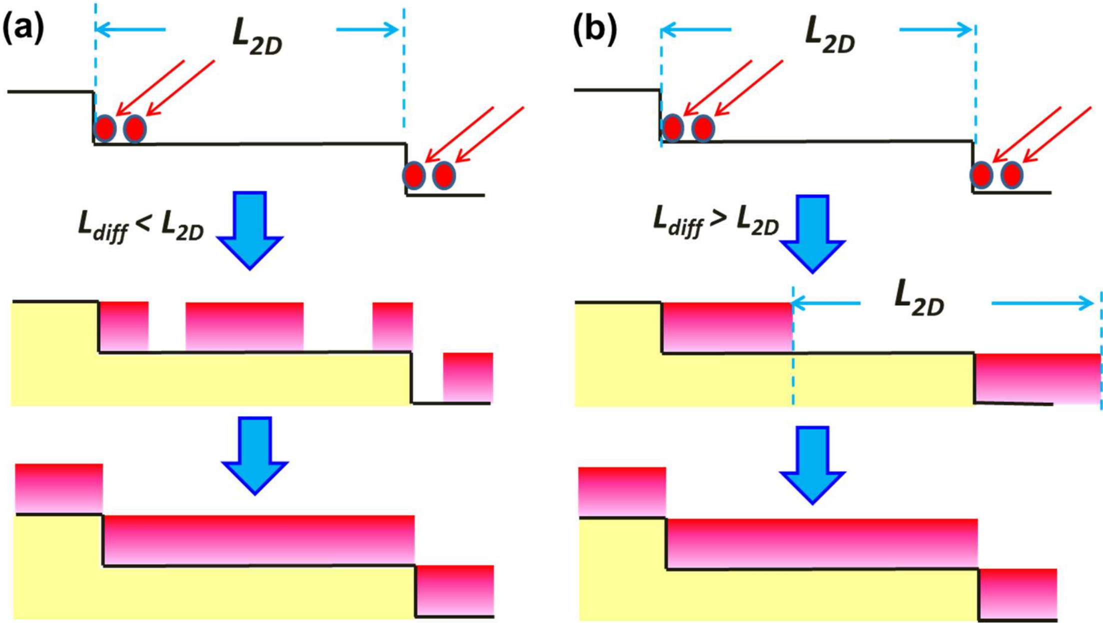

Figure 3-6. Layer-by-layer and Step-flow growth modes. (a) In the layer-by-layer growth mode, 2D nucleation occurs as a result of limited diffusion length. (b) Once the adatoms have enough kinetic energy to migrate over the terrace, step-flow mode is anticipated with a relatively constant RHEED intensity.

3.3. Magnetic topological insulators thin films growth

As mentioned in Section 1.3, introducing magnetic ions into the host TI materials is the most effective way to generate robust magnetism and open a gap of the surface states. In this section, we would like to present our work on the preparations of magnetically doped TI thin films by MBE.

3.3.1. Crystal structure of 3D topological insulators

The most commonly used 3D TIs are a tetradymite-type V-VI compound semiconductors, with the form of $A_2^{V}B_3^{VI}$ (A=Bi,Sb and B=Te,Se). Here, we take Bi_2Se_3 as the example. The crystal lattice is rhombohedral and belongs to a space group of $D_{3d}^5\left(R\overline{3}m\right)$ with five atoms in one unit cell. The essence of Bi_2Se_3 is characterized by the octahedral bonding (with dsp^3 and d^2sp^3 hybridizations) and a van der Waals gap separating five atom layer lamellae, called quintuple layer (QL). The sequence of layers within the lamellae is **$Se^{(1)}$ – Bi - $Se^{(2)}$ – Bi - $Se^{(1)}$** in the plane perpendicular to the trigonal axis, as shown in Fig. 3-7(a). The superscripts (1) and (2) denote differently bonded Se atoms. The bonding is primarily ionic and covalent within the layers (**$Se^{(1)}$ – Bi** and **Bi - $Se^{(2)}$**), and the van der Waals force dominates between the Se double layers (**$Se^{(1)}$ - $Se^{(2)}$**). Such Van der Waals gap gives the structure a distinctly anisotropic character similar to other layered materials, such as BaF_2, MoS_2, BN and graphene. Although the crystal system of Bi_2Se_3 is classified as a rhombohedral Bravais lattice, they are twinned together in groups of four into a larger hexagonal system. In a unit cell under the hexagonal representation, the lattice constant along the c-axis (lattice constant = 28.58 Å) is much larger than the lattice constant along a-axis (lattice constant = 4.14 Å) in Bi_2Se_3. This big difference in the lattice constants along different directions results in a highly anisotropic crystal structure. Therefore, to achieve epitaxial growth of Bi_2Se_3, the substrate should be chosen along (111) for diamond structure or (0001) for hexagonal structure.

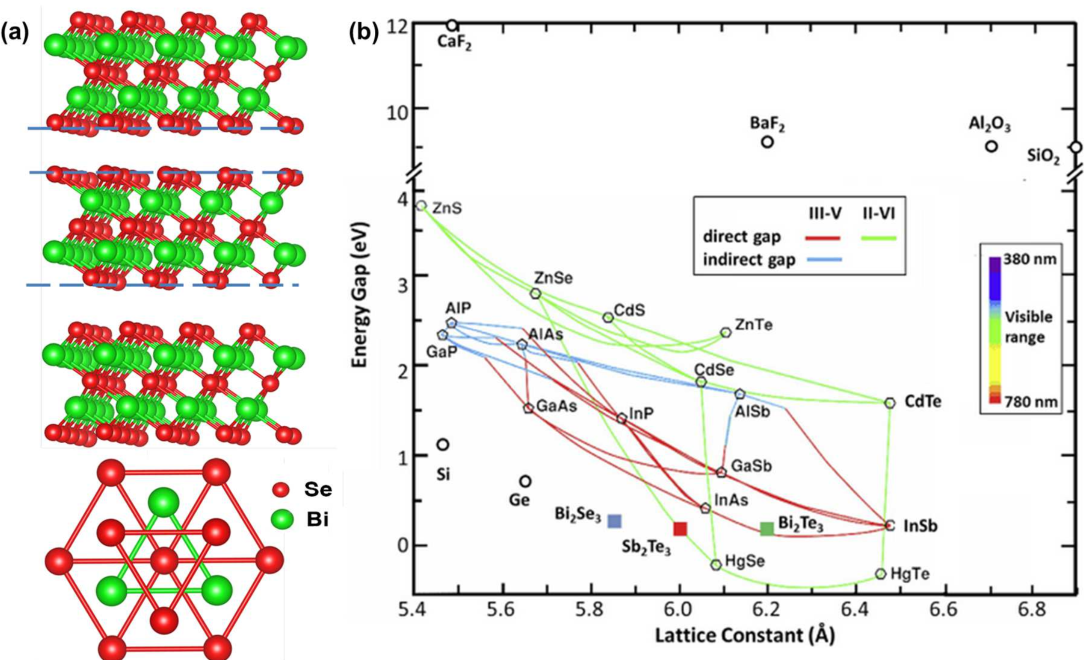

Figure 3-7. Crystal structure of 3D TIs and energy gap-lattice constant chart. (a) 3D view of Bi_2Se_3, highlighting the layered Se–Bi–Se–Bi-Se structure and the Van der Waals gap among neighboring QLs. (b) Lattice constants and energy gaps of different substrates and TI materials. Various substrates are marked by open symbols, while TI materials are marked by solid squares. Adopted from Ref. [127].

It is known that for conventional semiconductors with covalent or ionic-bonded structures, the epitaxial growth is only allowed on suitable substrates which have the same lattice constant. In contrast, owing to the presence of the Van der Waals bonds between the QLs of TI materials, the so-called Van der Waals epitaxy growth mechanism is quite different [128]. Due to the weak van der Waals interaction, the lattice matching condition is drastically relaxed. Consequently, a variety of substrates have been chosen for the growth of (magnetic) TIs in our group, and high-quality epitaxial (magnetic) TI thin films have been

prepared despite the large lattice mismatch between the films and the substrates, as will be elaborated in the following sections.

3.3.2. Cr-doped Bi_2Se_3 films grown on Si (111)

Thin films of Cr-doped Bi_2Se_3 are grown under an ultrahigh vacuum (UHV) system by MBE. High resistivity Si (111) wafers ($\rho > 10^5$ Ω·cm) are firstly cleaned with standard RCA method: first trichloroethylene (TCE), second acetone, and finally 100 % ethyl alcohol; each step the substrate is soaked in the solvent and sonicated for 10 to 15 minutes, and it is then removed from the solvent bath and dried by filtered dry nitrogen gas [129]. The substrates are then treated by the hydrofluoric acid (HF) wet etching (*i.e.,* the Si wafer is dipped into the 5% HF solution for a 30-second rinse) so that the surface dangling bonds are saturated by a layer of hydrogen atoms and the (111) surface is 1×1 reconstructed to further enhance the film quality [130]. Fig. 3-8(a) displays the RHEED pattern of the fresh H^+-terminated Si (111) surface. Both clear Kikuchi line and bright specular spot are observed, indicating the epi-ready 2D surface.

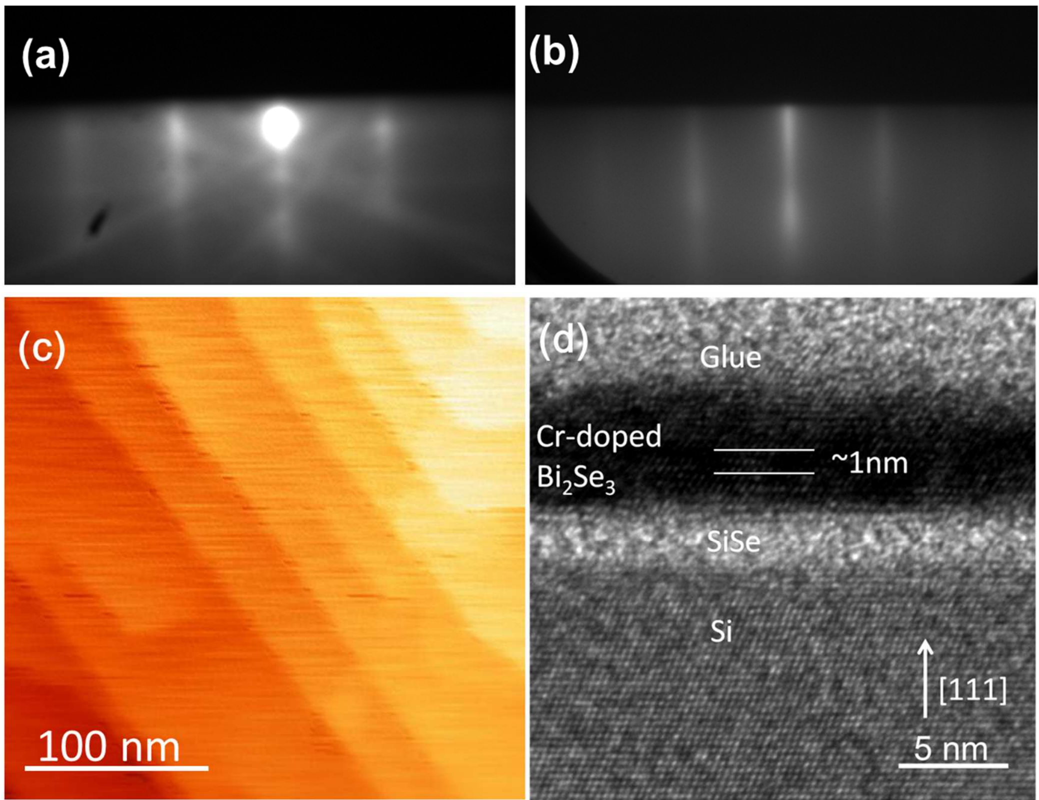

Figure 3-8. Cr-doped Bi_2Se_3 thin film grown on H^+-terminated Si (111) substrate. (a) RHEED pattern of the fresh H^+-terminated Si(111) surface. (b) RHEED pattern along $[11\bar{2}0]$ direction of an as-grown surface of $Bi_{2-x}Cr_xSe_3$ with a thickness of 7 QLs. (c) AFM image of the $Bi_{1.9}Cr_{0.1}Se_3$ thin film with the size of 0.3 µm × 0.3 µm. (d) HRTEM of the $Bi_{1.8}Cr_{0.2}Se_3$ grown on a Si (111) substrate. Adopted from Ref. [131].

During the growth, high-purity Bi (99.9999%) and Cr (99.99%) are evaporated by Knudsen effusion cells while single Se (99.99%) atom is produced by the SVTA cracker cell in order to avoid the formation of Se^2 or Se^4 clusters. Since the adhesion coefficient of Se is much less than that of Bi, the thin film growth is conducted under the Se-rich environment with a nominal Se to Bi ratio approximately 10:1, which is expected to reduce the Se vacancy defects [132]. In addition, the substrate is remained at a relatively high substrate temperature

(300 °C) to optimize both the surface migration rate and Cr solubility simultaneously. *In-situ* growth dynamics are monitored by our RHEED system, and the sharp streaky patterns in Fig. 3-8(b) manifest the 2D pseudomorphic growth. After the film growth, a 2 nm Al is evaporated to passivate the surface at room temperature. Al film is later naturally oxidized to form Al_2O_3 after the sample is taken out of the chamber, and such oxide layer effectively prevents the grown magnetic TI film from unwanted environment doping and aging effect [133].

The surface morphology of the thin film is examined AFM. Typical triangular terraces are revealed without visible clusters even with the Cr doping concentration reaching to as high as 20%. Figure 3-8(c) illustrates the AFM image of a $Cr_{0.1}Bi_{1.9}Se_3$ sample with a film thickness of 50 quintuple layers (QLs). The average terrace size is estimated to be 200 nm, which is comparable with the un-doped Bi_2Se_3 thin films grown on Si (111) substrates following a similar growth method [132]. Further structural characterization is proceeded by using HRTEM, as shown in Fig. 3-8(d), the layered structures of the 7QL single-crystalline $Cr_{0.1}Bi_{1.9}Se_3$ thin film can be clearly seen and the lattice spacing between (0003) planes is measured to be ~1 nm, corresponding to one quintuple layer. It also confirms that there are no clusters or second phase developed inside the crystalline structural matrix, within the resolution of the HRTEM. This result indicates that Cr atoms are most likely uniformly distributed inside the Bi_2Se_3 and the tetradymite quintuple layered structure is well maintained.

From Fig. 3-8(d), it is seen that there is an amorphous layer (~2nm) between the Si substrate and the MBE-grown Cr-doped Bi_2Se_3 films. Additional energy dispersive X-ray spectroscopy (EDX) analysis suggests that such interfacial layer is probably $SiSe_2$ which may be formed in the Se-rich environment during the initial annealing process [132]. Moreover, it was reported by C.Z Chang *et al.* that the substitutional Cr atoms in the host Bi_2Se_3 matrix might aggregate to form super-paramagnetic multimers which could locally open with surface gap (yet show no long-range FM order) and thus made the whole Cr-doped system too complicated for quantitative investigations [134].

3.3.3. Cr-doped $(BiSb)_2Te_3$ films grown on GaAs (111)B

In fact, the essence of Van der Waals growth is the non-existence of the dangling bonds. Accordingly, it is suggested best TI films can be obtained on the Van der Waals 2D materials. During the past five years, we have investigated various substrate materials, and so far our best growth is achieved on the GaAs (111)B substrate.

Unlike Si substrate cleaning process, semi-insulating ($\rho > 10^6$ Ω·cm) GaAs (111)B substrates are cleaned by acetone with ultrasonic for 10 minutes before loaded into the growth chamber. Then the substrates are annealed to 580 °C in order to remove the native oxide; the whole pre-anneal process is carried out under a Se-rich environment. During the growth, the GaAs substrate is maintained around 200 °C (growth temperature), with the Bi,

Sb, Te, and Cr shutters opened at the same time. The obtained ternary $(Bi_xSb_{1-x})_2Te_3$ is a non-stoichiometric alloy that has the same tetradymite QL structure. More importantly, from our previous experience, due to the presence of intrinsic vacancies and antisite defects, the MBE-grown Bi_2Te_3 films tend to be *n*-type while the Sb_2Te_3 films have *p*-type hole as the majority carrier [127, 135]. Therefore, by adjusting the Bi-to-Sb ratio, we can tune the carrier type of the compound TIs, as shown in Fig. 3-9(a). With additional structural engineering (*i.e.,* control the film thickness), we are able to prepare high-quality Cr-doped $(Bi_xSb_{1-x})_2Te_3$ thin films with suppressed bulk carrier density.

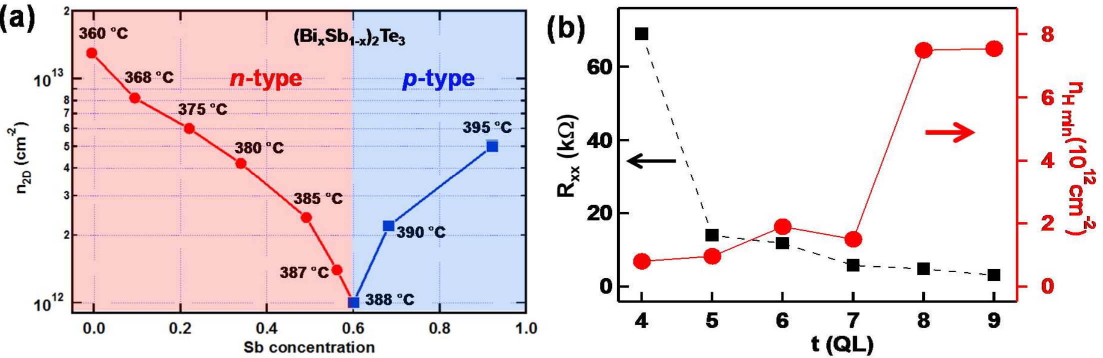

Figure 3-9. Tunable $(Bi_xSb_{1-x})_2Te_3$ compound TI system. (a) The carrier density as the function of Sb concentration. During the growth, the Bi flux is kept constant while the Sb cell temperature is modulated. Carrier type crossover from *n*-type to *p*-type occurs when Sb% > 60%. (b) Longitudinal resistance and carrier density as the function of film thickness. Lowest carrier density of 8×10^{11} $cm^2/V{\cdot}s$ has been achieved in thin films (d < 7 QL) with suppressed bulk contribution at T = 1.9 K.

In-situ growth dynamics of the Cr-doped $(Bi_xSb_{1-x})_2Te_3$ thin films are also monitored by RHEED. Figure 3-10(a) shows the as-grown RHEED patterns taken at t = 0 s, 30 s, and 65

s successively. Both the sharp 2D streaky lines and the bright zero-order specular spot persist during the entire growth process (and both features are much more pronounced than the Cr-doped Bi_2Se_3 growth), indicative of the single-crystalline feature of the sample. The smooth surface morphology is later confirmed by AFM as shown in Fig. 3-10(b) where typical TI triangular terraces are preserved without any Cr aggregations or clusters. Meanwhile, periodic RHEED oscillation is clearly observed during the film growth, as highlighted in Fig.3-10(c). By fitting the RHEED oscillation periods, the growth rate is extracted to be around 1 QL/min (Inset of Fig. 3-10(c)). From Section 3.2, we know that the RHEED patterns directly reflect the surface lattice morphology in the reciprocal *k*-space. Accordingly, we can inspect the as-grown surface configuration by using the *d*-spacing evolution between the two first-order diffraction lines as shown in Fig. 3-10(a). From Figs. 3-10(c) and (d), it can be seen clearly that the *d*-spacing drops quickly as soon as the growth starts, and the surface transition from the pristine GaAs to the $Cr_y(Bi_xSb_{1-x})_{2-y}Te_3$ has completed immediately after the formation of the first quintuple layer (QL). In addition, the degree of the *d*-spacing change (*i.e.*, -6.8%) corresponds to a Bi/Sb = 1 in the grown TI compound material.

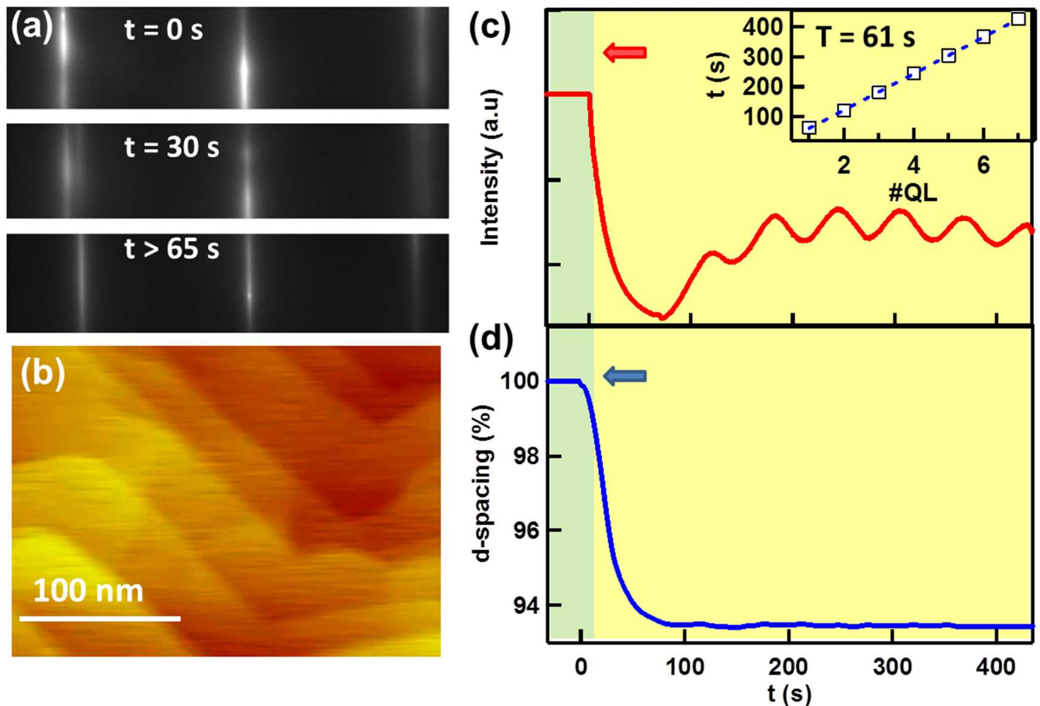

Figure 3-10. Cr-doped $(Bi_xSb_{1-x})_2Te_3$ grown on GaAs (111)B substrate. (a) RHEED patterns along $[11\bar{2}0]$ direction of the surface of Cr-doped $(Bi_{1-x}Sb_x)_2Te_3$ thin film taken at 0 s, 30 s, and 65 successively during growth. The surface configuration transits quickly from the GaAs to the TI layer. A sharp 2D pattern with a bright specular spot can be observed during the growth. (b) AFM image of the Cr-doped TI thin film with the size of 0.3 μm × 0.3 μm. (c) RHEED oscillations of intensity of the specular beam. Inset: the growth rate of 1 QL/min is determined from the RHEED oscillation period. (d) *d*-spacing evolution of the surface lattice during growth. After 1QL growth, the surface configuration from GaAs to $Cr(Bi_{1-x}Sb_x)_2Te_3$ has completed. Both arrows in (c) and (d) indicate the beginning of thin film growth. Adopted from Ref. [136].

After the sample growth, the EDX spectrometer is employed to perform elemental mappings. A thin layer of Pt is deposited during the Focused ion beam (FIB) process in order to protect the magnetic TI thin film. Figure 3-11(a) displays a typical high angle annular dark field (HAADF) image of the cross-section Cr-doped TI film from a heuristic perspective. The

white contrast from the TI film clearly indicates that the $Cr_y(Bi_xSb_{1-x})_{2-y}Te_3$ film is composed of much heavier atoms compared with the GaAs substrate. Specifically, the colored EDX maps collected from both the TI (Bi, Sb, Cr, and Te) and substrate (Ga and As) are illustrated individually in Figs. 3-11(b)-(g). The distribution of every component (especially Cr) is uniform and there is no substitutional or interstitial doping/diffusion from the GaAs substrate, therefore leaving the bottom TI surface intact. To elaborate the detailed structural characteristics of the epitaxial film, HRSTEM investigation is performed. As shown in Fig. 3-11(h), single-crystalline $Cr_y(Bi_xSb_{1-x})_{2-y}Te_3$ film with a sharp interface can be clearly seen on top of the GaAs substrate. At the same time, the corresponding zoom-in HRTEM image in Fig. 3-11(i) manifests the typical TI quintuple-layered structure. It is also identified that the van der Waals interactions between adjacent quintuple layers indeed induce a larger gap compared with the neighboring Bi/Sb-Te covalently-bonded sheets. Most importantly, the highly ordered hexagonal configuration also confirms that there is no Cr interstitial defects or second phase separation inside the TI thin film. Combined with Fig. 3-11(d) and the theoretical anticipations, it may suggest that the Cr dopants prefer the stable substitution formation inside the host TI matrix. Furthermore, from the overall EDX spectrum in Fig. 3-11(j), the chemical composition of the Cr-TI film is calculated to be $Cr_{0.2}(Bi_{0.5}Sb_{0.5})_{1.8}Te_3$, consistent with the *d*-spacing estimation in Fig. 3-10(d). From these data, we may conclude that high-quality Cr-doped TI thin films with low defects, well-defined surfaces, and uniform Cr distribution have been prepared by MBE.

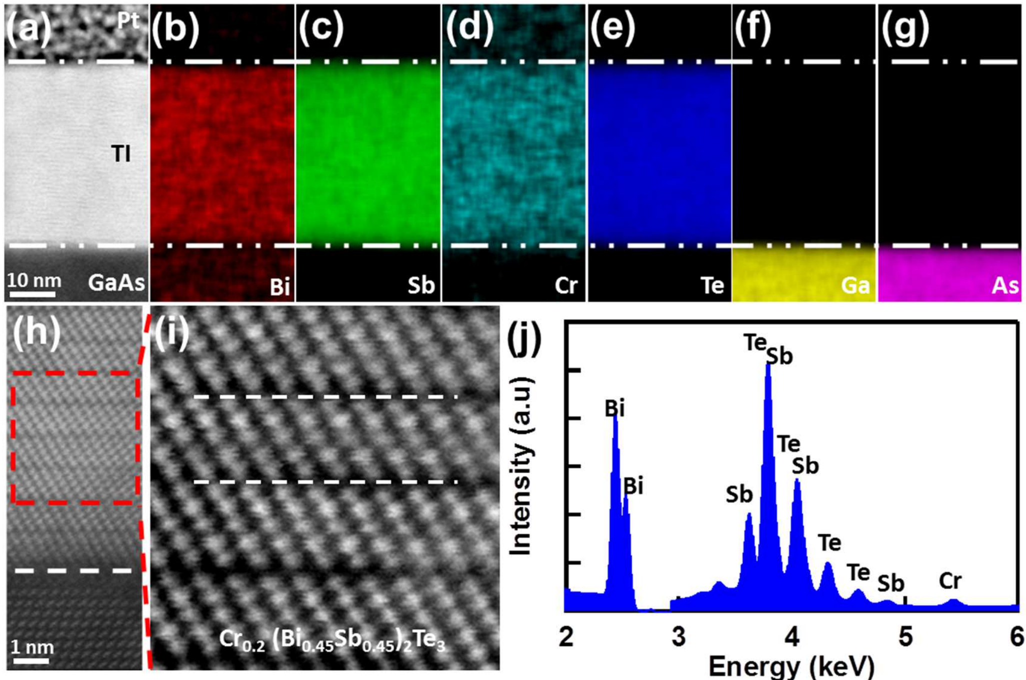

Figure 3-11. Crystalline structure and doping profile of the $Cr_{0.2}(Bi_{0.5}Sb_{0.5})_{1.8}Te_3$ thin film. (a) HAADF image of the cross-section $Cr_{0.2}(Bi_{0.45}Sb_{0.45})_{1.8}Te_3$ film grown on the GaAs substrate. (b)-(g) Distribution maps of each individual element: (b) Bi, (c) Te, (d) Cr, (e) Ta, (f) Ga, and (g) As. Cr dopants distribute uniformly inside the TI layer. (h) High-resolution cross-section STEM image, showing the epitaxial single-crystalline $Cr_{0.2}(Bi_{0.5}Sb_{0.5})_{1.8}Te_3$ thin film with a sharp TI – GaAs interface. (i) Zoom-in HRSTEM demonstrates the typical quintuple-layered crystalline structure of 3D TIs. Neither Cr segregations nor interstitial defects is detected. (j) EDX spectrum to examine the chemical element compositions. The Cr doping concentration is estimated to be 10%. Adopted from Ref. [136].

To understand the sharp interface between the Cr-doped $(Bi_{1-x}Sb_x)_2Te_3$ layer and the GaAs substrate (in contrast to the amorphous $SiSe_2$ formed between the Cr-doped Bi_2Se_3/Si counterpart), we carry out careful zoom-in HRTEM scanning and EDX mapping near the TI/GaAs interface. From Fig. 3-12(b), it is seen that the top atomic layer at the interface shows slightly brighter dots, compared with the underlying GaAs substrate, implying the

presence of other heavier atoms. This is probably due to the fact that the top layer of As are substituted by Se during the de-oxidization annealing under the Se-rich environment. A more solid evidence is given by the Se and Ga EDX mappings in Figs. 3-12(c) and (d), respectively. Since GaSe has a quadruple layered structure, with Se-Ga-Ga-Se alternative atomic layers along the *c*-axis, and the coupling between the two quadruple layers is predominantly of the van der Waals type. After the formation of GaSe buffer layer, the top-most Se atoms have no dangling bands, thus promoting the van der Waals epitaxial growth of TI [135]. Beside the sharp interface, Cr-doped $(Bi_{1-x}Sb_x)_2Te_3$ thin films possess another salient property over $Bi_{2-x}Cr_xSe_3$ regarding to the band topology, as we will elaborate in Chapter 4. As a result, the explorations of TRS-breaking physics and applications are mainly performed on the $Cr_y(Bi_xSb_{1-x})_{2-y}Te_3$ system in this Dissertation.

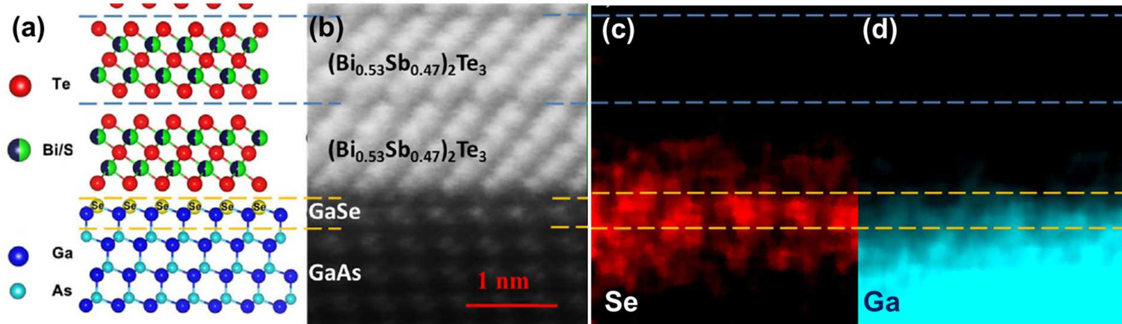

Figure 3-12. Cross-sectional TEM and EDX near the TI/GaAs interface. (a) Schematic diagram of the atomic layer structures of the TI film, interface and substrate. (b) HRTEM image exhibits the TI QL structure, the GaAs substrate and the GaSe buffer layer. The single GaSe layer is marked by the orange lines. (c)-(d) EDX distribution maps of Se and Ga, respectively. Adopted from Ref. [135].

3.4. Superconducting Quantum Interference Device

Superconducting quantum interference device (SQUID) magnetometer is the most sensitive device used to measure extremely subtle magnetic fields (as low as 10^{-14} T). A DC SQUID, in essence, consists of two Josephson junctions (which are two superconductors coupled by a weak link) connected in parallel on a closed superconducting loop. In the absence of any external magnetic field, the input current will split equally into the two branches. However, if an external magnetic field is applied to the ring, the current flow balance will be broken; in other words, the magnetic field changes the quantum-mechanical phase difference across each of the two junctions. These phase changes, in turn, affect the critical current I_C of the SQUID. In the extreme case when the current in either branch exceeds I_C, a non-zero voltage will appear across the junction. Accordingly, SQUID, in principle, functions as a magnetic flux-to-voltage transducer [137]. In this Dissertation, we use the Quantum Design Magnetic Properties Measurement System (MPMS) to carry out the SQUID measurements on our MBE-grown magnetic TI films.

3.4.1. SQUID results of $Bi_{2-x}Cr_xSe_3$ systems

In this study, a 50 QL $Bi_{1.9}Cr_{0.1}Se_3$ thin film sample is firstly grown on the Si (111) substrate, as described in Section 3.3.2. The phase transition information and the relation of magnetization as a function of temperature can be obtained by performing the Zero-Field

Cooling (ZFC) and Field Cooling (FC) measurements. An external magnetic field of 5 mT is applied perpendicular to the sample plane during these measurements. The bifurcation of ZFC and FC curves at 8 K in Figure 3-13(a) corresponds to a blocking temperature, which may be associated with the formation of coherent nanostructur during growth as also observed in Mn doped DMS [138]. In the meanwhile, the Curie temperature (T_C) is found to be 35 K in Fig. 3-13(a), where the magnetic momentum reduced to approximately zero, and above this temperature the material becomes paramagnetic (PM). However, the evolution of the DC magnetic susceptibility ($\chi = M/H$) on temperature above T_C does not follow the linear relationship manifested by the well-known Curie-Weiss Law [139]:

$$\chi \propto \frac{C}{(T - T_C)^{\alpha}} \tag{3-6}$$

where α is the critical exponent which modifies the susceptibility in the immediate vicinity of the Curie point, and the Curie constant C gives the information of the Lande g-factor and magnetic impurity density in the material [140]. Instead of a linear dependence, a curvature existing between two linear regions can be clearly seen in the inset of Fig. 3-13(a).

To understand the above unconventional ferromagnetism, detailed field-dependent characterizations are carried out. The magnetic hysteresis loops (M-H) taken at various temperatures (Fig. 3-13(b)) manifest the presence of FM ordering in the low temperature range ($T < 35$ K) with the coercivity field $H_C \approx 15$ mT at 5 K (Inset of Fig. 3-13(b)), and a saturation field around 0.2 T. The large volume susceptibility with the value of 7.3 (SI) at 5 K

inside the system is established probably via the van-Vleck model [49]. As temperature increases, the FM order is gradually suppressed, and finally the system becomes PM above T_C = 35 K.

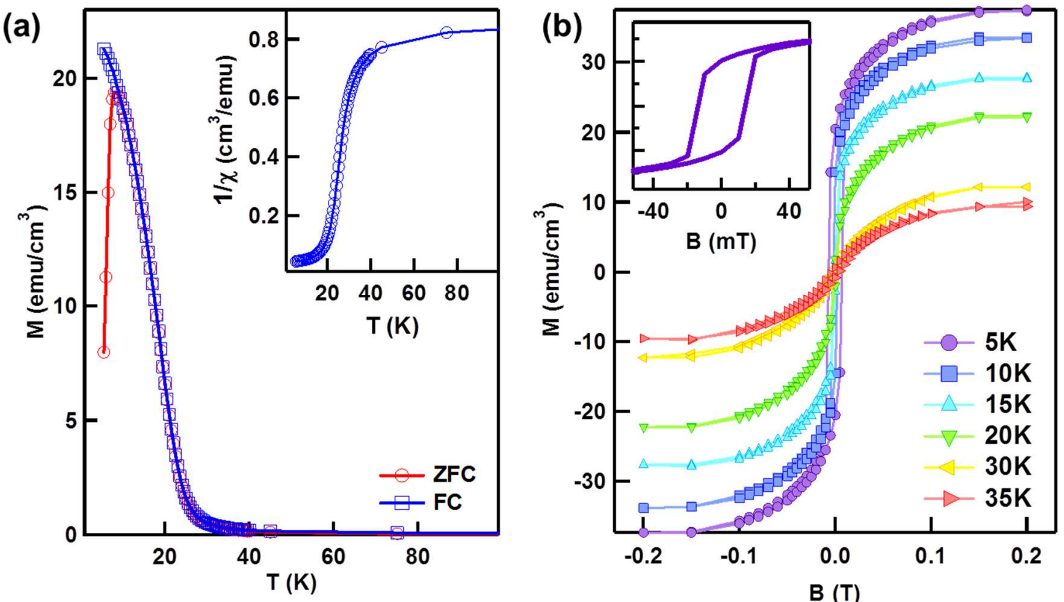

Figure 3-13. SQUID results of the 50 QL $Bi_{1.9}Cr_{0.1}Se_3$ sample grown on the Si (111) substrate. (a) Magnetization versus temperature for the sample under ZFC (red circles) and FC (blue squires) conditions. The external field is 5 mT perpendicular to the sample surface. Inset: Plot of $(\chi-\chi_0)^{-1}$ versus temperature *T*. This relation does not follow the linear Curie-Weiss law above T_C. (b) *M -H* loops of the 50 QL $Bi_{1.9}Cr_{0.1}Se_3$ thin film at 5 K, 10 K, 15 K, 20 K, 30 K, and 35 K. Inset: Zoom-in hysteresis loop at 5 K, the coercivity field is around 15 mT. Adopted from Ref. [131].

To comprehensively investigate the underlying interaction in the present system, for example, long range or nearest neighbor interactions, we study the FM-PM phase transition. Here we adopt the modified Arrott-Noakes equation of state [141]

$$(\frac{H}{M})^{1/\gamma} = \frac{T - T_C}{T_1} + (\frac{H}{M})^{1/\beta} \quad (3\text{-}7)$$

Provided that the linearized parallel straight lines are observed, one can thus experimentally determine the underlying dominant interaction by re-plotting *M-H* curves [141, 142]; for example, in the long range mean field model, these exponents are γ=0.5, β=1, while in the nearest neighbor 3-D Heisenberg model, the corresponding values change to γ=0.37, β=1.39. However, as depicted in Figs. 3-14 (a) and (b), rather than displaying the parallel straight lines, both plots display some continuous curvatures, even in the saturation region up to 0.8 T, and these effects turn to exclude the dominant long range interactions, as well as preclude us from giving an accurate estimation of the transition temperature [143]. In addition, the absence of "*S*" shape in the Arrott plot suggests that the underlying phase transition is of second order.

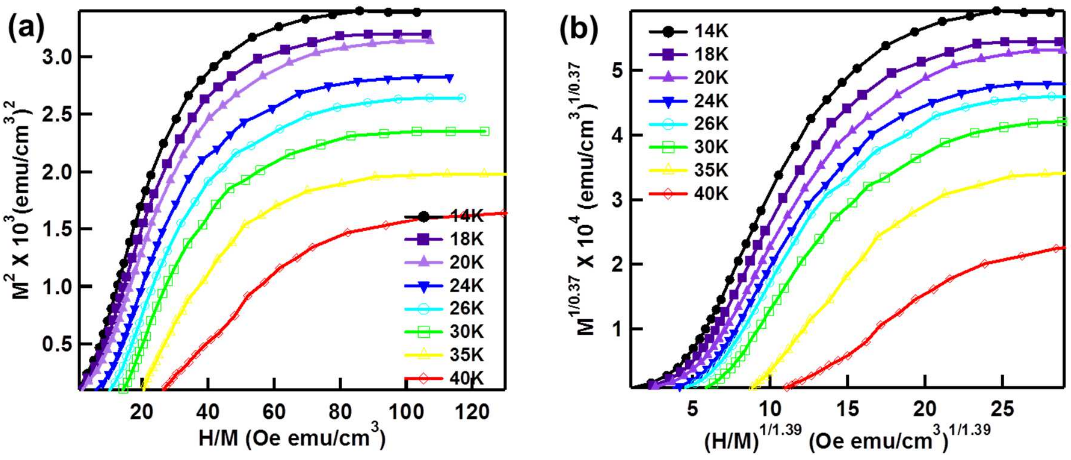

Figure 3-14. Arrott-Noakes plots of the 50 QL $Bi_{1.9}Cr_{0.1}Se_3$ sample grown on the Si (111) substrate. (a) Arrott plots of *H/M* versus M^2 for magnetic isotherms from 14 K to 26 K. (b)

Modified Arrott-Noakes plots of $(H/M)^{1/1.39}$ versus $M^{1/0.37}$ for data in (b). The applied magnetic field is always perpendicular to the sample surface, and the field range which covers from -0.8 T to 0.8 T is high enough to saturate the magnetic moment. Note that 1 Oe = 0.1 mT. Adopted from Ref. [131].

Given the above observed abnormal inverse susceptibility shown in Fig 3-14(b), as well as applicability of the modified Arrott-Noakes equation of the state, we suggest that these behaviors reflect the complicated magnetisms (*i.e.,* Van Vleck susceptibility [49] and super-paramagnetic orders from Cr-multimers [134]) in Cr-doped Bi_2Se_3 systems.

3.4.2. SQUID results of $Cr_y(Bi_xSb_{1-x})_{2-y}Te_3$ systems

The 50 QL $Cr_{0.3}(Bi_{0.5}Sb_{0.5})_{1.7}Te_3$ thin film sample is grown on the GaAs (111)B substrate and its magnetic properties are investigated by SQUID. The temperature dependent *M-H* hysteresis loops in Figure 3-15(a) clearly indicate the presence of FM order when $T <$ 15 K. Besides, the magnetic moment per Cr atom is estimated to be to ~2.8 μ_B from the saturation magnetization M_S under high filed above 0.2 T. This is consistent with the situation where most Cr^{3+} ions substitute the Bi/Sb sites in the host TI system. In the meanwhile, ZFC and FC measurements are performed on this sample, and the results are shown in Fig. 3-15(b). It is found that the onsite of PM-to-FM phase transition occurs at T = 15 K, and the blocking temperature of 8 K is also observed, similar to the $Bi_{2-x}Cr_xSe_3$ case (Fig. 3-13(a)). In addition, Fig. 3-15(c) compares the magnetizations when the sample is positioned parallel

(red solid circles) and perpendicular (blue solid diamonds) to the applied magnetic field at 5 K. It is seen that only the out-of-plane *M-H* curve exhibits the square-shaped hysteresis loop and reaches saturation at 0.2 T, while the in-plane magnetization is far from saturated even when B = 0.5 T. Accordingly, our SQUID results provide strong evidence to demonstrate the high anisotropy character with the magnetization easy-axis out-of-plane in the Cr-doped $(Bi_xSb_{1-x})_2Te_3$ system.

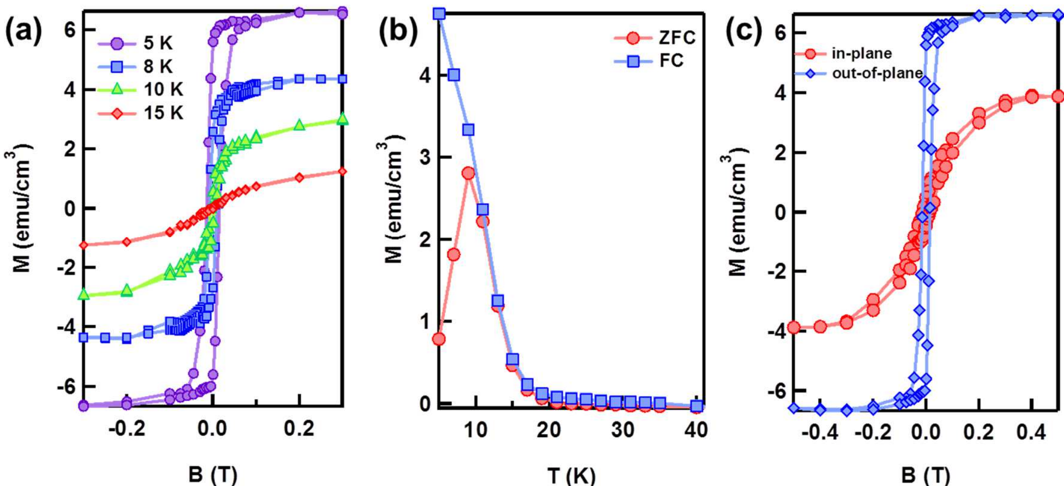

Figure 3-15. SQUID results of the 50 QL $Cr_{0.3}(Bi_{0.5}Sb_{0.5})_{1.7}Te_3$ sample grown on the GaAs (111)B substrate. (a) Temperature-dependent hysteresis *M-H* loops at 5 K, 8 K, 10 K, and 15 K, respectively. (b) Magnetization versus temperature for the same sample under ZFC (red circles) and FC (blue squires) conditions. The external field 5 mT is perpendicular to the sample surface. (c) Comparison of in-plane and out-of-plane *M-H* curves at 5 K. Adopted from Ref. [136].

3.5. Magneto-transport measurement

Magneto-transport measurement is one of the most powerful techniques to examine the electrical properties of various materials. By performing the four-point Hall measurement, we

are able to measure intrinsic transport parameters including the sample resistivity, carrier concentration and carrier type as functions of temperature, magnetic field, working frequency, and applied gate voltage. Moreover, for FM materials, hysteresis anomalous Hall resistance is developed, as we elaborated in Section 2.1. Accordingly, the magneto-transport measurement is also an effective method to study the magnetic properties of our MBE-grown magnetic TI samples.

From Eq. (2-2), it is known that the overall Hall resistance of a FM material consists of both the ordinary Hall ($R_o \cdot H$) and anomalous Hall ($R_A \cdot M(H)$) components. While R_o is solely related to the carrier density, R_A is affected by the longitudinal resistance R_{xx}. Figure 3-16(a) shows a typical AHE result of the MBE-grown $Cr_y(Bi_xSb_{1-x})_{2-y}Te_3$ film, where the well-shaped magnetic hysteresis loop can be clearly observed, indicating the presence of the robust FM order introduced by the Cr dopants. Furthermore, under a high applied magnetic field where the magnetization of the film reaches saturation, we obtain that $R_{xy} = R_0 H + M_s f(R_{xx})$. For the $Cr_y(Bi_xSb_{1-x})_{2-y}Te_3$ system, the magneto-resistance (MR) background in the diffusive regime (*i.e.,* the sample temperature is far above 0.3 K) is found to be relatively small (*i.e.,* less than 0.5 % when applied field changes from 1 T to 2 T, as shown in Fig. 3-16(b)), we can therefore approximately consider the anomalous Hall part, $M_s f(R_{xx})$, as a constant. As a result, we are able to fit R_{xy} with a strict line at high magnetic field, as shown in the inset of Figure 3-16(a). Such linear slope thus represents the ordinary

Hall coefficient R_0, which in turn gives the 2D carrier density in the thin film with $R_0 = -1/(n_s + n_{bulk})e$.

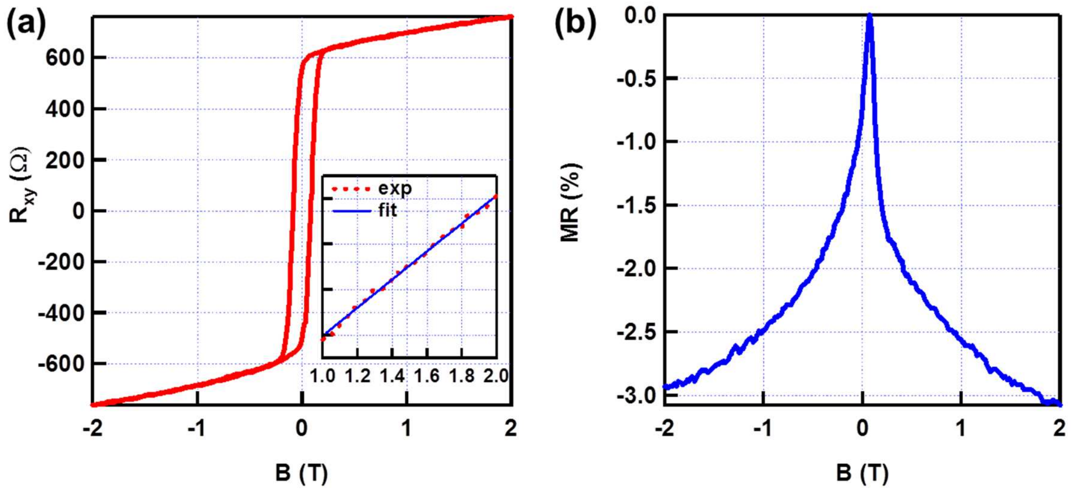

Figure 3-16. Magneto-transport measurement of 6 QL $Cr_{0.2}(Bi_{0.5}Sb_{0.5})_{1.8}Te_3$ thin film. (a) Anomalous Hall result with the well-defined hysteresis loop at 1.9 K. Linear slope at high magnetic field corresponds to the ordinary Hall coefficient R_0. (b) Longitudinal resistance indicates a small MR change at high field. Adopted from Ref. [136].

In contrast to the $Cr_y(Bi_xSb_{1-x})_{2-y}Te_3$ system, we need to point out that the AHE signals in the $Bi_{2-x}Cr_xSe_3$ samples are quite small [57, 131, 134], possibly due to the different Cr density of states (DOS) distributions and Fermi level positions in the host TI matrix [87, 144]. Consequently, it is difficult to quantitatively study the magnetic properties of $Bi_{2-x}Cr_xSe_3$ systems via the transport measurement.

3.6. Summary of Chapter 3

In this chapter, we provide a brief description about the MBE growth and present the growth results of the high-quality Cr-doped TI thin films. By carefully choosing the growth parameters (*i.e.,* substrate temperature, element flux rate, and annealing condition), single-crystalline films have been epitaxially grown on suitable substrates. The HRTEM is applied to highlight the well-maintained QL structures and the EDX mapping confirms the uniform distribution of the Cr dopants within the host TI matrix. In the meanwhile, both SQUID and magneto-transport measurements are carried out to investigate the magnetic and electrical properties of the MBE-grown Cr-doped TI samples. Compared with the $Bi_{2-x}Cr_xSe_3$ samples, we find that the $Cr_y(Bi_xSb_{1-x})_{2-y}Te_3$ thin films have great advantages: (1) the interface between the first $Cr_y(Bi_xSb_{1-x})_{2-y}Te_3$ QL and the GaAs (111)B substrate is atomically sharp; (2) the Fermi level position and carrier type are tunable by adjusting the Bi-to-Sb ratio; (3) pronounced AHE signals with well-developed hysteresis loops are observed; and (4) the non-trivial topological surface states are always maintained regardless of the Cr doping level. As we will elaborate in the following chapters, these salient features of the $Cr_y(Bi_xSb_{1-x})_{2-y}Te_3$ system enables us to realize QAHE as well as to manipulate different magnetisms and relevant magneto-electric responses.

Chapter 4

Interplay between Different Magnetisms in Cr-Doped Topological Insulators

In Section 1.3, we proposed that in magnetically doped TI systems, ferromagnetic moments can be developed through two major mechanisms: the van Vleck mechanism and the RKKY coupling. In the former case, due to the large spin susceptibility of the valence electrons in the band-inverted TI materials, the magnetic ions can thus be directly aligned by these local valence electrons without the assistance of itinerant electrons. Consequently, this "bulk ferromagnetism" is independent of the carrier density [49]. On the other hand, neighboring magnetic ions can also be coupled through the mediation of conduction carriers and this kind of coupling is referred to as the carrier-mediated RKKY interaction. Therefore, before we further utilize such materials for novel applications, it is important to quantify different FM orders, and to understand the interplay/controllability of each contribution.

4.1. Electric-field-controlled anomalous Hall effect

Given that RKKY and Van Vleck mechanisms have different responses to the external electric field, we can thus apply the electric-field-controlled magneto-transport measurements on the magnetic TI samples to distinguish both magnetisms. Accordingly, we first prepare a 6

QL $Cr_{0.04}(Bi_{0.5}Sb_{0.5})_{1.96}Te_3$ thin film with a nominal Cr doping concentration of 2% (the Bi-to-Sb ratio is optimized to be around 1:1 so that the Fermi level position of the as-grown sample is already inside the bulk gap). After growth, the $Cr_{0.04}(Bi_{0.5}Sb_{0.5})_{1.96}Te_3$ film is patterned into a micrometer-scale Hall bar geometry using conventional optical photolithography with subsequent CHF_3 dry etching of 18 s. A 20 nm thick high-κ Al_2O_3 dielectric layer is later deposited by ALD at 250 °C. Hall channel contacts are defined by *e*-beam evaporation after etching away the Al_2O_3 layer within the contact areas. A metal stack of Ti/Al (20 nm/100 nm) is directly deposited onto the exposed TI top surface. A top-gate metal scheme of Ti/Au (10 nm/90 nm) is finally achieved by the second step of photolithography and *e*-beam evaporation, as shown in Fig. 4-1(b).

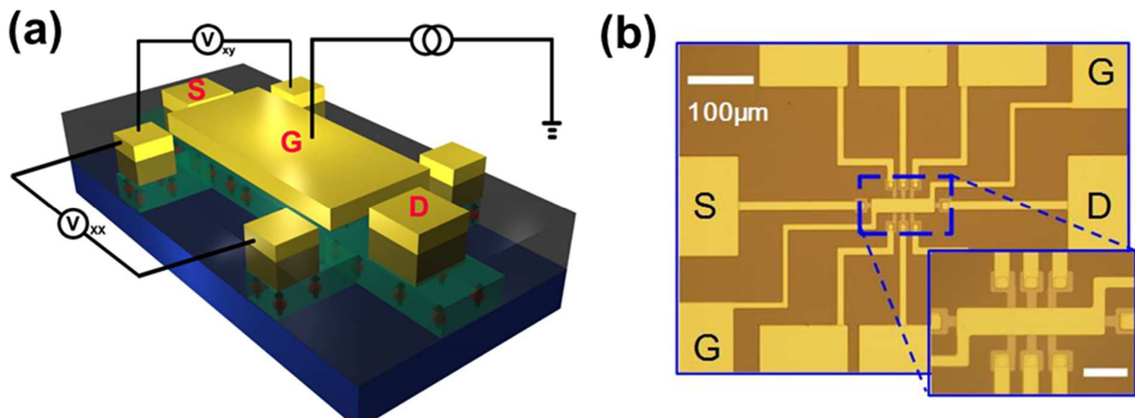

Figure 4-1. Top-gated Hall bar device structure used for exploring the gate-dependent anomalous Hall effect. The effective size of the channel is 10 μm (L) × 40 μm (W). Adopted from Ref. [136].

The gate-dependent AHE results of the 6 QL $Cr_{0.04}(Bi_{0.5}Sb_{0.5})_{1.96}Te_3$ sample are shown in Figure 4-2. It can be clearly seen that the R_{xy} curves become strictly linear when the applied magnetic field is larger than 1T, manifesting the dominant ordinary Hall component ($R_0 \cdot H$) in the high-field regime. Moreover, the carrier density at zero gate bias is found to be 1.1×10^{12} cm^{-2} at 1.9 K. As a result, the electric field provided by top gate (±12 V) can effectively tune E_F across the surface band gap, and therefore change the carrier type, as illustrated by the high-field R_{xy} slope change in Figure 4-2(b).

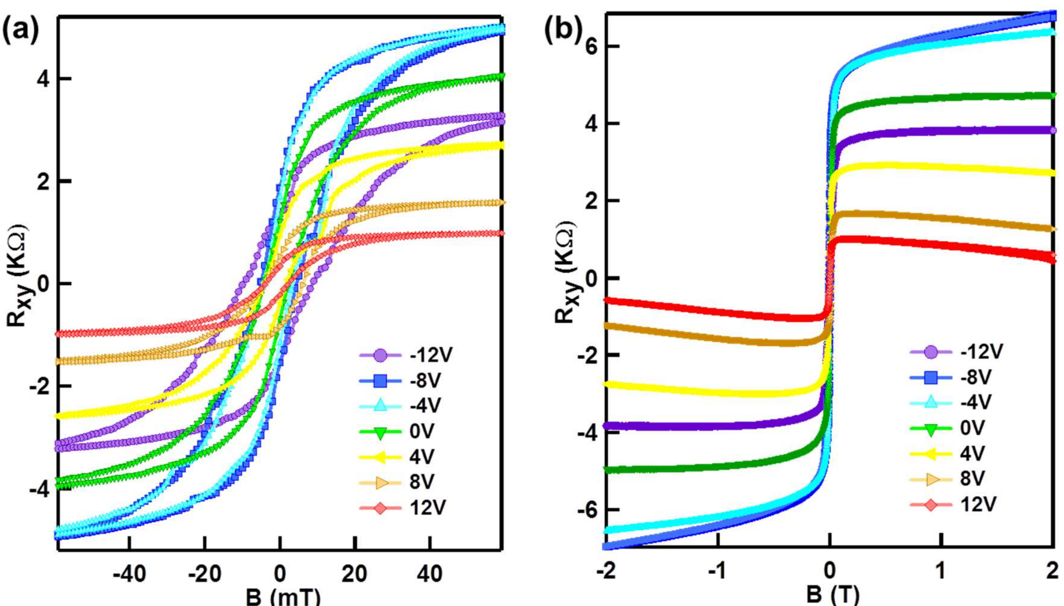

Figure 4-2. Gate-dependent anomalous Hall results for the 6 QL $Cr_{0.04}(Bi_{0.5}Sb_{0.5})_{1.96}Te_3$ sample. (a) [-60 mT, 60 mT] scale. (b) [-2 T, 2 T] scale. The applied top-gate voltage changes from -12 V to 12 V, and the sample temperature is 1.9 K. Adopted from Ref. [136].

After subtracting the linear ordinary Hall component, the nearly square-shaped hysteresis loops suggest the well-developed FM order with the easy magnetization axis

out-of-plane. More importantly, the magnetic hysteresis behavior varies dramatically when the sample is biased from *p*-type to *n*-type. Related to the ambipolar effect of the longitudinal resistance R_{xx} in Fig. 4-3(a), the change of the coercivity field H_C (red hollow circles) can be divided into two distinct regions as illustrated in Fig. 4-3(b) where the green and yellow parts represent the *p*-type and *n*-type) regions, respectively. Particularly, when the Fermi level is below the surface band gap (-12 V $< V_g <$ -2 V), H_C steadily reduces from 12 mT down to 5.5 mT, indicating a hole-mediated RKKY coupling signature; on the contrary, once the dominant conduction holes are depleted when $V_g > 0$ V, H_C slowly stops decreasing, and finally approaches its minimum value around 4 mT when E_F is far above the surface band gap. Similarly, the Curie temperature T_C (blue solid squares in Fig. 4-3(b)) which is determined from the temperature dependent R_{xy} curves (*i.e.,* the hysteresis window of R_{xy} disappears when the sample temperature is above T_C, as illustrated in Figs. 4-3(c) and (d)) also follows the reduction-and-saturation behavior by gate modulation, namely T_C decreases from 7.5 K (V_g = -12V) down to 4.7 K ($V_g > 5$ V). Given the fact that the hole-mediated RKKY interaction is completely suppressed in the region where E_F is far above the bulk valence band, both the remaining gate-independent H_C and T_C in the *n*-type region strongly support the presence of additional ferromagnetic contribution where the robust magnetic order is formed without the assistance of the itinerant carriers. We therefore may attribute the electric-field-independent magnetization to the bulk van Vleck ferromagnetism. Accordingly,

we may conclude that the gate-controlled AHE results in the 6 QL $Cr_{0.04}(Bi_{0.5}Sb_{0.5})_{1.96}Te_3$ sample reveal the co-existence of both hole-mediated RKKY and van Vleck mechanisms.

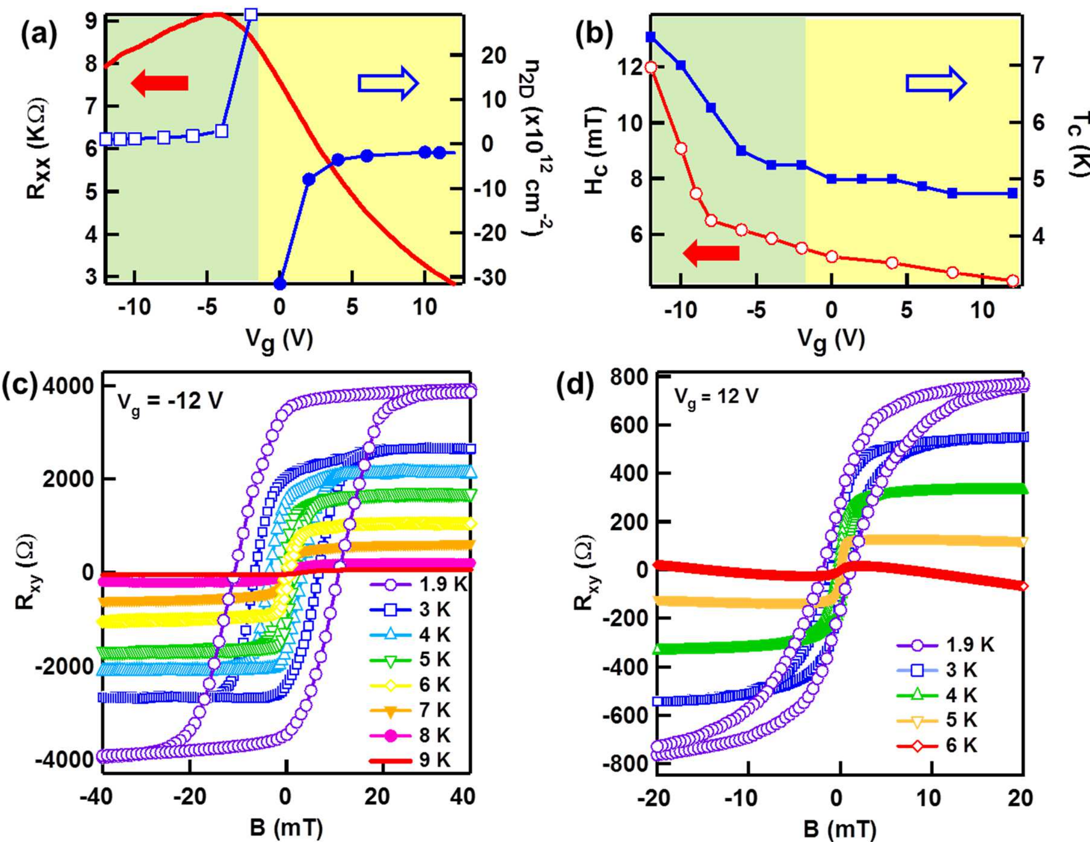

Figure 4-3. Electric-field-controlled ferromagnetism in the 6 QL $Cr_{0.04}(Bi_{0.5}Sb_{0.5})_{1.96}Te_3$ sample. (a) The observed ambipolar effect of R_{xx} (red solid lines) indicates that the Fermi level can be effectively tuned across the surface band gap. The Hall density (blue) determined from the linear R_{xy} curve at high field changes sign accordingly. (b) The changes of coercivity field H_C at 1.9 K (red hollow circles) and Curie temperature T_C (blue solid squares) with applied top-gate voltages. Both of them gradually decrease when the sample is biased from *p*-type to *n*-type, indicating the hole-mediated RKKY interaction signature. Temperature-dependent AHE effect of the 6 QL $Cr_{0.04}(Bi_{0.5}Sb_{0.5})_{1.96}Te_3$ thin film. The applied top-gate voltages are (c) V_g = -12 V and (b) V_g = +12 V. Adopted from Ref. [136].

4.2. Hole-mediated RKKY interaction in Cr-doped $(BiSb)_2Te_3$ system

In Section 1.3.3, we showed that the carrier-mediated RKKY interaction was found to be one of the dominant mechanisms to generate robust FM order in magnetic TIs, and the RKKY coupling strength strongly depend on the DOS distributions of both the mediating carrier $D(E_F)$ and magnetic ions $D_d(E_F)$.

In the case of Cr-doped tetradymite-based 3D TIs, particularly, the *p-d* coupling between the transition metal *d*-orbital (Cr^{3+}) and the itinerant carrier *p*-orbital is found to be strongest due to the wavefunction localization and symmetry argument, and the on-site *p-d* exchange coefficient $J(E)$ can be estimated by using the empirical model in which an itinerant carrier floating around the magnetic ion. It has the form [145]

$$J(E) = \iint \psi_p^*(\vec{r}_1)\psi_d^*(\vec{r}_2)(e^2 / R_{pd} + 3e^2 / R_{pCr^{3+}})\psi_d(\vec{r}_1)\psi_p(\vec{r}_2)d\vec{r}_1 d\vec{r}_2 \tag{4-1}$$

where ψ_p is the *p*-orbital wavefunction of the itinerant carrier, ψ_d is the *d*-orbital wavefunction of the localized Cr^{3+} ion, R_{pd} is the distance between the two mediating carriers, and $R_{pCr^{3+}}$ is the distance between the carrier and the Cr^{3+} ion center. From Eq. (4-1), we can reveal that $J(E_F) \propto D_d(E_F)$ in which more *d*-orbital density of states can generate larger on-site exchange strength. Given the fact that the overall RKKY interaction strength is proportional to $|J^2|$, we therefore conclude that the overall RKKY interaction also scales with $D_d(E_F)^2$ (*i.e.*, it strongly depends on the Fermi level position and carrier density) [146].

In J.M. Zhang *et al.*'s work, first-principles DFT calculations based on the density functional theory were performed to investigate the DOS distributions of Cr dopants inside the host Bi_2Se_3 and $(Bi_{0.5}Sb_{0.5})_2Te_3$ materials [58, 59, 136]. It is revealed in Fig. 4-3 that there is strong hybridization between the Cr *3d*-orbit and Se/Te *2p*-orbit, and $D_d(E)$ of the Cr ion is distributed majorly in the valence band, and reduced to almost zero above the Dirac point. As a result, it would be expected that itinerant holes can effectively couple neighboring Cr ions together while electrons rarely contribute to the mediating process due to the absence of $D_d(E_F)$ above the Dirac point.

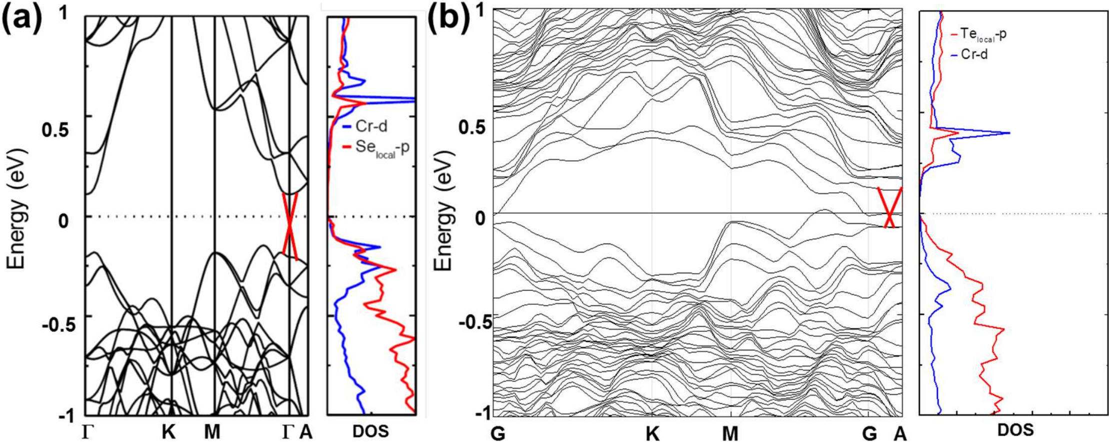

Figure 4-4. Energy band diagram and DOS distribution of Cr-doped 3D TIs. (a) Left: *ab initio* calculated energy band diagram and DOS of Cr *d*-orbital and Se *p*-orbital in $Bi_{2-x}Cr_xSe_3$, where x = 0.083. The red lines represent schematically the surface Dirac cone located at the Γ point. Adopted from Ref. [59]. (b) Energy band diagram and DOS of Cr *d*-orbital and Te *p*-orbital in $Cr_{0.08}(Bi_{0.5}Sb_{0.5})_{1.92}Te_3$ material. Adopted from Ref. [136].

4.3. Interplay between different FM orders – magnetic doping level

From the electric-field-controlled AHE results of the 6 QL $Cr_{0.04}(Bi_{0.5}Sb_{0.5})_{1.96}Te_3$ sample, it is concluded that both the hole-mediated RKKY coupling and the carrier-independent Van Vleck magnetism are possible in the system. In the following two sections, we present additional experimental results to quantify the interplay between these two contributions.

First of all, it is well-known that for any magnetic system, the magnetic ions doping level x_M is essential to the magnetization. Specifically, in the dilute limit where the direct coupling between local moments is negligible, the ferromagnetic susceptibility (and thus the overall magnetization) is proportional to x_M, following the Curie-Weiss form that [139]

$$\chi = \frac{C}{T - T_c} = \frac{x_M \mu_J^2}{3k_B(T - T_c)} \tag{4-2}$$

where $\mu_J = g\mu_B J(J+1)$ is the magnetic moment, g is the Landé g-factor, and J is the angular momentum quantum number. In recent years, relevant x_M-dependent experiments have been carried out in $Bi_{2-x}Cr_xSe_3$ [57, 131], $Bi_{2-x}Mn_xSe_3$ [67], $Bi_{2-x}Mn_xTe_3$ [63, 147], and $Sb_{2-x}Cr_xTe_3$ [70, 71] systems, and all the results exhibited such monotonically increasing relation between the total magnetic moments and x_M.

More importantly, the effect of the magnetic doping level on RKKY and van Vleck mechanisms can be further distinguished. By controlling the Cr doping levels during MBE growth, we first prepare a set of $Cr_x(Bi_{0.5}Sb_{0.5})_2Te_3$ samples with the same Bi/Sb ratio

(0.5/0.5) and film thickness (6 QL), but different Cr doping levels ranging from 5% to 20%. Top-gated Hall bar devices are later fabricated to investigate the electric-field-controlled magneto-transport properties. Figures 4-5(a)-(d) summarize the electric-field-controlled AHE results of four samples with Cr% = 5%, 10%, 15%, and 20%, respectively. Although increasing the Cr doping concentration introduces more carriers (*i.e.*, the 2D Hall density n_{2D} varies from 1.2×10^{12} cm^{-2} to 2.2×10^{13} cm^{-2} at 1.9 K), such defects are acceptable to maintain E_F inside the bulk band gap. From the extracted $H_c - V_g$ curves in Figures 4-5(e)-4(h), we observe that in the moderate doping region (5%, 10%, and 15%), the Cr-doped $(Bi_{0.5}Sb_{0.5})_2Te_3$ thin films all exhibit the hole-mediated RKKY coupling behaviors in the sense that the anomalous Hall resistance R_{xy} loops show a quick decrease of its coercivity field (H_C) when the majority holes are depleted. When the samples are further biased deep into the *n*-type region (*i.e* > 50 meV above the surface gap), H_C gradually saturates at finite values of 15 mT (5%), 37.5 mT (10%), and 68.5 mT (15%), respectively. On the contrary, when the Cr doping concentration increases up to 20% in Figure 4-5(d), even though the surface Fermi level has been effectively adjusted by 50 meV (Inset of Figure 4-5(h)), the hysteric window remains a constant of 100 mT and does not show any change with respect to the gate bias (Figure 4-5(h)).

From the band diagram/DOS distribution DFT calculations (Section 4.2) and the detailed comparison of the AHE differences in Figure 4-5, we now understand the effect of Cr doping on the two magnetization origins discussed above. When the Cr concentration is

smaller than 15%, the bulk van Vleck mechanism and the hole-mediation both exist in the system and contribute to the net magnetizations. With effective gate tuning, the carrier type and density can be adjusted, and the magnetic moment from the carrier-mediated RKKY exchange is therefore modulated. Given the fact that the DOS of the Cr^{3+} ions is distributed majorly below the Dirac point, the long-range RKKY coupling in the *p*-type region thus introduces much more robust ferromagnetic moments over the weaker bulk van Vleck term; it therefore becomes the dominant component in the magnetic TI samples with moderate Cr doping. We should point out here that it is difficult to further distinguish the mediating itinerant carriers since the topological surfaces are entangled with the bulk contribution in our uniformly Cr-doped TI samples. As more Cr atoms are incorporated into the TI system, on the one hand, the bulk van Vleck-type magnetism is expected to becomes more pronounced due to the stronger out-of-plane magnetic moments from the Cr ions; On the other hand, however, since excessive Cr atoms promote the formation of *n*-type Bi_{Te} anti-site defects [59], they therefore force the Fermi level E_F "pinned" far above the surface band gap. Under such circumstances, the hole-mediated RKKY coupling becomes diminished or even completely suppressed, leaving only the bulk van Vleck responses in heavily Cr-doped TI samples [66, 114]. As a result, by designing the Cr doping profile and electric-gating strategy, we demonstrate the valid approach to either enhance or suppress the magnetic contributions from different magnetisms.

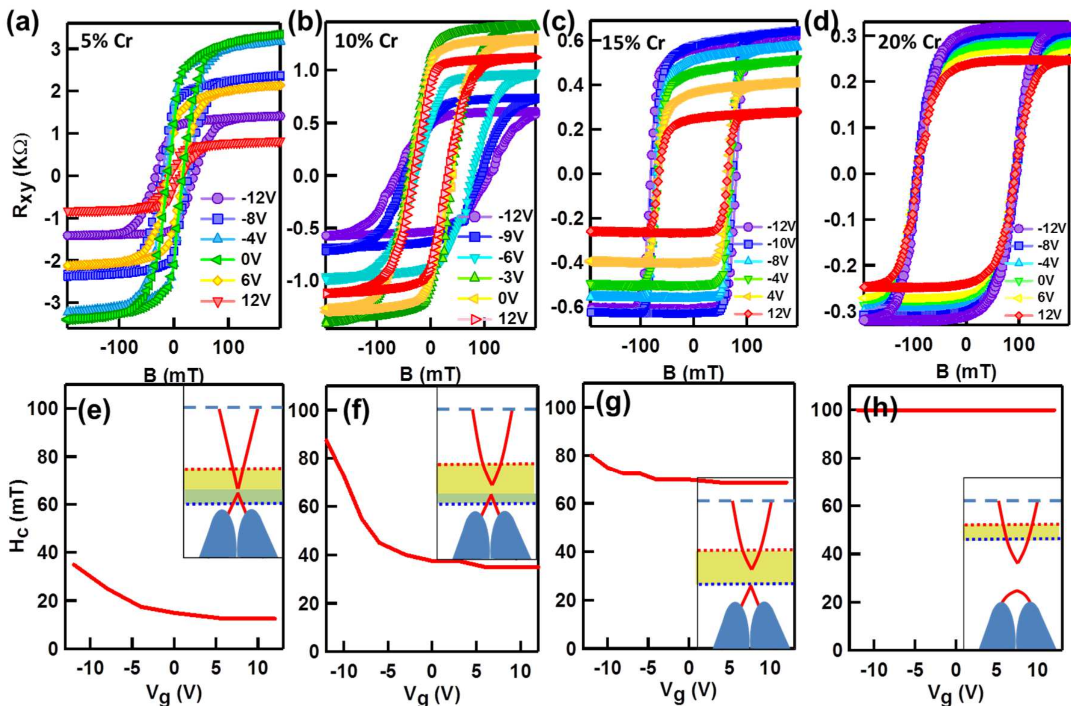

Figure 4-5. Gate-dependent AHE results for 6 QL $Cr_y(Bi_{1-x}Sb_x)_2Te_3$ thin films with different Cr doping concentrations. (a) Cr = 5%, (b) Cr = 10%, (c) Cr = 15%, and (d) Cr = 20%. (e-h) Gate-modulated coercivity field changes for these four samples, respectively. Inset: Illustration of the Fermi level position as adjusted by the top-gate voltages ranging from -12 V to +12 V. Adopted from Ref. [136].

Additionally, these magneto-electric effects can also be illustrated through the magneto-resistance (MR) results. Figures 4-6(a)-(d) give the electric-field-controlled three-dimensional normalized MR maps for the same samples studied in Fig. 4. Like hysteresis AHE curves, the butterfly-shaped double-split MR peaks are present, indicative of the remnant field generated by the ferromagnetic orders [62]. Meanwhile, the peak shifts with respect to the applied gate voltages also confirm the hole-mediated RKKY mechanism in the Cr-doped TI samples. Beside the hysteresis signals shown in the MR maps, the correlated

magneto-conductance (MC) curves which are defined as $\sigma_{xx} = R_{xx} / (R_{xx}^2 + R_{xy}^2)$ at low magnetic field provide us additional piece of information about the Cr-doped TI conduction behaviors in the quantum diffusive region [57, 112, 148]. Generally speaking, the quantum interference of surface Dirac fermions depends on the Berry phase ϕ. In the magnetically doped TI systems, the formed magnetic moment M_z forces the surface states open a band gap Δ, and thus drives the Berry phase to deviate from its original π-state to $\phi = \pi(1-\Delta/2E_F)$ [148]. The corresponding weak localization (WL) behaviors are studied in Figure 4-6(e) where the MC curves of Cr-doped $(Bi_{0.5}Sb_{0.5})_2Te_3$ thin film with Cr doping concentrations ranging from 2% to 20% are presented (we deliberately shift the magnetic peaks from H_C to the zero-point for direct comparison). With the increase of Cr dopants, it can be clearly seen that the negative MC cusps at low magnetic field become sharper, indicating the larger surface gap Δ induced by the stronger magnetic order. Following the modified two components Hikami-Larkin-Nagaoka (HLN) theory that [148, 149]

$$\Delta\sigma(B) = \sum_{i=0,1} \frac{\alpha_i e^2}{\pi h} [\psi(\frac{l_B^2}{l_{\phi i}^2} + \frac{1}{2}) - \ln(\frac{l_B^2}{l_{\phi i}^2})] \quad (4\text{-}3)$$

where ψ is the digamma function, $l_B = \sqrt{\hbar/(4e|B|)}$ is the magnetic length, and l_ϕ is the phase coherent length, we realize that the extracted WL weight factor α_0 increases from 0.3 (Cr% = 2%) to 0.48 (Cr% = 20%) and gradually approaches the ideal value of 0.5 (*i.e.*, $\Delta/2E_F$ = 1 and $\phi = 0$). On the contrary, the weak anti-localization factor α_1 is almost zero in all the $Cr_y(Bi_xSb_x)_{2-y}Te_3$ samples. Accordingly, the systematic changes of the MC phenomena

observed in Figure 4-6(e) are consistent with the AHE results, again verifying the correlation between the robust magnetisms in the Cr-doped TI thin films.

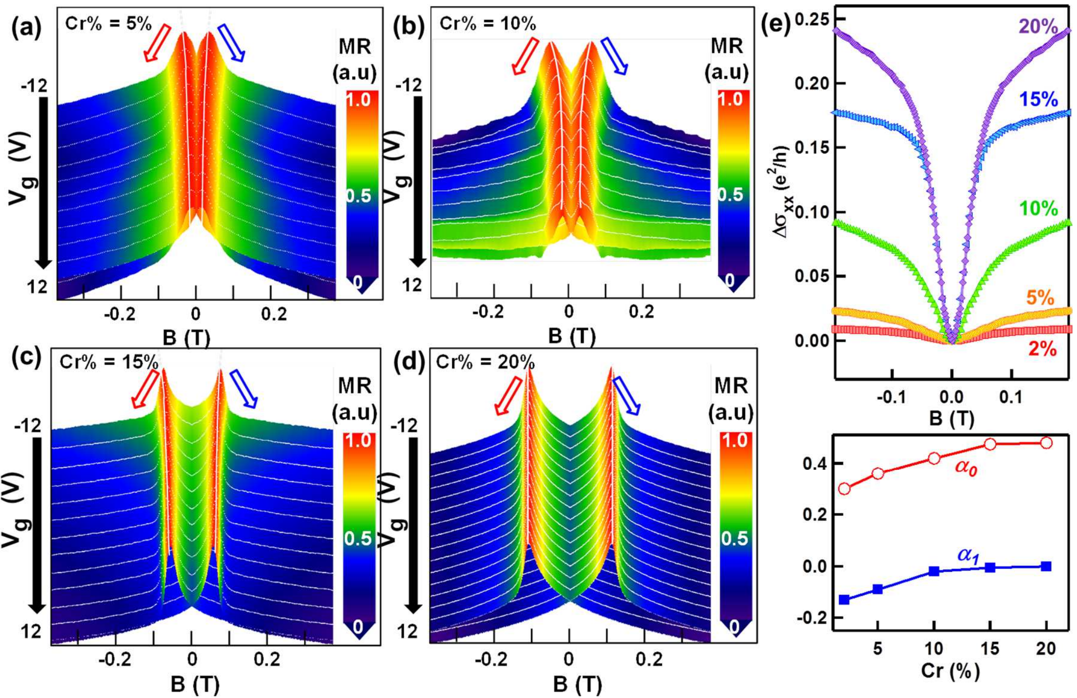

Figure 4-6. Gate-dependent Magneto-resistance for $Cr_y(Bi_{1-x}Sb_x)_2Te_3$ thin films with different Cr doping concentrations. (a) Cr = 5%, (b) Cr = 10%, (c) Cr = 15%, and (d) Cr = 20%. The measurements are carried out at 1.9 K with applied magnetic field out-of-plane. All of the four devices show the double-split butterfly MR curves. (e) Upper: Weak-localization behaviors when samples in (a) to (d) are biased in the *n*-type region where the magnetization is dominated by the bulk van Vleck term. With more Cr dopants, the positive WL cusp becomes sharper, indicating more deviation from the π-Berry phase. Lower: WL/WAL weight factors α_0 and α_1 extracted from MC curves in (e). Adopted from Ref. [136].

4.4. Interplay between different FM orders – band topology

Beside the magnetic ions doping level, the strength of ferromagnetism is also determined by the band topology of the host TI materials. In Section 1.3.4, it is argued that the strength of

matrix element $\langle nk|S_z|mk \rangle$ in Eq. (1-9) is determined by the mixing between the inverted conduction/valence bands (*i.e.,* SOC) [49]. In Bi_2Se_3, it is found that the SOC is mostly contributed from the Bi atoms [45]. As a result, the substitution of Bi atoms with much lighter transition elements (Cr or Fe) will significantly lower the SOC, and the overall Van Vleck susceptibility (*i.e.,* FM order) of Bi_2Se_3 is expected to get reduced by magnetic doping [150].

In 2013, J.S Zhang *et al.* calculated the band structures of the $Bi_{2-x}Cr_xSe_3$ materials with different Cr contents by DFT [151]. In Fig. 4-7(a), their calculations showed that the inverted gap amplitude shrank dramatically with increased Cr content x. Finally, when the band inversion between the conduction and valence bands disappeared at $x > 0.17$, the heavily-doped $Bi_{2-x}Cr_xSe_3$ would enter a topologically trivial DMS regime without the presence of bulk Van Vleck magnetism any more. (For comparison, since the Te element contributes giant SOC in Bi_2Te_3 and Sb_2Te_3 systems, the bulk band inversion would always hold regardless of the magnetic doping level [151]. Under such circumstances, robust Van Vleck order has been observed in heavily doped $Cr_x(BiSb)_2Te_3$ materials, as shown in Fig. 4-6(d)).

The topological phase transition due to magnetic doping is also confirmed from our angle-resolved photoemission spectroscopy (ARPES) experiments. Figure 4-7(b) shows the surface band *E-k* dispersion relations of the $Bi_{2-x}Cr_xSe_3$ films grown on the Si (111) substrate. The ARPES spectra reveal the systematic weakening of the surface states along with the

enlarged surface gap Δ, as the Cr doping concentration gradually increases from 0 to 10%. With further reducing the SOC and modifying the Berry phase away from the nontrivial π state[148], the topological surface are almost eliminated in the $Bi_{1.8}Cr_{0.2}Se_3$ film.

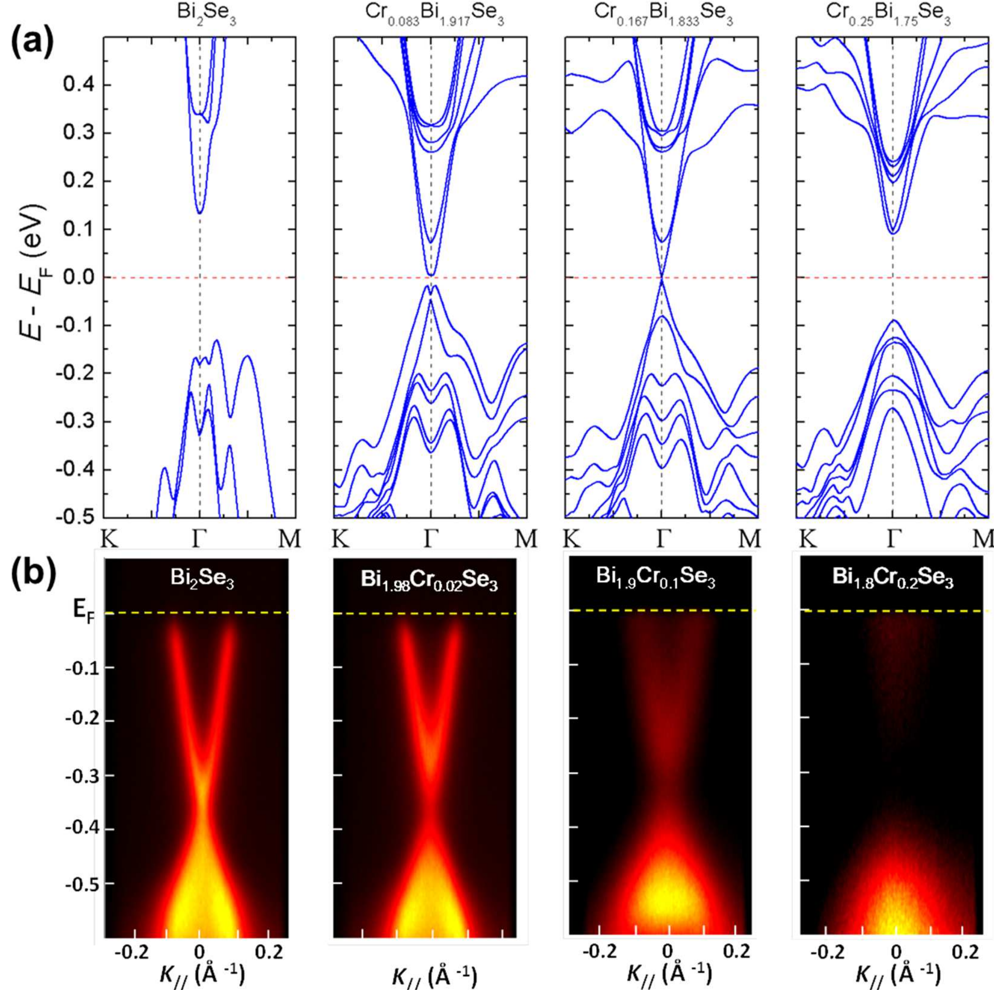

Figure 4-7. Magnetic doping effect on the band topology of the Cr-doped Bi_2Se_3 systems. (a) DFT-calculated bulk band structures of $Bi_{2-x}Cr_xSe_3$ with different Cr contents of x = 0, 0.083, 0.167, and 0.25, respectively. The red and blank broken lines indicate the positions of the Fermi level and the points. Adopted from Ref. [151]. (b) ARPES intensity maps of MBE-grown 50 QL $Bi_{2-x}Cr_xSe_3$ thin films with x = 0, 0.02, 0.1, and 0.2 on Si (111) along the *Γ–K* direction. All data are taken using 52 eV photons under the temperature of 10 K. Adopted from Ref. [131].

4.5. Summary of Chapter 4

In this chapter, we first report the gate-dependent magneto-transport measurements on the Cr-doped $(Bi_xSb_{1-x})_2Te_3$ thin films. With effective top-gate modulations, we demonstrate the presence of both the hole-mediated RKKY coupling and carrier-independent van Vleck magnetism in the magnetic TI systems. Most importantly, by varying the Cr doping concentrations from 2% to 20%, we unveil the interplay between the two magnetic orders and establish the valid approach to either enhance or suppress each individual contribution. On the other hand, for the Cr-doped Bi_2Se_3 systems, the change of Cr doping level gives rise to the FM-to-PM transition, indicating that the band topology of the host TI material would be one of the fundamental driving forces for the FM order.

The electric-field-controlled ferromagnetisms identified in the Cr-doped TI materials will serve as the fundamental step to further explore the TRS-breaking TI systems. More importantly, the realized robust Van Vleck component in $Cr_y(Bi_xSb_{1-x})_{2-y}Te_3$ systems is of great importance to further explore the quantum anomalous Hall effect in the magnetic TI systems, as we will elaborate in the following Chapter 5.

Chapter 5
Quantum Anomalous Hall Effect in Magnetic Topological Insulators

In Chapter 2, we showed that a 2D ferromagnetic insulator with a non-zero first Chern number (C_1) would give rise to the QAHE. In such Chern insulators, the chiral edge states are formed due to the TRS-breaking, and the spontaneous magnetization also localizes the dissipative states. Among all possible candidates, we proposed that by adding appropriate exchange splitting into the QSHE system, one set of the spin sub-bands would remain in the inversion regime while the other became topologically trivial, therefore driving the 2D magnetic TI system into a QAHE insulator (Fig. 2-11). In the meanwhile, we also discussed a more general case that the quantized Hall conductance could also be derived from the gapped top and bottom surfaces in 3D magnetic TI systems (Fig. 2-13), and if the exchange field strength and film thickness were properly adjusted so that higher sub-bands would get involved in the band topology transition, and QAHE with a tunable Chern number could, in principle, be realized. In Chapter 4, we also demonstrated that in the MBE-grown $Cr_y(Bi_xSb_{1-x})_{2-y}Te_3$ thin films, robust out-of-plane magnetization could be developed directly from the large van Vleck spin susceptibility in the host TI materials without the mediation of itinerant carriers (Fig. 4-5). By manipulating the Fermi level position and the magnetic doping, QAHE in the 2D regime was firstly observed in a 5 QL $Cr_{0.15}(Bi_{0.1}Sb_{0.9})_{1.85}Te_3$ film,

where a plateau of Hall conductance σ_{xy} of e^2/h and a vanishing longitudinal conductance σ_{xx} were observed at 30 mK [114]. Nevertheless, the increased bulk conduction in the thicker films was detrimental and obscured the observation of QAHE beyond the 2D hybridization thickness (> 6 QL). As a result, the universality of the QAHE phase and its related quantum transport phenomena in the 3D regime still remain unexplored.

5.1. Observation of QAHE in the Cr-doped $(BiSb)_2Te_3$ thin films

To prepare the magnetic TI materials with pronounced FM orders and insulating bulk states, single-crystalline Cr-doped $(Bi_xSb_{1-x})_2Te_3$ films are grown by MBE. Both the Cr doping level (12%) and the Bi/Sb ratio (0.3/0.7) are optimized so that the Fermi level positions of the as-grown samples are already close to the charge neutral point (*i.e.,* the bulk conduction is minimized). The growth is monitored by RHEED, and the film with a thickness of 10 QL is obtained after ten periods of RHEED oscillation, as shown in Fig. 5-1(b). In the meantime, HRSTEM is used to characterize the film structure and crystalline configuration. Figure 5-1(c) highlights the highly-ordered hexagonal structure of the 10 QL $Cr_{0.24}(Bi_{0.3}Sb_{0.7})_{1.76}Te_3$ film with an atomically sharp interface on top of the GaAs substrate, and the uniform Cr distribution inside the host TI matrix is also confirmed by the EDX spectrum.

To investigate the chiral transport properties in the QAHE regime, we deliberately fabricate the Hall bar devices with dimensions of 2 mm × 1 mm (*i.e.,* ten times larger than that used in Ref. [114]) In the diffusive transport region (T > 1 K), the 10 QL $Cr_{0.24}(Bi_{0.3}Sb_{0.7})_{1.76}Te_3$ film shows a typical semiconductor behavior, where the sample resistance monotonically increases as the sample temperature drops from 300 K to 1 K (Fig. 5-1(d)), indicating that the Fermi level is inside the bulk band gap. Besides, the Curie temperature (T_C) is found to be around 30 K from the temperature-dependent magnetization under the field-cooled condition, as shown in Inset of Fig. 5-1(d).

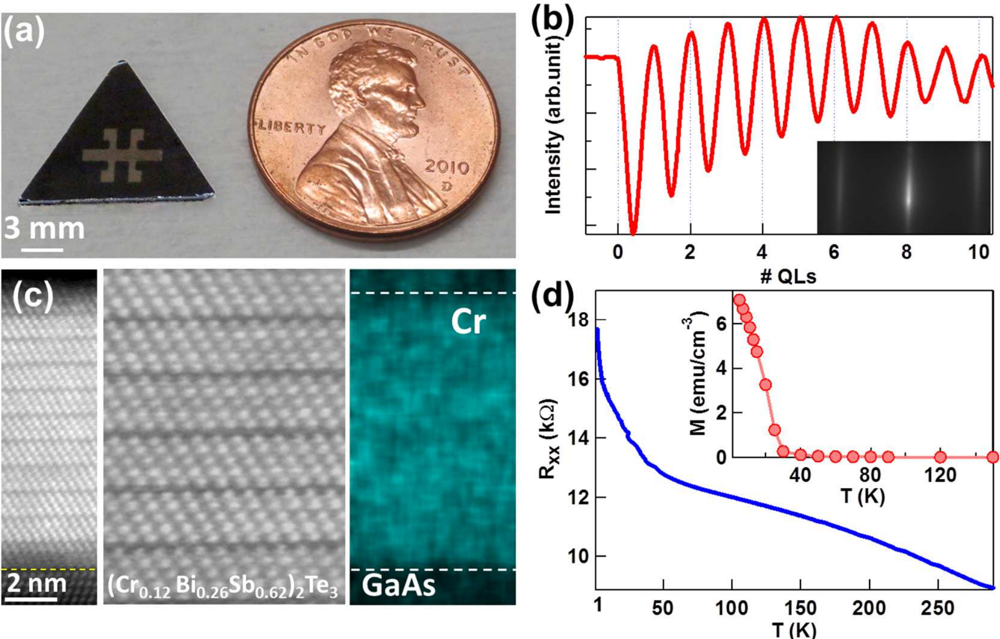

Figure 5-1. Cr-doped $(Bi_xSb_{1-x})_2Te_3$ film structure and properties. (a) The image of the Hall bar-structure with the dimension of 2 mm × 1 mm. (b) RHEED oscillation, showing that the grown Cr-doped $(Bi_xSb_{1-x})_2Te_3$ film has a thickness of 10 QL. Inset: RHEED pattern of the as-grown film. (c) Cross-sectional HRSTEM image, illustrating the crystalline structure of the 10 QL $Cr_{0.24}(Bi_{0.3}Sb_{0.7})_{1.76}Te_3$ film. The EDX mapping confirms that the Cr dopants distribute uniformly inside the TI layer. (d) Temperature-dependent resistance as temperature

drops from 300 K to 1 K. Inset: Magnetic moment under field-cooled condition. The applied field is 10 mT and the Curie temperature is estimated to be T_C = 30 K. Adopted from Ref. [152].

Figure 5-2 shows the magneto-transport results of the 10 QL $Cr_{0.24}(Bi_{0.3}Sb_{0.7})_{1.76}Te_3$ film. When T < 10 K, the Hall resistance R_{xy} in Fig. 5-2(a) develops a square-shaped hysteresis loop, indicating the robust FM order with an out-of-plane magnetic anisotropy, and the butterfly-shaped double-split longitudinal resistance R_{xx} is also observed at low temperature, as shown in Fig. 5-2(c). In the meanwhile, the temperature-dependent coercivity field H_C is extracted from Fig. 5-1(a). It can be clearly seen that H_C vanishes when the temperature is above 30 K, consistent with the $M_Z - T$ data which we presented in inset of Fig. 5-1(d). Furthermore, the anomalous Hall component nearly vanishes, leaving only the linear ordinary Hall signals. The corresponding Hall density extracted from the R_{xy} data at 35 K is 8.13 × 10^{11} cm^{-2} and the corresponding mobility is around 600 $cm^2/V\cdot s$.

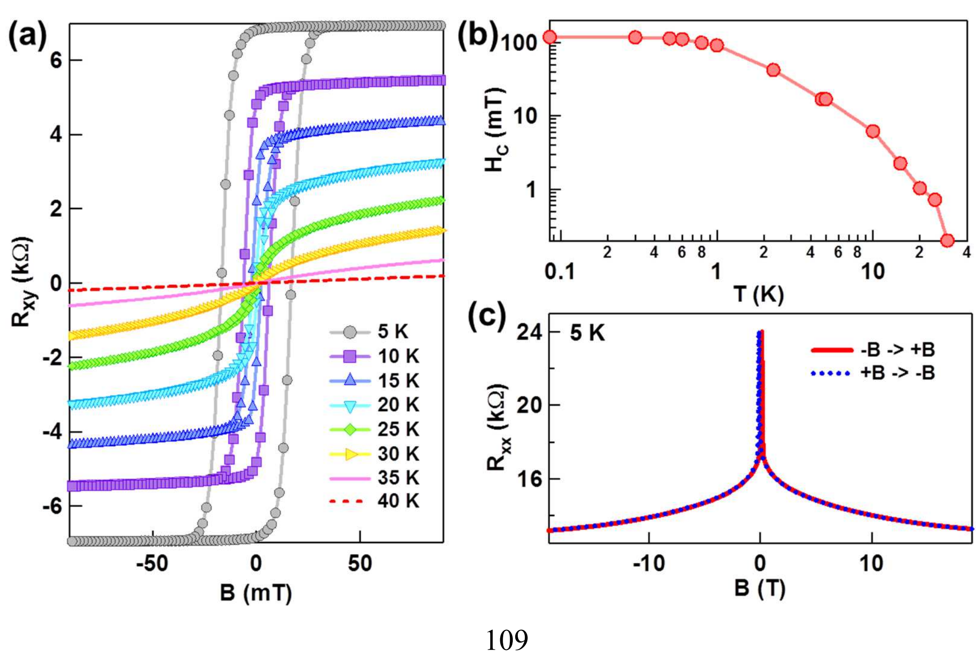

Figure 5-2. Anomalous Hall measurement of the 10 QL $Cr_{0.24}(Bi_{0.3}Sb_{0.7})_{1.76}Te_3$ film. (a) Temperature-dependent hysteresis R_{xy} curves above 5 K. (b) Temperature-dependent coercivity field H_C extracted from Figs.5-2(a). It can be observed that H_C diminishes to zero when T > 30 K, indicating $T_C \sim 30$ K. Our observation is consistent with the field-cooled magnetization result shown in Fig. 5-1(d). (c) Magneto-resistance result at 5 K. Adopted from Ref. [152].

Strikingly, Our 10 QL $Cr_{0.24}(Bi_{0.3}Sb_{0.7})_{1.76}Te_3$ film reaches the QAHE regime when the sample temperature falls below 85 mK. As demonstrated in Fig. 5-3(a) and 5-3(b), the $R_{xy} = R_{14,62}$ reaches the quantized value of h/e^2 (25.8 kΩ) at $B = 0$ T while $R_{xx} = R_{14,65}$ is nearly vanished. From Fig. 3.6(a), In the QAHE regime, since the TRS is broken by the FM moments, the electrons can only flow along one direction with the chiral conduction direction determined by the magnetization orientation [116]. Specifically, when the film is magnetized along $+z$ direction, the chirality determined by the Lorentz force makes the current flow counter-clockwise (or electron travels clockwise, as shown in the upper panel of Fig. 5-3(d)). Under such condition, the dissipationless edge current forces the voltage distributions along the longitudinal direction to be $V_6 = V_5 = V_1$ [153]. On the other hand, when the magnetization reverses its direction (lower panel of Fig. 5-3(d)), the edge current flows through the 2nd and 3rd contacts, thus making $V_2 = V_3 = V_1$ instead. Consequently, $R_{14,62} =(V_6 - V_2) / I$ is positive for the $M_Z > 0$ case, and change to negative sign if $M_Z < 0$. Meanwhile, except for the sharp MR peaks at the coercivity fields (± 0.12 T), the vanishing $R_{12,65}$ in the fully magnetized region is also anticipated since the presence of the dissipationless chiral edge states lead to zero voltage drop along the edge channel. Accordingly, the consistency

between the scenario described by Fig. 5-3(d) and our experimental observations clearly reveals the chiral edge transport nature of QAHE.

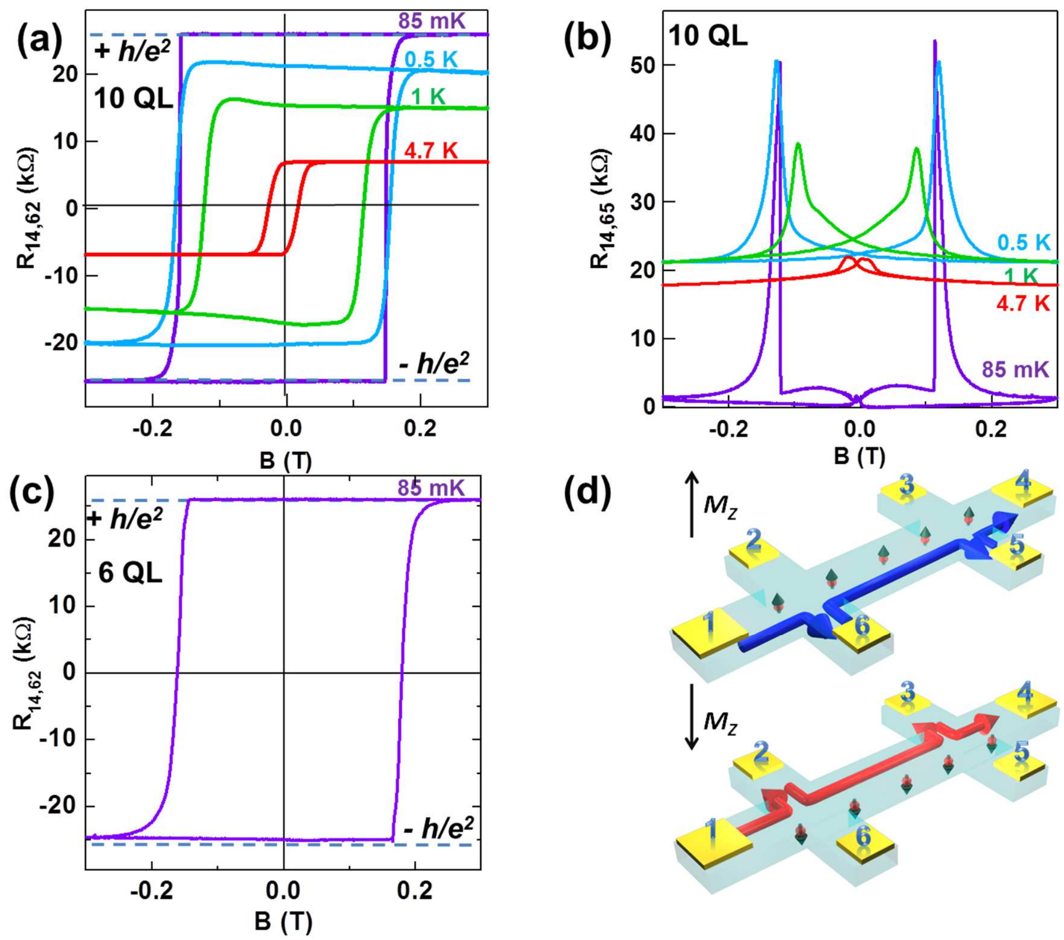

Figure 5-3. QAHE in the $Cr_{0.24}(Bi_{0.3}Sb_{0.7})_{1.76}Te_3$ thin films. (a) Hysteresis R_{xy}–B curves of the 10 QL film at different temperatures. For T < 85 mK, R_{xy} attains the quantized value of h/e^2. (b) Butterfly-shaped R_{xx}–B curves of the 10 QL film. In the QAHE regime, R_{xx} nearly vanishes at low fields. (c) QAHE is also observed in the 6 QL film at similar temperature of 85 mK. (d) Schematics of the chiral edge conduction in the QAHE regime. The current flows from the 1st contact to the 4th contact, and the magnetization of the Cr-doped TI film is along the *z*-direction. Adopted from Ref. [152].

Beside the 10 QL sample, it is important to highlight that the QAHE is also realized in the 6 QL (2D hybridization thickness) $Cr_{0.24}(Bi_{0.3}Sb_{0.7})_{1.76}Te_3$ film at 85 mK, as shown in Fig.

5-3(c). Therefore, the thickness-dependent results provide strong evidence that the stability of the QAHE phase in magnetic TIs is maintained as the film thickness varies across the hybridization limit (whereas in the QHE regime, the formation of the precise Landau level quantization requires the electrons to be strictly confined in the 2D region [123]).

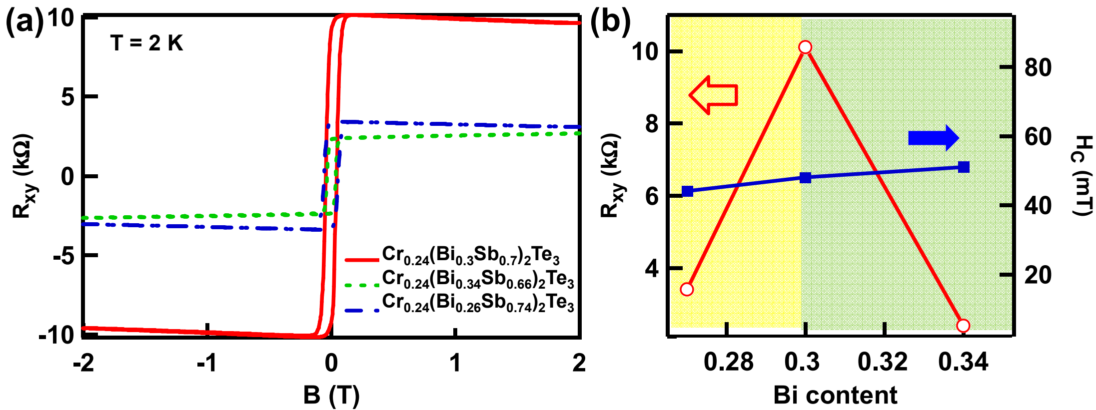

Figure 5-4. Importance of the Fermi level position on the QAHE state. (a) Anomalous Hall results of the three Cr-doped $(Bi_xSb_{1-x})_2Te_3$ samples with same film thickness of 10 QL, same Cr doping concentration of 12%, but different Bi contents ranging from 0.26 to 0.34. (b) The Bi/Sb ratio-dependent Hall resistance R_{xy} (hollow red circles) and the coercivity field H_C (solid blue squares). The data are extracted from Fig. 5-4(a). The yellow (blue) background represents the *n*-type (*p*-type) region. Adopted from Ref. [152].

In light of the importance of the Fermi level position, we also prepare additional two samples. Compared with the 10 QL $Cr_{0.24}(Bi_{0.3}Sb_{0.7})_{1.76}Te_3$ film (Sample **A**), the control samples (Samples **B** and **C**) have the same thickness (10 QL) and Cr doping level (12%), but slightly different Bi/Sb ratios (Bi content changes from 0.26 to 0.34) so that their Fermi level positions are different. Figure 5-4 shows the corresponding AHE results of these three samples at 1.9 K. It can be clearly observed that although their coercive fields H_C (magnetic

orders) are nearly the same, the Hall resistances R_{xy} of Samples **B** and **C** are much smaller. As illustrated in Fig. 5-4(b), the Fermi level perfectly resides inside the band gap for the Sample **A** case, while moving towards *n*-type (*p*-type) region in Sample **B** (Sample **C**). As a result, the observed rapid decrease of R_{xy} as the Fermi level moves away from the optimized point addresses that one of the most critical requirements to reach the QAHE state is to place the Fermi level within the surface band gap.

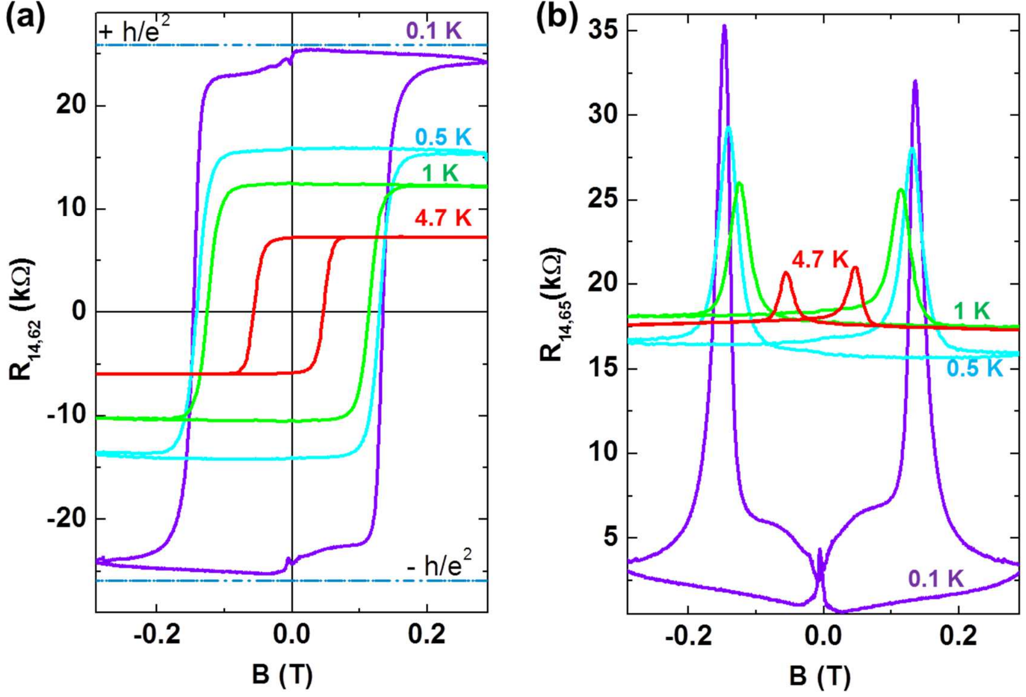

Figure 5-5. Quantum Anomalous Hall effect on the 10 QL $Cr_{0.4}(Bi_{0.3}Sb_{0.7})_{1.6}Te_3$ film (a) Temperature-dependent hysteresis R_{xy} curves. When the temperature is below 0.1 K, the sample almost reaches the QAHE regime. (b) Temperature-dependent magneto-resistance R_{xx} curves. Similar to Fig. 5-3(b), R_{xx} dramatically decreases as the film approaches the QAHE state. Adopted from Ref. [152].

Beside the 10 QL $Cr_{0.24}(Bi_{0.3}Sb_{0.7})_{1.76}Te_3$ film discussed above, we also observe the QAHE on another 10 QL $Cr_{0.4}(Bi_{0.3}Sb_{0.7})_{1.6}Te_3$ film with a higher Cr doping concentration of

20 %. As shown in Fig. 5-5(a), our magnetic TI film almost reaches the QAHE regime where $R_{xy} = R_{14,62} = \pm h/e^2$ and is nearly invariant with magnetic field when the sample is fully magnetized. Here, it is noted that the abnormal "humps" around zero-field are probably due to the unwanted influence from the indium contacts (*i.e.,* indium becomes superconducting below 0.1 K). Together with the thickness-dependent results, we may conclude that when appropriate spin-orbit interaction and perpendicular FM exchange strength are present in a bulk insulating magnetic TI film and the Fermi level resides inside the surface gap [49, 120, 150], the QAHE resistance is always quantized to be h/e^2, regardless of the device dimensions and magnetic doping levels.

5.2. Landauer-Büttiker Formalism

Compared with the magneto-transport results between the QHE (Fig. 2-4), QSHE (Fig. 1-5) and QAHE (Fig. 5-3), it is noted that for the chiral QHE/QAHE states, quantized Hall plateau and the vanishing (or minimum) longitudinal resistance are obtained; while for the helical QSHE state, $R_{xx} = h/2e^2$ and $R_{xy} = 0$ are revealed. In order to understand the quantum edge transport phenomena in these three quantum regimes, we thus apply the Landauer-Büttiker formalism that [153]

$$I_i = \frac{e^2}{h} \sum_j (T_{ji} V_i - T_{ij} V_j) \tag{5-1}$$

where I_i is the current flowing out of the ith contact into the sample per spin per ballistic channel, V_i is the voltage on the ith contact, and T_{ji} is the transmission probability from the ith to the jth contacts. In a standard six-terminal Hall bar structure shown in Fig. 5-6, the voltage bias is applied between the 1st and 4th contacts (*i.e.,* $V_1 = V$, $V_4 = 0$, and $I_1 = -I_4 = I$) and the other four contacts are used as the voltage probes such that $I_2 = I_3 = I_5 = I_6 = 0$. From Fig. 5-6(a), we know that for the chiral edge conduction case, the electrons can only flow along one direction without backscattering, and will reverse their chirality once the magnetization direction is switched. Accordingly, when the system is polarized (either by B or M) along $+z$ direction, the transmission coefficient is given by $(T_{i,i+1}, T_{i+1,i}) = (0, 1)$, and the overall transmission matrix in the QHE/QAHE cases follow

$$T_{QHE} = \begin{bmatrix} 1 & -1 & 0 & 0 & 0 & 0 \\ 0 & 1 & -1 & 0 & 0 & 0 \\ 0 & 0 & 1 & -1 & 0 & 0 \\ 0 & 0 & 0 & 1 & -1 & 0 \\ 0 & 0 & 0 & 0 & 1 & -1 \\ -1 & 0 & 0 & 0 & 0 & 1 \end{bmatrix} \qquad (5\text{-}2)$$

Applying Eq. (5-2) and the initial conditions in Eq. (5-1), we thus obtain $V_6 = V_5 = V_1 = (h/e^2)I$ and $V_2 = V_3 = V_4 = 0$. Therefore, the measured Hall conductance $\sigma_{xy} = \frac{I}{V_6 - V_2} = \frac{e^2}{h}$ and the longitudinal conductance is $\sigma_{xx} = \frac{I}{V_6 - V_5} = 0$.

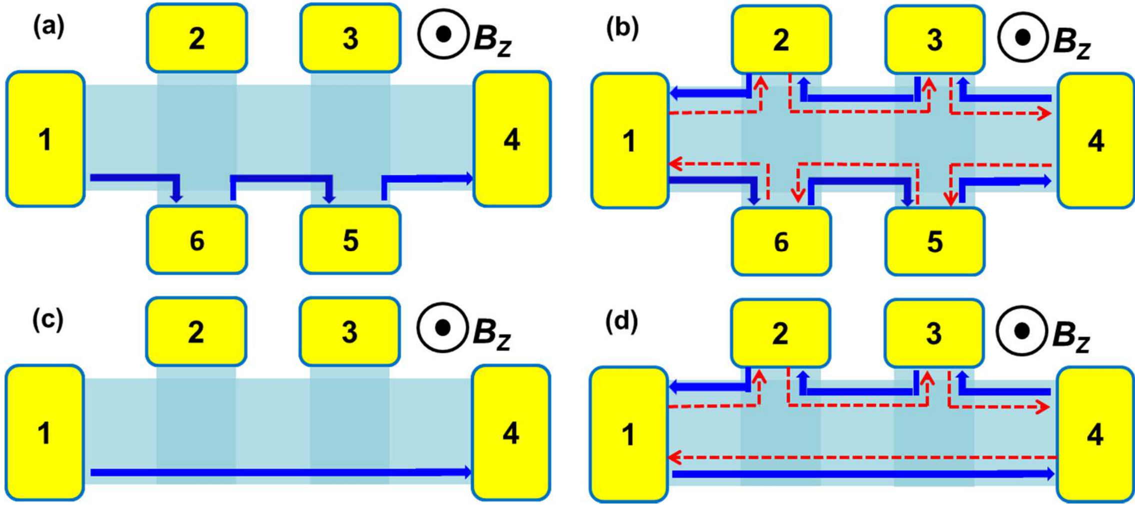

Figure 5-6. Chiral edge current conduction in the QHE/QAHE states and helical edge current conduction in the QSHE state with different device configurations. (a) and (b) represent the ordinary six-terminal Hall bar device, while (c) and (d) illustrate the π-bar (or H-bar) configuration. Solid blue arrow and dashed red arrow represent the spin-up and spin-down current conductions, respectively.

On the other hand, in the QSHE state, since TRS is well-protected, the helical edge states give rise to ($T_{i,i+1}$, $T_{i+1,i}$) = (1, 1), and the corresponding transmission matrix in the QSHE case is given by

$$T_{QSHE} = \begin{bmatrix} 2 & -1 & 0 & 0 & 0 & -1 \\ -1 & 2 & -1 & 0 & 0 & 0 \\ 0 & -1 & 2 & -1 & 0 & 0 \\ 0 & 0 & -1 & 2 & -1 & 0 \\ 0 & 0 & 0 & -1 & 2 & -1 \\ -1 & 0 & 0 & 0 & -1 & 2 \end{bmatrix} \tag{5-3}$$

Therefore, after substituting Eq. (5-3) into Eq. (5-1), we obtain (V_1, V_2, V_3, V_4, V_5, V_6) = (V, $2V/3$, $V/3$, 0, $V/3$, $2V/3$) and $I = I_1 = 2V_1 - V_2 - V_6 = \frac{2}{3}\frac{e^2}{h}V$. Consequently, we have

$\sigma_{xy} = \frac{I}{V_6 - V_2} = 0$ and $\sigma_{xx} = \frac{I}{V_6 - V_5} = \frac{I}{V/3} = \frac{2e^2}{h}$, consistent with the experimental results shown in Fig. 1-5.

In fact, given the universality of the Landauer- Büttiker formalism, we can calculate the voltage distributions of contacts in any device configuration. Figures 3.6(c) and (d) show the four-terminal π-bar (also called H-bar) configuration. In the QSHE state, following the same scenario provided above, we obtain that (V_1, V_2, V_3, V_4) = (V, $2V/3$, $V/3$, 0) and $I = I_1 = 2V_1 - V_2 - V_4 = \frac{4}{3}\frac{e^2}{h}V$. Accordingly, the measured longitudinal conductance σ_{xx} should be quantized to $4e^2/h$, and such expectation was experimentally confirmed in both the InAs/GaSb [39] and CdTe/HgTe [154] QW systems.

5.3. Physical Explanations about Chiral/Helical Edge Conductions

Although the quantized edge conduction can be understood from the Landauer-Büttiker formalism, as described in Section 5.2, the intrinsic physics behind the chiral and helical edge states still need to be further investigated. Especially for the disspationless edge conduction in the QSHE regime, it is difficult to comprehend why the measured longitudinal resistance along the edge channel is non-zero and why such value depends on the device configurations. Therefore, in this section, we will explain the quantum transport from a more fundamental physical point of view.

It is known that for a two-terminal ballistic transport, the coherent electron conduction would not introduce any modification to the potential distribution along the channel, and the voltage drop occurs only at the contact [153]. As a result, the measured resistance (conductance) between the neighboring two contacts is $R = R_0/M$ ($G = G_0 \cdot M$), where $R_0 = h/e^2$ ($G_0 = e^2/h$) is the quantized resistance (conductance) per coherent channel, and M is the number of coherent channels between the two contacts. Note that since the dissipationless conduction is scale-invariant, it is thus meaningless to define the resistivity (conductivity) in the quantum transport regime.

Next, in the system with multiple contacts, we point out that a contact is not a TRS breaking single-particle potential with matrix elements connecting counter-propagating edge channels with opposite spins. A contact is, ultimately, a reservoir of electrons which populates both channels incoherently. Furthermore, an ideal contact populates both channels with equal weight, *i.e.* it injects spin up and spin down electrons with equal probability. A right-moving electron entering a contact will disappear into the reservoir. Since the contact (except the source contact and drain contact) is assumed not to draw any current, the reservoir has to inject a new electron into the device. This new electron can be of either spin state, and bears no phase relationship with the previous electron. For an ideal contact, this electron has 1/2 probability of being injected as a left-mover, which is the origin of the resistance contributed by the contact. Note that this incoherent momentum-relaxing event is different

from usual coherent momentum relaxation caused by potential scattering in an ordinary (non-helical) 1D system [154].

On the contrary, in the QHE/QAHE cases where TRS is broken, the channels are chiral such that the edge current can only flow along one direction. Under such circumstance, even the contact breaks the coherence of the edge transport, the new electron injected from the contact has to continue the movement towards the right direction since left-moving is strictly prohibited by chirality. As a result, the longitudinal conductance is always quantized to be ne^2/h with n is the number of channels on each edge, and such value is independent of the presence of additional lateral contacts. Consequently, the quantization of the chiral conductance is always maintained constant and robust, regardless of whether transport is coherent or incoherent [154].

In fact, since R_0 (G_0) only describes one coherent channel, the de-phasing process due to every additional contact in the helical QSHE case effectively introduces additional R_0 along the edge. Consequently, the equivalent circuits for the six-terminal Hall bar device in the QSHE state is thus plotted in Fig. 5-7(d). By solving this equivalent circuit, we finally obtain that $V_{23} = V_{14}/3, V_{14} = (\frac{3}{2}R_0)I_{14}$, and $R_{23} = \frac{V_{23}}{I_{14}} = \frac{1}{3}\frac{V_{14}}{I_{14}} = \frac{1}{2}R_0 = \frac{h}{2e^2}$, which are again consistent with both the experimental data and the Landauer- Büttiker calculation results.

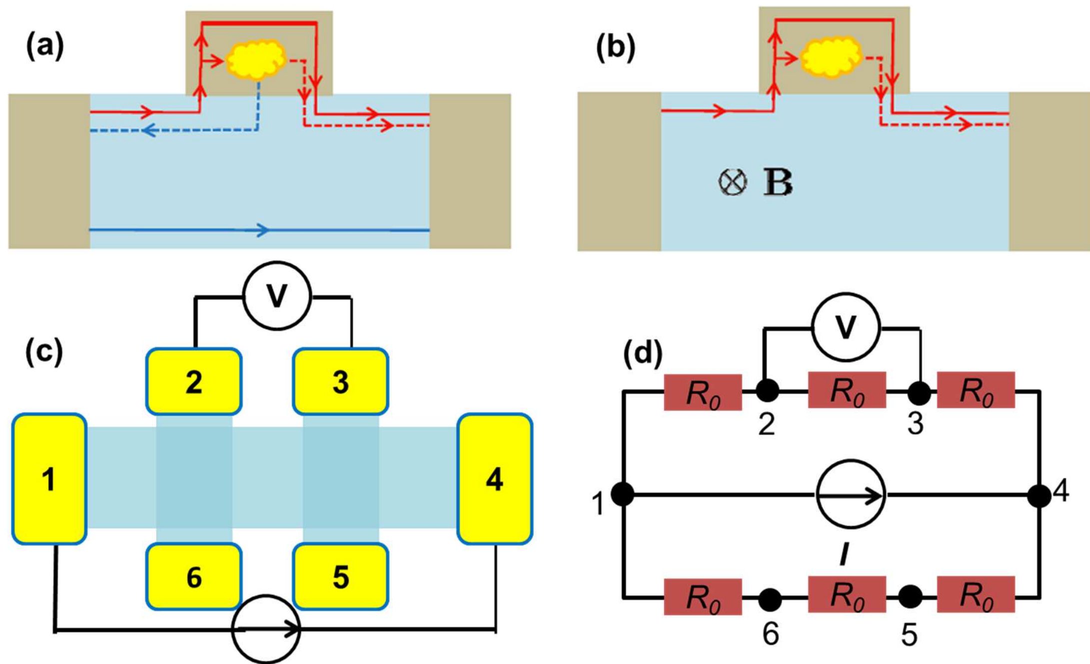

Figure 5-7. Contact effect and equivalent circuit of six-terminal Hall bar in the QSHE state. (a) De-phasing process in the QSHE state induced by the lateral contacts. (b) Due to the chirality, the contact does not affect the longitudinal dissipationless conduction in the QHE state. Adopted from Ref. [154]. (c) Schematic of the four-probe configuration in transport measurement. (d) Equivalent circuit of the six-terminal Hall bar considering the effect of the lateral contacts.

5.4. Dissipative side-surface edge conduction

Figure 5-8 shows the R_{xx}-T and R_{xy}-T results of the 10 QL $Cr_{0.24}(Bi_{0.3}Sb_{0.7})_{1.76}Te_3$ film at B = 3 T and 15 T in the low-temperature region (T < 1 K). Both the enhanced magnetization and the reduced thermal activations at lower temperatures help localize the bulk conduction channels, and thus drive the system from the regular diffusive transport regime (T > 1 K) towards the chiral edge conduction regime. As a result, R_{xx} diminishes rapidly as the sample

temperature drops, which is opposite to the $R_{xx} - T$ relation in the higher temperature region as shown in Fig. 5-1(d). Moreover, when the magnetic TI film reaches the QAHE state below 85 mK, we also observe a non-zero R_{xx} similar to the previously reported 5 QL $Cr_{0.15}(Bi_{0.1}Sb_{0.9})_{1.85}Te_3$ film case [114]. It is noted that the underlying mechanisms of the non-zero longitudinal resistances in these two systems are quite different. In particular, it was reported that when a large external magnetic field (B > 10 T) was applied, the 5 QL film was driven into a perfect QHE regime, and R_{xx} diminished almost to zero [114]. In contrast, it is apparent from Fig. 5-8(a) that the longitudinal resistance in our 10 QL $Cr_{0.24}(Bi_{0.3}Sb_{0.7})_{1.76}Te_3$ sample remains at 3 kΩ even when the applied magnetic field reaches 15 T.

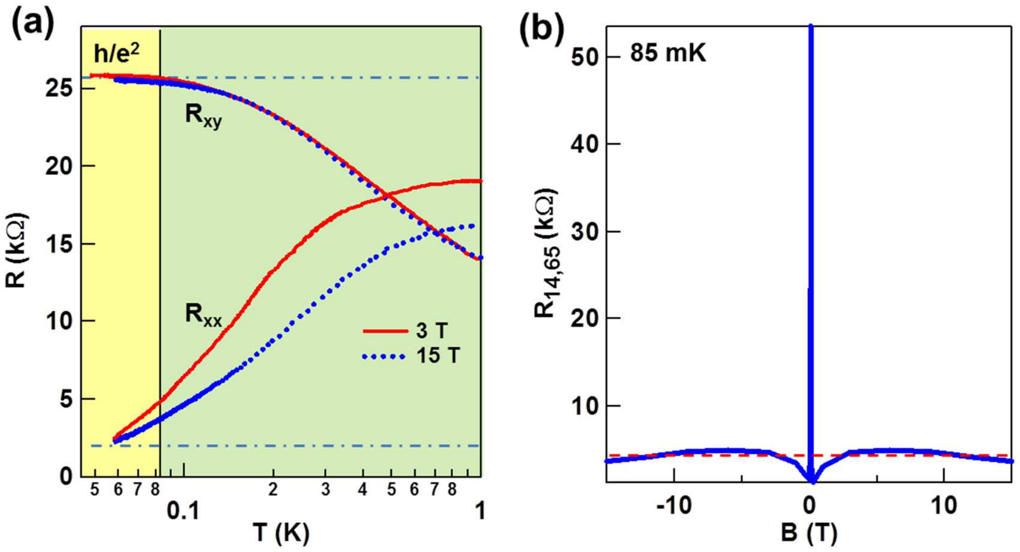

Figure 5-8. Non-zero longitudinal resistance in the 10 QL $Cr_{0.24}(Bi_{0.3}Sb_{0.7})_{1.76}Te_3$ film. (a) Temperature-dependent R_{xx} and R_{xy} of the 10 QL $Cr_{0.24}(Bi_{0.3}Sb_{0.7})_{1.76}Te_3$ film at B = 3 T and 15 T in the low-temperature region. (b) Magnetic field dependence of R_{xx} at 85 mK. R_{xx} in our 10 QL magnetic TI sample shows little field dependence when B > 3 T. Adopted from Ref. [152].

More importantly, unlike the bulk conduction case which has a typical parabolic MR relation (Fig. 3-2(c)), R_{xx} at T = 85 mK exhibits little field dependence when the magnetic field is larger than 3 T (Fig. 5-8(b)). Consequently, it may be suggested that the non-zero R_{xx} in the thicker 10 QL magnetic TI film is more likely associated with a unique dissipative edge conduction, whose origins cannot be simply attributed to either the variable range hopping (VRH) [114] or the gapless quasi-helical edge states [116] as proposed for the 5 QL magnetic TI film.

In order to explain the non-zero field-independent R_{xx} in our 10 QL $Cr_{0.24}(Bi_{0.3}Sb_{0.7})_{1.76}Te_3$ sample, let us consider a 3D ferromagnetic TI film with a uniform magnetization M pointing along the z-axis as illustrated in Fig. 5-9(a), the strong exchange field can significantly affect the surface state properties. For the top and bottom surface states, the Hamiltonian can be expressed as $\mathcal{H}_{tb} = \pm\hbar v_F\left[\left(k_x\sigma_y - k_y\sigma_x\right) + (\alpha\mu_0 M)\sigma_z\right]$, where α is a coupling constant between M and σ_z, thus indicating a massive Dirac cone with a gap $\Delta_g \sim 2\alpha\mu_0 M$ [119].On the other hand, the Hamiltonian of one x-z side surface is shown in the lower panel of Fig. 5-9(a), giving $\mathcal{H}_{xz} = \pm\hbar v_F\left[(k_x{+}\alpha'\mu_0 M)\sigma_z - k_y\sigma_x\right]$, where α' is typically different from α because of the anisotropic coupling of σ_z to the M along different directions [119]. Instead of being gapped, the Dirac point on the x-z side surface is shifted from the center (0, 0) to off-center ($-\alpha'\mu_0 M$, 0) in the momentum space [119]. One direct consequence is the removal of the backscattering suppression condition as illustrated in Fig. 5-9(b). For a non-spin-flip backscattering, the $\boldsymbol{k}$ to $-\boldsymbol{k}$ transition in a Dirac cone centered at (0,

0) is strongly suppressed due to the chirality conservation. On the contrary, in an off-centered Dirac cone, the backscattering is no longer suppressed by the chirality conservation, which results in a dissipative transport along the side surfaces. In addition, the corresponding spin texture and left-right transport coefficients in an off-centered Dirac cone are also expected to change as opposed to a centered Dirac cone. In contrast to the one-dimensional nature of the quasi-helical edge transport for the 5 QL film [114], which makes it quite sensitive to the magnetic field and gets suppressed at strong fields [116], here this side-surface dissipative transport is expected to have little dependence on magnetic field.

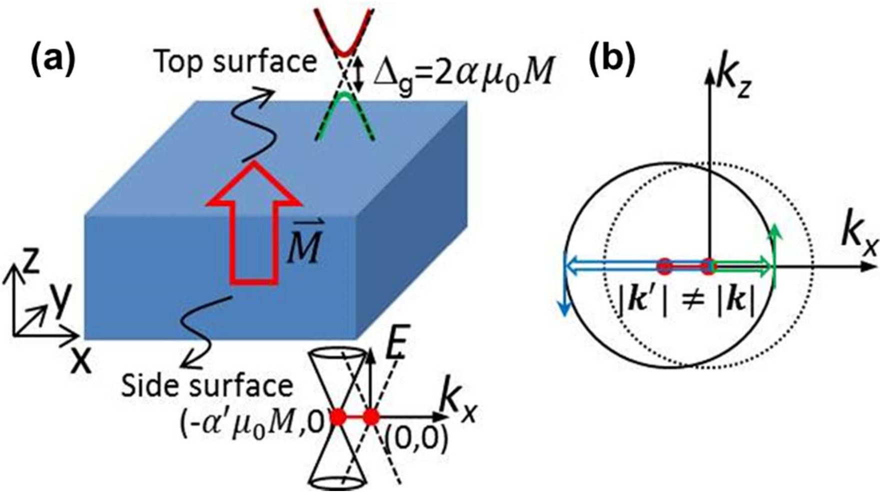

Figure 5-9. Possible side-surface conduction in 3D magnetic TIs. (a) Illustration of the top and side surface states in a uniformly magnetized topological insulator. (b) For an off-centered Dirac cone on the side surfaces, backscattering is no longer suppressed. Adopted from Ref. [152].

5.5. Non-local transport measurements

For conventional diffusive transport, it is known that $R = \rho L/W$, where ρ is the resistivity, L is the length, and W is the width. On the contrary, the presence of chiral edge states in the

QAHE regime lead to non-local transport, which invalidates the concept of Ohm's law [154]. To illustrate the chiral edge conduction feature for the QAHE state, we perform the non-local measurements on the six-terminal Hall bar device, as shown in the inset of Fig. 5-10. In this non-local configuration, the current is passed through contacts 1 (source) and 2 (drain) while the non-local resistances among contacts 3 to 6 are measured. Following the same scenario described in Section 5.2, we can apply Eq. (5-1) with the initial conditions that $V_1 = V$, $V_2 = 0$, $I_1 = -I_2 = I$, and $I_3 = I_4 = I_5 = I_6 = 0$. Accordingly, we obtain that

$$V_6 = V_5 = V_4 = V_3 = V_1 = (h/e^2)I, \quad M_Z > 0 \tag{5-4a}$$

$$V_6 = V_5 = V_4 = V_3 = V_2 = 0, \quad M_Z < 0 \tag{5-4b}$$

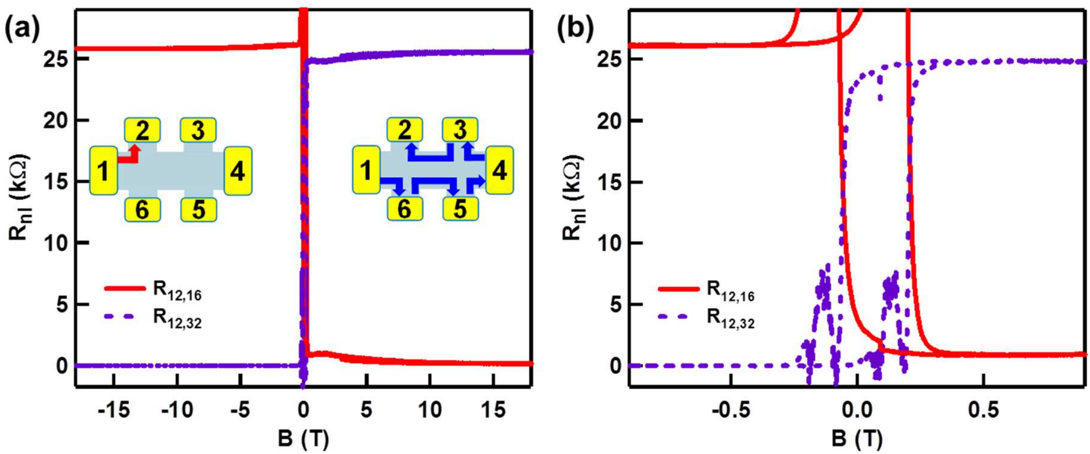

Figure 5-10. Field-dependent results for two non-local resistances $R_{12,16}$ and $R_{12,32}$. (a) [-18 T, 18 T] scale. (b) [-1 T, 1 T] scale. The measurements are performed at 20 mK on the 10 QL $Cr_{0.24}(Bi_{0.3}Sb_{0.7})_{1.76}Te_3$ film. Inset: illustrations of the QAHE edge channels under different magnetizations.

Experimentally, it is clearly observed from Fig. 5-10 that both the measured $R_{12,16}$ and $R_{12,32}$ show the zero-to-h/e^2 transition when the magnetization of the sample is switched by the applied magnetic field. In the meanwhile, the polarities of these two signals are consistent with Eq. (5-4): $R_{12,32}$ reaches 25.8 kΩ (Note that there is no power dissipation along the chiral edge channel, and the voltage drops only on the drain contact 2) when the film is magnetized along $+z$ direction while $R_{12,16}$ becomes quantized in the $-M_z$ regime. Therefore, Fig. 5-10 provides the direct evidence of the unique chiral edge conduction in the QAHE regime.

From Eq. (5-4), it is also concluded that in the ideal QAHE regime where the quantum transport is only featured by the dissipationless chiral edge conduction, there is no voltage drop among the four voltage probes (contacts 3-6), therefore leaving the non-local resistance of $R_{12,54}$ to be nearly zero regardless of the magnetization direction [155]. Now, if we consider the influence of the additional dissipative non-chiral edge channel as discovered in Fig. 5-8 for the 10 QL $Cr_{0.24}(Bi_{0.3}Sb_{0.7})_{1.76}Te_3$ film, there are two possible paths for the non-local signals: the voltage probes measure the voltage drop along the same edge where the QAHE edge state is present, and the voltage probes are away from the dissipationless chiral edge channel. To further verify the above argument, two different non-local configurations are investigated: in case **A**, the current is passed through contacts 1 (source) and 2 (drain) while the non-local resistance between contacts 5 and 4 ($R_{12,54}$) is measured (top inset of Fig. 5-11(a)); in case **B**, a quasi H-bar geometry is adopted such that contacts 2 and 6 are designated as the source/drain pads while contacts 3 and 5 are used as the voltage probes

($R_{26,35}$, top inset of Fig. 5-11(b)). In the QAHE regime (T < 85 mK), it can be clearly seen that both $R_{12,54}$ and $R_{26,35}$ display square-shaped hysteresis windows with H_C = 0.12 T, but their polarities are opposite. In other words, when B < -0.2 T, $R_{12,54}$ reaches the high-resistance state of 15 Ω while $R_{26,35}$ is at the low-resistance state close to zero. Here, we point out that the non-local resistances can be understood from the chirality of QAHE. In the inset of the bottom Fig. 4(a), for example, we show that when the film is magnetized along +z direction, the chirality forces the QAHE dissipationless current flow from contact 1 to contact 2 through the 1→6→5→4→3→2 contacts successively, and in turns "shorts" the contacts so that $V_6 = V_5 = V_4 = V_3 \sim V_1 = V$ [155]. As a result, the voltage drop between these contacts is negligible, and $R_{12,54}$ is driven into the low-resistance state (2 Ω). On the other hand, when the magnetization is reversed (-*z* direction), the 1st and 2nd contacts are directly connected through the upper edge (lower left panel of Fig. 5-11(a)), and the voltage probes from V_3 to V_6 are now away from the dissipationless QAHE channel. Consequently, the non-local signal only relates to the voltage drop caused by the dissipative edge channel, which gives rise to a larger value of $R_{12,54}$. The same transport principle can also be applied to the quasi H-bar non-local configuration (case **B**), and the illustrations of field-dependent conduction paths are consistent with the measured $R_{26,35}$ results, as shown in the bottom panels of Fig. 5-11(b). It is noted that, in contrast to the QAHE regime (T < 85 mK), both $R_{12,54}$ and $R_{26,35}$ are dominated by the larger bulk conduction component at a higher temperature of 4.7 K (*i.e.,* the non-local resistances are more than 10 times larger than those

probed at 85 mK). In such diffusive transport regime, the square-shaped hysteresis non-local signals are replaced by the ordinary parabolic MR backgrounds, and the polarity differences between $R_{12,54}$ and $R_{26,35}$ also disappear. To summarize, both the field-independent R_{xx} shown in Fig. 5-8(b) and the non-local resistances displayed in Fig. 5-11 confirm the coexistence of QAHE chiral edge channel and the additional dissipative edge conduction in the thick 10 QL Cr-doped TI sample.

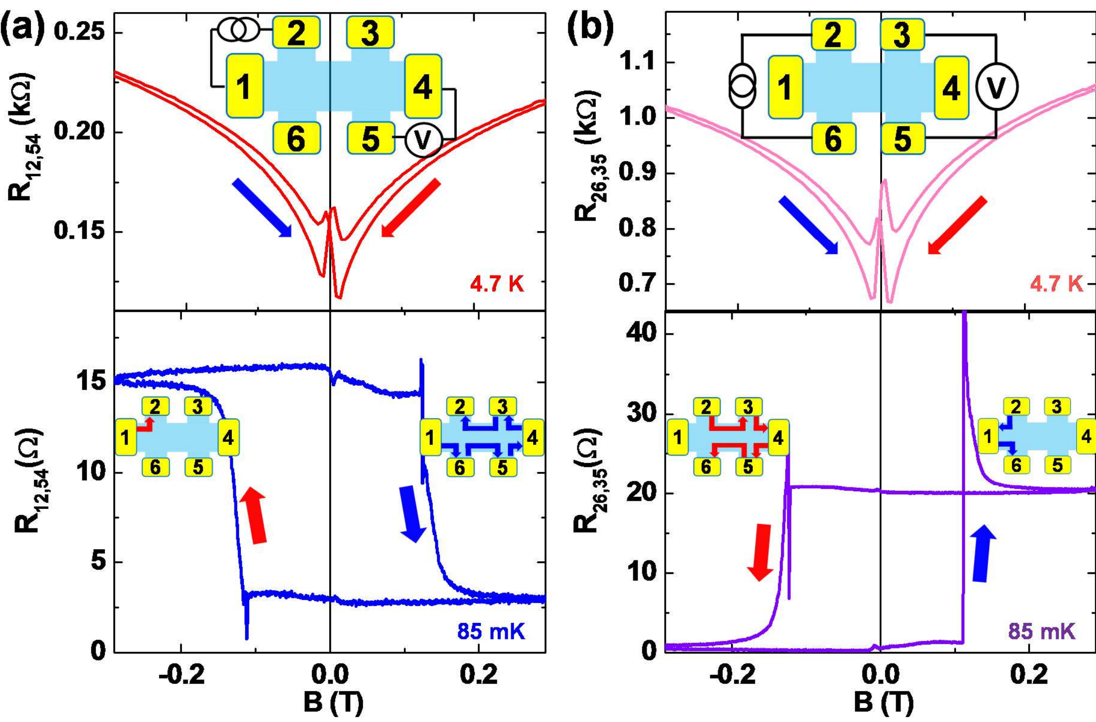

Figure 5-11. Temperature-dependent non-local results for both the six-terminal Hall bar and the quasi H-bar devices. (a) Case **A**: the current is applied through 1st to 2nd contact and the non-local voltages are measured between 4th and 5th contacts at T = 85 mK and 4.7 K. (b) Case **B**: the current is applied through 2nd to 6th contact and the non-local voltages are measured between 3rd and 5th contacts with different magnetizations. Inset: Illustrations of the QAHE channel under different magnetizations. The red solid arrow indicates that the magnetic field is swept from positive (+z) to negative (-z), whereas the blue solid arrow corresponds to the opposite magnetic field sweeping direction. Adopted from Ref. [152].

5.6. Re-capturing the quantum Hall trio

So far, we have explicitly showed the intrinsic mechanisms and distinct quantized edge transport phenomena for the three important quantum Hall effects. In this section, we would like to summarize and compare both the relations and differences between these quantum Hall trio, and show the advantages of QAHE for low-power interconnect applications.

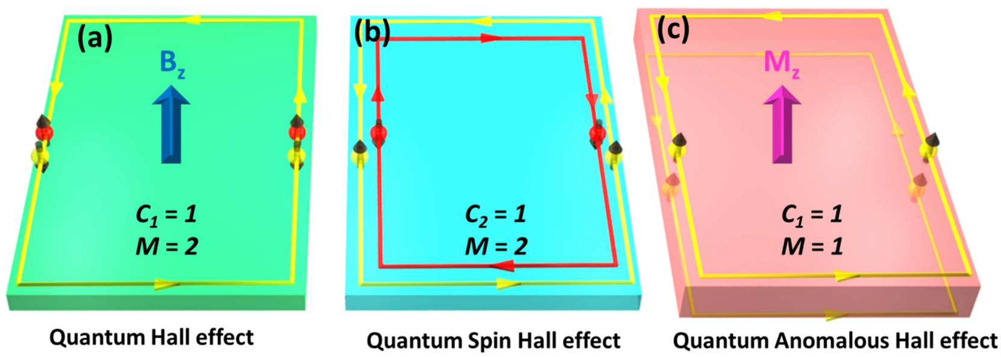

Figure 5-12. Illustration of the quantum Hall trio. (a) Quantum Hall case. External perpendicular magnetic field is required to localize dissipative channels and quantize LLs. Due to the TRS breaking, chiral edge conduction is dominant. (b) Quantum spin Hall case. Due to the protection of TRS and spin-momentum locking mechanism, opposite-spin electrons occupy opposite sides in the quantum spin Hall system. (c) Quantum Anomalous Hall case. The TRS is broken by magnetic doping. When the film is magnetized along +*z*-direction, only spin-up electrons flow through the edge clockwise. Note: The arrows represent the current directions (*i.e.,* opposite to the electron conduction directions).

It is known that QHE can only be realized in a $C_1 = 1$ Chern insulator where the bulk is insulating because of the discrete Landau levels (LLs) and the conduction channels only exist at the edges, as shown in Fig. 5-12(a) [153]. In the QHE regime, the external magnetic field

acts as a gauge field which couples to the momentum of the electrons and forces the electrons to make cyclotron motions in real space. In order to form the discrete LLs (*i.e.,* to change the band topology), the electrons need to complete the cyclotron motion circles before losing its momentum due to scattering, and this in turn requires the electrons to have a very high mobility. In addition, the precise LL quantization also requires the electrons to be confined in the 2D dimension so that the energy levels of these quantized orbitals take on discrete values, as given by Eq. (2-6). Therefore, once the Fermi level is located inside the gap between two neighboring LLs, the quantum chiral edge state readily appears while the bulk carriers are localized by the cyclotron orbitals. In other words, the realization of QHE demands a strong magnetic field and a high mobility material with a good 2D confinement [123].

The QSHE, on the other hand, does not need any external magnetic field. It is realized in systems where the strong spin-orbit interaction leads to the band inversion at the Γ point in the Brillouin zone. This band inversion makes the system into a $C_2 = 1$ ($C_1 = 0$) Chern insulator with the quantized channel number $M = 2$ [31]. Here the second Chern number is employed to describe the topology in the QSHE state. Because the TRS is preserved in such system (*i.e.,* the external magnetic field is zero), the resulting quantum edge states are helical instead of chiral, as shown in Fig. 5-12(b). Accordingly, when the Fermi level is placed inside the bulk band gap, the longitudinal conductance exhibits a quantized $2e^2/h$ helical conduction. It is noted that since the bulk band gap, which is determined by the spin-orbit interaction strength, is usually small (*i.e.,* up to 0.3 eV), the quantum helical edge conduction

is thus vulnerable to any intrinsic bulk impurity/defect-induced carrier states and band potential fluctuations. Consequently, the QSHE requires a very high material quality (*i.e.,* low bulk carrier density and high mobility). To date, the QSHE has only been realized experimentally in the HgTe/CdTe [34, 154] and InAs/GaSb [38, 39] QWs, and the quantization of the longitudinal resistance (conductance) is relatively weak.

Compared with QHE and QSHE discussed above, the QAHE involves both the strong spin-orbit interaction and the magnetic exchange interaction in a magnetic insulating system. In the QAHE regime with a robust magnetic moment, the strong spin-orbit interaction as well leads to the band inversion. However, the large exchange field from the spontaneous magnetization, as large as 100 T, can effectively couple with the spins of the band electrons, and split the spin-up and spin-down sub-bands in the opposite directions. It in turn results in one pair of the spin-resolved bands un-inverted while keeping the other pair still remains within the non-trivial topological state. As a result, in contrast to the QSHE state, the bulk topology is changed, the system becomes a $C_1 = 1$ Chern insulator, and the quantized QAHE chiral edge transport at zero external magnetic field can be achieved when the Fermi level is located in the massive Dirac surface band gap, as displayed in Fig. 5-12(c). In the meanwhile, compared with QHE, the TRS in the QAHE state is broken by the spontaneous magnetization rather than external magnetic field, and it does not require the formation of LLs. Accordingly, QAHE may have loose requirements on the film thickness and quality, (*i.e.*, our grown magnetic TI film has a relatively low mobility of 600 cm^2/Vs and the film is much thicker

than the 2D hybridization limit, but the quantized conduction of e^2/h is quite robust). In summary, the realization of QAHE requires an appropriate spin-orbit interaction, a strong exchange interaction (*i.e.,* in order to both splits the bands and localizes the bulk carriers) and an out-of-plane magnetic anisotropy; all of which are found to be satisfied in the Cr-doped $(BiSb)_2Te_3$ thin films.

5.7. Metal-to-insulator switching in quantum anomalous Hall states

Ever since the discovery of QHE [104], enormous efforts have been made elucidating the universal behavior of this quantum transport phenomenon [156-158]. Within the framework of 2D localization theorem, the renormalization group (RG) flow of the system can be well-described in the conductance plot, where stable points appear at (σ_{xx}, σ_{xy}) = (0, ne^2/h), in accordance with the nth LL (n is an integer). In the meanwhile, the quantum phase transition between neighboring LLs follows a continuous semicircle centered at (σ_{xx}, σ_{xy}) = (0, $(n\text{-}1/2)e^2/h$) with the scaling behavior dictated by the localization length [159-161]. In the extreme case of QHE when the applied magnetic field is so large that the ground LL exceeds the Fermi level, the 2DEG system will be driven into the so-called quantum Hall insulator state where the longitudinal resistance diverges as the temperature approaches absolute zero, yet the Hall resistance saturates towards the quantized value corresponding to the ground LL state [158, 162-164].

Following the footprint of QHE, J. Wang *et al.* recently applied a microscopic network model of quantum percolation to investigate the universal scaling of the QAHE plateau transition around the coercive field [165]. Generally, it was proposed that in an ideal 2D magnetic TI system, the competition between the FM exchange field and the quantum confinement-induced hybridization would change the band topology, therefore leading to the phase transition from the $C_1 = 1$ QAHE state to the $C_1 = 0$ insulating state. Under such circumstances, an intermediate zero Hall conductance ($\sigma_{xy} = 0$) plateau was expected to appear between the two QAHE states ($\sigma_{xy} = \pm e^2/h$), while the longitudinal conductance (σ_{xx}) should exhibit double peaks at the coercive fields. Unfortunately, due to the major challenge on growing high quality magnetic TIs within the 2D hybridization limit, experimental observations of the zero Hall plateau state in a quantum anomalous Hall insulator and the plateau transition from $\sigma_{xy} = \pm e^2/h$ to $\sigma_{xy} = 0$ in the QAHE regime have not been reported yet. Meanwhile, although there was an earlier attempt to interpret QAHE following the RG flow argument [166], the universality of this distinct QAHE phase remains to be ascertained.

In this section, we use the Cr-doped $(BiSb)_2Te_3$ films grown on semi-insulating GaAs (111)B substrates via MBE to study QAHE and its related phase diagram. The growth condition and chemical composition of the film are carefully optimized such that the bulk defect density is minimized and the Fermi level is already within the surface gap without additional electric field tuning. In order to generate the hybridization surface state gap m_0 [49, 111], the film thickness used here is precisely chosen as 6 QL. After careful *in-situ* surface

passivation, we carry out standard four-point magneto-transport measurements on the 6 QL $Cr_{0.24}(Bi_{0.3}Sb_{0.7})_{1.76}Te_3$ Hall bar device with dimensions of 2 mm × 1 mm, as illustrated in Fig. 5-13(a). Figure 5-13(b) shows the quantization of the anomalous Hall resistance (R_{xy} = h/e^2 ~ 25.81 kΩ) up to T = 0.26 K. The sign of the quantized R_{xy} with respect to the magnetization direction is consistent with the chiral conduction property, as elaborated in Section 5.1. Likewise, the magneto-resistance (R_{xx}) results are plotted in Fig. 5-13(c). The striking feature here is that at the base temperature T = 0.02 K, R_{xx} increases dramatically from almost a vanishing value (R_{xx_min} ~ 20 Ω) at zero field to a giant peak (R_{xx_PEAK} ~ 380 kΩ) at the coercivity field (H_C = ± 0.12 T); both R_{xx_PEAK} and the corresponding MR ratio (> 10^6 %) are much larger than those reported previously [114, 152, 166-168]. It is noted that the steep divergence of R_{xx} at zero LL was also observed in graphene under high magnetic field[169]. However, the underlying mechanisms are quite different. For the graphene case, it was believed that the increased exchange interaction at high $B_{\perp}$ would split the spin degeneracy of graphene around the Dirac point, and lifted the original fourfold degenerate Dirac cone by a Zeeman gap [169-171]. In contrast, both the giant R_{xx_PEAK} at small H_C and its temperature-dependent behavior shown in our 2D magnetic TI film (Fig. 5-13(d)) can be understood from the magnetic multi-domain network model at the QAHE phase transition regime, as we will explain in details below.

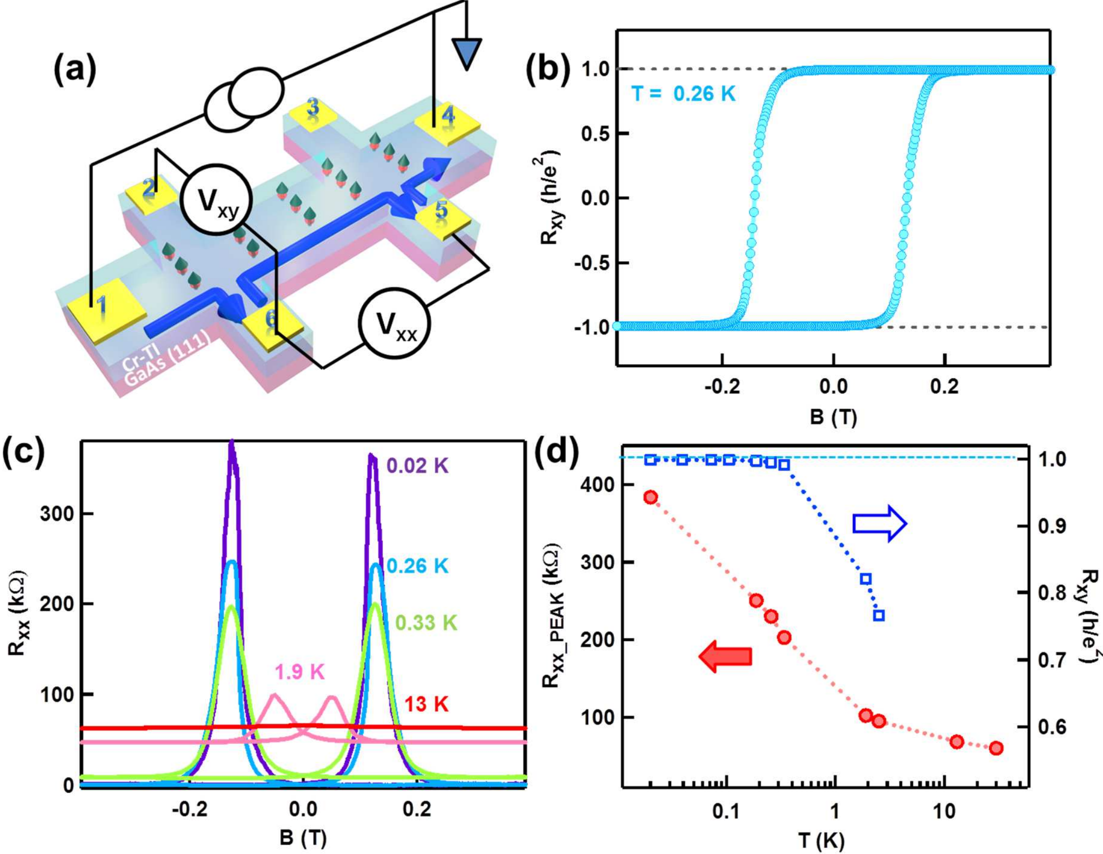

Figure 5-13. Quantum anomalous Hall effect in the 6 QL $Cr_{0.24}(Bi_{0.3}Sb_{0.7})_{1.76}Te_3$ film. (a) Schematic of the mm-sized Hall bar structure and four-point Hall measurements based on the MBE-grown magnetic TI thin film. (b) Quantum anomalous Hall results at T = 0.26 K. The Hall resistances are quantized to be ± h/e^2 where the signs are determined by the chirality of the edge conduction. (c) Temperature-dependent magneto-resistance results. At the coercive fields, the peak of R_{xx} quickly diverges at lower temperatures. (d) Temperature-dependent R_{xx_PEAK} and R_{xy} extracted from Figs. 5-13(b) and (c). The anomalous Hall resistance R_{xy} becomes quantized up to 0.3 K, and the giant R_{xx_PEAK} resolved at 0.02 K is around 380 kΩ, the largest value obtained among all reported QAHE systems. Adopted from Ref. [172].

In the next step, we re-plot the QAHE data on the basis of conductance in Fig. 5-14 by using the reciprocal ρ - σ tensor conversion given by

$$\sigma_{xx} = \frac{\rho_{xx}}{\rho_{xx}^2 + \rho_{xy}^2}, \qquad \sigma_{xy} = \frac{\rho_{xy}}{\rho_{xx}^2 + \rho_{xy}^2} \tag{5-5}$$

Remarkably, two intermediate plateau with σ_{xy} = 0 are clearly developed at H_C = ±0.12 T when T = 0.02K. In the meantime, σ_{xx} also show two double-peaks around H_C, consistent with the theoretical prediction [165]. Here, we would like to re-capture the essence of the proposed multi-domain network model. In principle, for a 2D magnetic TI system, there are two mechanisms to open the surface state gap: one is the hybridization gap m_0 between the top and bottom surface states due to quantum confinement, and the other is the exchange field gap Δ_M introduced by the FM ordering along the z-direction [49, 165]. In the QAHE regime with $|\Delta_M| > |m_0|$, all the magnetic domains in the FM TI are aligned along the same direction, and the corresponding Chern number of the system is $C_1 = \Delta_M/|\Delta_M| = \pm 1$. Consequently, there is only one pair of edge states propagating along the sample edge with $\sigma_{xy} = C_1 \cdot e^2/h = \pm e^2/h$. On the other hand, the zero Hall plateau occurs around the coercivity field during the magnetization reversal process with the mean value of $\Delta_M \sim 0$. Accordingly, the system is transitioned into an insulating state where the first Chern number becomes C_1=0 and $\sigma_{xy} = C_1 \cdot e^2/h = 0$. Microscopically, when the applied magnetic field is around H_C, the 6 QL magnetic TI film is driven into a multi-domain structure with each microscopic magnetic domain being switched from up to down randomly, as shown in Fig. 5-14(c). When the localization length is small enough at low temperatures, the tunneling between chiral edge

states at the domain walls is suppressed, and the total conduction in the multi-domain network is thus minimized.

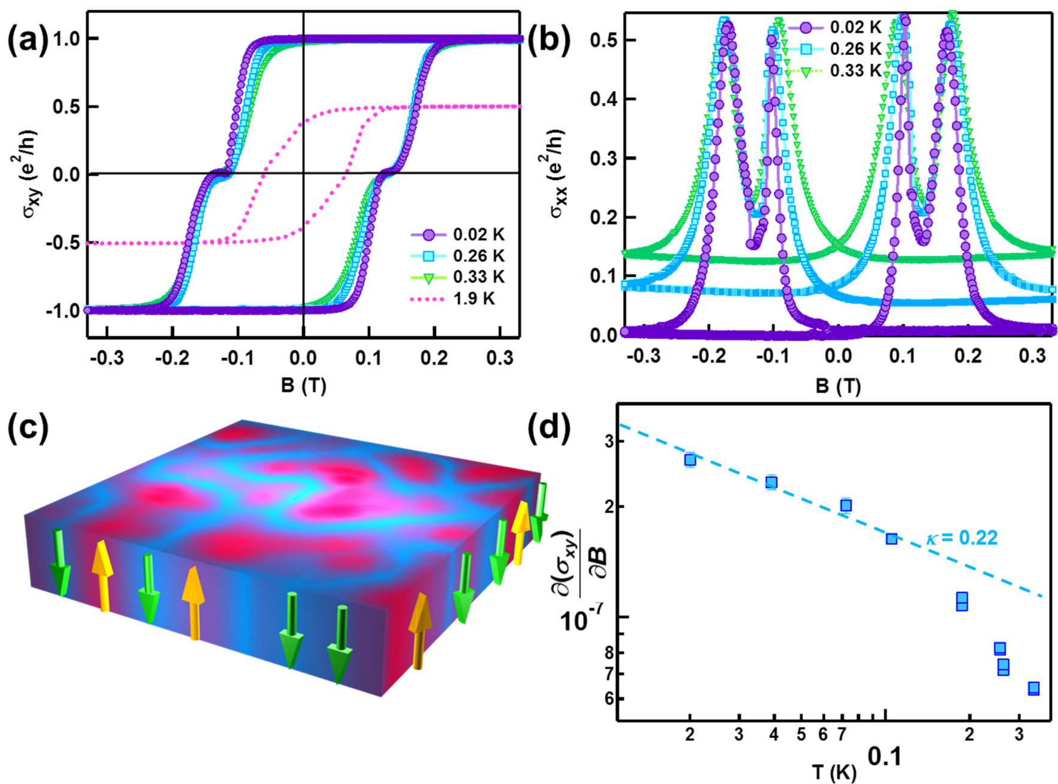

Figure 5-14. Quantum phase transition of quantum anomalous Hall effect. (a) Magnetic field dependent σ_{xy} at different temperatures. Zero Hall plateau at $\pm H_C$ are developed between the two QAHE states up to 0.33 K. (b) Magnetic field dependent σ_{xx} at different temperatures. Even when the film already deviates from the perfect QAHE state at T = 0.33 K, both the zero σ_{xy} and double-peaked σ_{xx} still persist. (c) Schematic of the multi-domain network formed during the magnetization reversal process. The upward green arrows and downward yellow arrows denote the up ($\Delta_M > |m_0|$) and down ($\Delta_M < -|m_0|$) magnetic domains. (d) Temperature-dependent transition slope $S = (\partial\sigma_{xy} / \partial H)_{\max}$ extracted from Fig. 5-14(a). When $T < 0.1$ K, $S \propto T^{-\kappa}$ follows the power low scaling behavior with $\kappa = 0.22$. Adopted from Ref. [172].

Equally important, it is noted that the insulating state in the 2D QAHE case is different from the quantum Hall insulator in conventional 2DEG systems in terms of resistivity. In particular, as $T \rightarrow 0$, the zero-Hall plateau QAHE insulator approaches ($\rho_{xx} \rightarrow \infty$, $\rho_{xy} \rightarrow 0$), while the QHE insulator exhibits ($\rho_{xx} \rightarrow \infty$, $\rho_{xy} \rightarrow \nu h/e^2$) where ν is the lowest LL filing factor [158, 163]. This is due to the differences of the band structures: for magnetic TI, the linear Dirac-cone-like surface states enable the Fermi level to be located at the Dirac point; yet for ordinary 2DEG with parabolic energy dispersion relation, no zero LL is allowed, and the minimum value of ρ_{xy} thus has to saturate at a non-zero ground quantized value of $\nu h/e^2$. Even for QHE in 2D Dirac fermion system (*i.e.,* graphene) with zeroth LL [173], the observed zero-energy state ($\rho_{xx} \rightarrow \infty$, $\rho_{xy} \rightarrow 0$) at high magnetic field [169] is microscopically different from the multi-domain network discussed above. Therefore, the magneto-conductance results of our 6 QL $Cr_{0.24}(Bi_{0.3}Sb_{0.7})_{1.76}Te_3$ film in Figs. 5-14(a) and (b) provide direct evidence of the quantum phase transition between the $C_1 = 1$ QAHE state and the $C_1 = 0$ insulating state in the massive Dirac fermion context.

Moreover, the temperature dependence of the zero Hall plateau is also investigated. Figs. 5-14(a) and (b) present the measured σ_{xy} and σ_{xx} data at several temperatures, respectively. It is seen that with increasing temperature, the zero Hall plateau near H_C gradually narrows (Fig. 5-14(a)), and the σ_{xx} double-peaks also widens at high temperatures (Fig. 5-14(b)); when the sample further warms up, both these intermediate features cannot be resolved any more at $T = 1.9$ K. As suggested by J. Wang *et al.*, temperature-dependent σ_{xy}

slope $S = (\partial\sigma_{xy} / \partial H)_{max}$ is displayed in Fig. 5-14(d) to study the scaling behavior of the QAHE plateau transition. Although S is found to monotonically decrease versus temperature, we should point out that there are some quantitative differences between the theoretical proposal and our experimental results. First, unlike the simulation results [165], both zero σ_{xy} plateau and double-split σ_{xx} persist even when the system has already deviated from the perfect quantization case at 0.33 K (σ_{xy} = 0.992 e^2/h and σ_{xx} picks up a relative large background signal of 0.127 e^2/h). Second, the temperature–dependence of S seems not to follow the predicted simple $S \propto T^{-\kappa}$ relation in the entire temperature range (0.02 K to 0.33 K); yet when $T < 0.1$K, the power law scaling is fitted quite well with $\kappa = 0.22$, which is just one half of $\kappa = 0.42$ measured in the QHE transition [160]. The possible reasons for the above differences may be due to the fact that the coercivity shifts when 0.1K < T < 0.33 K compared to T < 0.1 K (Fig. 5-15(b)), and extra thermally activated bulk carriers would also contribute to the transport (*i.e.,* R_{xx} increases dramatically when T > 0.1K, as highlighted in the Inset of Fig. 5-15(a)) [168], therefore complicating the slope of σ_{xy} in the high temperature regime.

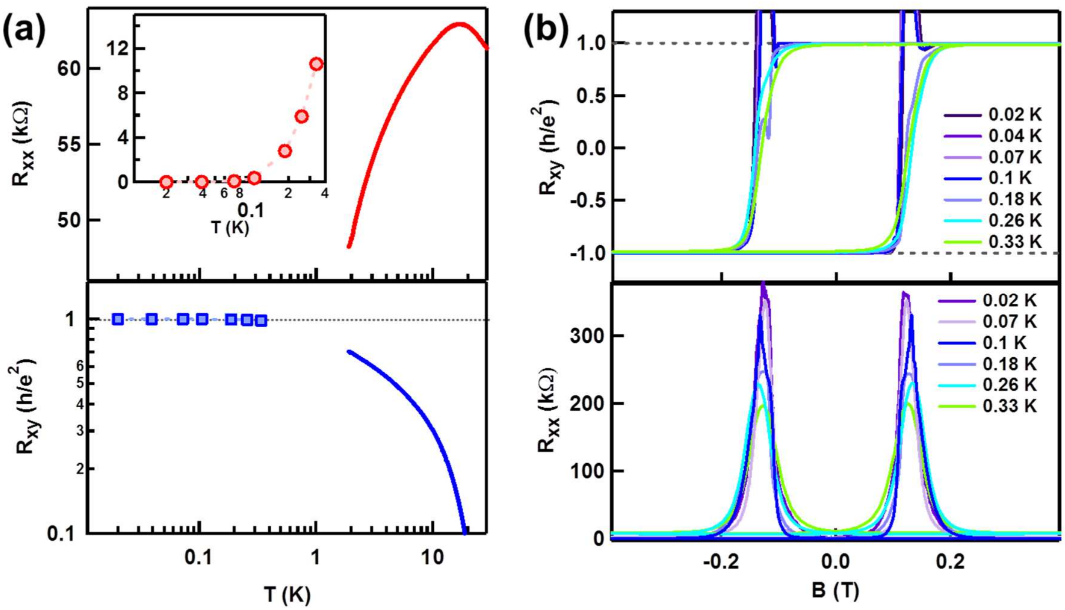

Figure 5-15. Temperature-dependent magneto-transport results of the 6 QL $Cr_{0.24}(Bi_{0.3}Sb_{0.7})_{1.76}Te_3$ film. (a) Temperature-dependent R_{xx} and R_{xy} at low temperatures. When T < 15 K, R_{xx}(1T) starts to decrease, and the R_{xy} - T curve follows a single power law behavior. (b) The complete magneto-transport data of R_{xy} and R_{xx} for the 6 QL $Cr_{0.24}(Bi_{0.3}Sb_{0.7})_{1.76}Te_3$ film. Adopted from Ref. [172].

5.8. Mapping the semicircle QAHE phase diagram

In light of the importance of QAHE phase transition, we further performed the angle-dependent measurements. In Section 3.5, we have shown the Cr-doped $(BiSb)_2Te_3$ thin films develop robust out-of-plane FM order in the QAHE regime. If the applied magnetic field is not perfectly perpendicular to the film, the induced in-plane magnetic component would tilt the Cr magnetization, and thereby helps to modulate the strength of Δ_M as well. Figures 5-16(a) and (b) show the magneto-transport results of the 6 QL $Cr_{0.24}(Bi_{0.3}Sb_{0.7})_{1.76}Te_3$ film as the tilted angle θ of the Hall-bar device with respect to the

magnetic field is varied from 90° (out-of-plane) to 180° (in-plane). It is observed that with small magnetic field sweeping (-0.5 T < B < 0.5 T) at T = 0.02 K, the quantization of R_{xy} is relatively robust as long as θ < 150° (in terms of conductance plot, both zero-Hall plateau and double-peaked σ_{xx} persist in such angle range, as illustrated in Fig. 5-17). On the other hand, as both B and θ increase, the system starts to deviate from the QAHE state. In the extreme case when the film is rotated almost parallel with the magnetic field (θ = 180° ± 5°), the measured in-plane magneto-resistance reflects a rather insulating feature: the corresponding dashed purple curve in Fig. 16(b) strongly suggests the system is rapidly approaching toward an angle-induced insulating state with R_{xx} > 400 kΩ. Note that due to the giant perpendicular anisotropy in the Cr-doped TI systems, out-of-plane magnetic domains might still be formed in this case when θ ~ 180° [60, 174].

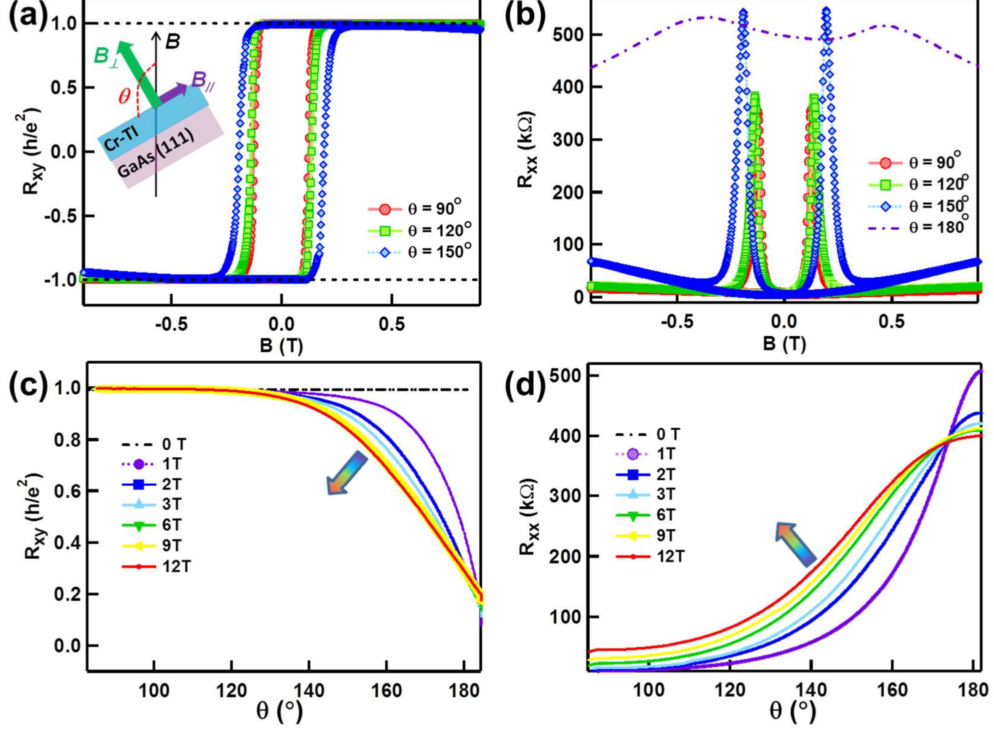

Figure 5-16. Angle-dependent transport measurements in the quantum anomalous Hall regime. (a) Quantum anomalous Hall results when the 6 QL magnetic TI film is rotated to θ = 90°, 120°, and 150°, respectively. The external magnetic field is swept between -1 T and +1 T. The sample temperature is 0.02 K. (b) Magneto-resistance results of the sample under different tilted angle θ at T = 0.02 K. The film enters the QAHE insulating state when it is rotated parallel to B. Angle-dependent (c) R_{xy} and (d) R_{xx} under different fixed B at T = 0.02 K. All curves tend to converge at two critical points at (R_{xx}, R_{xy}) = (0, h/e^2) and (~15 h/e^2, 0). Adopted from Ref. [172].

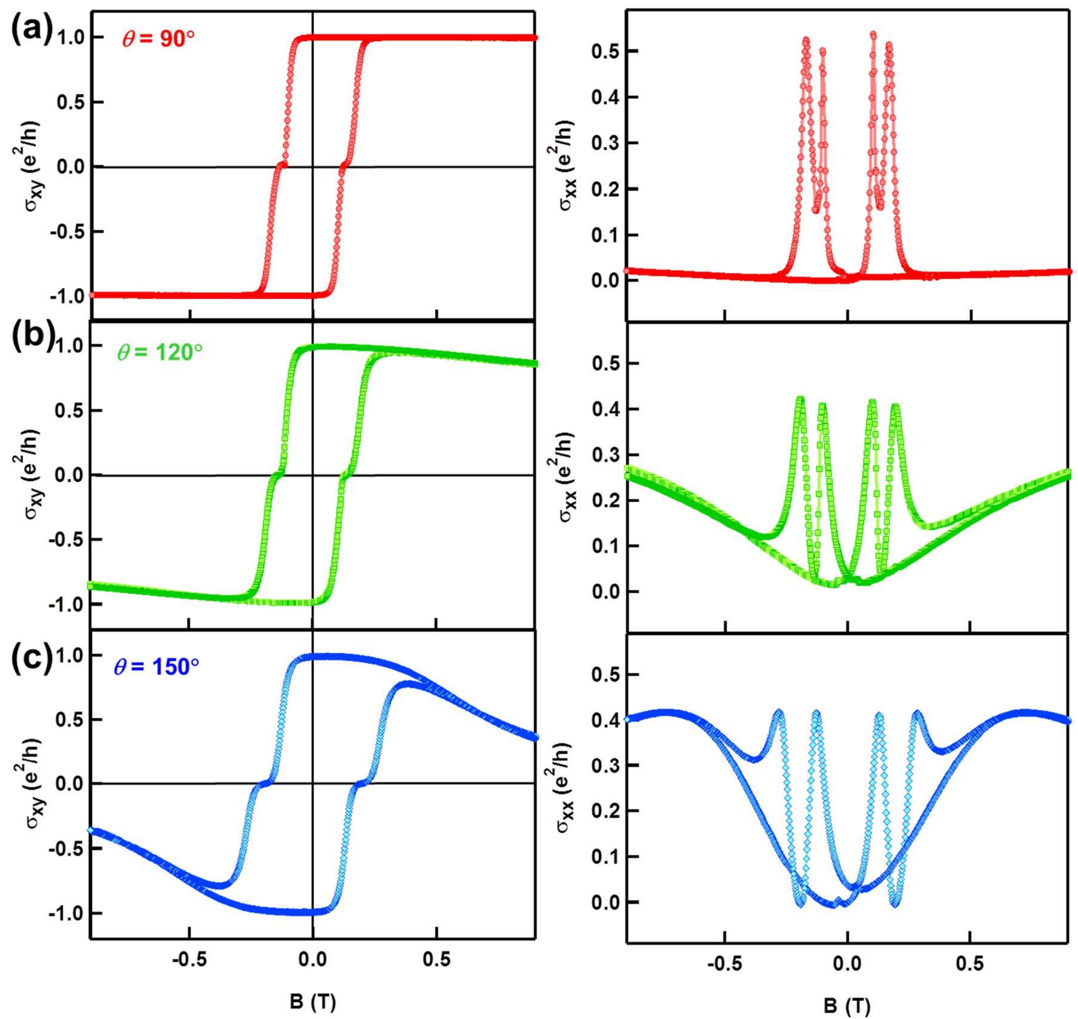

Figure 5-17. Angle-dependent magneto-conductance (left-σ_{xy} and right-σ_{xx}) results of the 6 QL $Cr_{0.24}(Bi_{0.3}Sb_{0.7})_{1.76}Te_3$ film in the QAHE regime. (a) θ = 90° (same as Figs. 5-14(a) and (b)), (b) θ = 120°, and (c) θ = 150°. Corresponding magneto-resistance results are

shown in Figs. 5-16(a) and (b). The hysteresis σ_{xy} curves at all these three tilted angles develop the zero Hall plateau feature, and σ_{xx} show the double-split peaks as well.

A more detailed experiment is carried out subsequently that both R_{xx} and R_{xy} are recorded when the 6 QL magnetic TI film is continuously rotated from 90° to 180°, under different fixed applied magnetic fields. From Figs. 5-16(c) and (d), it is clear that the system undergoes the smooth quantum phase transition with respect to θ. Most importantly, we find that both R_{xx} and R_{xy} curves for $B \geq 1$ T tend to converge at critical points [R_{xx}(90°) = 0, R_{xx}(180°) ~ 15 h/e^2] and [R_{xy}(90°) = h/e^2, R_{xy}(180°) = 0], while different magnetic fields only modulate the transition process in between: R_{xy} rolls off the h/e^{2}quantization line more quickly and the divergence of R_{xx} occurs at smaller θ when B increases.

We can further visualize the angle-assisted QAHE phase transition in Fig. 5-18. Significantly, when displayed in the σ_{xy} - σ_{xx} plot, all θ-dependent curves for B ≥ 1T, which have been manually shifted vertically by (B-1)×0.1e^2/h for comparison in Fig. 5-18(a), follow a single continuous semicircle which is centered at (σ_{xx}, σ_{xy}) = (0, e^2/2h) with the radius of e^2/2h. Meanwhile, another interesting finding in Figs. 5-18(a) and (b) is the importance of the in-plane magnetic field $B_{//} = B\cdot\cos\theta$ on the universal QAHE phase diagram. If we divide the conductance semicircle into three angle regions (red dots for [90°, 120°], green dots for [90°, 150°], and blue dots for [150°, 180°]), and track the evolutions of each component versus the applied magnetic field, we see that it is the strength of $B_{//}$ rather than the $B_{//}$ / $B_{\perp}$ ratio that determines the QAHE phase transition. As highlighted by the dashed curves in Fig. 3-18(a), it

is evident that even $B_{//} / B_{\perp} = \tan^{-1}\theta$ is always smaller than 1 within [90°, 120°], the in-plane $B_{//}$ under high magnetic fields (B > 1T) still manage to force the conduction deviate from the dissipationless (0, h/e^2) point, and such spread-out trend becomes more pronounced with increased B (and thus $B_{//}$). In contrast, as long as the total magnetic field B is smaller than the critical magnetic field (B_0 ~ 1 T), the semicircle phase transition cannot be completed even when θ = 180° ($B_{//,max} = B$), as manifested in the upper panel of Fig. 5-18(b). Finally, by combining both the field-dependent results of Fig. 5-14 and the angle-dependent data of Fig. 5-18(a) (θ ⊆ [90°, 270°], B = 1 T) together in the σ_{xy} - σ_{xx} plot, we produce a single semicircle curve in Fig. 5-18(c), illustrating the similar QAHE phase transition feature between the C_1 = 0 zero Hall plateau state and the two C_1 = ± 1 QAHE states. Given that the scaling rule of localization in the multi-domain configuration is temperature-dependent [165], the deviation from the two QAHE-characterized (0, 0) and (0, e^2/h) points is indeed found to become more obvious with increasing T, as shown in Fig. 5-18(d).

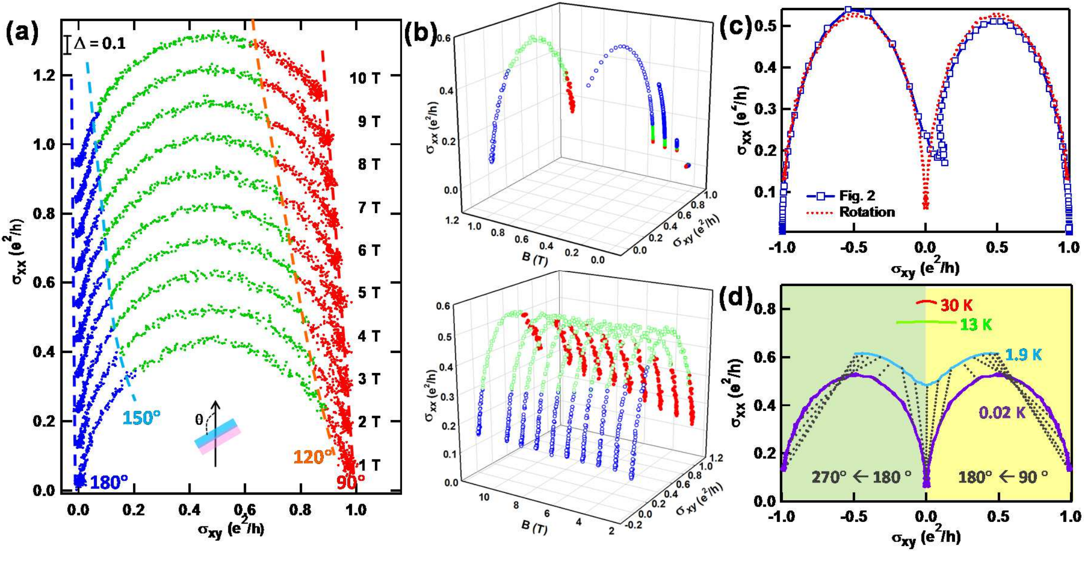

Figure 5-18. Universal phase diagram of quantum anomalous Hall effect in the 2D regime. (a) Angle-assisted QAHE phase transition in the (σ_{xx}, σ_{xy}) plot. The data are extracted from Figs. 5-16(c) and (d). The 6 QL Cr-doped TI film is continuously rotated from 90°(out-of-plane) to 180° (in-plane) with respect to the applied magnetic field direction. All curves overlap with each other following the single semicircle relation. Data are shifted vertically by (B-1)×0.1e^2/h for convenient comparison. (b) Magnetic field dependent QAHE phase diagram in the 3D plot. When $B_{//}$ < 0.5 T, the semicircle transition cannot be completed. (c) Compare the field-dependent results in Fig. 5-14 with the angle-dependent data in Fig. 5-18(a) ($\theta \subseteq$ [90°, 270°] and B = 1 T). Identical QAHE phase transition between the C_I = 0 insulating state and the two C_I = ± 1 QAHE states is manifested. (d) Temperature-dependent (σ_{xx}, σ_{xy}) plot. As T increases, the intrinsic localization scaling rule diverts the system from the original QAHE and insulating states. The dotted lines link the data points with the same angles ($\theta \subseteq$ [90°, 270°] with each step of 10°) between 0.02 K and 1.9 K. Adopted from Ref. [172].

Compared with the universal QAHE phase diagram, it is found that, similar conductance semicircles have been extensively investigated to describe the global phase diagram of QHE [156-159], yet we emphasize here that the microscopic physics between the QHE and QAHE phase transitions are different. Specifically speaking, the QHE phase diagram is closely related to the LL quantization. The corresponding quantum Hall plateau transitions happen when the Fermi level across mobility edges, which are due to disorder-induced localization-delocalization transitions [157]. Concurrently, the quantum Hall insulator is achieved when the applied $B_{\perp}$ is large enough to drive the ground LL overlaps with E_F [163, 164]. On the contrary, in the QAHE state, the zero quantized Hall plateau is the result of the multi-domain formation and a network of chiral edge states at domain walls during the magnetization reversal process [165]. As a result, the phase transition to the zero Hall plateau state in the QAHE regime can be obtained at a much

smaller magnetic field, as addressed in Figs. 5-14 and 5-18. Furthermore, since the first Chern number in the QAHE state is determined by the competition between magnetic exchange gap and hybridization gap [165], it is thus suggested that in 3D magnetic TIs where higher subbands may participate into the band topology transition [120], new QAHE phases with tunable C_1 are expected, and relevant phase transition can thus be further modulated by film thickness.

5.9. Summary of Chapter 5

In this chapter, we investigate the chiral transport of the QAHE state and its related quantum phase transition in the millimeter-size $Cr_{0.24}(Bi_{0.3}Sb_{0.7})_{1.76}Te_3$ films. Due to the high sample quality achieved by the non-equilibrium MBE growth and robust magnetism at low temperatures, the quantized Hall conductance of e^2/h is found to persist even when the film thickness varies across 2D hybridization limit (from 6 QL to 10 QL). The robust dissipationless chiral edge states at zero magnetic field not only reflect the unique quantum transport character of the QAHE, but also reveal the distinctions between QAHE and the other two quantum phases (QHE and QSHE): particularly, both large spin-orbit coupling and magnetic exchange interaction enable the quantized edge transport beyond 2D limit without invoking the formation of LLs (different from QHE), and the chirality makes the dissipationless conduction be immune to any de-coherence (in contrast to QSHE).

Surprisingly, for the 10 QL $Cr_{0.24}(Bi_{0.3}Sb_{0.7})_{1.76}Te_3$ sample, a non-zero longitudinal resistance is detected and it is found to be insensitive to external magnetic fields, suggesting the influence of the film thickness on the dissipative edge channel in the QAHE regime. Non-local transport measurements are further performed and the results indicate the possible presence of the non-chiral side surface propagation modes. The extension of QAHE into the three-dimensional thickness region addresses the universality of this quantum transport phenomenon and motivates the exploration of new QAHE phases with tunable Chern numbers. In addition, the observation of the scale-invariant dissipationless chiral propagation on a macroscopic scale makes a major stride towards ideal low-power interconnect applications.

On the other hand, when additional quantum confinement is introduced, we report the experimental observation of the metal-to-insulator switching between two opposite QAHE plateau states in the 6 QL $Cr_{0.24}(Bi_{0.3}Sb_{0.7})_{1.76}Te_3$ film. Owing to the highly insulating bulk state, we observe the giant longitudinal resistance peak and zero Hall conductance plateau at the coercivity field up to 0.3 K, and they manifest the presence of the quantum anomalous Hall insulating state within the magnetic multi-domain network context. Moreover, by studying the angle-dependent quantum transport behaviors, the 2D massive Dirac fermion-featured QAHE phase diagram is mapped out to show that the QAHE state with the first Chern number $C_1 = 1$ is transitioned into the $C_1 = 0$ insulating state, and the conductance tensor (σ_{xx}, σ_{xy}) follows a universal semicircle relation, regardless of the applied magnetic

field strength. Our results address that the quantum phase transitions in both QAHE and QHE regimes are in the same universality class, yet the microscopic details are different. In addition, the realization of the quantum anomalous Hall insulator from both the field-driven and angle-dependent methods at small magnetic fields unveils new ways to explore quantum phase-related physics and applications.

Chapter 6

Surface-related Ferromagnetism and Giant Spin-Orbit Torques in Magnetic Topological Insulator Heterostructures

Till now, all the experiments in Chapters 3-5 are based on the uniformly-doped magnetic TI systems. In fact, as we showed in Fig. 1-7(a), the functionalities of TRS-breaking physics and applications can be further enhanced if additional structural engineering is introduced. For example, it is noted that since the magnetic dopants distribute homogeneously inside uniform magnetic TI thin films, it is thus difficult to quantify the surface-related magnetism from the total signals (which contain the bulk, top and bottom surfaces). Alternatively, if the TI surface states are well-separated from the bulk magnetic ions, the Dirac-fermion-related magnetism can be easily distinguished. In the meanwhile, the integration of both TIs and magnetic TIs into the single heterostructures will enable us to better manipulate the band topology as well as the magnetic exchange coupling. Therefore, in this chapter, we would like to describe how we utilize the advantage of MBE to prepare the TI/Cr-doped TI bilayer samples, and investigate both the surface-related magneto-electric responses and giant spin-orbit torques in such heterostructures.

6.1. TI/Cr-doped TI heterostructures by MBE

To investigate the interaction between the magnetic impurities and surface Dirac carriers in magnetically doped TIs, high quality Cr-doped $(Bi_xSb_{1-x})_2Te_3$ thin films are first prepared using MBE. In contrast to the conventional uniform doping method, we use a modulation-doped method to produce the $(Bi_xSb_{1-x})_2Te_3$ /$Cr_Z(Bi_ySb_{1-y})_{2-Z}Te_3$ bilayer films by accurately controlling the Cr-dopant distribution profiles along the epitaxial growth direction [175-177]. The schematic layout and corresponding energy band diagram of such bilayer structures are shown in Fig. 6-1(a). During the sample growth, we use real-time RHEED to *in-situ* monitor the growth dynamics. Specifically, sharp streaky lines with the bright specular spot persist the entire growth period, indicating a smooth 2D growth mode. In the meanwhile, by counting the RHEED oscillations displayed in Fig. 6-1(b), we are able to control the thickness of both the Cr-doped TI and pure TI layers with high accuracy (*i.e.,* deviation < ±0.1 nm compared with the designed value). Crystalline structure characterization is performed using HRSTEM. Figure 6-1(c) reveals the atomically sharp TI – GaAs interface and highly-ordered tetradymite-type QL structure. Such epitaxially-ordered lattice configuration also confirms that there is no second phase segregation inside the TI thin film within the resolution of HRSTEM. In addition, the Bi/Sb composition ratio (*x, y*) and the Cr doping level are determined by the EDX spectroscopy as shown in Fig. 6-1(d). In contrast to the lower figure, the absence of the Cr peak in the upper EDX spectrum provides strong

evidence that the Cr atoms only distribute inside the bottom 6 QL $Cr_{0.08}(Bi_{0.59}Sb_{0.41})_{1.92}Te_3$ layer, while the top 3 QL layer is free of magnetic impurities.

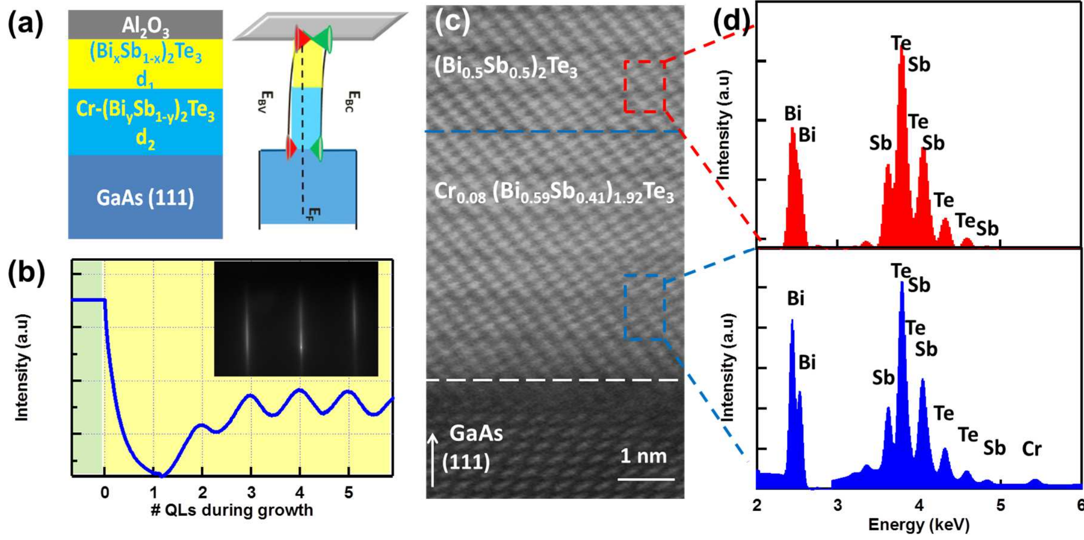

Figure 6-1. Modulation-doped $(Bi_xSb_{1-x})_2Te_3$ / $Cr_z(Bi_ySb_{1-y})_{2-z}Te_3$ bilayer structure. (a) Schematic layout and energy band diagram for the bi-layer device consisting of one $(Bi_xSb_{1-x})_2Te_3$ layer on top of another $Cr_z(Bi_ySb_{1-y})_{2-z}Te_3$ layer. The composition ratio of *x*, *y*, and *z* is carefully chosen so that the two channels have similar low conductivities and bulk carrier densities. (b) RHEED oscillations used to monitor the growth conditions and control the thin film thickness. Inset: A streaky RHEED pattern along the $[11\bar{2}0]$ direction of the as-grown surface that indicates a 2D growth mode. (c) HRSTEM image of the bilayer thin film. Typical quintuple-layered crystalline structure and sharp TI – GaAs interface can be clearly observed. No Cr segregations are detected, which indicates a uniform Cr distribution in the magnetic TI material matrix. (d) EDX spectrum of $(Bi_{0.5}Sb_{0.5})_2Te_3$ and $Cr_{0.08}(Bi_{0.59}Sb_{0.41})_{1.92}Te_3$ layers. Adopted from Ref. [145].

We have demonstrated in previous chapters that a moderate Cr doping of about 10% is sufficient enough to force the Dirac-cone-like surface open the band gap. In this study, to ensure a solid comparison, all of the modulation-doped TI bilayer samples we prepare have

identical $Cr_{0.16}(Bi_{0.59}Sb_{0.41})_{1.84}Te_3$ bottom layers with the same film thickness of 6 QL, Bi/Sb ratio of 0.59/0.41, and the Cr doping concentration of 8%. Figure 6-2(a) displays the RHEED parameters in all TI/Cr-doped TI samples. The change of *d*-spacing values from initial GaAs (111)B surface has a little variation, and same RHEED oscillation periods are observed, both of which well-demonstrate the consistency of our MBE-grown thin films. In addition, Fig. 6-2(b) illustrates the AHE results of the three modulation-doped TI samples used in the following MOKE measurements: Sample **A** has a 6 QL $Cr_{0.16}(Bi_{0.59}Sb_{0.41})_{1.84}Te_3$ with a uniform Cr-doping profile, and it serves as the control sample; Sample **B** and Sample **C** share the same 6 QL $Cr_{0.16}(Bi_{0.59}Sb_{0.41})_{1.84}Te_3$ designs in the bottom, but differ in the top undoped $(Bi_{0.5}Sb_{0.5})_2Te_3$ layer thickness, namely d_l = 3QL for Sample **B** and d_l = 6 QL for Sample **C**. By extracting the linear slopes from the R_{xy} curves at high magnetic field, we observe nearly the same Hall densities at 2.8 K, namely 4.01×10^{12} cm^{-2} for Sample **A**, 3.89×10^{12} cm^{-2} for Sample **B**, and 3.73×10^{12} cm^{-2} for Sample **C**. Consequently, both the RHEED and magneto-transport measurements confirm the reliability of the descriptions and comparisons in this chapter.

As for the top undoped TI layers in these samples, we adjust the Bi/Sb ratio to be 0.5/0.5 so that the electrical conductivity is similar to that of the bottom $Cr_{0.16}(Bi_{0.59}Sb_{0.41})_{1.84}Te_3$ layer (*i.e.,* the current density is uniform in the heterostructures to avoid any shunting effect), as shown in Figs. 6-2(c) and (d). More importantly, the low densities obtained in both layers further ensure that the Fermi level E_F locates well-inside the bulk band-gap, therefore

minimizing the bulk conduction in the following electric-field-controlled transport measurements.

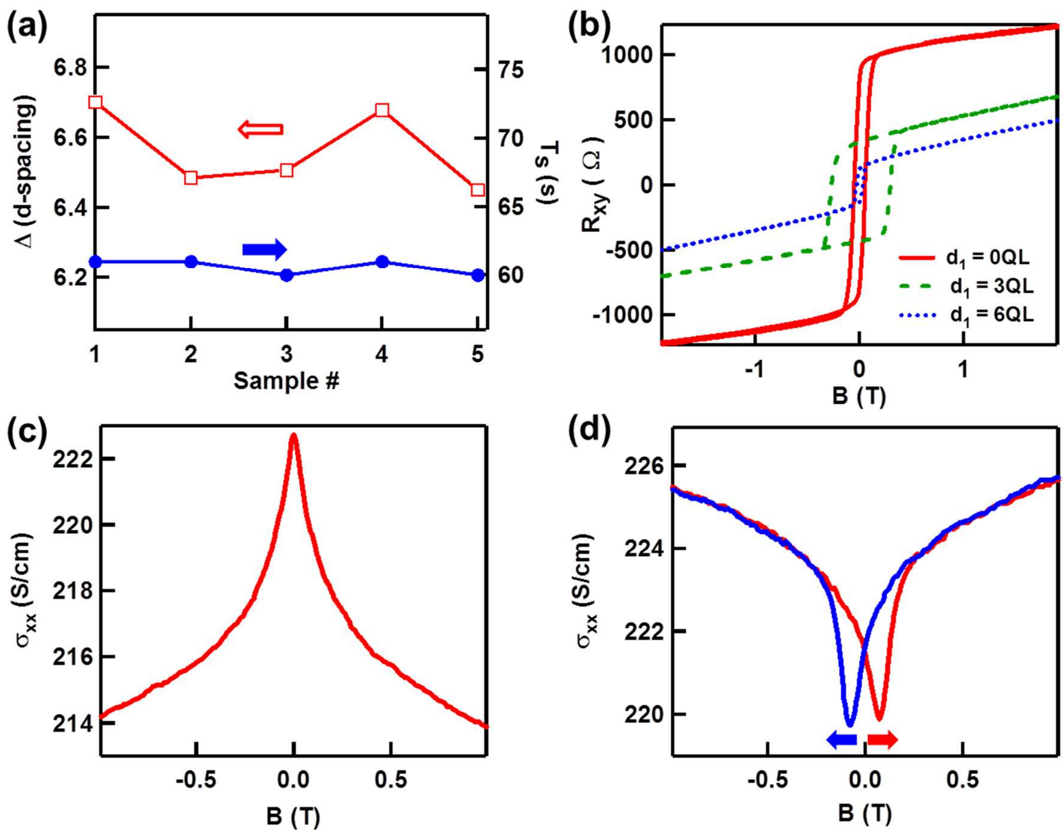

Figure 6-2. Optimization of the TI/Cr-doped TI bilayer structures. (a) Comparisons of *d*-spacing change as well as growth rate among the bottom Cr-doped layer of several modulation-doped samples. (b) AHE results of the three TI/Cr-doped TI samples used in the following MOKE experiments. Magneto-conductance data showing similar conductance for the (c) 6 QL $(Bi_{0.5}Sb_{0.5})_2Te_3$ and (d) 6 QL $Cr_{0.16}(Bi_{0.59}Sb_{0.41})_{1.84}Te_3$ thin films on GaAs (111)B substrate at 1.9 K. The external magnetic field is applied perpendicular to the samples, and the arrows indicate the sweeping directions of the field. Adopted from Ref. [145].

6.2. Polar-mode MOKE measurements

The main objective of the following sections is to investigate the surface-related magnetism in the modulation-doped TI heterostructures. We first perform the MOKE

measurement since it offers a straightforward quantification of the magnetizations. The MOKE measurement is based on the magneto-optic Kerr effect, which uses the elliptical polarized reflected light to probe the magnetic property of materials. Arising from the out-of-plane magnetic anisotropy in the Cr-doped TI systems, polar geometry MOKE mode is used in our experiments, as shown in Fig. 6-3. Moreover, since the FM order in our Cr-doped TI sample can only be formed below 20 K, we thus integrate the MOKE system with additional temperature-controlled cryostats to carry out the low-temperature measurements (*i.e.,* down to 2.8 K with liquid helium cooling and good vacuum).

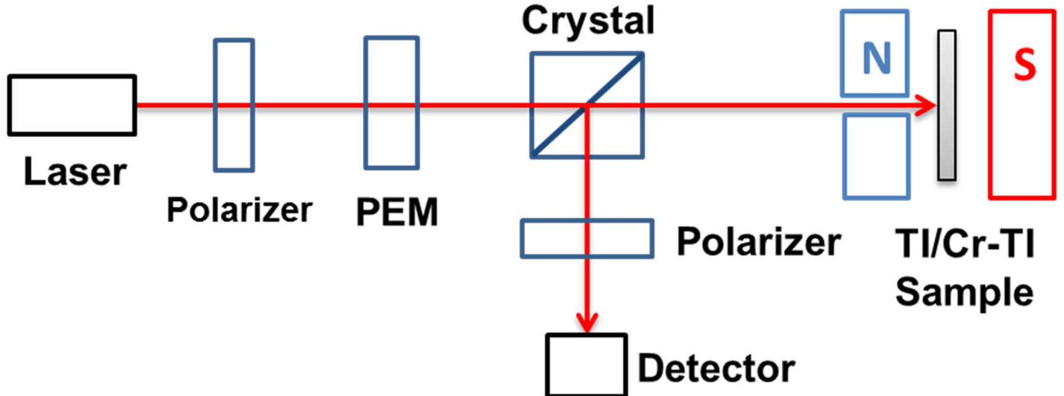

Figure 6-3. Schematic optical bench setup of the polar MOKE measurement. Adopted from Ref. [145].

In the MOKE measurements, a standard 633 nm helium-neon laser is used as the light source. In order to estimate the penetration depth of such light, we first apply the generic Maxwell Equations as

$$\begin{cases} \nabla \times \vec{E} = -\mu\mu_0 \dfrac{\partial \vec{H}}{\partial t}, & \nabla \cdot \varepsilon_0 \vec{E} = \rho \\ \nabla \times \vec{H} = \sigma \cdot \vec{E} + \varepsilon\varepsilon_0 \dfrac{\partial \vec{E}}{\partial t}, & \nabla \cdot \vec{H} = 0 \end{cases} \tag{6-1}$$

where ε, σ, and μ are the permittivity, conductivity, and magnetic permittivity of a continuous, infinite and isotropic media, respectively. Under an AC excitation, the electric field in the TI thin film is in the form of $E = E_0 \exp[i\omega(\frac{n}{c}z - t)]$, where the refractive index is given by

$$\frac{\omega^2 n^2}{c^2} = \omega\mu\mu_0(i\sigma + \omega\varepsilon\varepsilon_0) \tag{6-2}$$

By solving the AC Drude model combined with Eq. (6-2), we can obtain both the real and imaginary parts as

$$\begin{cases} n^2 = \dfrac{1}{2}\{[1 + (\dfrac{\sigma}{\omega\varepsilon\varepsilon_0})^{1/2}] + 1\} \\ \kappa^2 = \dfrac{1}{2}\{[1 + (\dfrac{\sigma}{\omega\varepsilon\varepsilon_0})^{1/2}] - 1]\} \end{cases} \tag{6-3}$$

Under the Taylor expansion approximation, we further obtain the absorption coefficient $\alpha = 4\pi\kappa / \lambda_0$. By substituting Eq. (6-2) with measured parameters of the $(Bi_{0.5}Sb_{0.5})_2Te_3$ material, we finally get the penetration depth (d_p) of 340 nm at room-temperature, and reduces to 46 nm at low temperature. Accordingly, the MOKE signals reflect the overall magnetization of the whole TI/Cr-doped TI bilayer sample (which has the film thickness around 10 nm).

Figure 6-4 shows the field-dependent MOKE results of Samples **A**, **B**, and **C** at different temperatures (the sample descriptions are given in Section 6.1). All of these three samples display nearly square-shaped ferromagnetic hysteresis loops at low temperatures, suggesting the robust ferromagnetic order with the easy axis perpendicular to these thin films. However, the magnitudes of their MOKE signals are dramatically different. On the one hand, when the top layer thickness d_I is 3 QL, the coercivity field H_C at T = 2.8 K has enlarged by more than 5 times (*i.e.,* from 4.5 mT to 30 mT) compared with the control sample. On the other hand, H_C does not change monotonically with d_I. Instead, when the top surface is 6 QL away from the bottom layer, we observe the minimum H_C of only 2.5 mT. Similarly, if we extract the Curie temperature T_C from the H_C - T curves in Figs. 6-4(d) – (f), we have the highest T_C (10.9 K) for Sample **B**, compared with 7.4 K and 6.9 K in Samples **A** and **C**, respectively. Here, since the identical bottom Cr-doped TI layers of the three samples contribute the same "bulk" magnetization, the change of both H_C and T_C among them hence can only be associated with the separation between the top surface and the bulk Cr ions. Therefore, both the unique d_I-dependent magnetization behavior and the enhancement of T_C in Sample **B** may provide us with the direct evidence about the presence of the surface-related ferromagnetism in modulation-doped TI thin films.

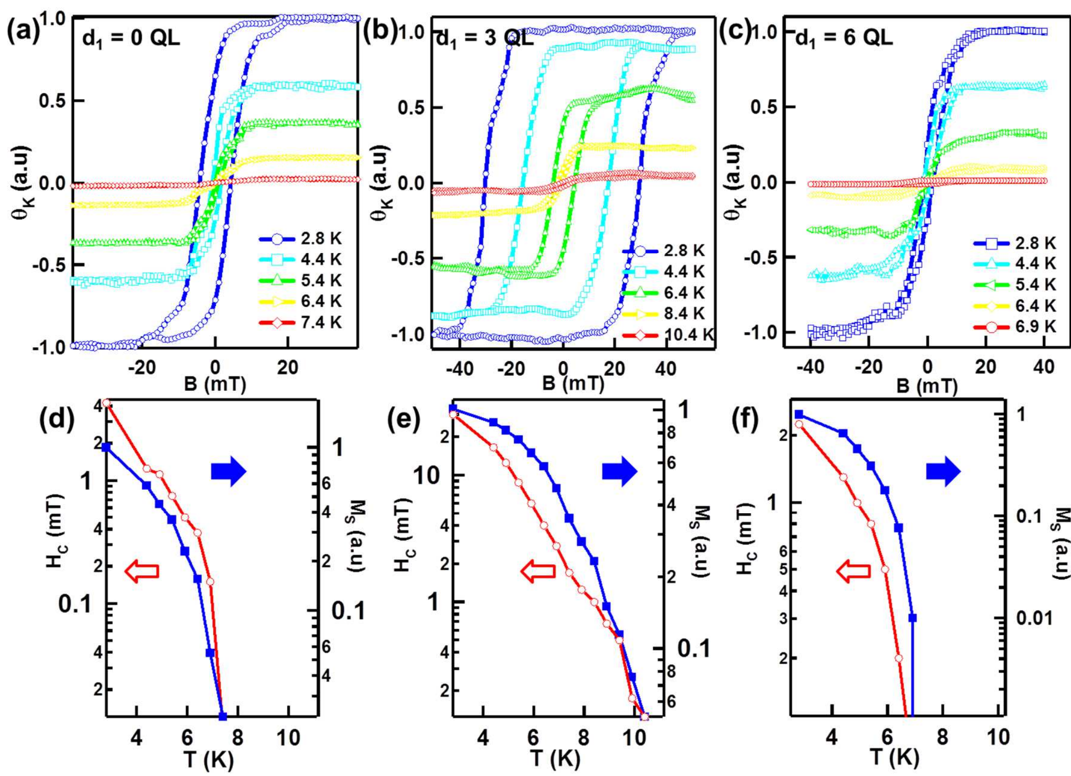

Figure 6-4. Temperature-dependent magnetization MOKE measurement. (a)-(c) Out-of-plane *M-H* hysteresis loops of Samples **A**, **B**, and **C** measured by the polar-mode MOKE setup. All of the modulation-doped samples have the same 6 QL $Cr_{0.16}(Bi_{0.59}Sb_{0.41})_{1.84}Te_3$ bottom layer, with different top layer thicknesses (0QL, 3QL, and 6QL). The largest magnetization is produced in the 3 QL TI / 6 QL Cr-doped TI structure. (d)-(f) The extraction of the saturated magnetization M_s and coercivity field H_C from MOKE measurements. Adopted Ref. [145].

6.3. Surface-related ferromagnetism in TI/Cr-doped TI heterostructures

To further investigate the intrinsic mechanism of the surface-related magnetic response, we fabricate μm-size top-gated Hall bar devices to carry out the electric-field-controlled magneto-transport measurements on the modulation-doped TI heterostructures. Due to the

low defects achieved in the growth, the electric field provided by top gate (±12 V) can tune the E_F across the Dirac point, and the characteristic ambipolar field effects are observed in all the five low-carrier-density samples where both the carrier type and carrier density are well-controlled, as presented in Figs. 6-5(a) - (e). Therefore, with the effective gate tuning, we are able to fully investigate the topological surface-related magnetism under different carrier-mediated conditions.

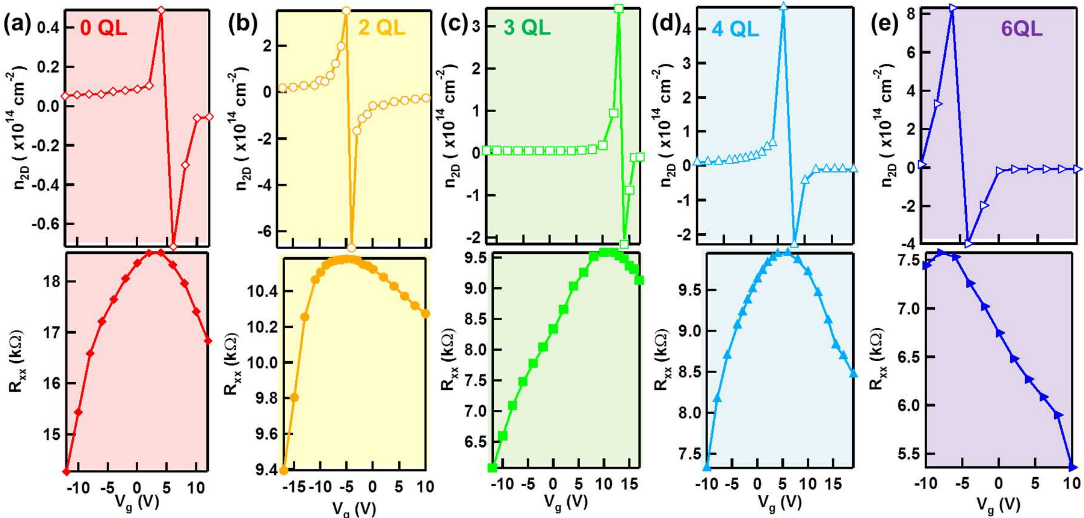

Figure 6-5. Ambipolar effects and gate-modulations in TI/Cr-doped TI samples. All samples have the same 6 QL $Cr_{0.16}(Bi_{0.59}Sb_{0.41})_{1.84}Te_3$ bottom layer while the thicknesses of top $(Bi_{0.5}Sb_{0.5})_2Te_3$ films are chosen as (a) 0 QL, (b) 2 QL, (c) 3 QL, (d) 4 QL, and (e) 6 QL, respectively. The measurements are performed at 1.9 K. Adopted from Ref. [145].

Figures 6-6(a) – (d) present the top-gate-dependent AHE results in four $(Bi_{0.5}Sb_{0.5})_2Te_3$ / $Cr_{0.16}(Bi_{0.59}Sb_{0.41})_{1.84}Te_3$ bilayer films with different top TI layer thicknesses: d_I = 2 QL, 3QL, 4QL, and 6QL, respectively. When d_I is below 6 QL, the hysteresis R_{xy} loops in Figs

6-6(a) – (c) all exhibit a typical hole-mediated RKKY coupling feature in the *p*-type region, where the magnetic hysteresis window gradually shrinks as the holes are depleted by the increase of V_g. Similar to the MOKE data in Fig. 6-4, it is also interesting to observe that the AHE signal (in terms of H_C) is most enhanced when d_I = 3 QL. On the other hand, when the top layer thickness is further increased to d_I = 6 QL, the electric-field has no effect on the AHE signal at all, and H_C remains at 20 mT for all applied V_g, as shown in Fig. 6-6(d). Apart from the d_I-dependent AHE measurements, information regarding novel magneto-electric effects is also obtained from the MR results. Figs 6-6(e) – (h) provide three-dimensional normalized MR maps as a function of applied V_g for the same samples as shown in Figs. 6-6(a) – (d). Conventional butterfly-shaped double-split MR peaks are observed, and the peak positions that deviate from B = 0 T directly indicate the remnant field generated by the ferromagnetic moments. In agreement with the AHE observations, the tunability of the MR peak position by external electric-field depends on the top layer thickness d_I, and the separation of the split peaks reaches the maximum value (*i.e.,* 140 mT in Fig. 6-6(f)) in the "optimized" d_I = 3 QL sample. More importantly, as long as d_I < 6 QL, the MR curves always display a WL effect, where the conduction of the surface carriers is affected by the underneath Cr impurities and the corresponding destructive quantum interference in turn gives rise to the negative MR cusps at low magnetic field [57, 148]. On the contrary, the development of the negative weak WAL cusp around zero magnetic field becomes pronounced only when d_I increases to 6 QL (Fig. 6-6(h)). Together with the gate-insensitive

hysteresis behaviors, the d_1-dependent WL-to-WAL crossover may imply that the re-appearance of massless Dirac-fermions on the top surface given that the separation d_1 is large enough to prevent strong magnetic coupling from the underlying magnetic impurities [178, 179].

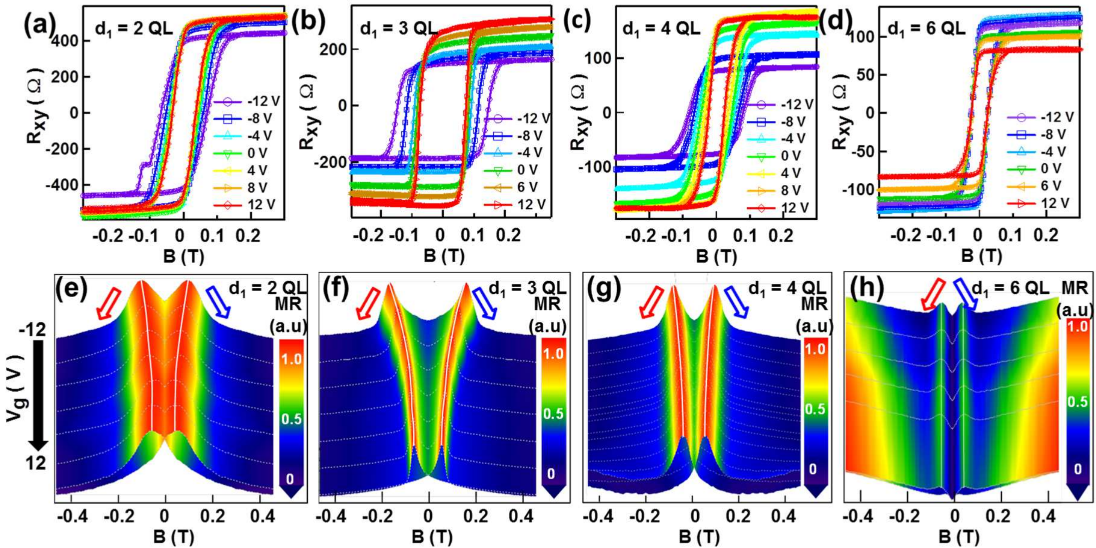

Figure 6-6. Surface-mediated magneto-electric effects in TI/Cr-doped TI bilayers. (a)-(d) Gate-dependent anomalous Hall effects on top-gated $(Bi_{0.5}Sb_{0.5})_2Te_3$ / $Cr_{0.16}(Bi_{0.59}Sb_{0.41})_{1.84}Te_3$ bilayer structures. The bottom layer thickness is fixed as 6 QL, and the top layer thickness d_1 is selected from 2 QL, 3 QL, 4 QL, and 6 QL, respectively. The surface-related magneto-electric effect becomes most significant when d_1 = 3 QL, and disappears once $d_1 \geq 6$ QL. All of the data are collected at T = 1.9 K. (e)-(h) Electric-field-controlled longitudinal magneto-resistance MR on top-gated $(Bi_{0.5}Sb_{0.5})_2Te_3$ / $Cr_{0.16}(Bi_{0.59}Sb_{0.41})_{1.84}Te_3$ bilayer heterostructures with different top layer thicknesses. Arrows indicate the sweeping directions of the magnetic field. Typical butterfly shapes are observed, and the change of peak positions by gate bias is consistent with the change in the AHE curves. The WAL peak appears when $d_1 \geq 6$ QL, and it may indicate the recovery of massless Dirac-fermions on the surface. Adopted from Ref. [145].

In order to quantitatively examine the d_1-dependent magneto-electric responses, we subsequently compare the H_C - V_g results of the TI/Cr-doped TI bilayer samples with their top

layer thicknesses varying from 0 QL to 5 QL in Figure 6-7(a). Here, the unveiled monotonically decreasing relation of $H_C - V_g$ in the *p*-type region (*i.e.,* -12 V < V_g < 5 V) possibly suggests that one of the prevailing magnetic mechanisms in the $Cr_{0.16}(Bi_{0.59}Sb_{0.41})_{1.84}Te_3$-based bilayer films (with d_I < 6 QL) is introduced by the hole-mediated RKKY interaction. Indeed, as we will elaborate in the following Section 6.4, similar to bulk itinerant carriers, the surface holes are also much more favored for mediating the *p-d* exchange coupling in the Cr-doped $(Bi_xSb_{1-x})_2Te_3$ TIs compared with surface electrons, given the fact that the DOS of the *3d* Cr ion mostly distributes below the Dirac point in the bulk band gap. In the meanwhile, due to the effective Fermi level tuning, the coercivity fields H_C are found to achieve over 100% modulation via gate-voltage control in all samples with d_I varying from 0 QL to 4 QL; the most pronounced change is obtained in the 3 QL TI / 6 QL Cr-doped TI sample, as illustrated in Figure 6-7(b). Specifically, H_C decreases steadily from 135 mT down to 65 mT with the depletion of the holes, and the corresponding electric-field-controlled coercivity field change (ΔH_C = 70 mT) is three times larger than the uniformly doped control sample (ΔH_C = 20 mT). It is important to point out that the Debye length λ_D (which is the characteristic length over which the charge carrier density in a material is affected by an external electric field through the electrostatic effects) of our grown modulation-doped TI bilayer films is estimated to be less than 3 nm at 1.9 K when the samples are biased in the inversion/accumulation regions(*i.e.,* with the electron/hole carrier density much larger than 10^{17} cm^{-3}) [6, 180, 181]. Based on our device geometry (Fig.

4-1), it implies that the applied top-gate voltage is only able to tune the Fermi level of the top surface states. Accordingly, we may conclude that the magneto-electric responses among the modulation-doped TI hetero-structures in the *p*-type regions are predominantly due to the variations of the surface-related ferromagnetism, and the pronounced enhancement of ΔH_C may reflect the optimization of the magnetic RKKY coupling between neighboring Cr ions through top surface states. Furthermore, it should be also noted that since the screening effect limits the effect of the external electric-field beyond the top surface region when the surface Fermi level is tuned away from the Dirac point, the bulk magnetizations (*i.e.,* van Vleck mechanism or bulk-carrier-mediated RKKY interaction) hence are almost irrelevant to the top-gate bias. Under the circumstance where the top-surface-related magnetic order is minimized, both the carrier-independent AHE signals observed in the d_1 = 6 QL sample (Figure 6-6(d)) and the non-zero magnetization remaining in the *n*-type regions for d_1 < 6 QL samples (V_g > 5 V in Figure 6-7(a)) can possibly be attributed to the bulk ferromagnetism (*i.e.,* not mediated by the top-surface-related effects).

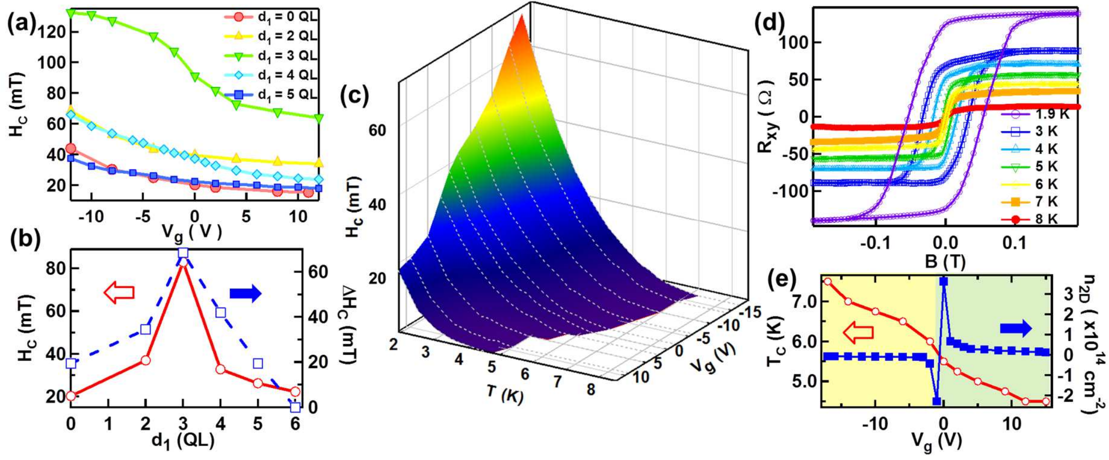

Figure 6-7. Manipulation of surface-related ferromagnetism in TI/Cr-doped TI heterostructures. (a) Gate-controlled coercivity field H_C of modulation-doped structures. The Cr-doped TI layer is fixed as 6 QL $Cr_{0.16}(Bi_{0.59}Sb_{0.41})_{1.84}Te_3$, whereas the thickness of the top undoped TI layer changes from 0 QL to 5 QL. All data are measured at 1.9 K. (b) Comparisons of the both the "neutral point" H_C and gate-controlled coercivity field change ΔH_C in modulation-doped samples with varying top surface thickness d_I. The "neutral point" is defined as the position where the surface Fermi level is tuned close to the Dirac point. (c) Three-dimensional map of the coercivity field H_C under different gate biases and temperatures for the 4 QL $(Bi_{0.5}Sb_{0.5})_2Te_3$ / 6 QL $Cr_{0.16}(Bi_{0.59}Sb_{0.41})_{1.84}Te_3$ thin film. Curie temperature T_C is estimated from the temperature-dependent AHE effect where the hysteresis behavior disappears above T_C. Many different data for various gate biases are used to construct Fig. 6-7(c). (d) Temperature-dependent anomalous Hall effect of the 4 QL TI / 6 QL Cr-doped TI thin film under the applied gate voltage of -8V. (e) Electric-field dependent Curie temperature and 2D carrier density n_{2D} as functions of V_g. The overall Hall density n_{2D} exhibits a sign change at $V_g = 0$ V. T_C decreases monotonically when the majority carriers are changed from *p*-type to *n*-type, which is consistent with the hole-mediated RKKY mechanisms on the top surface. Ref. [145].

In addition to the above realization of intrinsic magnetism, understanding the underlying magnetic phase transition and the Curie temperature is equally important. Figure 6-7(c) shows a three-dimensional map of T_C in which T_C is estimated from the evolution of the coercivity field H_C under different temperatures and the gate voltages in the 4 QL TI / 6 QL Cr-doped TI bilayer sample. Since T_C is the measure of the transition from the FM to PM state, the magnetic hysteresis window is therefore expected to be closed (*i.e.,* H_C becomes zero) when the temperature is above T_C. As an example, the temperature evolution of H_C under a fixed electric field of $V_g = -12$ V is given in Figure 6-7(d), and the Curie temperature is extracted to be $T_C = 7.3 \pm 0.2$ K. Besides, Figure 6-7(e) displays the gate-dependent T_C and the corresponding carrier density $n_{2D} - V_g$ curves. As V_g increases progressively from negative

to positive, T_C reduces, and the calculated Hall density systematically changes from *p*-type to *n*-type, which confirms the presence of the hole-mediated RKKY mechanism.

Finally, d_1-dependent magnetic results (*i.e.,* H_C and T_C) of Samples **A**, **B**, and **C** are summarized in Fig. 6-8. The highly consistency between the MOKE and AHE data again manifests the importance of the magnetic interaction range, and the optimization of the surface-related ferromagnetism in the 3 QL $(Bi_{0.5}Sb_{0.5})_2Te_3$ / 6 QL $Cr_{0.16}(Bi_{0.59}Sb_{0.41})_{1.84}Te_3$ bilayer sample.

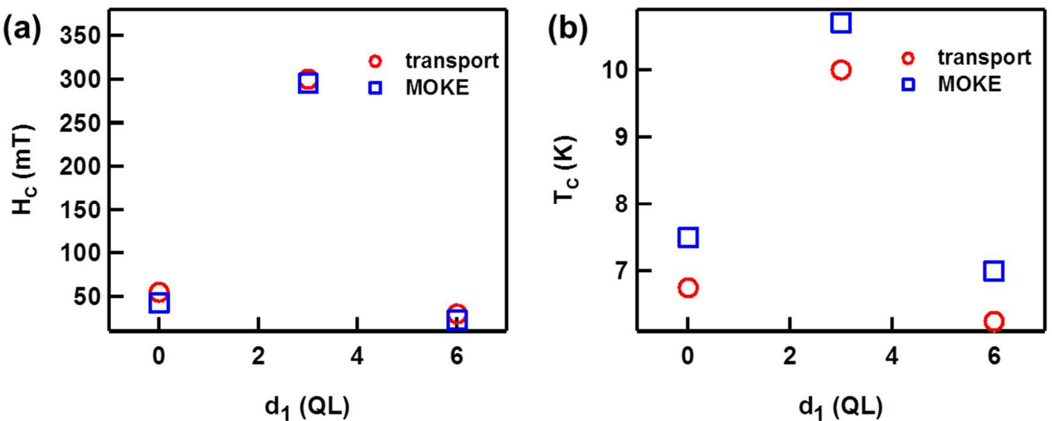

Figure 6-8. Optimization of surface-related ferromagnetism. d_1-dependent (a) coercivity field and (b) FM phase transition Curie temperature in samples **A**, **B** and **C**.

6.4. Dirac-fermion-related ferromagnetism

Section 1.3 only presents the bulk magnetic properties of the magnetic TIs. On the other hand, given the unique Dirac-cone-like linear energy band structure of the topological surface states, it was proposed that two magnetic impurities could be coupled over a much longer

distance through surface carriers without oscillation when the Fermi level approached the Dirac point [82, 83, 182]. Under such predictions, it is reasonable to conclude that the surface-mediated RKKY coupling strength should also become maximized near the Dirac point. However, the above electric-field-controlled AHE measurements on the TI/Cr-doped TI heterostructures clearly showed a hole-mediated behavior in magnetic TI materials, in contrast to the theoretical prediction. In this section, in order to resolve such ambiguity, we will show that Dirac holes are much more favorable for the surface-mediated RKKY interaction in the Cr-doped $(BiSb)_2Te_3$ system due to the particular DOS distributions of the *d*-orbital Cr^{3+} ions.

In principle, the generic RKKY long-range exchange model discussed in Section 1.3 is still valid except that the Green function, which is used to describe the TI surface states, is now given by [82]

$$G(\vec{R}_{ij}) = -\frac{E}{4\hbar^2 v_F^2}[iH_0^{(1)}(\frac{R_{ij}E}{\hbar v_F}) \mp \hat{z}\cdot(\vec{\sigma}\times\hat{n})H_1^{(1)}(\frac{R_{ij}E}{\hbar v_F})] \tag{6-4}$$

where $H_\nu^{(1)}$ is the ν-order Hankel function of the first kind. After combing Eq. (1-5) with Eq. (6-4), the surface-carrier-mediated RKKY interaction can be written as [82]

$$H_{1,2}^{RKKY} = F_1(R,E_F)\vec{S}_1\cdot\vec{S}_2 + F_2(R,E_F)(\vec{S}_1\times\vec{S}_2)_y + F_3(R,E_F)S_1^y S_2^y \tag{6-5}$$

where the range function F_1 gives rise to the Heisenberg-like term, F_2 represents the Dzyaloshinskii-Moriya-like term, and F_3 stands for the Ising-like term. According to Zhu *et*

al.'s calculations, all these range functions, F_1-F_3, still have the oscillation period of π/k_F [183-185], where k_F is the Fermi wave vector, and their magnitudes all scale with (J^2/R^3) [82]. When the surface Fermi energy level moves towards the Dirac point, the oscillation period of the RKKY interaction will diverge since the Fermi wavelength $\lambda_F = 1/k_F$ becomes infinity as k_F approaches zero [182], and thus neighboring magnetic impurities can always be coupled through the itinerant carriers when λ_F is much larger than the average distance between them, as shown in the inset of Figure 6-9(a).

On the other hand, however, we should point out that in addition to λ_F, the surface-mediated RKKY interaction is also related to the DOS distributions of both the mediating surface carriers and magnetic dopants, as we elaborated in Section 1.3 [79]. Since the DOS of Dirac surface states have the form that $D(E_F) = E_F/(\pi\hbar^2 v_F^2) = k_F/(\pi\hbar v_F)$, it is thus inversely proportional to λ_F. As a result, the overall strength of surface RKKY interaction is counterbalanced by the oscillation period (π/k_F) and D(E_F) ($\propto k_F$). In particularly, as the Fermi level approaches the Dirac point, fewer Dirac fermions around the Fermi level will take part in the surface-mediated RKKY interaction process even though λ_F becomes larger, and the two effects combined lead to a finite surface RKKY coupling in the vicinity of the Dirac point. In order to quantitatively study the surface-mediated RKKY interaction in magnetic TIs, here, we show one example of a moderate-doped $Cr_{0.16}(Bi_{0.59}Sb_{0.41})_{1.84}Te_3$ sample. In particular, with the Cr doping level of 8%, we find that the average distance between neighboring Cr^{3+} ions is $R = 11$ Å. If we further assume that the

on-site exchange parameter J is a constant of 7eVÅ^2 (the same value used in Ref. [82]), we have the range function of surface-related RKKY interaction in Fig. 6-9(b). Surprisingly, it can be seen that the range functions in the $Cr_{0.16}(Bi_{0.6}Sb_{0.4})_{1.84}Te_3$ system almost remain constant, regardless of the Fermi level position (with respect to the Dirac point).

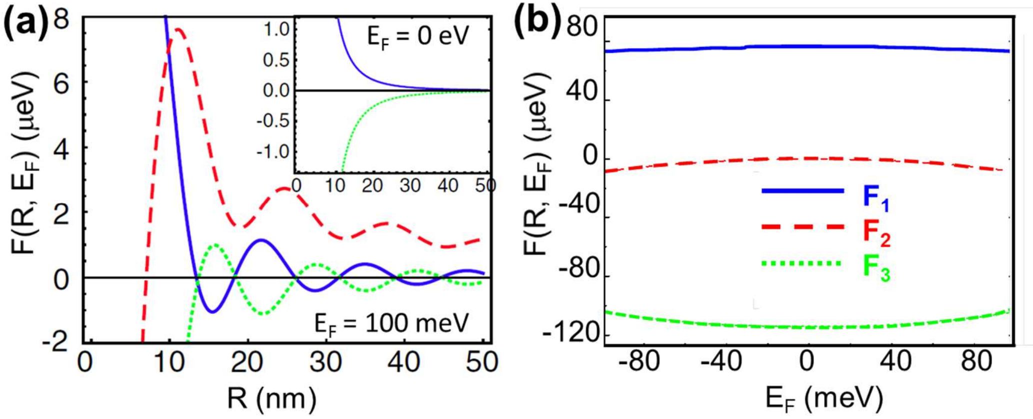

Figure 6-9. The range functions of surface-related RKKY interaction with fixed exchange parameter. (a) The range functions (F_1-F_3) of the surface RKKY interaction as a function of the distance R between localized spin when E_F is 100 meV above the Dirac point. The inset shows the intrinsic case (E_F = 0). Adopted from Ref. [82]. (b) The range functions (F_1-F_3) of the surface RKKY interaction as a function of the Fermi energy E_F for the $Cr_{0.16}(Bi_{0.59}Sb_{0.41})_{1.84}Te_3$ sample. In both (a) and (b), the on-site exchange parameter J is assumed to be a constant of 7eVÅ^2.

More importantly, as we elaborated in Section 1.3, the on-site exchange parameter J is directly related to the magnetic ion d-orbital density of states distribution $D_d(E_F)$, and therefore its magnitude is also dependent on the Fermi level position (rather than a fixed number). Combined with the DOS distribution of the Cr^{3+} ions $D_d(E_F)$ which is majorly

distributed below the Dirac point (Fig. 4-4(b)), it is concluded that Dirac holes can effectively align neighboring Cr ions, and the surface-related ferromagnetism is manifested in the *p*-type region, similar to the bulk RKKY case. Accordingly, the above scenario is consistent with our experiment results.

6.5. TI/Cr-doped TI bilayer model

To understand the optimization behavior of the surface-mediated magneto-electric effect in the TI/Cr-doped TI bilayer device, we can propose the realistic model based on two factors. First of all, it is known that both the magnetic dipole and exchange interactions from the bottom magnetic layer will force the top surface open a surface gap Δ_0. In our TI/Cr-doped TI bilayer systems, since the mediating carriers itinerate within the top surface states, the resulting exchange coupling, and thus the gap opening, will thus decay exponentially with the separation distance (d_1). Because the RKKY coupling is a second-order-perturbation interaction, its exchange strength is thus inversely proportional to the energy difference between the ground and the excited states (*i.e.,* Δ_0) [186]. On the other hand, however, since the density of surface carriers follows the $n_s(d) \propto e^{-2d/D_0}$ distribution relation and D_0 characterizes the penetration depth of the surface states with a typical value of 2 ~ 3 QLs [187, 188], it is expected that as d_1 becomes larger, fewer surface Dirac fermions will participate into the RKKY mediating process, therefore weakening the surface-related

RKKY coupling strength. Accordingly, if we take these two competing factors into consideration, the overall d_1-dependent surface-related RKKY exchange strength $< \Phi(d_1) >$ follows

$$< \Phi(d_1) >= \Phi_0 e^{-2d_1/D_0} \frac{\Delta_0}{\Delta_1 e^{-d_1/D_1} + \Delta_{dipole}} \tag{6-6}$$

where Φ_0 is the RKKY interaction strength in the uniformly Cr-doped TI film and $\Delta_0=\Delta_1+\Delta_{dipole}$ is the total surface gap opening which takes into account both the direct magnetic exchange field (Δ_1) and the long-range magnetic dipolar field (Δ_{dipole}) from the doped Cr ions. Based on Eq. (6-6), it is obvious to see that as the thickness d_1 increases, the carrier density will drop rapidly which further decreases the $\Phi_0 e^{-2d_1/D_0}$ part; on the contrary, the reduced surface Dirac fermion gap $\Delta(d_1)$ in the denominator enhances the RKKY interaction. For the $d_1 = 0$ case, Eq. (6-6) reduces to the uniformly doped case that $< \Phi(d_1) >= \Phi_0$, while in the opposite extreme condition where $d_1 = \infty$, $< \Phi(d_1) >$ returns back to zero, corresponding to the surface-bulk decoupled condition. By fitting Eq. (6-6) with the our experiment data, we obtain the d_1-dependent $< \Phi(d_1) >$ behavior in Fig. 6-10(b). In addition, the optimized condition d_1 = 3 QL (*i.e.,* $\partial(< \Phi(d_1) >)/\partial d_1 = 0$) is consistent with Fig. 6-7(b), manifesting the fundamental surface-related RKKY mechanism.

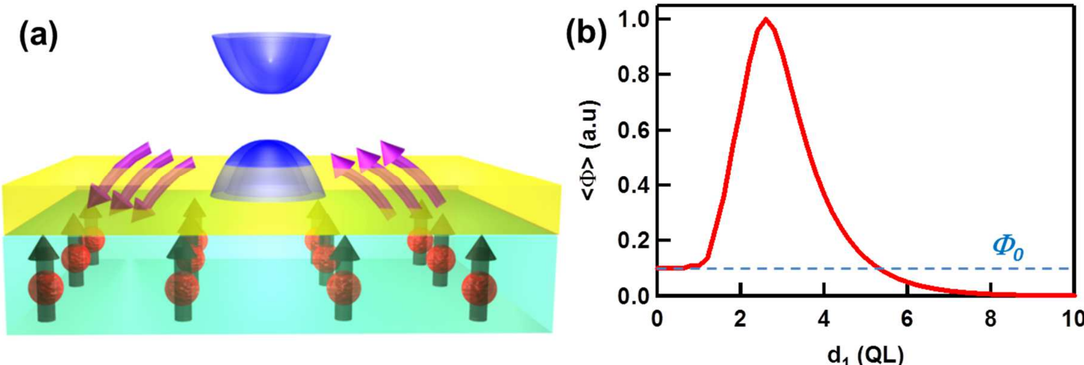

Figure 6-10. Coupling between surface carriers and magnetic dopants. (a) Schematic representations of the surface-related magneto-electric effects in the TI/Cr-doped TI bilayer structures with optimized top layer thickness d_1 = 3 QL. (b) Simulation results of the surface-mediated RKKY coupling strength as the function of d_1. Adopted from Ref. [145].

6.6. Current-induced magnetization switching in TI/Cr-doped TIs

So far, we have discussed about the influence of the FM orders on the band topology. In the meanwhile, the giant SOC in the bulk TI matrix can also affect the magnetizations. In fact, it has been observed in the heavy metals (Pt, Ta) with strong SOC, applied in-plane charge current can control the magnetization dynamics in an adjacent ferromagnet layer (Co, CoFeB) due to the spin-orbit torques (SOTs) [189-196]. Compared with the heavy metal/ferromagnetic heterostructures (HMFHs), in our conductive TI/Cr-doped TI bilayer heterostructures, a dominant spin accumulation in the TI layer with spin polarized in the transverse direction is expected when passing a charge current along the y-direction due to the SHE in the bulk and the spin polarization arising from the Rashba-type interactions at the

interfaces. A strong enhancement of the interfacial spin accumulation can be expected due to the spin-momentum locking of the topological surface states [197].

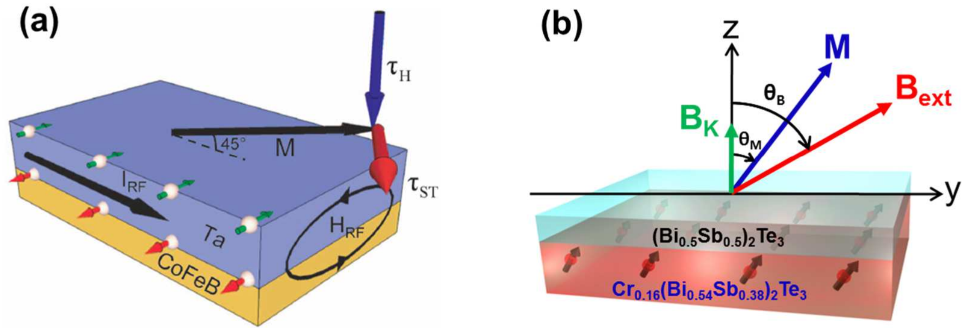

Figure 6-11. Bilayer structures used for the SOTs study. (a) Schematic of conventional HMFHs device. The SHE in the top heavy metal layer (Ta) generates spin current, and such spin current can apply efficient SOTs to the bottom FM layer (CoFeB), and in turn changes its magnetization direction. Adopted from Ref. [189]. (b) In our MBE-grown TI/Cr-doped TI system, the top TI layer provides giant SOC while the bottom Cr-doped TI serves as the FM layer. Adopted from Ref. [174].

The accumulated spins' angular momentum can be directly transferred to the magnetization M and therefore affect its dynamics. In particular, the complete form of the Landau–Lifshitz–Gilbert (LLG) equation which includes the SOT is given by [198, 199]

$$\frac{d\vec{m}}{dt} = -|\gamma|\mu_0(\vec{m}\times\vec{H}_{ex}) + \frac{\alpha}{\|\vec{m}\|}(\vec{m}\times\frac{d\vec{m}}{dt}) + \lambda_1 I[\vec{m}\times(\vec{m}\times\hat{x})] + \lambda_2 I[\hat{x}\times\vec{m}] \quad (6\text{-}7)$$

where γ is the gyromagnetic ratio, I is the charge current conducting along the longitudinal direction, $\vec{m}$ is magnetization vector, and α is the damping coefficient. In general, we have both the spin-transfer like torque $\lambda_1 I[\vec{m}\times(\vec{m}\times\hat{x})]$ and the field like torque $\lambda_2 I[\hat{x}\times\vec{m}]$.

Accordingly, we illustrate the four stable states in Fig. 6-12(a) where the applied DC current, I_{dc}, conducts along the longitudinal direction (*i.e.*, ±*y*-axis), and the external magnetic field is also applied along the ±*y*-axis in order to determine the stable states of *M*. It can be seen that in the presence of a constant external magnetic field in the *y*-direction, the *z*-component magnetization M_z can be switched, depending on the DC current conduction direction [194]; likewise, when the applied DC current is fixed, M_z can also be switched by changing the in-plane external magnetic field.

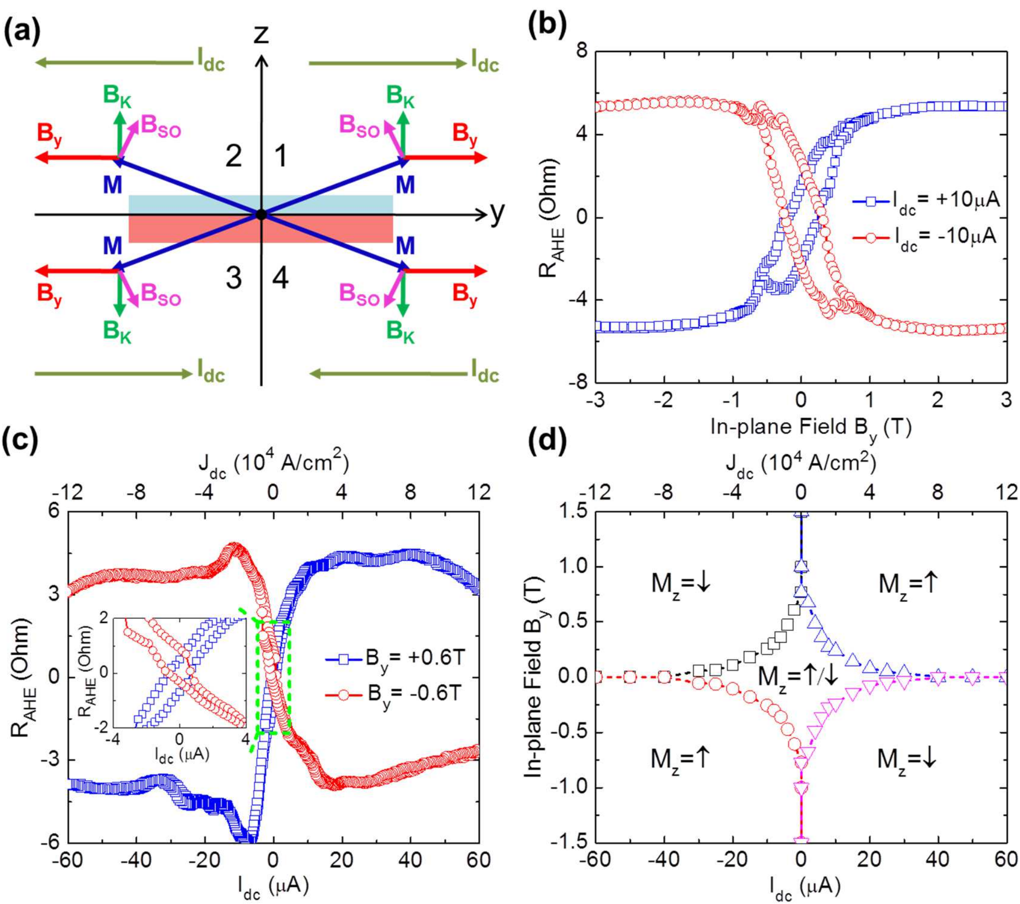

Figure 6-12. Magnetization switching due to the SOT induced by an in-plane DC current. (a) Schematic of the four stable magnetization states (panels 1-4) when passing a large DC current, I_{dc}, and applying an in-plane external magnetic field, B_y, along the ±*y*

directions. (b) The AHE resistance R_{AHE} as a function of the in-plane external magnetic field when passing a constant DC current with I_{dc} = +10 μA (blue squares) and I_{dc} = +10 μA (red circles) along the Hall bar at 1.9K, respectively. (c) Current-induced magnetization switching in the Hall bar device at 1.9K in the presence of a constant in-plane magnetic field B_y = +0.6 T (blue squares) and B_y = -0.6 T (red circles), respectively. Inset: expanded scale to show the hysteresis windows. (d) Phase diagram of the magnetization state in the presence of an in-plane external magnetic field B_y and a DC current I_{dc}. The dashed lines and symbols (obtained from experiments) represent switching boundaries between the different states. In all panels, the symbol ↑ means $M_z > 0$ and ↓ means $M_z < 0$. Adopted from Ref. [174].

Based on the above scenario, we carry out the (I_{dc}-fixed, B_y-dependent) and the (B_y-fixed, I_{dc}-dependent) experiments at 1.9K; the results are shown in Figs. 6-12(b) and (c), respectively. Specifically, when I_{dc} = +10 μA (blue squares in Fig. 6-12(b)), the AHE resistance R_{AHE} goes from negative to positive as the applied in-plane magnetic field B_y gradually changes from -3T to 3T, indicating the z-component magnetization M_z switches from -z to +z. In contrast, when I_{dc} = -10 μA, the AHE resistance reverses sign (red circles in Fig. 6-12(b)) and M_z varies from +z to -z as B_y is swept from -3T to 3T. It is noted that in both cases the AHE resistance hysteresis loops comply with Fig. 6-12(a). At the same time, when we scan the DC current I_{dc} under a given fixed magnetic field, we also observe similar magnetization switching behavior: the AHE resistance R_{AHE} changes from negative to positive for B_y = +0.6 T (blue squares in Fig. 6-12(c)), but reverses its evolution trend (*i.e.*, changes from positive to negative) for B_y = +0.6 T (red circles in Fig. 6-12(c)). In this case, the small hysteresis window in R_{AHE} is clearly visible on expanded scale as shown in the inset of Fig. 6-12(c). Consequently, both the (I_{dc}-fixed, B_y-dependent) and the (B_y-fixed, I_{dc}-dependent) magnetization switching behaviors clearly demonstrate that the magnetization

can be effectively manipulated by the current-induced SOT in our TI/Cr-doped TI bilayer heterostructures. We summarize these switching behaviors in the phase diagram in Fig. 6-12(d). For the four corner panels in Fig. 6-12(d) where the field value B_y and I_{dc} are large, the magnetization state is deterministic; however, in the central panel where B_y and I_{dc} are small, both magnetization states, up and down, are possible; this behavior agrees well with the hysteresis windows, as shown in Figs. 6-12(b) and (c), where in the low B_y and small I_{dc} region the two magnetization states are both allowed. Based on this phase diagram, it can be clearly seen that the magnetization can be easily switched with only tens of μA DC current (*i.e.*, below 8.9×10^4 A/cm^2 in current density J_{dc}), suggesting that the current-induced SOT in our TI/Cr-doped TI bilayer heterostructures is quite efficient.

6.7. Giant spin-orbit torque in TI/Cr-doped TI heterostructures

In order to quantitatively analyze the current-induced SOT in the TI/Cr-doped TI bilayer system, we further carry out second harmonic measurements of the AHE resistance to calibrate the effective spin-orbit field (B_{SO}) arising from the SOT. In particular, by sending an AC current, $I_{ac}(t) = I_0 \sin(\omega t)$, into the Hall bar device, the alternating effective field, $B_{eff}(t) = B_{SO} \sin(\omega t)$, causes the magnetization M to oscillate around its equilibrium position, which gives rise to a second harmonic AHE resistance $R_{AHE}^{2\omega} = -\frac{1}{2}\frac{dR_{AHE}}{dI} I_0$, where the

second harmonic AHE resistance $R_{AHE}^{2\omega}$ contains information of B_{SO}, given by the simple formula as

$$R_{AHE}^{2\omega} = -\frac{1}{2}\frac{R_A B_{SO}}{(|B_Y| - K)} \tag{6-8}$$

where R_A is the out-of-plane saturation AHE resistance. In Fig. 6-13(a), we show the second harmonic AHE resistance $R_{AHE}^{2\omega}$ as a function of the in-plane external magnetic field when the input AC current is given as $I_{ac}(t) = I_0 \sin(\omega t)$, where I_0 = 2 μA and ω = 15.8 Hz are used. It is found that when the in-plane external magnetic field is larger than the saturation field (*i.e.*, $|B_y| > K$), the Cr-doped TI layer is in a single domain state and polarized in the same direction as B_y, as illustrated in regions I and III in Fig. 6-13(a). Following Eq. (6-8), it is noted that the magnetization M will be polarized and the oscillation magnitude induced by the AC current will decrease if we further increase B_y, thus causing $R_{AHE}^{2\omega}$ to scale as $1/(|B_y| - K)$. By fitting the $R_{AHE}^{2\omega}$ versus B_y curve in the large field region with the above formula, we find the effective field value, $B_y \sim \pm 26.2$ mT, pointing along $+z$ or $-z$-axis depending on the direction of B_y, which is consistent with the definition of B_{SO}. Consequently, the scaling relation of $R_{AHE}^{2\omega}$ confirms that the measured 2nd-Harmonic signal indeed comes from the SOT-induced magnetization oscillation around its equilibrium position.

In addition, we also investigate the strength of the field-like torque (Eq. (6-7)) by rotating the applied magnetic field in the xz-plane (transverse to the current direction). The obtained results are plotted in Fig. 6-13(b). It can be seen that the effective field is negative at $\theta_B = 0$

and changes to positive at $\theta_B = \pi$, which means the effective field is pointing along the $-x$ direction for both cases. From Fig. 6-13(b) we can obtain that the effective field due to the field-like torque versus AC current density ratio is 0.0005 mT/(A/cm^2), which is one order of magnitude smaller than the one revealed from the spin transfer-like SOT.

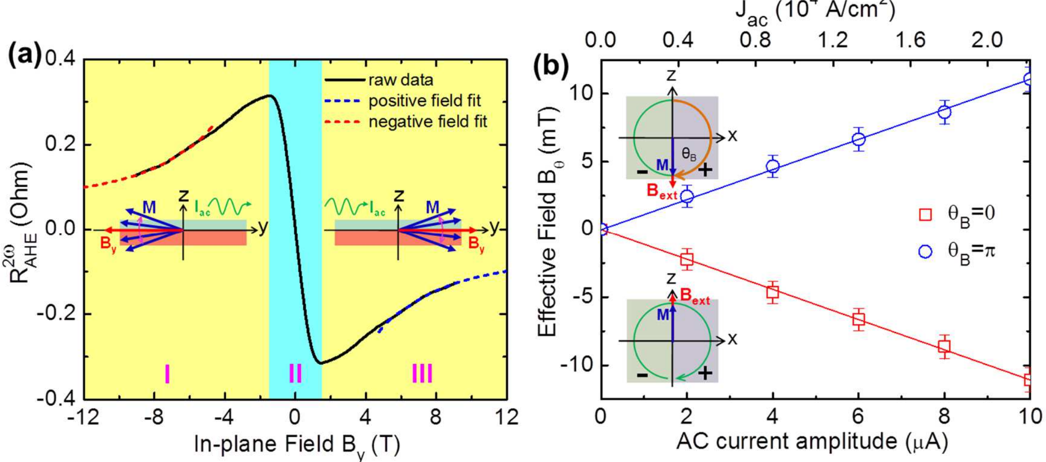

Figure 6-13. Giant spin-orbit torque realized in the TI/Cr-doped TI structures. (a) Second harmonic AHE resistance as a function of the in-plane external magnetic field. The shaded regions I, II, and III represent a single domain state pointing in the $-y$ direction, magnetization reversal, and a single domain state pointing in the $+y$ direction, respectively. The solid black line is the experimental raw data. The dashed lines denote the fitting proportional to $1/(|B_y| - K)$ in the negative field region (red line) and in the positive field region (blue line), respectively. Inset figures in regions I and III show the magnetization oscillation around its equilibrium position when passing an AC current. (b) The transverse effective spin-orbit field as a function of the AC current amplitude I_{ac} for two different θ_B angles in the xz-plane, $\theta_B = 0$ and π, respectively. In the experiments, the applied magnetic field magnitude is fixed at 2 T and the temperature is kept at 1.9 K. Straight lines in the figure are linear fittings. Adopted from Ref. [174].

6.8. Summary of Chapter 6

In this chapter, we explore the $(Bi_zSb_{1-z})_2Te_3/Cr_x(Bi_ySb_{1-y})_{2-x}Te_3$ bilayer films using the modulation-doped growth method. By controlling the separation between the top topological surface and the bottom Cr-doped magnetic TI layer, we identify the presence of surface-related ferromagnetism from the MOKE measurements. Furthermore, with effective gate modulation, the surface-mediated magnetization of the TI/Cr-doped TI hetero-structures can be either amplified or suppressed, depending on the structure engineering. These electrically controllable topological surface phenomena may help us to broaden the understanding of magnetic topological insulators and expand the functionality of TI-based devices. It may also offer new opportunities to utilize the TI heterostructures (*i.e.,* quantum wells and superlattices), in which interactions among different layers may result in even more exotic physics and applications.

In the meanwhile, borrowing the same principle of HMFHs, we demonstrate experimentally the magnetization switching via giant SOT induced by an in-plane current in the modulation-doped TI/Cr-doped TI bilayer heterostructures. The critical current density required for switching is as low as 8.9×10^4 A/cm^2 at 1.9 K. Moreover, using the second harmonic analysis of the AHE results, we find that the effective field to current ratio, as well as the spin-Hall angle tangent, is nearly three orders of magnitude larger than those reported in HMFHs. In conclusion, the giant SOT and ultra-low magnetization-switching current density revealed in our TI/Cr-doped TI bilayer heterostructures are significant. More

importantly, since the large SOC is the intrinsic property of the TI materials, it is expected that the TI-related SOT can persist even at room-temperature. Recently, A.R Melinik *et al.* reported a large SOT measured in the ferromagnetic permalloy ($Ni_{81}Fe_{19}$) – Bi_2Se_3 heterostructures at room temperature [200], again suggesting that TIs could enable efficient electrical manipulation of magnetic materials. In summary, the new progress on the SOTs-related study in TIs and their heterostructures may open up a new route dedicate to the innovative spintronics applications such as ultra-low power dissipation memory and logic devices.

Chapter 7

Conclusion and Perspective

When the SOC is strong enough to invert the conduction and valence bands in the material it creates a new state of matter, known as the time-reversal-invariant Z_2 TIs. With the unique gapless Dirac-cone-like linear *E-k* dispersion relation and the spin-momentum-locking mechanism along the surface, TIs are regarded as one of the most intriguing 2D materials, which arises broad interest among condensed-matter physics, material science, nano-electronics, spintronics, and energy harvesting applications. In parallel with the pursuit of the massless Dirac fermions, it is of equal significance to break the TRS of the TI surfaces by introducing the perpendicular magnetic interaction. In this TRS-breaking regime, the opened surface gap will give rise to a variety of novel physical phenomena such as the quantum anomalous Hall effect, single chiral mode conduction, and axion electrodynamics.

In this Dissertation, we outline our work on the magnetic TI systems and the TRS-breaking related phenomena. First of all, by using MBE growth method, we are able to prepare single crystalline Cr-doped $(BiSb)_2Te_3$ thin films with low bulk defects and well-protected topological surfaces. In the meantime, the high-resolution scanning TEM and EDX analysis provide the direct evidence that Cr ions distribute uniformly inside the host TI

system without any segregations or second phase separation. Such salient features provide us opportunities to elucidate different magnetic interactions in the magnetic TI systems.

Experimentally, we demonstrate the presence of both the hole-mediated RKKY coupling and the carrier-independent bulk van Vleck magnetism in the MBE grown Cr-doped TI samples from the top-gate-modulated magneto-transport measurements. In addition, by deliberately designing the Cr doping profile and electric-gating strategy, we realize the interplay between the aforementioned two magnetic interactions and establish the valid approach to either enhance or suppress each individual contribution. Specifically, in the moderate Cr-doped TI thin films, the applied electric field enables us to tune the surface Fermi level across the Dirac point, and therefore leads to the dramatic modulation of coercivity field exceeding 100% when the majority of the charge changes the carrier-type. On the other hand, when excessive Cr ions are introduced, the electrically controllable ferromagnetism is greatly suppressed, and robust ferromagnetic order is formed through van Vleck responses without the presence of mediating carriers. We believe these unique magneto-electric responses identified in the Cr-doped TI materials will serve as the fundamental step not only to explore the TRS-breaking TI systems but also to further expand the functionality of TI-based device for spintronics applications.

In terms of the quantum Hall trio study, we present our experimental observation of macroscopic millimeter-scale QAHE in $Cr_{0.24}(Bi_{0.3}Sb_{0.7})_{1.76}Te_3$ films across the 2D hybridization limit. Even for the thick films (10QLs), the spontaneous magnetization in our

magnetic TI film can effectively suppress bulk diffusive channels and the quantized Hall conductance of e^2/h is observed up to 85 mK for a large mm sample size. In the meanwhile, the realization of the QAHE regime in the thick magnetic TI film implies that QSHE may not be the prerequisite of QAHE; instead, once a non-zero first Chern number is formed, robust dissipationless edge conduction can always be expected in such exotic ferromagnetic insulators. Moreover, both the field-independent MR behavior and hysteresis non-local transport results in the QAHE regime indicate the presence of additional edge channels in the 10 QL film, which may result from the topological side surface states. The latter has an important implication of how nonlocal transport can be designed.

On the other hand, with additional quantum confinement, we present the first experimental observation of the QAH insulating state and the e^2/h-to-zero Hall plateau transition in the 6 QL $Cr_{0.24}(Bi_{0.3}Sb_{0.7})_{1.76}Te_3$ film up to 0.3 K (and the onsite of diffuse-to-quantum transport transition occurs as high as 20 K). We show that such QAH metal-to-insulator switching can only be achieved in high-quality samples with truly bulk insulating state and precise film thickness control. The realized zero Hall plateau and double-split longitudinal conductance are manifested from the band topology change determined by the tunable magnetic exchange-induced surface gap. Moreover, from both the field-driven and angle-assisted approaches, we establish the global QAH phase diagram in a single semicircle plot which continuously connects two quantized conductance points regardless of external magnetic fields. Such QAH phase diagram is similar to that of the

quantum Hall state, but with a totally different microscopic mechanism. Together with the demonstration of the scale-invariance of QAHE, our results thus make a major stride towards ideal low-power interconnect applications in information communication architectures. In addition, our observation of QAHE in 3D magnetic TI regime also suggests that new Chern insulators with higher numbers of QAHE conductance plateaus may be realized.

In Chapter 6, by adopting a modulation-doped growth method, we are able to design unique TI/Cr-doped TI bilayer structures with a systematic variation of chromium doping profiles. Such a unique design of the device structure provides us with an excellent platform to adjust and separate the topological surface states and the bulk magnetizations. Accordingly, we demonstrate a direct manipulation of the surface-mediated magneto-electric coupling in the modulation-doped TI bilayer-based field-effect transistors. Remarkably, uniform electric field applied inside the sample enables the surface Fermi level to move progressively across the Dirac-point, and leads to the dramatic modulation of coercivity field exceeding 100% when the majority of the surface charge changes the carrier-type. More substantially, the optimization of bilayer design provides us with another important control parameter to engineer the surface states. Specifically, the magnetic ordering can be tuned to be maximized in a 3 QL TI/ 6 QL Cr-doped TI structure, where the ferromagnetic phase transition temperature increases by 3 K compared with a uniformly doped film, and the coercivity is enhanced from 19 to 84 mT at 1.9 K. The surface-induced electric-field-controlled effect can also be completely switched-off when the top un-doped layer thickness is large than the

effective exchange length of 6QL. The unprecedented modulation-doped TI material structures and the ability to manipulate the surface-induced magneto-electric effects mark an important milestone in the development of TI materials and set a new stage for applications of the novel TI-based devices nanoelectronics in spintronics. In contrast with reported results carried on uniformly doped materials, our work may lead to a new discovery and development of new influential phenomena such as quantum anomalous Hall effect, chiral mode dissipationless conduction, and exotic particles (dyons, axions and majorana fermions) based on the time-reversal-broken surface states.

In addition to the controllable surface-related ferromagnetism, we also present our experimental results of magnetization switching via the giant SOT induced by in-plane current in the TI/Cr-doped TI heterostructures. Specifically, we observe the magnetization switching behaviors through both the (current-fixed, field-dependent) and (field-fixed, current-dependent) measurements. Intriguingly, the switching is extremely efficient that it requires only tens of μA DC current (*i.e.,* $\sim 10^4$ A/cm^2 in current density). Compared with the reported HMFH systems which all require mA-scale current (*i.e.,* above10^7 A/cm^2 in current density), our modulation-doped TI heterostructures are thus much more efficient to generate the SOT via the in-plane charge current. Equally important, we investigate quantitatively the current-induced SOT in our TI/Cr-doped TI bilayer heterostructures by measuring the effective spin-orbit field using the second harmonic measurement method. We find that the effective field to current ratio, as well as the spin-Hall angle tangent, is nearly three orders of

magnitude larger than those reported in HMFHs. Consequently, the giant SOT observed in our TI/Cr-doped TI bilayer heterostructures may unfold a new research field dedicated to heterostructures that integrate TIs and magnetic materials, and may also lead to the innovations of new SOT-related ultra-low-power spintronics devices.

In summary, all the research highlights we present in this Dissertation exhibit bright prospects and great opportunities for the magnetic TI systems, yet more efforts are required to propel the magnetic TI research towards a higher stage. For example, the QAHE state currently can only be realized at extremely low temperature, possibly due to the non-ideal sample quality (*i.e.,* surface roughness and intrinsic defects) and the tradeoff between the inverted band topology and the magnetic exchange strength. In the meanwhile, the relative low Curie temperature of the magnetic TI layer limits the performance of the TI/Cr-doped TI heterostructures at room-temperature. To overcome such challenges, the search of new TIs and Chern insulators with larger band gap is of first priority. Simultaneously, ferromagnetic/anti-ferromagnetic insulators with robust out-of-plane magnetization are also imperative. Nevertheless, with endowed unparalleled wisdom and creativity of the human society, I believe the next technology revolution featured by ultra-fast, multifunctional, low-power, non-volatile spintronics is more than foreseeable; and I would like to end this Dissertation with an old Chinese proverb “Long as the way is; I see no ending. Yet I will search high and low with my will unbending”.

References

[1] G. E. Moore, Lithography and the Future of Moores Law, *Integrated Circuit Metrology, Inspection, and Process Control IX,* 2439, 2-17, (1995).

[2] G. E. Moore, Cramming more components onto integrated circuits (Reprinted from Electronics, pg 114-117, April 19, 1965), *Proceedings of the IEEE,* 86, 82-85, (1998).

[3] G. E. Moore, Progress in digital integrated electronics, *IEDM Tech. Digest,* (1975).

[4] P. K. Bondyopadhyay, Moore's law governs the silicon revolution, *Proceedings of the IEEE,* 86, 78-81, (1998).

[5] Y. Taur and T. H. Ning, *Fundamentals of Modern VLSI Devices*: Cambridge University Press, (1998).

[6] S. M. Sze and K. K. Ng, *Physics of Semiconductor Devices*: Wiley, (2006).

[7] N. S. Kim, T. Austin, D. Blaauw, T. Mudge, F. Krisztian, J. S. Hu*, et al.*, Leakage current: Moore's law meets static power, *Computer,* 36, 68-74, (2003).

[8] T. Mudge, Power: A first-class architectural design constraint, *Computer,* 34, 52-58, (2001).

[9] A. Danowitz, K. Kelley, J. Mao, J. P. Stevenson, and M. Horowitz, CPU DB: Recording Microprocessor History, *Communications of the ACM,* 55, 55-63, (2012).

[10] D. J. Frank, R. H. Dennard, E. Nowak, P. M. Solomon, Y. Taur, and H. S. P. Wong, Device scaling limits of Si MOSFETs and their application dependencies, *Proceedings of the IEEE,* 89, 259-288, (2001).

[11] J. Wang and M. Lundstrom, Does source-to-drain tunneling limit the ultimate scaling of MOSFETs?, *International Electron Devices 2002 Meeting, Technical Digest,* 707-710, (2002).

[12] F. Assad, Z. B. Ren, D. Vasileska, S. Datta, and M. Lundstrom, On the performance limits for Si MOSFET's: A theoretical study, *IEEE Transactions on Electron Devices,* 47, 232-240, (2000).

[13] K. Natori, Scaling limit of the MOS transistor-A ballistic MOSFET, *IEICE Transactions on Electronics,* E84c, 1029-1036, (2001).

[14] Z. Or-Bach. *Paradigm shift: Semi equipment tells the future*. (2014).

[15] S. A. Wolf, D. D. Awschalom, R. A. Buhrman, J. M. Daughton, S. von Molnar, M. L. Roukes*, et al.*, Spintronics: A spin-based electronics vision for the future, *Science,* 294, 1488-1495, (2001).

[16] S. A. Wolf, A. Y. Chtchelkanova, and D. M. Treger, Spintronics - A retrospective and perspective, *IBM Journal of Research and Development,* 50, 101-110, (2006).

[17] S. A. Wolf, D. Treger, and A. Chtchelkanova, Spintronics: The future of data storage, *MRS Bulletin,* 31, 400-403, (2006).

[18] S. A. Wolf, J. W. Lu, M. R. Stan, E. Chen, and D. M. Treger, The Promise of Nanomagnetics and Spintronics for Future Logic and Universal Memory, *Proceedings of the IEEE,* 98, 2155-2168, (2010).

[19] I. Zutic, J. Fabian, and S. Das Sarma, Spintronics: Fundamentals and applications, *Reviews of Modern Physics,* 76, 323-410, (2004).

[20] I. Zutic, J. Fabian, and S. C. Erwin, Bipolar spintronics: Fundamentals and applications, *IBM Journal of Research and Development,* 50, 121-139, (2006).

[21] G. Schmidt, D. Ferrand, L. W. Molenkamp, A. T. Filip, and B. J. van Wees, Fundamental obstacle for electrical spin injection from a ferromagnetic metal into a diffusive semiconductor, *Physical Review B,* 62, R4790-R4793, (2000).

[22] D. L. Smith and R. N. Silver, Electrical spin injection into semiconductors, *Physical Review B,* 64, 045323, (2001).

[23] I. Zutic, J. Fabian, and S. C. Erwin, Spin injection and detection in silicon, *Physical Review Letters,* 97, 026602, (2006).

[24] B. T. Jonker, G. Kioseoglou, A. T. Hanbicki, C. H. Li, and P. E. Thompson, Electrical spin-injection into silicon from a ferromagnetic metal/tunnel barrier contact, *Nature Physics,* 3, 542-546, (2007).

[25] Y. Zhou, W. Han, L. T. Chang, F. X. Xiu, M. S. Wang, M. Oehme*, et al.*, Electrical spin injection and transport in germanium, *Physical Review B,* 84, 125323, (2011).

[26] H. J. Zhu, M. Ramsteiner, H. Kostial, M. Wassermeier, H. P. Schonherr, and K. H. Ploog, Room-temperature spin injection from Fe into GaAs, *Physical Review Letters,* 87, 016601, (2001).

[27] J. Moore, Topological Insulators the Next Generation, *Nature Physics,* 5, 378-380, (2009).

[28] J. E. Moore, The birth of topological insulators, *Nature,* 464, 194-198, (2010).

[29] X. L. Qi, T. L. Hughes, and S. C. Zhang, Topological field theory of time-reversal invariant insulators, *Physical Review B,* 78, 195424, (2008).

[30] X. L. Qi and S. C. Zhang, The quantum spin Hall effect and topological insulators, *Physics Today,* 63, 33-38, (2010).

[31] X. L. Qi and S. C. Zhang, Topological insulators and superconductors, *Reviews of Modern Physics,* 83, 1057, (2011).

[32] M. Z. Hasan and C. L. Kane, Colloquium: Topological insulators, *Reviews of Modern Physics,* 82, 3045-3067, (2010).

[33] Y. L. Chen, J. H. Chu, J. G. Analytis, Z. K. Liu, K. Igarashi, H. H. Kuo*, et al.*, Massive Dirac Fermion on the Surface of a Magnetically Doped Topological Insulator, *Science,* 329, 659-662, (2010).

[34] M. Konig, S. Wiedmann, C. Brune, A. Roth, H. Buhmann, L. W. Molenkamp*, et al.*, Quantum spin hall insulator state in HgTe quantum wells, *Science,* 318, 766-770, (2007).

[35] C. L. Kane and E. J. Mele, Quantum spin Hall effect in graphene, *Physical Review Letters,* 95, 226801, (2005).

[36] C. L. Kane and E. J. Mele, Z_2 topological order and the quantum spin Hall effect, *Physical Review Letters,* 95, 146802, (2005).

[37] B. A. Bernevig, T. L. Hughes, and S. C. Zhang, Quantum spin Hall effect and topological phase transition in HgTe quantum wells, *Science,* 314, 1757-1761, (2006).

[38] I. Knez, R.-R. Du, and G. Sullivan, Evidence for Helical Edge Modes in Inverted InAs/GaSb Quantum Wells, *Physical Review Letters,* 107, 136603, (2011).

[39] L. J. Du, I. Knez, G. Sullivan, and R. R. Du, Observation of Quantum Spin Hall States in InAs/GaSb Bilayers under Broken Time-Reversal Symmetry, http://arxiv.org/abs/1306.1925, (2013).

[40] J. E. Moore and L. Balents, Topological invariants of time-reversal-invariant band structures, *Physical Review B,* 75, 121306, (2007).

[41] R. Roy, Topological phases and the quantum spin Hall effect in three dimensions, *Physical Review B,* 79, 195322, (2009).

[42] L. Fu, C. L. Kane, and E. J. Mele, Topological insulators in three dimensions, *Physical Review Letters,* 98, 106803, (2007).

[43] L. Fu and C. L. Kane, Topological insulators with inversion symmetry, *Physical Review B,* 76, 045302, (2007).

[44] D. Hsieh, D. Qian, L. Wray, Y. Xia, Y. S. Hor, R. J. Cava*, et al.*, A topological Dirac insulator in a quantum spin Hall phase, *Nature,* 452, 970-U5, (2008).

[45] H. J. Zhang, C. X. Liu, X. L. Qi, X. Dai, Z. Fang, and S. C. Zhang, Topological insulators in Bi_2Se_3, Bi_2Te_3 and Sb_2Te_3 with a single Dirac cone on the surface, *Nature Physics,* 5, 438-442, (2009).

[46] Y. Xia, D. Qian, D. Hsieh, L. Wray, A. Pal, H. Lin*, et al.*, Observation of a large-gap topological-insulator class with a single Dirac cone on the surface, *Nature Physics,* 5, 398-402, (2009).

[47] D. Hsieh, Y. Xia, D. Qian, L. Wray, F. Meier, J. H. Dil*, et al.*, Observation of Time-Reversal-Protected Single-Dirac-Cone Topological-Insulator States in Bi_2Te_3 and Sb_2Te_3, *Physical Review Letters,* 103, 146401, (2009).

[48] Y. L. Chen, J. G. Analytis, J. H. Chu, Z. K. Liu, S. K. Mo, X. L. Qi*, et al.*, Experimental Realization of a Three-Dimensional Topological Insulator, Bi_2Te_3, *Science,* 325, 178-181, (2009).

[49] R. Yu, W. Zhang, H. J. Zhang, S. C. Zhang, X. Dai, and Z. Fang, Quantized Anomalous Hall Effect in Magnetic Topological Insulators, *Science,* 329, 61-64, (2010).

[50] L. A. Wray, S. Y. Xu, Y. Q. Xia, D. Hsieh, A. V. Fedorov, Y. S. Hor, *et al.*, A topological insulator surface under strong Coulomb, magnetic and disorder perturbations, *Nature Physics,* 7, 32-37, (2011).

[51] S. Y. Xu, M. Neupane, C. Liu, D. M. Zhang, A. Richardella, L. Wray, *et al.*, Hedgehog spin texture and Berry's phase tuning in a magnetic topological insulator, *Nature Physics,* (2012).

[52] S. V. Eremeev, V. N. Men'shov, V. V. Tugushev, P. M. Echenique, and E. V. Chulkov, Magnetic proximity effect at the three-dimensional topological insulator/magnetic insulator interface, *Physical Review B,* 88, 144430, (2013).

[53] W. D. Luo and X. L. Qi, Massive Dirac surface states in topological insulator/magnetic insulator heterostructures, *Physical Review B,* 87, 085431, (2013).

[54] M. R. Lang, M. Montazeri, M. C. Onbasli, X. F. Kou, Y. B. Fan, P. Upadhyaya, *et al.*, Proximity Induced High-Temperature Magnetic Order in Topological Insulator - Ferrimagnetic Insulator Heterostructure, *Nano Letters,* 14, 3459-3465, (2014).

[55] P. Wei, F. Katmis, B. A. Assaf, H. Steinberg, P. Jarillo-Herrero, D. Heiman, *et al.*, Exchange-Coupling-Induced Symmetry Breaking in Topological Insulators, *Physical Review Letters,* 110, 186807, (2013).

[56] Q. I. Yang, M. Dolev, L. Zhang, J. F. Zhao, A. D. Fried, E. Schemm, *et al.*, Emerging weak localization effects on a topological insulator-insulating ferromagnet (Bi_2Se_3-EuS) interface, *Physical Review B,* 88, 081407, (2013).

[57] M. H. Liu, J. S. Zhang, C. Z. Chang, Z. C. Zhang, X. Feng, K. Li, *et al.*, Crossover between Weak Antilocalization and Weak Localization in a Magnetically Doped Topological Insulator, *Physical Review Letters,* 108, 036805, (2012).

[58] J. M. Zhang, W. M. Ming, Z. G. Huang, G. B. Liu, X. F. Kou, Y. B. Fan, *et al.*, Stability, electronic, and magnetic properties of the magnetically doped topological insulators Bi_2Se_3, Bi_2Te_3, and Sb_2Te_3, *Physical Review B,* 88, 235131, (2013).

[59] J. M. Zhang, W. G. Zhu, Y. Zhang, D. Xiao, and Y. G. Yao, Tailoring Magnetic Doping in the Topological Insulator Bi_2Se_3, *Physical Review Letters,* 109, 266405, (2012).

[60] A. S. Nunez and J. Fernandez-Rossier, Colossal anisotropy in diluted magnetic topological insulators, *Solid State Communications,* 152, 403-406, (2012).

[61] J. J. Cha, J. R. Williams, D. S. Kong, S. Meister, H. L. Peng, A. J. Bestwick*, et al.*, Magnetic Doping and Kondo Effect in Bi_2Se_3 Nanoribbons, *Nano Letters,* 10, 1076-1081, (2010).

[62] J. G. Checkelsky, J. T. Ye, Y. Onose, Y. Iwasa, and Y. Tokura, Dirac-fermion-mediated ferromagnetism in a topological insulator, *Nature Physics,* 8, 729-733, (2012).

[63] Y. S. Hor, P. Roushan, H. Beidenkopf, J. Seo, D. Qu, J. G. Checkelsky*, et al.*, Development of ferromagnetism in the doped topological insulator $Bi_{2-x}Mn_xTe_3$, *Physical Review B,* 81, 195203, (2010).

[64] H. Li, Y. R. Song, M. Y. Yao, F. Yang, L. Mao, F. F. Zhu*, et al.*, Carriers dependence of the magnetic properties in magnetic topological insulator $Sb_{1.95-x}Bi_xCr_{0.05}Te_3$, *Applied Physics Letters,* 101, 072406, (2012).

[65] B. Li, Q. Y. Fan, F. H. Ji, Z. Liu, H. Pan, and S. Qiao, Carrier dependent ferromagnetism in chromium doped topological insulator $Cr_y(Bi_xSb_{1-x})_{2-y}Te_3$, *Physics Letters A,* 377, 1925-1929, (2013).

[66] C. Z. Chang, J. S. Zhang, M. H. Liu, Z. C. Zhang, X. Feng, K. Li*, et al.*, Thin Films of Magnetically Doped Topological Insulator with Carrier-Independent Long-Range Ferromagnetic Order, *Advanced Materials,* 25, 1065-1070, (2013).

[67] D. M. Zhang, A. Richardella, D. W. Rench, S. Y. Xu, A. Kandala, T. C. Flanagan*, et al.*, Interplay between ferromagnetism, surface states, and quantum corrections in a magnetically doped topological insulator, *Physical Review B,* 86, 205127, (2012).

[68] Z. H. Zhou, Y. J. Chien, and C. Uher, Ferromagnetic interlayer exchange coupling in semiconductor SbCrTe/Sb_2Te_3/SbCrTe trilayer structures, *Applied Physics Letters,* 89, 232501, (2006).

[69] Z. H. Zhou, Y. J. Chien, and C. Uher, Thin-film ferromagnetic semiconductors based on $Sb_{2-x}V_xTe_3$ with T_C of 177 K, *Applied Physics Letters,* 87, 112503, (2005).

[70] Z. H. Zhou, Y. J. Chien, and C. Uher, Thin film dilute ferromagnetic semiconductors $Sb_{2-x}Cr_xTe_3$ with a Curie temperature up to 190 K, *Physical Review B,* 74, 224418, (2006).

[71] J. S. Dyck, C. Drasar, P. Lost'ak, and C. Uher, Low-temperature ferromagnetic properties of the diluted magnetic semiconductor $Sb_{2-x}Cr_xTe_3$, *Physical Review B,* 71, 115214, (2005).

[72] Y. J. Chien, Z. H. Zhou, and C. Uher, Growth and transport properties of $Sb_{2-x}V_xTe_3$ thin films on sapphire substrates, *Journal of Crystal Growth,* 283, 309-314, (2005).

[73] V. A. Kul'bachinskii, A. Y. Kaminskii, K. Kindo, Y. Narumi, K. Suga, P. Lostak*, et al.*, Low-temperature ferromagnetism in a new diluted magnetic semiconductor $Bi_{2-x}Fe_xTe_3$, *Jetp Letters,* 73, 352-356, (2001).

[74] J. Choi, H. W. Lee, B. S. Kim, H. Park, S. Choi, S. C. Hong*, et al.*, Magnetic and transport properties of Mn-doped Bi_2Se_3 and Sb_2Se_3, *Journal of Magnetism and Magnetic Materials,* 304, E164-E166, (2006).

[75] J. S. Dyck, P. Hajek, P. Losit'ak, and C. Uher, Diluted magnetic semiconductors based on $Sb_{2-x}V_xTe_3$ ($0.01 < x < 0.03$), *Physical Review B,* 65, 115212, (2002).

[76] H. Ohno, A. Shen, F. Matsukura, A. Oiwa, A. Endo, S. Katsumoto*, et al.*, (Ga,Mn)As: A new diluted magnetic semiconductor based on GaAs, *Applied Physics Letters,* 69, 363-365, (1996).

[77] Y. Ohno, D. K. Young, B. Beschoten, F. Matsukura, H. Ohno, and D. D. Awschalom, Electrical spin injection in a ferromagnetic semiconductor heterostructure, *Nature,* 402, 790-792, (1999).

[78] H. Munekata, H. Ohno, S. Vonmolnar, A. Segmuller, L. L. Chang, and L. Esaki, Diluted Magnetic III-V Semiconductors, *Physical Review Letters,* 63, 1849-1852, (1989).

[79] M. A. Ruderman and C. Kittel, Indirect Exchange Coupling of Nuclear Magnetic Moments by Conduction Electrons, *Physical Review,* 96, 99-102, (1954).

[80] T. Kasuya, A Theory of Metallic Ferromagnetism and Antiferromagnetism on Zeners Model, *Progress of Theoretical Physics,* 16, 45-57, (1956).

[81] K. Yosida, Anomalous Electrical Resistivity and Magnetoresistance Due to an *s-d* Interaction in Cu-Mn Alloys, *Physical Review,* 107, 396-403, (1957).

[82] J. J. Zhu, D. X. Yao, S. C. Zhang, and K. Chang, Electrically Controllable Surface Magnetism on the Surface of Topological Insulators, *Physical Review Letters,* 106, 097201, (2011).

[83] D. A. Abanin and D. A. Pesin, Ordering of Magnetic Impurities and Tunable Electronic Properties of Topological Insulators, *Physical Review Letters,* 106, 136802, (2011).

[84] C. H. Ziener, S. Glutsch, and F. Bechstedt, RKKY interaction in semiconductors: Effects of magnetic field and screening, *Physical Review B,* 70, 075205, (2004).

[85] T. Jungwirth, K. Y. Wang, J. Masek, K. W. Edmonds, J. Konig, J. Sinova*, et al.*, Prospects for high temperature ferromagnetism in (Ga,Mn)As semiconductors, *Physical Review B,* 72, 165204, (2005).

[86] J. H. Van Vleck, *The theory of electric and magnetic susceptibilities*: Oxford University Press, (1952).

[87] N. Nagaosa, J. Sinova, S. Onoda, A. H. MacDonald, and N. P. Ong, Anomalous Hall effect, *Reviews of Modern Physics,* 82, 1539-1592, (2010).

[88] E. H. Hall, On a New Action of the Magnet on Electric Currents, *Am. J. Math,* 2, 287-92, (1879).

[89] E. H. Hall, On the "Rotational Coefficient" in Nickel and Cobalt, *Phil. Mag.,* 12, 157-72, (1881).

[90] Y. K. Kato, R. C. Myers, A. C. Gossard, and D. D. Awschalom, Observation of the spin hall effect in semiconductors, *Science,* 306, 1910-1913, (2004).

[91] J. Smit, The Spontaneous Hall Effect in Ferromagnetics I, *Physica,* 21, 877-887, (1955).

[92] J. Smit, The Spontaneous Hall Effect in Ferromagnetics II, *Physica,* 24, 39-51, (1958).

[93] N. A. Sinitsyn, Q. Niu, J. Sinova, and K. Nomura, Disorder effects in the anomalous Hall effect induced by Berry curvature, *Physical Review B,* 72, 045346, (2005).

[94] N. A. Sinitsyn, Q. Niu, and A. H. MacDonald, Coordinate shift in the semiclassical Boltzmann equation and the anomalous Hall effect, *Physical Review B,* 73, 075318, (2006).

[95] N. A. Sinitsyn, Semiclassical theories of the anomalous Hall effect, *Journal of Physics-Condensed Matter,* 20, 023201, (2008).

[96] X. J. Wang, D. Vanderbilt, J. R. Yates, and I. Souza, Fermi-surface calculation of the anomalous Hall conductivity, *Physical Review B,* 76, 195109, (2007).

[97] F. D. M. Haldane, Berry curvature on the Fermi surface: Anomalous Hall effect as a topological Fermi-liquid property, *Physical Review Letters,* 93, 206602, (2004).

[98] J. Sinova, S. O. Valenzuela, J. Wunerlich, C. H. Back, and T. Jungwirth, spin Hall effect, *arXiv.org,* 1411.3249v1, (2014).

[99] M. I. Dyakonov and V. I. Perel, Current-Induced Spin Orientation of Electrons in Semiconductors, *Physics Letters A,* A 35, 459-&, (1971).

[100] J. E. Hirsch, Spin Hall effect, *Physical Review Letters,* 83, 1834-1837, (1999).

[101] J. Wunderlich, B. Kaestner, J. Sinova, and T. Jungwirth, Experimental observation of the spin-Hall effect in a two-dimensional spin-orbit coupled semiconductor system, *Physical Review Letters,* 94, 047204, (2005).

[102] L. Onsager, Interpretation of the de Haas-van Alphen Effect, *Philosophical Magazine,* 43, 1006-1008, (1952).

[103] A. B. Fowler, F. F. Fang, W. E. Howard, and P. J. Stiles, Magneto-Oscillatory Conductance in Silicon Surfaces, *Physical Review Letters,* 16, 901, (1966).

[104] K. V. Klitzing, G. Dorda, and M. Pepper, New Method for High-Accuracy Determination of the Fine-Structure Constant Based on Quantized Hall Resistance, *Physical Review Letters,* 45, 494-497, (1980).

[105] D. J. Thouless, M. Kohmoto, M. P. Nightingale, and M. Dennijs, Quantized Hall Conductance in a Two-Dimensional Periodic Potential, *Physical Review Letters,* 49, 405-408, (1982).

[106] F. D. M. Haldane, Model for a Quantum Hall-Effect without Landau-Levels - Condensed-Matter Realization of the Parity Anomaly, *Physical Review Letters,* 61, 2015-2018, (1988).

[107] Y. B. Zhang, Y. W. Tan, H. L. Stormer, and P. Kim, Experimental observation of the quantum Hall effect and Berry's phase in graphene, *Nature,* 438, 201-204, (2005).

[108] K. S. Novoselov, A. K. Geim, S. V. Morozov, D. Jiang, M. I. Katsnelson, I. V. Grigorieva*, et al.*, Two-dimensional gas of massless Dirac fermions in graphene, *Nature,* 438, 197-200, (2005).

[109] Y. Xu, I. Miotkowski, C. Liu, J. F. Tian, H. Nam, N. Alidoust*, et al.*, Observation of topological surface state quantum Hall effect in an intrinsic three-dimensional topological insulator, *Nature Physics,* 10, 956-963, (2014).

[110] C. X. Liu, X. L. Qi, X. Dai, Z. Fang, and S. C. Zhang, Quantum anomalous Hall effect in $Hg_{1-y}Mn_yTe$ quantum wells, *Physical Review Letters,* 101, 146802, (2008).

[111] Y. Zhang, K. He, C. Z. Chang, C. L. Song, L. L. Wang, X. Chen*, et al.*, Crossover of the three-dimensional topological insulator Bi_2Se_3 to the two-dimensional limit, *Nature Physics,* 6, 584-588, (2010).

[112] M. R. Lang, L. He, X. F. Kou, P. Upadhyaya, Y. B. Fan, H. Chu*, et al.*, Competing Weak Localization and Weak Antilocalization in Ultrathin Topological Insulators, *Nano Letters,* 13, 48-53, (2013).

[113] H. Z. Lu, W. Y. Shan, W. Yao, Q. Niu, and S. Q. Shen, Massive Dirac fermions and spin physics in an ultrathin film of topological insulator, *Physical Review B,* 81, 115407, (2010).

[114] C. Z. Chang, J. S. Zhang, X. Feng, J. Shen, Z. C. Zhang, M. H. Guo*, et al.*, Experimental Observation of the Quantum Anomalous Hall Effect in a Magnetic Topological Insulator, *Science,* 340, 167-170, (2013).

[115] H. Z. Lu, A. Zhao, and S. Q. Shen, Quantum Transport in Magnetic Topological Insulator Thin Films, *Physical Review Letters,* 111, 146802, (2013).

[116] J. Wang, B. Lian, H. J. Zhang, and S. C. Zhang, Anomalous Edge Transport in the Quantum Anomalous Hall State, *Physical Review Letters,* 111, 086803, (2013).

[117] T. Jungwirth, Q. Niu, and A. H. MacDonald, Anomalous Hall effect in ferromagnetic semiconductors, *Physical Review Letters,* 88, 207208, (2002).

[118] Z. Fang, N. Nagaosa, K. S. Takahashi, A. Asamitsu, R. Mathieu, T. Ogasawara*, et al.*, The anomalous Hall effect and magnetic monopoles in momentum space, *Science,* 302, 92-95, (2003).

[119] R. L. Chu, J. R. Shi, and S. Q. Shen, Surface edge state and half-quantized Hall conductance in topological insulators, *Physical Review B,* 84, 085312, (2011).

[120] J. Wang, B. A. Lian, H. J. Zhang, Y. Xu, and S. C. Zhang, Quantum Anomalous Hall Effect with Higher Plateaus, *Physical Review Letters,* 111, 136801, (2013).

[121] K. He, X. C. Ma, X. Chen, L. Lu, Y. Y. Wang, and Q. K. Xue, From magnetically doped topological insulator to the quantum anomalous Hall effect, *Chinese Physics B,* 22, 067305, (2013).

[122] H. Jiang, Z. H. Qiao, H. W. Liu, and Q. Niu, Quantum anomalous Hall effect with tunable Chern number in magnetic topological insulator film, *Physical Review B,* 85, 045445, (2012).

[123] M. Stone, *Quantum Hall Effect*: World Scientific, (1992).

[124] M. B. Panish, Molecular-Beam Epitaxy, *Science,* 208, 916-922, (1980).

[125] A. Ichimiya and P. I. Cohen, *Reflection high-energy electron diffraction*: Cambridge University Press, (2004).

[126] J. H. Neave, P. J. Dobson, B. A. Joyce, and J. Zhang, Reflection High-Energy Electron-Diffraction Oscillations from Vicinal Surfaces-a New Approach to Surface-Diffusion Measurements, *Applied Physics Letters,* 47, 100-102, (1985).

[127] L. He, X. F. Kou, and K. L. Wang, Review of 3D topological insulator thin-film growth by molecular beam epitaxy and potential applications, *Physica Status Solidi-Rapid Research Letters,* 7, 50-63, (2013).

[128] A. Koma, Vanderwaals Epitaxy - a New Epitaxial-Growth Method for a Highly Lattice-Mismatched System, *Thin Solid Films,* 216, 72-76, (1992).

[129] K. K. Christenson, S. M. Smith, and D. Werho, Removing Metallic Contaminants in an RCA-2 Clean as a Function of Blend Ration and Temperature, *Microcontamination,* 12, 47-53, (1994).

[130] K. Ueno, M. Sakurai, and A. Koma, Van-Der-Waals Epitaxy on Hydrogen-Terminated Si(111) Surfaces and Investigation of Its Growth-Mechanism by Atomic-Force Microscope, *Journal of Crystal Growth,* 150, 1180-1185, (1995).

[131] X. F. Kou, W. J. Jiang, M. R. Lang, F. X. Xiu, L. He, Y. Wang*, et al.*, Magnetically doped semiconducting topological insulators, *Journal of Applied Physics,* 112, 063912, (2012).

[132] L. He, F. X. Xiu, Y. Wang, A. V. Fedorov, G. Huang, X. F. Kou*, et al.*, Epitaxial growth of Bi_2Se_3 topological insulator thin films on Si (111), *Journal of Applied Physics,* 109, 103702, (2011).

[133] M. R. Lang, L. He, F. X. Xiu, X. X. Yu, J. S. Tang, Y. Wang*, et al.*, Revelation of Topological Surface States in Bi_2Se_3 Thin Films by In Situ Al Passivation, *Acs Nano,* 6, 295-302, (2012).

[134] C. Z. Chang, P. Z. Tang, Y. L. Wang, X. Feng, K. Li, Z. C. Zhang*, et al.*, Chemical-Potential-Dependent Gap Opening at the Dirac Surface States of Bi_2Se_3 Induced by Aggregated Substitutional Cr Atoms, *Physical Review Letters,* 112, 056801, (2014).

[135] L. He, X. F. Kou, M. R. Lang, E. S. Choi, Y. Jiang, T. X. Nie*, et al.*, Evidence of the two surface states of $(Bi_{0.53}Sb_{0.47})_2Te_3$ films grown by van der Waals epitaxy, *Scientific Reports,* 3:3406, 2013).

[136] X. F. Kou, M. R. Lang, Y. B. Fan, Y. Jiang, T. X. Nie, J. M. Zhang*, et al.*, Interplay between Different Magnetisms in Cr-Doped Topological Insulators, *Acs Nano,* 7, 9205-9212, (2013).

[137] J. Clarke, SQUID fundamentals, *Squid Sensors: Fundamentals, Fabrication and Applications,* 329, 1-62, (1996).

[138] F. X. Xiu, Y. Wang, J. Kim, A. Hong, J. S. Tang, A. P. Jacob*, et al.*, Electric-field-controlled ferromagnetism in high-Curie-temperature $Mn_{0.05}Ge_{0.95}$ quantum dots, *Nature Materials,* 9, 337-344, (2010).

[139] J. M. Coey, *Magnetism and magnetic materials*: Cambridge University Press, (2010).

[140] R. K. Wangsness, Exchange Coupling and the Curie-Weiss Law, *Journal of Chemical Physics,* 20, 1656-1656, (1952).

[141] A. Arrott, Criterion for Ferromagnetism from Observations of Magnetic Isotherms, *Physical Review,* 108, 1394-1396, (1957).

[142] A. Arrott and J. E. Noakes, Approximate Equation of State for Nickel near Its Critical Temperature, *Physical Review Letters,* 19, 786, (1967).

[143] W. Jiang, X. Zhou, and G. Williams, Is a griffiths phase a prerequisite for colossal magnetoresistance?, *Physical Review Letters,* 99, 177203, (2007).

[144] W. L. Lee, S. Watauchi, V. L. Miller, R. J. Cava, and N. P. Ong, Dissipationless anomalous Hall current in the ferromagnetic spinel $CuCr_2Se_{4-x}Br_x$, *Science,* 303, 1647-1649, (2004).

[145] X. F. Kou, L. He, M. R. Lang, Y. B. Fan, K. Wong, Y. Jiang*, et al.*, Manipulating Surface-Related Ferromagnetism in Modulation-Doped Topological Insulators, *Nano Letters,* 13, 4587-4593, (2013).

[146] G. M. Dalpian and S. H. Wei, Carrier-mediated stabilization of ferromagnetism in semiconductors: holes and electrons, *Physica Status Solidi B-Basic Solid State Physics,* 243, 2170-2187, (2006).

[147] J. S. Lee, A. Richardella, D. W. Rench, R. D. Fraleigh, T. C. Flanagan, J. A. Borchers*, et al.*, Ferromagnetism and spin-dependent transport in *n*-type Mn-doped bismuth telluride thin films, *Physical Review B,* 89, 174425, (2014).

[148] H. Z. Lu, J. R. Shi, and S. Q. Shen, Competition between Weak Localization and Antilocalization in Topological Surface States, *Physical Review Letters,* 107, 076801, (2011).

[149] H. Z. Lu and S. Q. Shen, Weak localization of bulk channels in topological insulator thin films, *Physical Review B,* 84, 125138, (2011).

[150] H. Jin, J. Im, and A. J. Freeman, Topological and magnetic phase transitions in Bi_2Se_3 thin films with magnetic impurities, *Physical Review B,* 84, 134408, (2011).

[151] J. S. Zhang, C. Z. Chang, P. Z. Tang, Z. C. Zhang, X. Feng, K. Li*, et al.*, Topology-Driven Magnetic Quantum Phase Transition in Topological Insulators, *Science,* 339, 1582-1586, (2013).

[152] X. F. Kou, S. T. Guo, Y. B. Fan, L. Pan, M. R. Lang, Y. Jiang, *et al.*, Scale-Invariant Quantum Anomalous Hall Effect in Magnetic Topological Insulators beyond the Two-Dimensional Limit, *Physical Review Letters,* 113, 137201, (2014).

[153] S. Datta, *Electronic transport in mesoscopic systems*: Cambridge university press, (1997).

[154] A. Roth, C. Brune, H. Buhmann, L. W. Molenkamp, J. Maciejko, X. L. Qi, *et al.*, Nonlocal Transport in the Quantum Spin Hall State, *Science,* 325, 294-297, (2009).

[155] C. W. J. Beenakker and H. Vanhouten, Quantum Transport in Semiconductor Nanostructures, *Solid State Physics-Advances in Research and Applications,* 44, 1-228, (1991).

[156] S. L. Sondhi, S. M. Girvin, J. P. Carini, and D. Shahar, Continuous quantum phase transitions, *Reviews of Modern Physics,* 69, 315-333, (1997).

[157] B. Huckestein, Scaling Theory of the Integer Quantum Hall-Effect, *Reviews of Modern Physics,* 67, 357-396, (1995).

[158] S. Kivelson, D. H. Lee, and S. C. Zhang, Global Phase-Diagram in the Quantum Hall-Effect, *Physical Review B,* 46, 2223-2238, (1992).

[159] C. P. Burgess, R. Dib, and B. P. Dolan, Derivation of the semicircle law from the law of corresponding states, *Physical Review B,* 62, 15359-15362, (2000).

[160] H. P. Wei, D. C. Tsui, M. A. Paalanen, and A. M. M. Pruisken, Experiments on Delocalization and Universality in the Integral Quantum Hall-Effect, *Physical Review Letters,* 61, 1294-1296, (1988).

[161] A. M. M. Pruisken, The Integral Quantum Hall-Effect - Shortcomings of Conventional Localization Theory, *Nuclear Physics B,* 295, 653-657, (1988).

[162] D. Shahar, D. C. Tsui, M. Shayegan, R. N. Bhatt, and J. E. Cunningham, Universal Conductivity at the Quantum Hall Liquid to Insulator Transition, *Physical Review Letters,* 74, 4511-4514, (1995).

[163] M. Hilke, D. Shahar, S. H. Song, D. C. Tsui, Y. H. Xie, and D. Monroe, Experimental evidence for a two-dimensional quantized Hall insulator, *Nature,* 395, 675-677, (1998).

[164] M. Hilke, D. Shahar, S. H. Song, D. C. Tsui, Y. H. Xie, and M. Shayegan, Semicircle: An exact relation in the integer and fractional quantum Hall effect, *Europhysics Letters,* 46, 775-779, (1999).

[165] J. Wang, B. Lian, and S. C. Zhang, Universal scaling of the quantum anomalous Hall plateau transition, *Physical Review B,* 89, 085106, (2014).

[166] J. G. Checkelsky, R. Yoshimi, A. Tsukazaki, K. S. Takahashi, Y. Kozuka, J. Falson*, et al.*, Trajectory of the anomalous Hall effect towards the quantized state in a ferromagnetic topological insulator, *Nature Physics,* 10, 731-736, (2014).

[167] C. Z. Chang, W. W. Zhao, D. Y. Kim, H. J. Zhang, B. A. Assaf, D. Heiman*, et al.*, High-precision realization of robust quantum anomalous Hall state in a hard ferromagnetic topological insulator, *arXiv:1412.3758,* (2014).

[168] A. J. Bestwick, E. J. Fox, X. F. Kou, L. Pan, K. L. Wang, and D. Goldhaber-Gordon, Precise quantization of anomalous Hall effect near zero magnetic field, *arXiv:1412.3189,* (2014).

[169] J. G. Checkelsky, L. Li, and N. P. Ong, Zero-energy state in graphene in a high magnetic field, *Physical Review Letters,* 100, 206801, (2008).

[170] K. Nomura and A. H. MacDonald, Quantum Hall ferromagnetism in graphene, *Physical Review Letters,* 96, 256602, (2006).

[171] K. Yang, S. Das Sarma, and A. H. MacDonald, Collective modes and skyrmion excitations in graphene SU(4) quantum Hall ferromagnets, *Physical Review B,* 74, 075423, (2006).

[172] X. F. Kou, L. Pan, J. Wang, Y. B. Fan, E. S. Choi, W. L. Lee*, et al.*, Mapping the global phase diagram of quantum anomalous Hall effect, *arXiv:1503.04150,* (2015).

[173] L. A. Ponomarenko, R. Yang, R. V. Gorbachev, P. Blake, A. S. Mayorov, K. S. Novoselov*, et al.*, Density of States and Zero Landau Level Probed through Capacitance of Graphene, *Physical Review Letters,* 105, 136801, (2010).

[174] Y. B. Fan, P. Upadhyaya, X. F. Kou, M. R. Lang, S. Takei, Z. X. Wang*, et al.*, Magnetization switching through giant spin-orbit torque in a magnetically doped topological insulator heterostructure, *Nature Materials,* 13, 699-704, (2014).

[175] S. Judaprawira, W. I. Wang, P. C. Chao, C. E. C. Wood, D. W. Woodard, and L. F. Eastman, Modulation-Doped MBE Gaas-N-$Al_xGa_{1-x}As$ MESFETs, *Electron Device Letters,* 2, 14-15, (1981).

[176] S. F. Yoon, Y. B. Miao, K. Radhakrishnan, and H. L. Duan, Mobility enhancement in MBE-grown $In_xGa_{1-x}As/In_{0.52}Al_{0.48}As$ modulation-doped heterostructures, *Superlattices and Microstructures,* 19, 159-167, (1996).

[177] S. L. Wu and S. J. Chang, High performance δ-modulation-doped Si/SiGe heterostructure FET's grown by MBE, *Solid-State Electronics,* 43, 1313-1316, (1999).

[178] M. O. Nestoklon, N. S. Averkiev, and S. A. Tarasenko, Weak localization of two-dimensional Dirac fermions beyond the diffusion regime, *Solid State Communications,* 151, 1550-1553, (2011).

[179] H. T. He, G. Wang, T. Zhang, I. K. Sou, G. K. L. Wong, J. N. Wang*, et al.*, Impurity Effect on Weak Antilocalization in the Topological Insulator Bi_2Te_3, *Physical Review Letters,* 106, 166805, (2011).

[180] B. Sacepe, J. B. Oostinga, J. Li, A. Ubaldini, N. J. G. Couto, E. Giannini*, et al.*, Gate-tuned normal and superconducting transport at the surface of a topological insulator, *Nature Communications,* 2:575, (2011).

[181] X. X. Yu, L. He, M. R. Lang, W. J. Jiang, F. X. Xiu, Z. M. Liao*, et al.*, Separation of top and bottom surface conduction in Bi_2Te_3 thin films, *Nanotechnology,* 24, 015705, (2013).

[182] Q. Liu, C. X. Liu, C. K. Xu, X. L. Qi, and S. C. Zhang, Magnetic Impurities on the Surface of a Topological Insulator, *Physical Review Letters,* 102, 156603, (2009).

[183] T. Jungwirth, J. Sinova, J. Masek, J. Kucera, and A. H. MacDonald, Theory of ferromagnetic (III,Mn)V semiconductors, *Reviews of Modern Physics,* 78, 809-864, (2006).

[184] T. Dietl, A. Haury, and Y. M. dAubigne, Free carrier-induced ferromagnetism in structures of diluted magnetic semiconductors, *Physical Review B,* 55, R3347-R3350, (1997).

[185] J. Konig, T. Jungwirth, and A. H. MacDonald, Theory of magnetic properties and spin-wave dispersion for ferromagnetic (Ga,Mn)As, *Physical Review B,* 64, 184423, (2001).

[186] G. Rosenberg and M. Franz, Surface magnetic ordering in topological insulators with bulk magnetic dopants, *Physical Review B,* 85, 195119, (2012).

[187] Y. Y. Li, G. A. Wang, X. G. Zhu, M. H. Liu, C. Ye, X. Chen*, et al.*, Intrinsic Topological Insulator Bi_2Te_3 Thin Films on Si and Their Thickness Limit, *Advanced Materials,* 22, 4002-4007, (2010).

[188] W. Zhang, R. Yu, H. J. Zhang, X. Dai, and Z. Fang, First-principles studies of the three-dimensional strong topological insulators Bi_2Te_3, Bi_2Se_3 and Sb_2Te_3, *New Journal of Physics,* 12, 065013, (2010).

[189] L. Q. Liu, C. F. Pai, Y. Li, H. W. Tseng, D. C. Ralph, and R. A. Buhrman, Spin-Torque Switching with the Giant Spin Hall Effect of Tantalum, *Science,* 336, 555-558, (2012).

[190] K. Garello, I. M. Miron, C. O. Avci, F. Freimuth, Y. Mokrousov, S. Blugel*, et al.*, Symmetry and magnitude of spin-orbit torques in ferromagnetic heterostructures, *Nature Nanotechnology,* 8, 587-593, (2013).

[191] J. Kim, J. Sinha, M. Hayashi, M. Yamanouchi, S. Fukami, T. Suzuki*, et al.*, Layer thickness dependence of the current-induced effective field vector in Ta vertical bar CoFeB vertical bar MgO, *Nature Materials,* 12, 240-245, (2013).

[192] G. Q. Yu, P. Upadhyaya, Y. B. Fan, J. G. Alzate, W. J. Jiang, K. L. Wong*, et al.*, Switching of perpendicular magnetization by spin-orbit torques in the absence of external magnetic fields, *Nature Nanotechnology,* 9, 548-554, (2014).

[193] I. M. Miron, G. Gaudin, S. Auffret, B. Rodmacq, A. Schuhl, S. Pizzini*, et al.*, Current-driven spin torque induced by the Rashba effect in a ferromagnetic metal layer, *Nature Materials,* 9, 230-234, (2010).

[194] I. M. Miron, K. Garello, G. Gaudin, P. J. Zermatten, M. V. Costache, S. Auffret*, et al.*, Perpendicular switching of a single ferromagnetic layer induced by in-plane current injection, *Nature,* 476, 189-U88, (2011).

[195] I. M. Miron, T. Moore, H. Szambolics, L. D. Buda-Prejbeanu, S. Auffret, B. Rodmacq*, et al.*, Fast current-induced domain-wall motion controlled by the Rashba effect, *Nature Materials,* 10, 419-423, (2011).

[196] P. P. J. Haazen, E. Mure, J. H. Franken, R. Lavrijsen, H. J. M. Swagten, and B. Koopmans, Domain wall depinning governed by the spin Hall effect, *Nature Materials,* 12, 299-303, (2013).

[197] O. V. Yazyev, J. E. Moore, and S. G. Louie, Spin Polarization and Transport of Surface States in the Topological Insulators Bi2Se3 and Bi2Te3 from First Principles, *Physical Review Letters,* 105, 266806, (2010).

[198] A. Brataas, A. D. Kent, and H. Ohno, Current-induced torques in magnetic materials, *Nature Materials,* 11, 372-381, (2012).

[199] Z. Li and S. Zhang, Magnetization dynamics with a spin-transfer torque, *Physical Review B,* 68, 024404, (2003).

[200] A. R. Mellnik, J. S. Lee, A. Richardella, J. L. Grab, P. J. Mintun, M. H. Fischer*, et al.*, Spin-transfer torque generated by a topological insulator, *Nature,* 511, 449, (2014).